Sub-micron Holographic Grating Masks replicated by X-ray Contact Printing for Integrated Optics.

Kenneth Maxfield Thomas B.A., M.Sc.

A thesis submitted for the degree of Doctor of Philosophy
in the Faculty of Engineering in the University of Glasgow,

November 1989

ProQuest LLC.
789 East Eisenhower Parkway
P.O. Box 1346
Ann Arbor, MI 48106 – 1346

to my parents

Nubibus atris
Condita nullum
Fundere possunt
Sidera lumen
Si mare volvens
Turbidus Auster
Misceat aestum,
Vitrea dudum
Parque serenis
Unda diebus
Mox resoluto
Sordida caeno
Visibus obstat
Quique vagatur
Montibus altis
Defluus amnis
Saepe resistit
rupe soluti
Obice saxi
Tu quoque si vis
Lumine claro
Cernere verum
Tramite recto
Carpere callem,
Gaudia pelle,
Pelle timorem
Spemque fugato
Nec dolor adsit.
Nubila mens est
Vinctaque frenis
Haec ubi regnant.

Anicius Manlius Severinus Boethius,
floruit c. AD 480 - 524,
Philosophiae Consolationis I, vii, 1-31.

Stars in the dark clouds hid
Can give no light.
When the south wind's storm
Stirs up the rolling breakers of the sea,
The wave once glass-clear, calm
As settled days,
Now muddied with the stirred-up bottom sand
Obscures our sight.
A river wandering down the hills
Can be dammed and stopped by fallen rock
From the high crags.
You too, if you want
Clearly to see the truth
And to walk the right road straight,
Cast out joy,
Cast out fear,
Rid yourself of hope and grief.
The mind is clouded, checked,
Where these hold sway.

Acknowledgements.

The completion of this project would not have been possible without the help of many people of whom I can only thank a few here.

First I would like to take this opportunity to thank Professor J. Lamb for providing the facilities in the Electronics and Electrical Engineering Department for this research. Particularly my thanks go to my supervisor Professor C.D.W. Wilkinson for his interest and support, both in this work and with the regard to the author's welfare. I would also warmly like to thank Professor R.M. De La Rue for taking an active interest in the work and for many useful discussions; also Professor S.P. Beaumont for his helpful suggestions.

Much of the vacuum system for the x-ray unit was rebuilt with the assistance of Mr. Jimmy Young without whose help this work could not have been done. I would also like to thank Mr. Harry Anderson for discussions on some of the mechanical designs and Mr. George Thornton for getting them realised within a remarkably short period of time; Mrs. Lois Hobbs for teaching me photolithography and how to be clean in the cleanroom; Mr. Ray Darkin for operation of the dry etching machines, Mr. Bob Harkins for making the photomasks, and Miss Helen Wallace for the photography.

I would especially like to thank Mr. Ray Hutchins for his friendly enthusiasm and encouragement especially in the early part of the project and his comments on this thesis while it was being written. In this connection, I would also like to thank Mrs. Jennifer Thompson for her constructive criticism and plain speaking.

This work would not have been possible without the day to day support of the technical staff down in the Nanoelectronics Research Centre: Mr. Andy Stark, Mr. Douglas MacIntyre, Mr. Dave Gourlay, and Miss. Helen Wallace.

Thanks are also due to the other members of the Nanoelectronics Group for making life down on the third basement a little brighter and more bearable.

I would also like to thank Dr. Edwin Pun, who was my industrial supervisor, and also Dr. Marco Federighi for their help while I was down at GEC Hirst Research Centre in fulfilment of my CASE award obligations.

Financial support was provided by a Science and Engineering Research Council CASE award with GEC. While this award is gratefully acknowledged, I feel it is necessary to point out that my maintenance during this period of research was only possible with the additional help from an understanding bank manager, and from the generosity of my supervisor, the department and friends.

Last, but not least, I am grateful for the love and support of my friends who have made my time in Glasgow very pleasant.

Kenneth M. Thomas,
Glasgow, October 1989

Note on the references.

References appearing in the chapters are indicated by principle author and date:
e.g. [Thomas 1988] or where the author is mentioned in the text simply by the date:
e.g. experiments performed by Clark [1988]. The full references, arranged alphabetically, are listed after the appendices. If two or more papers appeared in the same year with the same principal author, these are distinguished in the chapters by adding *a*, *b*, etc. after the date:
e.g. [Dill 1975 a], [Dill 1975 b].

Summary of work.

The work presented in this thesis covers a wide spectrum of topics concerned with the development of a lithographic system to print periodic structures. Such structures are incorporated in integrated optical devices such as 1 st order Distributed Feedback (DFB) InGaAsP / InP semiconductor lasers and waveguide filters. The gratings were defined by holographic lithography and reproduced by x-ray contact printing.

Holographic lithography can be used to produce large area submicron gratings but its success depends upon the reflectivity of the substrate and on the processing of the resist. X-ray lithography, on the other hand is conceptually a much simpler technology and has the advantage that resist exposure is relatively insensitive to the substrate. The technique may provide a simple reliable route to high resolution (<100 nm linewidths) pattern replication with a potentially high throughput.

A two mirror symmetric interferometer arrangement was used to define the gratings. Collimating lenses were not used. A theoretical analysis of gaussian beam interference was used to predict the size of variations in period from the plane wave case.

Holographic gratings with periods down to 187 nm were exposed in AZ 1350 J photoresist with the UV lines of an argon ion laser.

Conventional thin resist holography was used to define thin resist (0.15 μm AZ 1350 J) patterns which were reactive ion etched (RIE) into GaAs wafers (360 nm period) using a CH_4: H_2 plasma.

Thick resist holographic and O_2 RIE techniques were developed to produce thick metal absorber patterns (0.3 μm high), lines and metal dot arrays, suitable for a high contrast (10:1) mask for x-ray contact printing. The metal dot arrays were produced by double holographic exposure of resist followed by angled metal evaporation (shadowing) along the lattice planes, O_2 RIE and lift-off processes.

The use of the metal patterns as masks for subsequent etching or diffusion (ion exchange in glass) into the underlying material was demonstrated.

The use of a spin - on anti reflection coating (ARC) under the resist was shown to eliminate coherent reflection effects inside the resist during holographic exposure.

Polyimide in solution was spun on to microscope coverslips and cured to form an x-ray mask substrate. Polyimide membrane x-ray masks are cheap to produce and can be conformed into intimate contact with the sample to be printed. After definition of the gold absorber pattern, a 0.3 μm polyimide layer is spun over the metal to protect it during the subsequent etching step and to provide extra strength. After attachment to metal rings the glass was dissolved away in hydrofluoric acid to produce free standing polyimide membranes 1.3 μm thick, 15 mm in diameter. The membranes are coated with a 60 nm layer of gold-palladium alloy, which is optically transparent, to form a conductive layer and to allow registration.

A soft x-ray contact printing system was designed and built to transfer the mask patterns into 0.2 μm thick PMMA (BDH) resist layers with copper L_{α} radiation [1.33 nm]. The x-ray source is an electron bombardment type; based on a VG - EG 2 electron evaporator gun. The anode was a copper hearth. A sample stage was designed to allow simple registration between sample and mask. Intimate contact between mask and sample which is necessary for high contrast pattern replication at 100 nm linewidths was achieved by an electrostatic hold-down mechanism.

285 nm period gold grating patterns were transferred into vertical walled resist patterns after 6 hour exposures at 300 W e-gun power with negligible resist shrinkage after development. The resist was developed in 1:3 mixture MIBK : IPA at 23°C for 30 seconds. Gratings were replicated on Si and Ti-coated glass substrates. The contact printing process is insensitive to the substrate material.

A 2 D array of square PMMA dots of sub-100 nm side and 285 nm period, was produced on a chip (5 mm x 5 mm area) by a double x-ray exposure of a gold grating on a polyimide membrane mask.

The polyimide masks can be reused (at least five times in these experiments). Further studies of distortions in the mask and PMMA resist response to x-ray exposure remain to be done.

Table of Contents.

Chapter 1. Introduction.

Chapter Layout.

1.1. Introduction.

Pattern generation techniques for grating devices.

The initial aim of this project was to develop an x-ray contact printing system to fabricate sub-micron diffraction gratings suitable for first order distributed feedback GaInAsP / InP semiconductor lasers[1] [Thomas 1988]. Currently the gratings for these devices are directly written onto the laser substrates either by electron beam or holographic lithographies. These pattern generation techniques are very sophisticated and labour intensive, so that they are inconvenient for mass production. Commercially produced DFB lasers tend to use second or third order gratings with periods twice or three times the fundamental period in order to ease the fabrication problems. A replication process from a previously defined grating mask would be much simpler.

In this work soft x-ray contact printing (x-ray lithography) using a copper electron bombardment source and a polyimide membrane mask system was developed to print grating patterns. X-ray lithography is the short wavelength analogue of optical contact printing and in principle provides a low cost, high through-put, parallel printing process. Once a mask has been patterned, further masks can be replicated from it.

Although the development of x-ray printing systems is an active area of research, the technology is far from mature. There are many reports in the literature of devices fabricated using x-ray printing, including recently of a DFB laser made by a Japanese group [Nakao 1989], but no such

[1]Review articles describing DFB structures include [Haus 1983], [Yariv 1973, 1977], [Kogelnik 1971, 1972, 1979], [Hunsperger 1984].

lasers are available yet commercially.

Information derived from the simple contact printing system used in this work is directly applicable to other systems using synchrotron or laser plasma sources. Mask technologies, resist materials, and resolution limits are all interchangeable. The main limitation of the low power systems is the longer exposure times that result from their exposure geometry (Chapter 5).

Before describing the project structure in detail, it is helpful to discuss some of the advantages and limitations of primary patterning techniques in the fabrication of several types of device.

Sub micron grating devices with periods below 400 nm are being used in an increasing number of applications both in integrated optics and in nanoelectronics. The grating dimensions required are much smaller than can be produced by conventional optical contact printing. For most simple integrated optical devices such as waveguide filters [Yi-Yan 1978, 1980] and couplers, defined on low refractive index media, the periods range between 200 nm and 500 μm. First order distributed feedback (DFB) laser diodes or optical filters made on III-V semiconductor substrates require much finer gratings because of the larger refractive indices of these materials at their lasing wavelengths. An AlGaAs / GaAs DFB laser with an emission wavelength at 860 nm needs a grating period of about 110 nm, while GaInAsP / InP lasers with emission wavelengths between 1.3 μm and 1.55 μm need grating periods between 235 nm and 270 nm. In these devices, the overall grating length is small, generally less than 500 μm, but it must be perfectly periodic.

There are some special applications for non-uniform gratings such as wavelength demultiplexers and focusing couplers which require period variations (chirps) [Suhara 1986] or DFB lasers which incorporate phase shifted grating elements to suppress the unwanted second axial mode [Haus 1983].

Gratings required for nanoelectronic applications [Jaros 1989] are either used to define structures which tightly confine the electrons in low dimensional semiconductor devices such as quantum wire and quantum dot arrays, or modulate the semiconductor band structure such as lateral surface superlattice (LSSL) devices. The first two applications need uniform structures of <100 nm linewidths. Here the periodicity of the array is secondary; it ensures uniformity and increases the signal strength. The periodicity is important in LSSL devices, and structures for coupling microwave frequencies into surface plasmon waves.

Holographic lithography.

Typically the laser technique is used to uniformly pattern large areas (several cm^2) of a photoresist coated wafer. The success of this process depends on the substrate reflectivity. Reflectivity causes a lateral standing wave in the resist which affects its exposure especially near the resist substrate boundary. A further processing step, such as dry etching, is needed to produce a high aspect ratio (amplitude-mark ratio) photoresist structure which is cut down to the substrate.

The minimum grating period that can be recorded by the laser technique is limited by the exposure wavelength and the angle of incidence. The minimum grating period that can be recorded using the UV lines of the argon ion and helium cadmium lasers (351.1 nm and 325 nm respectively) are of the order of 180 nm which is not fine enough for a AlGaAs / GaAs DFB laser. In practice the angle of incidence cannot easily be increased above 70° (the theoretical minimum occurs at 90°).

The grating period can be reduced by exposing the substrate through a high index medium instead of air. For example, the sample may be simultaneously exposed and developed in a developer bath (SED technique) or exposed through a high refractive index medium matched to the resist coated sample (the front prism technique). Although 100 nm period gratings have been produced using such methods, these processes are not particularly convenient if a large number of samples is to be patterned.

Electron beam lithography.

Complex grating patterns, curved gratings, chirps and phase jumps are more readily made using e-beam lithography. Although chirped gratings can be made holographically, for example by introducing curvature into one of the wavefronts with a suitable lens, and bilayer resist processes for producing phase jumps in a holographic grating have been reported, these techniques are very restricted in application. An e-beam writing system exposes patterns that are computer generated. The pattern is defined in terms of pixel elements which are then addressed in sequence by the scanning electron beam. Unwanted exposure is prevented by a beam blanking system [Smith 1974, 1986 a], [Wilkinson 1986].

The ultimate resolution of e-beam is well in the sub-100 nm range. The minimum area of an isolated pixel that can be addressed is determined by the beam spot size (< 80 Å). Typically features are patterned two or more pixels wide. For lower resolution work a smaller magnification,

i.e. larger spot size, is used.

There is a proximity effect in the resist, due to backscattering of the 50 KeV electron beam from the substrate, which makes the exposure of closely spaced fine features difficult. Higher resolution work can be done on thin membranes where the backscattering from the substrate is less.

The area that can be written without using a step and repeat control of the sample stage is small due to scan coil errors at large beam displacements. Large areas of grating can be made using a step and repeat scheme, but eliminating the phase errors between the grating areas is difficult.

E-beam lithography can make the fine grating patterns required for DFB laser diodes but it is very time consuming and uneconomic. Long times are required to serially write large area high resolution patterns such as quantum dot arrays.

X-ray contact printing[2].

Soft x-rays in the 1.0 nm to 5.0 nm wavelength range expose an e-beam resist through a membrane mask transparent to x-rays on which an absorber layer has been patterned. The mask is either in intimate contact with the sample or there is a gap of a few microns between them. The membrane layer may be a semiconductor or a polymer and the absorber layer is usually several hundred nanometers of gold [Spiller 1977].

The resolution of the process is limited by the range in the resist of the secondary electrons produced by x-ray absorption. Below a wavelength of 5.0 nm, diffraction effects are much smaller than the secondary electron range which increases rapidly with photon energy[3].

At the carbon K_α wavelength (4.4 nm) the secondary electron range and diffraction effects are of the same magnitude. The carbon wavelength thus represents the optimum for high resolution reproduction ~ 10 nm. A copper L_α source at 1.33 nm is an alternative choice; there is a reduction

[2]The x-ray technique on its own is not really a lithography, since the pattern generation has to be done by other means. Thus the term *x-ray lithography* should be reserved for both patterning and printing techniques, since together they form a complete lithographic system.

[3]The low energy of the secondary electrons (< 1 keV) in x-ray exposure compared with the energies in e-beam exposure (50 keV) means that fine structures can be replicated with less damage.

in resolution (~25 nm-50 nm) but a higher x-ray power is obtainable than from an amorphous carbon source. To obtain high resolution, intimate contact between the mask and sample is essential.

Electron bombardment x-ray sources usually approximate to point sources. The quantum efficiency for most target materials is low $<10^{-4}$, and the radiation is emitted into 2π solid angle. Large mask-source separations are necessary to minimise geometrical distortions in the printed image caused by the finite extent of the source. The flux density at the mask is small and hence exposure times are long (several hours). Higher brightness sources (synchrotrons and laser induced plasmas) are being researched but these tend to be large and expensive. Synchrotron sources are used at low wavelengths (< 1.0 nm i.e. large secondary electron ranges). Combined with large mask-sample gaps (40 μm to allow registration etc.) this means a decrease in resolution:> 0.3 μm.

The requirements for x-ray masks are rigorous: the mask substrates must be transparent to x-rays and to light; therefore they must be thin (and as a result fragile), they must be flat, dimensionally stable and of large area (> 10 mm diameter). Very soft x-ray masks must be extremely thin; at the C / Cu wavelengths, a 1 μm polyimide layer introduces a significant attenuation (~ 40 %). A suitable mask technology has yet to be established.

Several mask systems have been proposed; rigid crystalline membranes made from SiC and Si_3N_4 (or SiN) are used in synchrotron systems. Polymer membranes are preferred with very soft sources.

Self supporting polyimide membranes up to several centimeters in diameter can be made by spin coating a solution of precursor material onto a glass or semiconductor substrate. After a high temperature bake, the polymer chains become completely cross-linked producing a film which is chemically inert. After patterning the absorber layer, the underlying substrate is dissolved away in HF acid to leave the plastic film. A thin conductive layer is deposited on the film to form an electrode. The membrane is flexible enough to be conformed into intimate contact with a sample. This is done by applying a small p. d. across the mask and sample (10 V - 50 V). The mask is less likely to be damaged while in intimate contact because of its conformability.

Outline of this research.

Following some work done by Smith's group at MIT [Smith 1977], a polyimide membrane x-ray mask scheme has been adopted. Grating patterns with periods between 400 nm and 187 nm were defined in thick photoresist layers on polyimide coated glass substrates. By evaporating nichrome metal at grazing incidence to the grating planes, an etch mask is formed for the subsequent oxygen reactive ion etching (RIE) process. The development of the dry etch process allows much higher aspect ratio resist gratings with vertical side walls to be produced. Previous work had relied on fragile Si_3N_4 layers with much thinner resist [Dumas 1985]. Much thicker metal layers (0.3 μm at 100 nm linewidth) can be lifted-off from these structures allowing much higher contrast[4] x-ray masks to be produced by this process than by thin resist methods (10:1 compared to 3:1).

As the contact printer is currently designed, 5 mm x 5 mm chips coated in PMMA resist are exposed in under six hours. To date the equipment has been used to replicate 285 nm Au grating masks on Si and on Ti - coated glass. The dot array produced by a double exposure of the 285 nm period mask represents the state of the art. Sub-100 nm linewidth structures 0.2 μm high with a square cross section have been produced uniformly over 25 mm^2. As can be seen from the micrographs in Chapter 5, the PMMA images have extremely vertical walls, and there is little shrinkage. These results, coupled with the reusability of the mask indicate the promise of the technique for further work.

The holographic technique was developed to look at the direct production of grating structures on semiconductor materials and glasses by metallisation and dry etching techniques. These structures can themselves be used as masks for ion implantation, ion exchange (to make waveguides) or subsequent etching. Several applications will be described in Chapter 4.

Dry etching techniques were investigated to create arrays of quantum dots from the double holographic exposure of a photoresist layer. Sub-50 nm linewidth structures were made in GaAs by this method.

---

[4]The contrast is defined as the ratio of the flux densities passing through the mask to that passing through mask and absorber.

1.2.Survey of the following chapters.

Chapter 2 presents an introduction and a review of the laser interference technique. A simple plane wave model is used to predict the intensity patterns produced during exposure in a photoresist layer spun onto a reflective substrate. Both symmetric and asymmetric incidence cases are considered. A final section discusses the limitations due to the approximation of the incident gaussian beams to plane waves and its effect on the optical uniformity of the gratings.

The optical bench is described in Chapter 3. The experimental techniques are presented along with the different types of grating exposure; thick or thin resist layers on transparent or reflective substrates; very large period gratings (exterior prism technique) and very short period gratings (U.V.); two dimensional gratings.

Chapter 4 describes the transfer of the resist patterns to the underlying substrate by O_2 RIE and the metallisation of the grating patterns to form the x-ray absorber. Further applications of the RIE processes such as two dimensional gratings (dots) are discussed. There is a section on CH_4 / H_2 RIE into GaAs through a thin photoresist mask which was intended to lead to a DFB laser. Finally the use of a gold grating mask for ion beam milling to produce a phase grating in an ion exchanged glass waveguide is described.

Chapter 5 outlines the X-ray replication process; its advantages and limitations, and provides technical details of the exposure system, the mask fabrication process and the exposure of the samples.

Chapter 6 includes a summary and the conclusion. Further experimental work for both the holographic and x-ray systems are described. The appendices provide additional information. A program of work to fabricate a double ion exchanged Bragg filter at first order for 860 nm radiation is described in Appendix 5, along with a brief discussion of Bragg reflection.

Chapter 2. Grating Definition by Laser Interference: Discussion.

Chapter Layout.

2.1. Holographic lithography.

Photoresist gratings.

In 1967 Rudolph and Shmahl [1970] produced fine period diffraction gratings in a positive photoresist layer by exposing it to a laser interference pattern. This technique became known as Holographic Lithography because the grating can be considered to be the hologram of a point source at infinity, i.e. a plane wave.

The resist coated blank is placed in the overlap area of two expanded (collimated) laser beams. Irradiation with blue light induces chemical changes in the photoresist making it more soluble in an alkaline developer solution[1]. The spatial variations in intensity translate into variations in resist thickness after development. Exposure and development can be performed separately (ED technique) or simultaneously (SED technique).

The interference technique allows much finer period diffraction gratings (< 10000 lines mm^{-1}) over large areas (up to 350 mm diameter) to be produced than can be made by conventional ruling engines. Interference gratings are much more uniform optically than those made by mechanical techniques; there are no random or periodic errors and no ghosts or grass [Palmer 1975]. Uniformity is however affected by the flatness of the substrate and the optical quality of the beams.

Gratings with a smoothly increasing period or curved lines can be produced by introducing a spherical or cylindrical lens into one of the beams [Livanos 1977], [Katzir 1977], [Shellan 1977],

[1]Photoresist should be understood to mean positive photoresist. Negative resists tend to swell on development and are not suitable for high resolution patterning.

[Gerber 1987], but such gratings can be more conveniently formed by e-beam lithography [Suhara 1986].

Interference gratings were first used for spectroscopic purposes but were soon applied to integrated optics. Although some use was made of the actual photoresist grating itself [Yi-Yan 1980], these structures are quite lossy and are easily damaged, especially by solvents. The photoresist grating is usually used as a mask for either etching [Yi-Yan 1980], [Flanders 1974] or material deposition onto a waveguide layer.

Photoresist characterisation.

The developed profile of a photoresist pattern depends on many parameters such as exposure energy [Beesley 1969], developer concentration and time, substrate reflectivity [Widmann 1975], [Walker 1975], the ambient humidity and temperature while the film was being prepared, and critically on the temperature and duration of the photoresist baking process [Dill 1977]. It is necessary to predict the profile of a grating since it determines the efficiency with which energy is diffracted into the various orders [Beesley 1970]; an obvious example of this is blazing; slanted grooves redistribute the energy into higher orders thus increasing the resolution of the grating [Hecht 1974]. Knowledge of the profile is necessary for subsequent processing of an integrated optical device.

Fortunately there is a great amount of information on photoresists, mainly for optical lithography, to be found in the literature [AZ series technical data], [Washo 1977], [Shaw 1977].

A mathematical model of positive photoresist (AZ 1350 J) exposure was presented by Dill [1975 a, b, c.]; this model was used to predict the developed resist profile after exposure of an optical mask feature.

Photoresists are typically three component materials, consisting of a base resin which gives the resist its film making properties, a photoactive compound, which serves to inhibit dissolution of the photoresist in the developer and volatile solvents to make the material liquid for application. After the resist is spun, the film is baked at 75°C - 90°C for half an hour to drive off the solvents.

The destruction of the inhibitor by the absorption of light increases the dissolution of the base resin in the developer. Dill proposed that the rate of destruction of the inhibitor was proportional

to the local intensity inside the resist and that the resist absorption could be described in terms of a constant and an intensity dependent inhibitor concentration term:

$$\frac{\partial I(x,t)}{\partial x} = -I(x,t)[A\,M(x,t) + B] \qquad (2.1.1.)$$

and

$$\frac{\partial M(x,t)}{\partial t} = -I(x,t)M(x,t)C \qquad (2.1.2.)$$

where I (x, t) is the local intensity in the resist layer at a depth x and t is the time, M (x, t) is the normalised inhibitor concentration and A, B, C, are constants for a resist film prepared at a given bake temperature, determined by examining the optical transmittance of a photoresist film with time.

Equations (2.1.1), (2.1.2) can be solved numerically by dividing the resist into very thin sublayers which can be considered as optically uniform. The intensity is computed for small time increments so that the changes in the inhibitor concentration are kept small. Defining transmission and reflection coefficients for each layer in terms of the intensity dependent absorption of the resist allows the decrement in M (x, t) to be calculated in each layer for a given time interval. This process is continued until the required exposure dose has been given to the resist. Coherent reflections from the substrate can be easily included in this model. Spatial variations in intensity are accounted for by dividing the resist surface into areas which receive different exposure energies. The effects of development were predicted from an experimentally determined power law relationship between development rate and inhibitor concentration.

Dumas [1985] extended this model to include oblique incidence and used the lithography program SAMPLE[2] to produce developed profiles for thin resist holographic gratings from his inhibitor concentration maps.

Since the profile requirements in this work were not stringent, a more empirical ED technique was adopted. Photoresist parameters (AZ 1350 J, AZ 1450 J) were determined experimentally (Chapter 3) and from data determined by Yi-Yan [1978] and Pun [1983] in this department.

---

[2]'Simulation and modelling of profiles in lithography and etching (S.A.M.P.L.E.)', Electronics Research Laboratory, Dept. Electrical Engineering and Computer Science, University of California, Berkeley 94720.

Holographic grating exposure.

The exposure of holographic gratings is affected by the standing wave which appears in resist exposed on reflecting substrates; the resist is under-exposed at standing wave nodes. Careful calculation of resist thicknesses must be made to ensure exposure of the resist at the surface.

A plane wave treatment of the intensity patterns that are produced in the resist layer during exposure is given in section 2.2., but some of the main results will be listed here. The period of the interference fringes, Λ, is calculated to be:

$$\Lambda = \frac{\lambda_0}{2 \sin\theta} \qquad (2.1.3.)$$

where λ_0 is the vacuum exposure wavelength, and 2 θ is the angle between the beams, figure 3.2.

The period of the vertical standing wave is given by:

$$P = \Lambda . \left(\frac{4 n^2 \Lambda^2}{\lambda_0^2} - 1 \right)^{-\frac{1}{2}} \qquad (2.1.4.)$$

where n is the refractive index of the resist. n = 1.665 at 457.9 nm for AZ 1350 J.
Plots Λ against θ_1, P against Λ, and the refractive index against wavelength are given in figure 2.1. (a.)-(c.).

Thin resist processes.

Vertical or undercut resist walls are required for the successful deposition and lift-off of material from resist structures. Otherwise the deposited material forms a continuous film protecting the resist from the solvents and preventing a clean lift-off.

Submicron grating resist structures, formed on reflective substrates, are not usually developed down to the substrate. The resist thickness is usually less than P / 2. These gratings are used as masks for etching but not for lift-off.

It is possible to make high aspect ratio gratings which are cleaned out down to the substrate in thick resist layers on semiconductors [Zaidi 1988], the minimum period is limited to about 700 nm. The development of such a structure relies on the vertical development rate through the exposure intensity minima being much faster than the development rate parallel to the grating. The

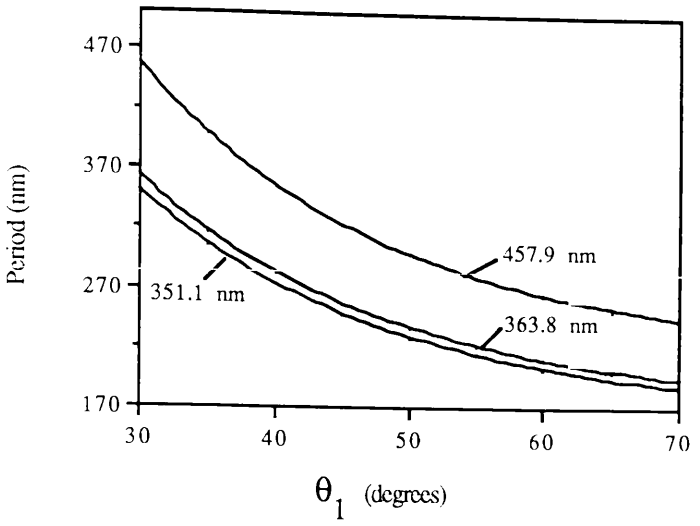

Figure 2.1.(a.) Grating period Λ as a function of angle of incidence θ_1 for the argon ion laser exposure wavelengths 351.1 nm, 363.8 nm and 457.9 nm.

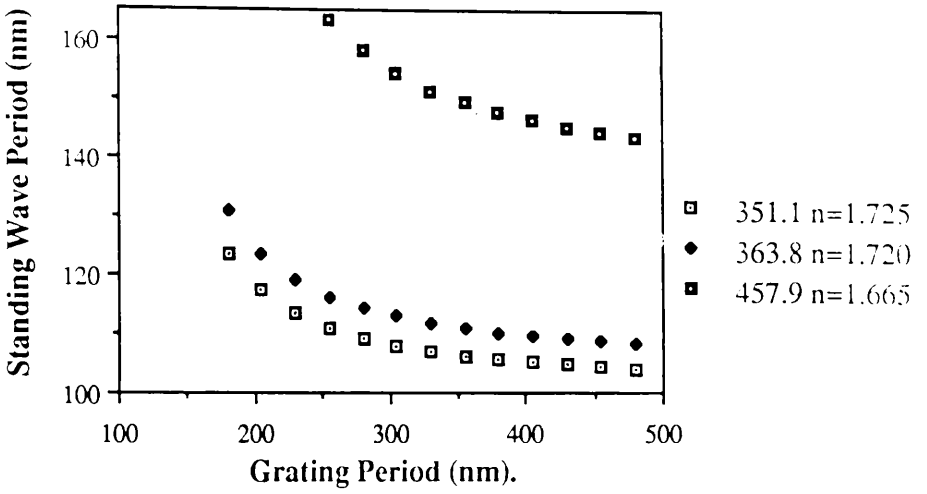

Figure 2.1.(b.) Standing wave period P, plotted against Λ, for the three argon ion laser exposure wavelengths.

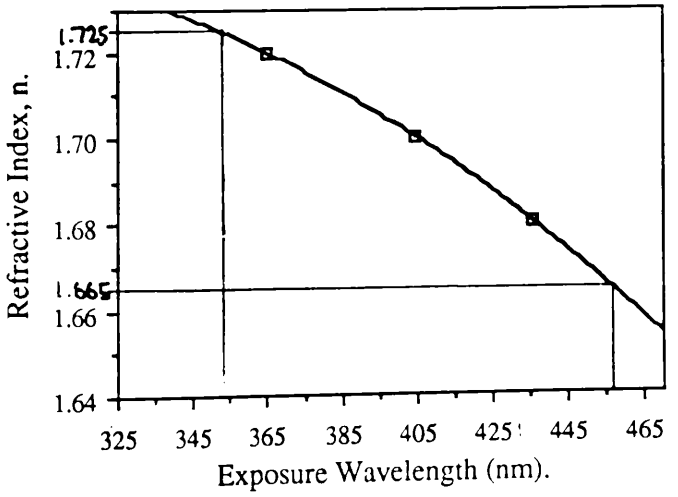

Figure 2.1.(c.) Refractive index of AZ 1350 J (source Dill (1975a)).

smaller the grating period, the thinner the resist layer has to be to prevent the grooves from becoming undercut.

An undercut profile is produced when the underlying substrate has been coated with a quarter wave dielectric layer [Efremow 1981]. The resist is now completely developed away at the base where it was fully exposed. Again the resist thickness is less than P / 2, so that the thickness of metal that can be deposited is limited to under ~70 nm. Dumas [1985] hoped to exploit this technique to make an X-ray mask by making the dielectric layer serve as the membrane mask substrate (see Chapter 5.).

Thick resist processes.

The evaporation and lift-off of thicker metal layers (< 0.3 μm) requires a thick resist technique. Such a technique was described by Anderson [1983] and used by Plotnik [1985] to make high contrast x-ray masks. A holographic grating is exposed at the surface of the resist layer and the pattern is transferred to the substrate dry etching through a mask defined by the grating. This mask can be produced in several ways; (a) either the grating can be angle evaporated with a metal (shadowing) or (b) another material with a different etch rate is applied to planarise the surface (in this case the surface is etched until the masking material is isolated in the grooves) [Smith 1986].

The thick resist holography technique has been used extensively in this work. The experimental details will be outlined in chapters 3, 4. In their 1983 paper Anderson et al report significant attenuation of the standing wave by the thick resist layer. They exposed their samples using the 333.6 nm argon ion laser line, which is near to the absorption maximum of the resist in the UV at 350 nm [AZ data]. In these experiments reflections from the back of the glass substrates were still present using the 351.1 nm argon ion line. Reflectivity effects on transparent substrates can be eliminated by using a back prism arrangement (Chapter 3.).
On semiconductors the resist is spun to a depth of (n + 0.5).P, n integer, to obtain maximum exposure at the surface.

Front Prism Technique.

At a given laser exposure wavelength the grating period is decreased by increasing θ up to a maximum value (> 70°). Yi-Yan [1978] and Dumas [1985] both reported degradation of the grating due to increased reflectivity at the higher incidence angles. This has not been observed here. The

ultimate limit on Λ is $(\lambda_0 / 2)$ $(\theta = 90°)$, which is not achieved in practice.

Grating periods smaller than the $(\lambda_0 / 2)$ limit can be made by exposing the sample through a high refractive index medium. This is the basis of the front prism technique described by Dalgoutte [1975] and Shank and Schmidt [1973].

A high index prism is index matched to a layer of photoresist which is exposed through it (figure 2.2.). Using a He Cd laser at 325 nm with a 45° half angle quartz prism Shank et al managed to make a 110 nm period grating. Obviously optical contact is very important, to avoid unwanted reflections and to couple the light efficiently into the photoresist. It is difficult to find a suitable high index fluid that does not attack the resist and can be removed afterwards. Shank and Schmidt used Xylene as the matching fluid; Yi-Yan [1978] used carbon tetrachloride. Both chemicals are among the few solvents that don't attack resist, but both are extremely toxic. We have recently obtained high index matching fluids (up to 1.70) (Cargille labs) which should simplify the processing. The oils are removed from the samples by immersing the slides in xylene before development.

Λ is given by:

$$\Lambda = \frac{\lambda_0}{2 n_p \cos\left(\psi + \sin^{-1}\left[\frac{1}{n_p} \sin\theta_e\right]\right)} \qquad (2.1.5.)$$

where θ_e is the external angle of incidence at the prism face, ψ is the prism half angle and n_p is the prism index Plots of Λ against θ_e at different values of ψ for an LAC A691547 Lanthanum crown glass prism are given in figure 2.2. The two families of curves in the figure are drawn for positive and negative values of θ_e, an exposure wavelength of 457.9 nm and a prism refractive index of 1.705. From the figure it is clear that smaller grating periods are best exposed using a negative value for θ_e since Λ varies much slower with θ_e.

Although this technique is difficult to use, it does allow gratings to be made with periods small enough for first order GaAs / AlGaAs DFB lasers or Bragg filters (see Chapter 6).

Control of grating depth - SED technique.

The problem of producing high diffraction efficiency photoresist gratings repeatably had been discussed by Beesley and Castledine [1970]. Grating uniformity can be controlled by monitoring the diffraction efficiency with a HeNe laser during development [Nakano 1988].

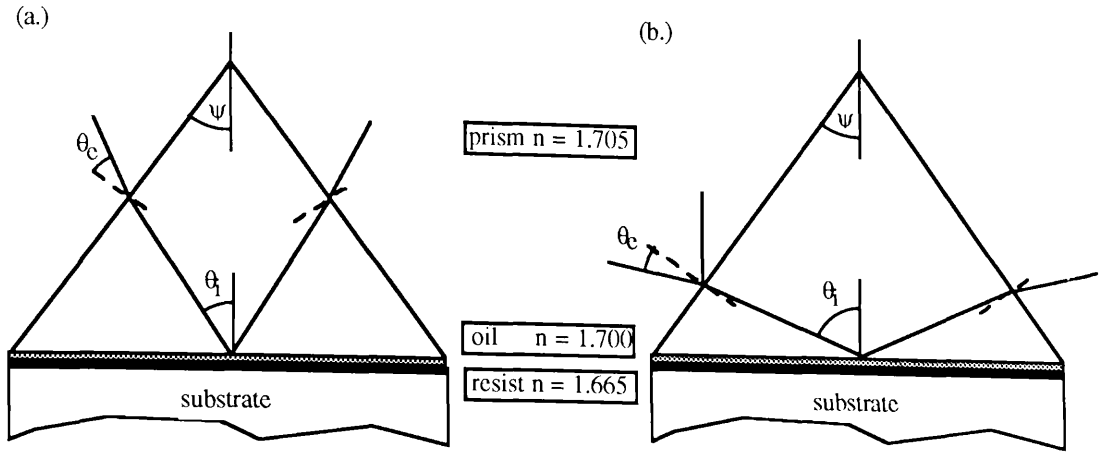

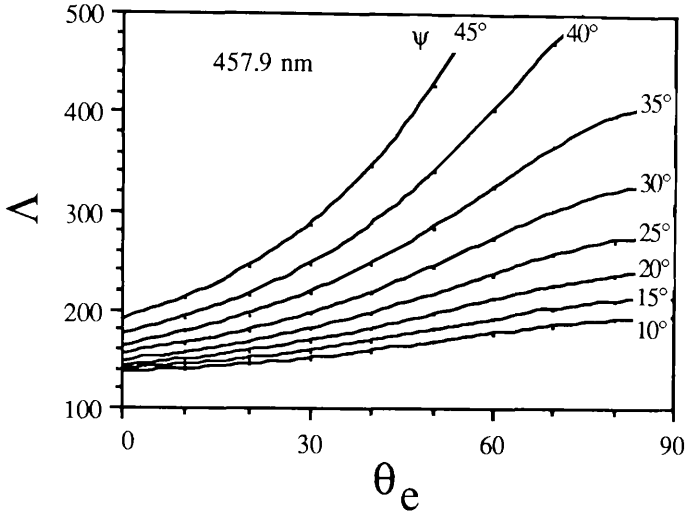

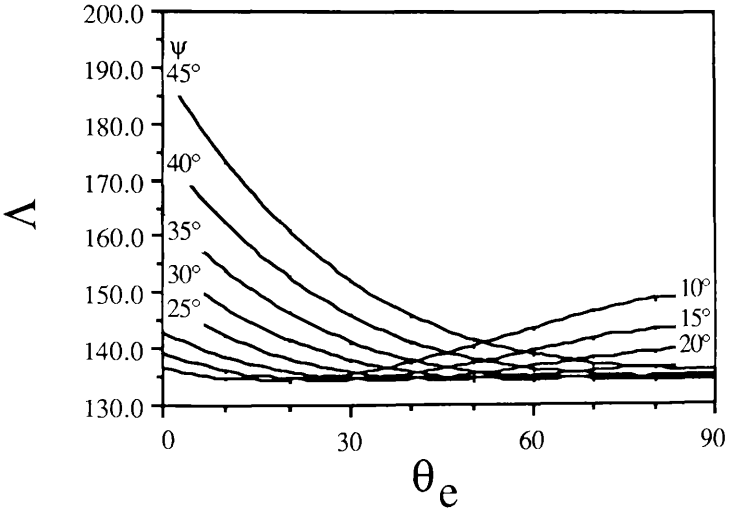

Figure 2.2. Front prism technique: (a.), (c.): positive angles of incidence.
(b.), (d.): negative angles of incidence.

Tsang and Wang [1974 a, b, c.] reported a simultaneous exposure and development (SED) technique which produces deep grating grooves with sharp edges. The samples are exposed in a prism-like bath, the walls made from optical flats. Grating groove depth is controlled via diffraction efficiency measurements. The period is given by (2.1.5.) with $n_p = 1.33$, the refractive index of the developer. Groove profiles produced in the ED technique tend to be rounder; this is because exposure throughout the resist is not uniform: when the resist is fully exposed at the bottom surface, it is over-exposed at the top surface. In the SED technique, however, the development rate increases with depth due to the cumulative exposure of the resist. Since the resist develops away as soon as it is sufficiently exposed, deep grooves with narrow lines are formed.

The success of the SED technique depends on the exposure apparatus; problems were experienced in previous work in this department [Yi-Yan] with the destruction of the cement which bonds the plates together, due to the action of the developer.

The SED technique is used with thin resist layers (< 0.2 μm) and problems occur due to undercutting with very fine periods (< 0.3 μm), so that this technique was not explored in this work.

Laser induced photochemical etching of semiconductors for DFB lasers has recently been reported. This method is similar to SED except that the samples are not coated with resist and a photochemical etch replaces the developer. The results seem promising [Bäcklin 1987], [Podlesnik 1989].

2.2. A plane wave model for holographic gratings.

A great deal of insight into grating formation can be obtained using a simple electromagnetic field model. For the case of collimated laser beams the wavefronts can be considered planar. These wavefronts are incident in medium 1 (refractive index n_1) at angles $\pm \theta_1$ to the normal to the photoresist surface (medium 2, refractive index n_2). Medium 1 is usually air or can be glass or developer if the front prism or the SED techniques are being used. The substrate forms medium 3 (refractive index n_3), figure 2.3., but see also figure 3.8.

The grating period produced inside the photoresist layer can be calculated and predictions can be made about the effects of substrate reflectivity.
Multiple amplitude reflections of the type $r_{23}.r_{21}.E_0$ are neglected. Here r_{ij} is the amplitude reflection coefficient for a wave incident in medium i onto medium j; E_0 is the electric field amplitude in the resist layer.

The model considers the photoresist layer to be a purely dielectric film without absorption so that n_2 assumed to be real. In reality, photoresist is a non linear medium whose absorption changes with exposure. Although qualitative predictions for the positions of intensity maxima and minima inside the resist can be made [Johnson 1978], the intensity distributions derived from the model will be slightly different to the final developed profile which depends on the resist non-linearities, its processing, exposure and development parameters.

The electric field vectors are plane polarised perpendicular to the plane of incidence (s-polarisation) at the resist surface by the Brewster windows on the laser plasma tube. The p-polarisation case is much more complicated [Johnson 1978] and will not be considered further.

The electric field vector lies along the y direction; the resist substrate interface lies along the x direction and the depth of the resist normal to the substate surface is measured along the z direction.

In the resist layer the complex electric fields[3] vary as:

[3]Complex quantities are written in bold italics except for j, the root of -1.

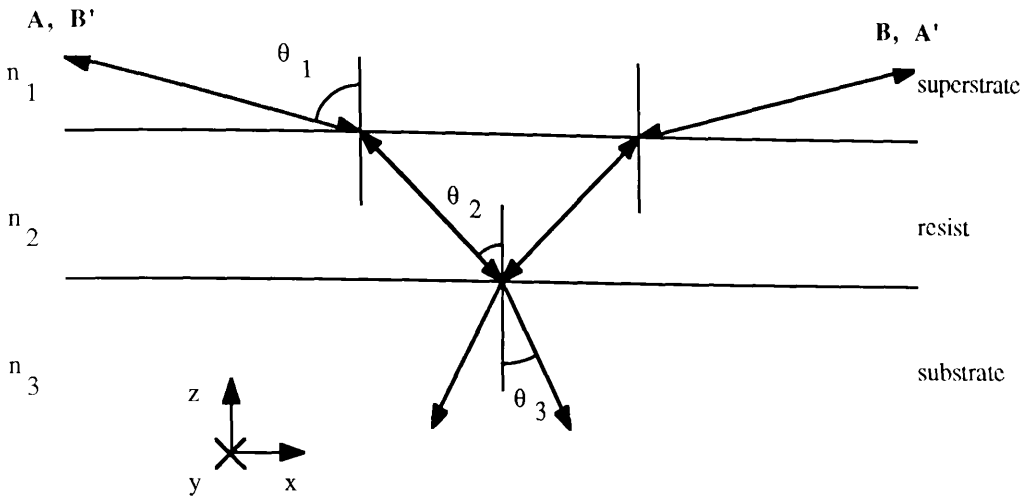

$$\Lambda = \frac{\lambda_0}{2 \sin \theta_1}$$

Figure 2.3. Three layer system for the plane wave model of holographic exposure (symmetric incidence).

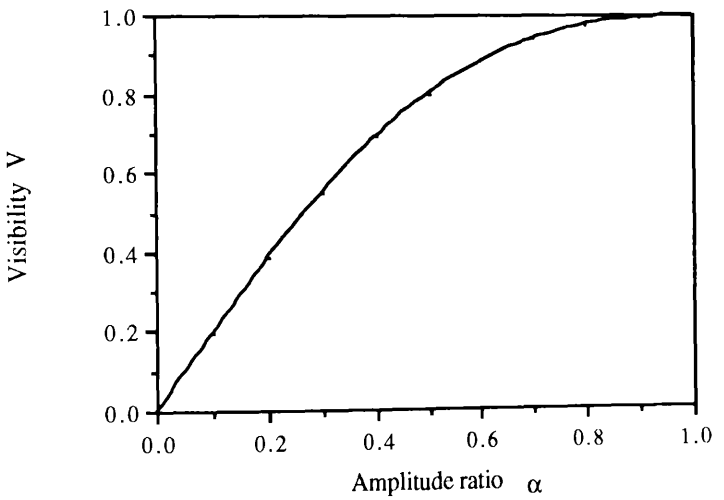

$$V = \frac{2\alpha}{1 + \alpha^2}$$

Figure 2.4. Plot of fringe visibility V against beam amplitude ratio α.

$$\boldsymbol{A}_y(x,z,t) = E_a e^{j(\omega t - k x \sin\theta_2 + k z \cos\theta_2)} \quad (2.2.1.)$$

$$\boldsymbol{B}_y(x,z,t) = E_b e^{j(\omega t + k x \sin\theta_2 + k z \cos\theta_2)} \quad (2.2.2.)$$

$$\boldsymbol{A'}_y(x,z,t) = \boldsymbol{r} E_a e^{j(\omega t - k x \sin\theta_2 - k z \cos\theta_2)} \quad (2.2.3.)$$

$$\boldsymbol{B'}_y(x,z,t) = \boldsymbol{r} E_b e^{j(\omega t + k x \sin\theta_2 - k z \cos\theta_2)} \quad (2.2.4.)$$

$\boldsymbol{A}_y$ and $\boldsymbol{B'}_y$ are the scalar amplitudes of the incident and reflected wavefronts on the LHS and $\boldsymbol{B}_y$ and $\boldsymbol{A'}_y$ are the scalar amplitudes of the incident and reflected wavefronts on the RHS of figure 2.3; $k = 2\pi n_2 / \lambda_0$.

$\boldsymbol{r}$ is the amplitude reflection coefficient, considered complex ($\boldsymbol{r} = r e^{j\phi}$) for waves incident from the resist onto the substrate ($\boldsymbol{r} = \boldsymbol{r}_{23}$). Dropping the subscript y, the total electric field in layer 2: $\boldsymbol{E}_t$ is :

$$\boldsymbol{E}_t(x,z,t) = (\boldsymbol{A}_y + \boldsymbol{B}_y + \boldsymbol{A'}_y + \boldsymbol{B'}_y) \quad (2.2.5.)$$

The photoresist pattern is determined by the intensity distribution, $I(x,z) \sim \boldsymbol{E}_t \boldsymbol{E}_t^*$:

$$\begin{aligned} I(x,z) = {} & E_a^2 + E_b^2 + r^2 (E_a^2 + E_b^2) \\ & + 2 E_a E_b (1 + r^2) \cos(2 k x \sin\theta_2) \\ & + 2 r (E_a^2 + E_b^2) \cos(2 k z \cos\theta_2 - \phi) \\ & + 4 r E_a E_b \cos(2 k x \sin\theta_2) \cos(2 k z \cos\theta_2 - \phi) \end{aligned} \quad (2.2.6.)$$

ϕ is the phase change caused by the reflection.

Several limiting cases of equation (2.2.6.) will now be discussed.

Case 1. Equal intensity beams. Zero substrate reflectivity

($E_a = E_b = E_0$, $\boldsymbol{r} = 0$). Physically this case corresponds to a glass slide contacted with index matching oil to a prism of the same refractive index which has had two of its faces painted matt black to make them absorbing, or the exposure of a sample where an anti-reflection coating has been put below the resist layer, Chapter 3.

Equation (2.2.6.) reduces to:

$$I(x) = 2 E_0^2 (1 + \cos(2 k x \sin \theta_2)) \qquad (2.2.7.)$$

The intensity is periodic in the x direction with period Λ given by $2 k \Lambda \sin \theta_2 = 2 \pi$ or:

$$\Lambda = \frac{\lambda_0}{2 n_2 \sin \theta_2} \qquad (2.2.8.)$$

Equation (2.2.8.) can be expressed in terms of θ_1, the incidence angle in air as:

$$\Lambda = \frac{\lambda_0}{2 \sin \theta_1} \qquad (2.2.8.a.)$$

The fringe visibility V, is defined by:

$$V = \frac{I_{max} - I_{min}}{I_{max} + I_{min}} \qquad (2.2.9.)$$

Substituting $I_{max} = 4 E_0^2$ and $I_{min} = 0$ in (2.2.9.) gives V = 1. In this case fringes of perfect visibility are formed throughout the resist layer.

Case 2. Different Intensity Beams. Zero reflectivity.

($E_a = \alpha E_0$, $E_b = E_0$, $r = 0$, $0 \leq \alpha \leq 1$) As described in Chapter 3, there is a 10 % intensity difference between the beams for UV laser exposures (351.1 nm). The beam splitter used is coated for operation at 325 nm. This intensity difference gives rise to a reduction in the visibility of the interference fringes.

$$I(x) = E_0^2 (1 + \alpha^2 + 2 \alpha \cos(2 k x \sin \theta_2)) \qquad (2.2.10.)$$

The period is unchanged but I_{max} and I_{min} are now $E_0 (1 + \alpha)^2$ and $E_0 (1 - \alpha)^2$ and the fringe visibility becomes:

$$V = \frac{2 \alpha}{1 + \alpha^2} \qquad (2.2.11.)$$

It is significant that V is a very slowly varying function of α for large α (Figure 2.4.). α = 0.95 for a 10% intensity difference, i.e. V = 0.999. The fringe visibility is unchanged although I_{max} is reduced to $0.25.(1 + \alpha)^2$ of its value in Case 1. Substituting $\alpha = 0.95$, I_{max} is reduced by

5 %. Note that I_{min} is non zero.

Case 3. Equal amplitude, finite reflectivity.

This case corresponds to resist on metals or semiconductor $E_a = E_b$.

$$I(x,z) = 2 E_0^2 (1 + r^2 + 2 r \cos(2 k z \cos\theta_2 - \phi)) \times (1 + \cos(2 k x \sin\theta_2)) \qquad (2.2.12.)$$

The first bracket in equation (2.2.12.) represents a lateral standing wave in the z direction of period P. This standing wave perfectly modulates the grating pattern along x in the z direction for unity reflectivity. This standing wave limits the resist thickness that can be used. For resist on semiconductors, the resist just above the substrate is not exposed, because a standing wave minimum forms there.

Since the refractive indices of semiconductors and metals are complex, their reflection coefficients have phases between 0 and π. As an example consider the case of resist spun on silicon . Silicon has a refractive index $n_3 = (4.575 - 0.1305\ j)$ at 457.9 nm so that r = 0.494, $\phi = 0.98\ \pi$ (see Appendix 1.).

According to equation (2.2.12.), the positions of minima in the standing wave pattern depend on ϕ:

$\cos(2 k z \cos\theta_2 - \phi) = -1$ or

$(2 k z \cos\theta_2 - \phi) = (2 m + 1)\pi$, where m = 0, 1, etc.

When $\phi = 0$, as it is in the case of resist on glass $n_2 > n_3$, the first minimum occurs at $z = \pi / 2 k \cos\theta_2$ (m = 0). An intensity maximum is formed at the substrate surface.

When $\phi = \pi$ as it would be for resist spun on sapphire for example, a minimum occurs at $z = 2\pi / 2 k \cos\theta_2$ (m = 0), but there is also a minimum at z = 0 since this value of z is equal to P.

When $\phi = 0.96\ \pi$ for resist on silicon (see figure 2.5.), the minimum occurs at $z = - 0.02\ \pi / 2 k \cos\theta_2$.

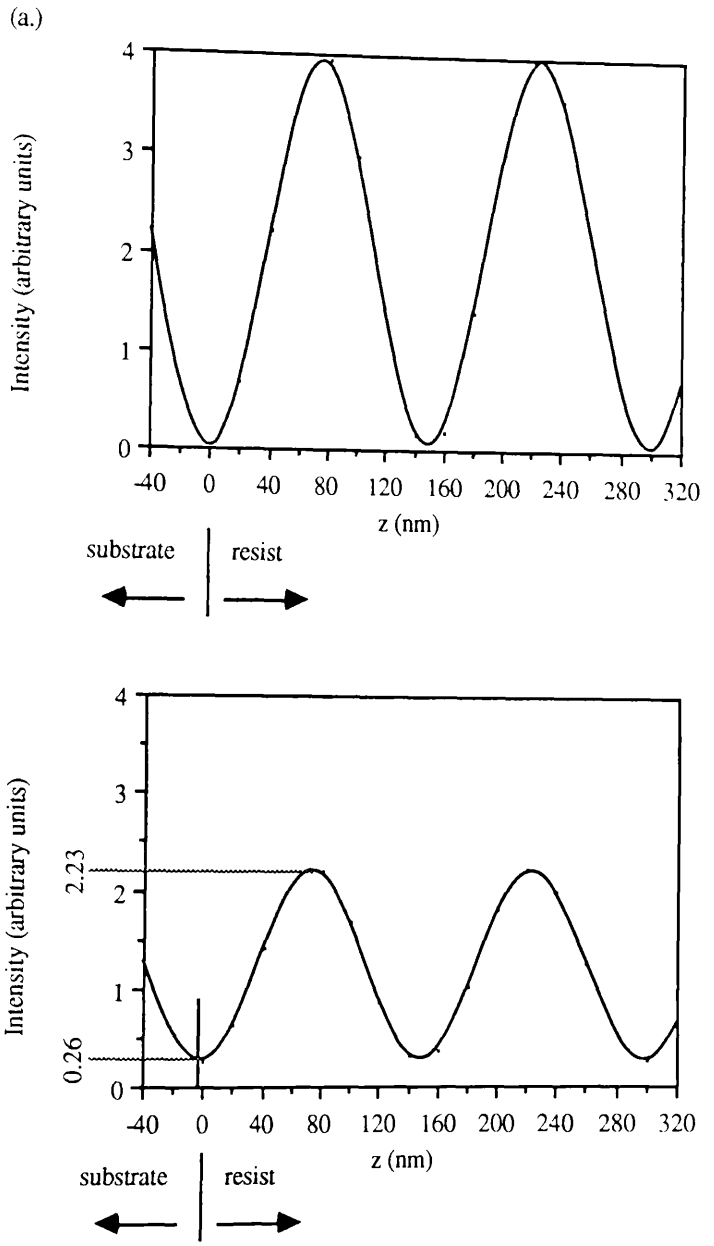

Figure 2.5. Relative intensity plots for standing waves at a grating maximum:

(a.) on a perfect reflector ($r = 1, \phi = \pi$)

(b.) on a silicon substrate ($r = 0.494, \phi = 0.96\pi$)

z = 0 represents the substrate boundary; n.b. the fields are rapidly attenuated inside the substrate, below z = 0, the fields are shown only to explain the phase at z = 0.

P can be expressed in terms of the grating period Λ as:

$$P = \Lambda \left(4 n_2^2 \left(\frac{\Lambda}{\lambda_0}\right)^2 - 1\right)^{-\frac{1}{2}} \qquad (2.2.13.)$$

Plots of P against Λ for various λ_0 are given in figure 2.1.(b.).

The difference in exposure seen by the resist at various depths can be appreciated by looking at the ratio *R* of standing wave intensities I_{max} (z max), I_{max} (z min) occurring at a grating maximum.

$$R = \frac{I_{max}(z_{max})}{I_{max}(z_{min})} = \left[\frac{1 + r}{1 - r}\right]^2 \qquad (2.2.14.)$$

This result is independent of the individual incident beam intensities as can be seen from eqn (2.2.6.) with $E_a = \alpha E_0$ and $E_b = E_0$:

$$I(x, z) = E_0^2 (1 + \alpha^2 + 2\alpha \cos(2 k x \sin\theta_2)) \times (1 + r^2 + 2 r \cos(2 k z \cos\theta_2 - \phi)) \qquad (2.2.15.)$$

I_{max} (z max) is $(1 + \alpha)^2(1 + r)^2$ and I_{max} (z min) is $(1 + \alpha)^2(1 - r)^2$.

Putting r = 0.435 into (2.7.14) gives a ratio of 6.45. A small reflectivity has a large effect on this standing wave ratio.

I_{max} (z max) is $(1 + \alpha)^2(1 + r)^2 / 4$ of its value in Case 1. Substituting $\alpha = r = 1$ into the preceding expression indicates that exposure times on highly reflecting substrates are 1 / 4 of their values in Case 1.

Case 4. Non-symmetric incidence.

The following section extends the plane wave model to look at the case of beams[4] incident on a reflecting sample at angles ϕ, θ; $\phi > \theta$. Figure 2.6.

The resulting expression for the intensity in the resist on a reflecting substrate becomes very complicated since the reflection coefficient is a function of ϕ, θ, and will be different for each beam.

[4]s-polarisation.

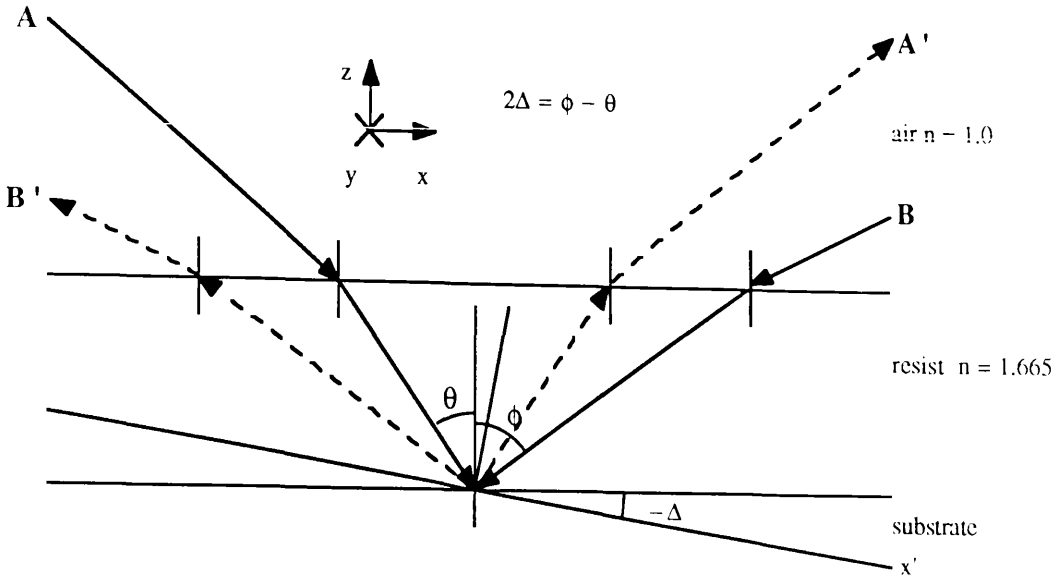

Figure 2.6.(a.). Three layer system for the plane wave model of holographic exposure (asymmetric incidence). A, B are the incident wavefronts, A', B' are the reflected wavefronts.

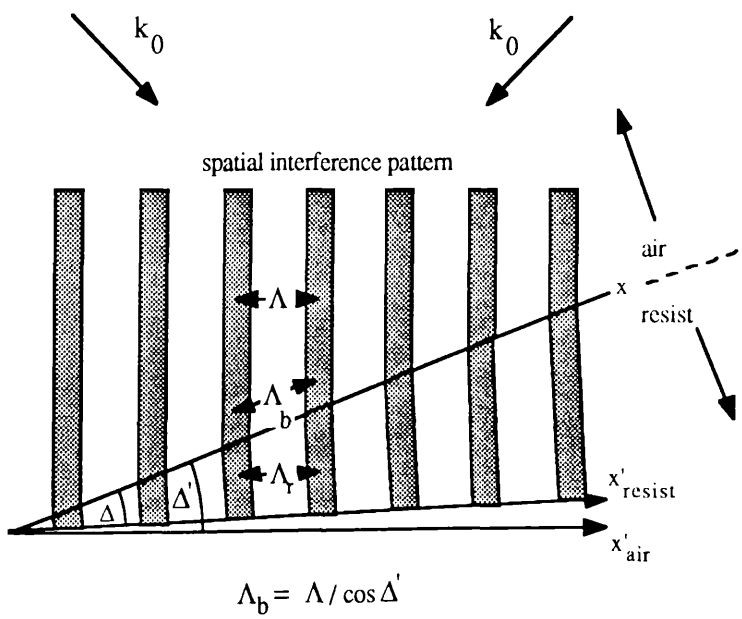

Figure 2.6.(b.). The grating period recorded in a resist layer tilted through an angle Δ' to the spatial interference pattern is increased from Λ to Λ_b. The resist layer lies along the x axis.

Δ' is the slant angle in air, which determines the recorded grating period along x. Δ is the slant angle in the resist which determines the grating blaze via equation (3.2.4.)

Wave $\boldsymbol{A}$ is incident at θ, and wave $\boldsymbol{B}$ is incident at ϕ. The reflected waves are $\boldsymbol{B'}(\phi)$ and $\boldsymbol{A'}(\theta)$. All the **E** vectors are polarised along the y direction.

Put $\boldsymbol{r}_{a,b} = |r_{a,b}| e^{j\psi_{a,b}}$:

The fields are:

$$\boldsymbol{A}(x,z,t) = E_a e^{j(\omega t - k x \sin\theta + k z \cos\theta)} \tag{2.2.16}$$

$$\boldsymbol{B}(x,z,t) = E_b e^{j(\omega t + k x \sin\phi + k z \cos\phi)} \tag{2.2.17}$$

$$\boldsymbol{A'}(x,z,t) = r_a E_a e^{j(\omega t - k x \sin\theta - k z \cos\theta + \psi_a)} \tag{2.2.18}$$

$$\boldsymbol{B'}(x,z,t) = r_b E_b e^{j(\omega t + k x \sin\phi - k z \cos\phi + \psi_b)} \tag{2.2.19.}$$

Putting $\phi - \theta = 2\Delta$ (ϕ, θ on opposite sides of the normal to the surface), $\phi + \theta = 2\beta$; after some manipulation we obtain an expression for the intensity:

$$\begin{aligned} I(x,z) = {} & E_a^2 (1 + r_a^2) + E_b^2 (1 + r_b^2) \\ & + 2 E_a E_b [\cos(2k(x\cos\Delta - z\sin\Delta)\sin\beta) \\ & \quad + r_a r_b \cos(2k(x\cos\Delta + z\sin\Delta)\sin\beta + \psi_b - \psi_a) \\ & \quad + r_a \cos(2k(x\sin\beta + z\cos\beta)\cos\Delta - \psi_a) \\ & \quad + r_b \cos(2k(-x\sin\beta + z\cos\beta)\cos\Delta - \psi_b)] \\ & + 2 r_a E_a^2 \cos(2k z\cos\theta - \psi_a) \\ & + 2 r_b E_b^2 \cos(2k z\cos\phi - \psi_b) \end{aligned} \tag{2.2.20.}$$

The expression can be simplified by setting $E_a = E_b = E_0$ and either $r_a = r_b = 0$ or 1 (zero or unity reflectivity).

In the absence of reflectivity and assuming $E_a = E_b = E_0$, I (x,z) becomes:

$$I(x,z) = 2 E_0^2 [1 + \cos(2k(x\cos\Delta - z\sin\Delta)\sin\beta)] \tag{2.2.21.}$$

Equation (2.2.21.) represents a grating of period (λ_0 / 2 sin [(θ + ϕ) / 2]) along a new axis x' oriented at an angle - Δ to the x axis. Along the x axis the grating is blazed. The blazed grating produced in the x,y plane is simply the projection of the grating produced along x'.

Note that this expression (2.2.21.) has been derived inside the resist layer. θ' and ϕ' outside the resist will be different. The values of Δ and β will be different in air and in resist.

In air, equation (2.2.21.) can be written as

$$I(x,z) = 2 E_0^2 [1 + \cos (2 k_0 (x \cos \Delta' - z \sin \Delta') \sin \beta')] \qquad (2.2.22.)$$

where the primed quantities refer to the air and k_0 is the vacuum wavevector.

In resist the equation becomes:

$$I(x,z) = 2 E_0^2 [1 + \cos (2 k_0 n (x \cos \Delta - z \sin \Delta) \sin \beta)] \qquad (2.2.23.)$$

where and n is the resist refractive index. Rewriting equations (2.2.22.), (2.2.23.) in terms of θ', ϕ', θ and ϕ we see that the grating period along the surface (z = 0) will be the same by virtue of Snell's law.

$$I(x, z) = 2 E_0^2 \left(1 + \cos 2 k_0 [\frac{x}{2} (\sin \theta' + \sin \phi') + \frac{z}{2} (\cos \theta' - \cos \phi')] \right)$$

$$I(x, z) = 2 E_0^2 \left(1 + \cos 2 k_0 n [\frac{x}{2} (\sin \theta + \sin \phi) + \frac{z}{2} (\cos \theta - \cos \phi)] \right)$$

(2.2.24.)

As an example consider a 356.2 nm spatial interference pattern (β' = 40°) recorded with the normal to the sample making an angle Δ' = 15°, to the bisector of the two beams.
In this case θ' = 25°, ϕ' = 55°, but θ and ϕ in the resist are now 14.7° and 29.5°, so that Δ is 14.8° and β is 22.1°. Along the x' axis in the resist, the grating period Λ_r is

$$\Lambda_r = \frac{\lambda_0}{2 n \sin \beta} \qquad (2.2.25.)$$

which is 365.5 nm for the above example.

2.3. Grating period uniformity; a gaussian beam model.

In the holographic arrangement used in this work, the gratings were formed by the interference of two gaussian beams diverging from the spatial filters. It is important to understand the effects of this curvature of the wavefronts on the resulting grating.

The treatment may be simplified by assuming that the gaussian beams intersect orthogonally to one another, the spatial filter separation from the intersection point is the same, and the beams are both s-polarised, figure 2.7. The model presented here may be generalised to include different spatial filter distances and values of θ other than 45°.

Equidistant gaussian beam waists.

The gaussian beam waists are both the same distance a away from their intersection point, O. The beams have the same size beam waists ω_0, and the same phase at the beam waists. The beam waists are located at (0, - a), (- a, 0). The grating is recorded in the plane OP oriented at - 45° to the x axis.

A gaussian beam propagating with its waist at $z = 0$ along the z axis has the form:

$$E(x,y,z) = (\omega_0 / \omega(z))\, e^{- r^2 / \omega^2(z)}\, e^{- j (k [z + r^2 / 2 R(z)] - \eta(z))} \qquad (2.3.1.)$$

z_0 is the confocal beam parameter given by:

$$z_0 = \pi \omega_0^{\,2} / \lambda \qquad (2.3.5.)$$

and $k = 2 \pi / \lambda$. The spot size $\omega(z)$ is defined by

$$\omega^2(z) = \omega_0^{\,2}(1 + z^2 / z_0^{\,2}) \qquad (2.3.2.)$$

where ω_0 is the spot size at the beam waist. The other terms are:

$(- j k z)$ - the plane wave propagation term,

$(- r^2 / \omega^2(z))$ - the gaussian intensity function, normal to the the z axis,

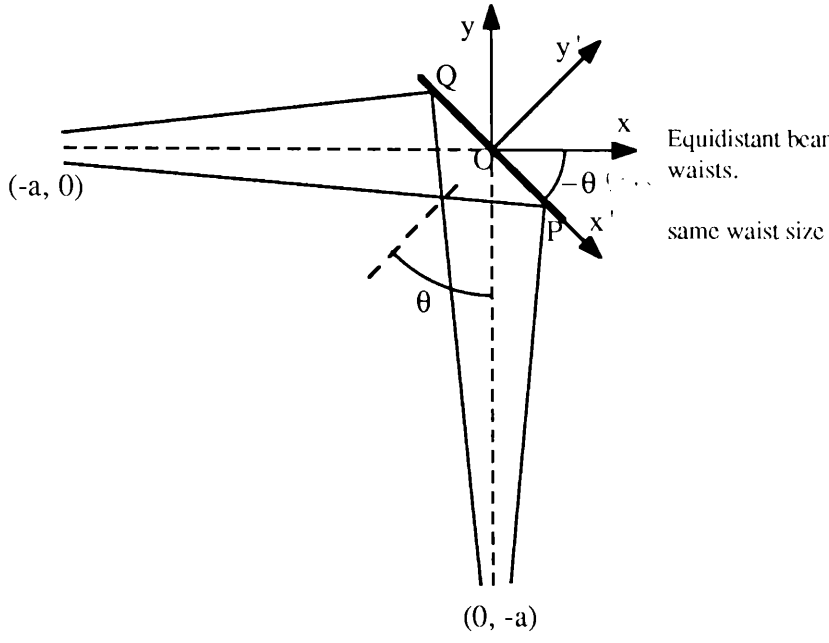

Figure 2.7. Geometry for gaussian beam model.

$r^2 = x^2 + y^2$,

$\eta(z)$ - a slowly varying phase function given by:

$$\eta(z) = \tan^{-1}(z / z_0) \qquad (2.3.3.)$$

$(-r^2 j k / 2 R(z))$ - a phase term depending on wavefront curvature,

$R(z)$ - the radius of curvature of the gaussian beam, given by:

$$R(z) = z (1 + z_0^2 / z^2) \qquad (2.3.4.)$$

For each of the two beams, there will be a variation in x or y in the plane of the resist as we move over OP and hence variations in $\omega(x)$, $\omega(y)$, $\eta(x)$, $\eta(y)$ $R(x)$ and $R(y)$. It is helpful to begin the analysis by a consideration of the order of magnitude of these terms. Take the spatial filter to O distance as 25 cm and ω_0 as 10 μm.

Consider the one dimensional case for a beam propagating along the z axis. The beam waist is at $z = 0$ and we want to know how the parameters change for a 1 cm change in z at $z = 0.25$ m.

$z_0 = 6.86 \times 10^{-4}$ m, $\omega = 3.64 \times 10^{-3}$ m at $z = 0.25$ m

(1.) *Variation in $\omega(z)$*: From eqn (2.3.2.) we have:

$$\frac{d\omega(z)}{dz} = \frac{\omega_0^2 z}{z_0^2 \omega(z)}$$

$$\frac{\Delta\omega(z)}{\omega(z)} = \frac{z \Delta z}{z_0^2 + z^2} = 0.04; \qquad \Delta\omega = 1.5 \times 10^{-4} \text{ m}$$

(2.) *Variation in R(z):*

$$\frac{dR(z)}{dz} = 1 - \frac{z_0^2}{z^2}; \qquad \Delta R = 10^{-2}\ \text{m.}$$

$$\frac{\Delta R(z)}{R} = \frac{z^2 - z_0^2}{z\left(z^2 + z_0^2\right)}\Delta z \approx \frac{\Delta z}{z} = 0.04.$$

(3.) *Variation in $\eta(z)$:*

$$\frac{d\eta(z)}{dz} = \frac{z_0}{z^2 + z_0^2} \approx \frac{z_0}{z} = 2.74\times10^{-3}$$

$$\frac{\Delta\eta}{\eta} = 1.74\times10^{-5}; \qquad \eta(0.25) = 1.568$$

$\eta(z)$ varies slowly and can be treated as a constant.

E_1 and E_2 are the fields propagating along the positive x and positive y directions.

$$E_i(x,y,z) = (\omega_0 / \omega(x_i + a))\, e^{-r_i^2/\omega^2(x_i + a)} \cdot e^{-jk((x_i + a) + r_i^2/2R(x_i + a))} \qquad (2.3.6.)$$

where i = 1, 2 and denotes beam 1, 2. x_i = x or y and $r_i^2 = y^2 + z^2$ or $x^2 + z^2$ for beam 1 and beam 2 respectively. $\eta(x_i)$ can be taken as zero.

A new set of axes x', y' are defined parallel and perpendicular to OP with their origin at O. x' and y' are rotated through an angle (- θ) with respect to the x axis:

$$\begin{aligned} x &= x'\cos(-\theta) - y'\sin(-\theta) &&= x'\cos\theta + y'\sin\theta \\ y &= y'\sin(-\theta) + y'\cos(-\theta) &&= -x'\sin\theta + y'\cos\theta \\ z &= z' \end{aligned} \qquad (2.3.7.)$$

In the grating plane y' = 0, and since θ is 45°, cos θ = sin θ = 1 / √2. θ is also the angle which determines the grating period through eqn (2.2.8.).

Along OP we can represent x, y as:

$$x = x' / \sqrt{2}$$
$$y = - x' / \sqrt{2} \qquad (2.3.8.)$$

The intensity is given by $|E_t = E_1 + E_2|^2$ where E_t is:

$$E_t(x,y,z) = A_1 e^{- j k (x + a + r^2 / 2 R(x + a))} + A_2 e^{- j k (y + a + r^2 / 2 R(y + a))} \qquad (2.3.9.)$$

where $r_i^2 = r^2 = x'^2 / 2 + z^2$ and A_i is given by:

$$A_i = (\omega_0 / \omega(x_i + a)) e^{- r^2 / \omega^2 (x_i + a)} \qquad (2.3.10.)$$

using the identity:

$$|a_1 e^{j \beta_1} + a_2 e^{j \beta_2}|^2 = a_1^2 + a_2^2 + 2 a_1 a_2 \cos(\beta_1 - \beta_2)$$

we have I (x', 0, z') becomes:

$$I(x', 0, z') = A_1^2 + A_2^2 + 2 A_1 A_2 \cos [2 k x' / \sqrt{2} + k r^2 / 2 (1 / R(a + x' / \sqrt{2}) - 1 / R(a - x' / \sqrt{2}))] \qquad (2.3.11.)$$

From eqn (2.3.13) we see immediately that on the beam axis (x' = 0) the grating period is the same as for the plane wave case.

Before determining how the period changes as we move over x' in the grating plane, the value

of Λ at the edge of the grating must be obtained first.

The grating edge is defined by point Q, where the beam waist meets the plane OP. For beam 1 this corresponds to a value of x given by the solution of:

$$\omega_0^2\left(1+\frac{(x+a)^2}{z_0^2}\right)=x^2 \qquad (2.3.12.)$$

solving for x:

$$x=\frac{\omega_0}{z_0^2-\omega_0^2}\left(a\omega_0 \pm z_0\sqrt{a^2+z_0^2-\omega_0^2}\right) \qquad (2.3.13.)$$

and since $a \gg z_0, \omega_0$; x becomes:

$$x=\frac{\omega_0\, a}{z_0-\omega_0} \qquad (2.3.14.)$$

Equation (2.3.14) predicts a value for $x = 3.79 \times 10^{-3}$ m. This is just a little bigger than $\omega(0.25) = 3.64 \times 10^{-3}$ m. This is quite reasonable. The value of x' corresponding to the intersection of the beam waist with the grating plane is $x / \sqrt{2} = 5.23 \times 10^{-3}$ m, so the grating diameter is approximately 10.5 mm.

An expression is needed for the difference of the reciprocal radii of curvature:

$$\Delta(1/R) = [1/R\,(a + x'/\sqrt{2}) - 1/R\,(a - x'/\sqrt{2})]$$

Substituting into equation (2.3.4.) we obtain:

$$\Delta\left(\frac{1}{R}\right)=\frac{2x'/\sqrt{2}\left(z_0^2+x'^2/2-a^2\right)}{\left(x'^2/2+z_0^2+a^2\right)^2-4a^2x'^2/2} \qquad (2.3.15.)$$

Since z_0^2 is very much smaller than $(x'^2/2 \pm a^2)$, it can be neglected:

$$\Delta\left(\frac{1}{R}\right) = \frac{2\,x'/\sqrt{2}}{x'^{2}/2 - a^{2}} \qquad (2.3.15a.)$$

The difference in 1 / R at $x'/\sqrt{2} = 3.79 \times 10^{-3}$ m is - 0.121 m^{-1}. The wavefront dependent part of the argument of equation (2.3.11.) is proportional to $\phi = (r^2 / 2)\,\Delta(1 / R)$ where r depends on x' sin θ and z. In other words, away from the central point O, the grating has not only a chirp in the x' direction (z = 0) but also the grating lines become curved because of the dependence on z. We will look at the on axis (z =0) effects. r is just $x'/\sqrt{2}$ and φ becomes:

$$\phi(x') = \frac{(x'/\sqrt{2})^{3}}{x'^{2}/2 - a^{2}} \qquad (2.3.16.)$$

At the grating edge φ has a value of - 8.71 x 10^{-7} m. As x' increases by Λ(x'), the argument of the cosine in equation (2.3.11.), $\psi = 2\,k\,x'/\sqrt{2} + k\,\phi(x')$, increases by 2 π:

$$\psi + 2\pi = 2\,k\,(x' + \Lambda(x'))/\sqrt{2} + k\,\phi(x' + \Lambda(x')) \qquad (2.3.17.)$$

$$2\,k\,\Lambda(x')/\sqrt{2} + k\,(\phi(x' + \Lambda(x')) - \phi(x')) = 2\pi$$

and

$$\phi(x' + \Lambda'(x')) - \phi(x') = \Lambda'(x')/\sqrt{2}\,\frac{\partial\phi}{\partial x} + \frac{\Lambda'(x')^{2}/2}{2}\,\frac{\partial^{2}\phi}{\partial x^{2}} + \ldots + \text{higher order terms} \qquad (2.3.18.)$$

where $x = x'/\sqrt{2}$

$$\phi(x) = \frac{x^{3}}{x^{2} - a^{2}}.$$

$$\frac{\partial\phi}{\partial x} = \frac{x^{2}(x^{2} - 3a^{2})}{(x^{2} - a^{2})^{2}} = -6.90 \times 10^{-4}$$

and

$$\frac{\partial^2 \phi}{\partial x^2} = \frac{2a^2 x (x^2 + 3a^2)}{(x^2 - a^2)^3} = -0.36$$

evaluated at $x = 3.79 \times 10^{-3}$ m

As $\Lambda(x')$ is typically a few hundred nanometers, the second term of equation (2.3.18.) is smaller than the first term by a factor of 1.2×10^{-4} and can be neglected. Equations (2.3.17.) and (2.3.18.) become:

$$2k\Lambda/\sqrt{2} + k\Lambda/\sqrt{2}\ (\partial\phi / \partial x) = 2\pi$$

and

$$\Lambda = \Lambda(0)\left(1 + (1/2)\,\partial\phi / \partial x\right)^{-1} \qquad (2.3.19.)$$

where $\Lambda(0)$ is the period predicted by the plane wave model (equation (2.2.8a)). Substituting $\partial\phi / \partial x = -6.90 \times 10^{-4}$ in (2.3.19.) allows an estimate of the magnitude of the chirp to be made.

$\Lambda / \Lambda(0) = 1.00035$ a chirp of under 1 part in 10^3 over approximately 5 mm of grating.

Phase differences over the grating length due to chirping.

The grating chirp has an effect on the radiation diffracted from the grating. Consider radiation diffracted at some angle α from such a grating illuminated normally with coherent radiation, figure 2.8.

Suppose that the unperturbed period is Λ_1 and the period of the n th corrugation, $\Lambda_n \approx \Lambda_1$, changes only very gradually over a very large number of repeats, then the angular distribution of the diffraction orders is to a first approximation unaffected. Each new repeat in the grating, however, adds an additional small path difference, δr_n, between the radiation scattered from adjacent scattering centres to the $\Lambda_1 \sin\alpha$ that appears from the unperturbed grating. δr_n is very small but

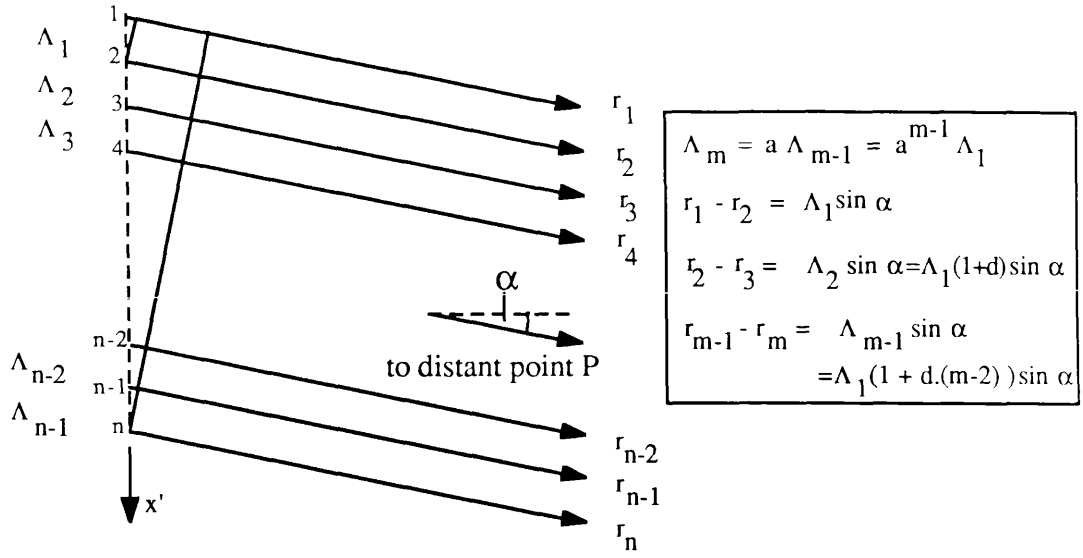

Figure 2.8.(a.) Geometry for chirped grating calculation.

The grating consists of n scattering centres; adjacent separation Λ_m in the x' direction. The distance from point m to point P at an angle α to the normal to the grating plane is r_m.

a is the chirp factor = 1 + d where d « 1, hence $a^{m-1} \approx 1 + d.(m-1)$.

The path differences $r_1 - r_m$ determine the phase differences between the contributions over the grating relative to point 1 and hence determine the final field at P. This is

$$r_1 - r_m = \Lambda_1 \sin\alpha \left((m-1) + \sum_{n=1}^{m-2} n.d\right)$$

The first term in the brackets is the unperturbed grating term, the summation represents the extra path differences caused by the chirp. There will be complete cancelation of light contributions over the grating if the summation equals Λ_1. Note that the summation forms an arithmetic series and has a sum (m-2).(m-1) d / 2.

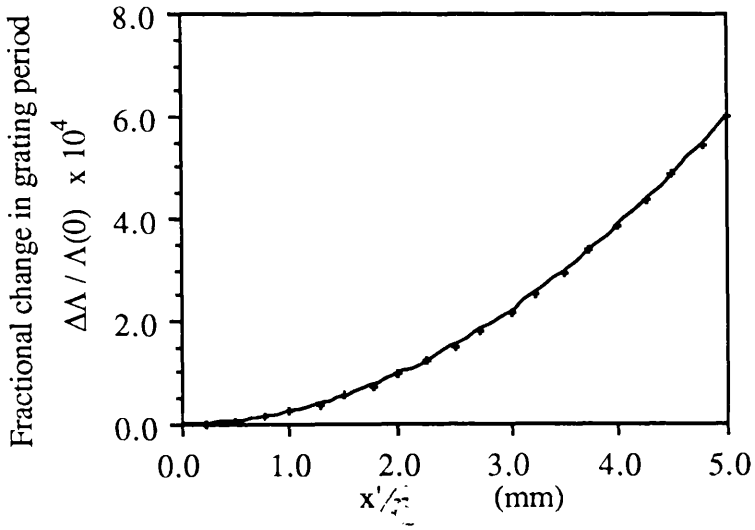

Figure 2.8.(b.) Plot of fractional change in period $\Delta\Lambda / \Lambda(0)$ against grating coordinate x'.

over the whole grating area $\Sigma_n \delta r_n$ becomes significant.

If $\Sigma_n \delta r_n$ equals Λ_1 then an extra 2 π phase difference appears for radiation diffracted from the edges of the grating. If the grating contains N repeats, this condition is met by

$$(\Sigma_n \Lambda_n - N.\Lambda_1) \sin \alpha = \Sigma_n \delta r_n = \Lambda_1 \qquad (2.3.20.)$$

where the summation runs from n =1 to n = N.

In the far field radiation from different parts of the grating will cancel itself out, since for radiation from any point on the grating, there is always a point another point which produces radiation π out of phase with it.

It is important to calculate the magnitude of $\Sigma_n \delta r_n$ for the interference gratings. Semiconductor DFB lasers are usually only 300 μm or so long, so that $\Sigma_n \delta r_n$ should be quite small over this distance. Gratings required for spectroscopic use are a lot larger[5] (at least 5 cm or so in diameter) so $\Sigma_n \delta r_n$ is also going to be much larger.

Calculation of $\Sigma_n \delta r_n$ for interference gratings.

The grating period, equation (2.3.19.) can be rewritten as

$$\Lambda(x) = \Lambda(0)\left(1 - \frac{x^2(x^2 - 3a^2)}{2(x^2 - a^2)^2}\right) \qquad (2.3.21.)$$

This function is plotted as $(\Lambda - \Lambda(0)) / \Lambda(0)$ against $x = x'/\sqrt{2}$ in figure 2.8.b.
Near to x = 0, Λ is only a very slowly varying function of x. $\Sigma_n \Lambda_n$ is calculated using a generating function, figure 2.9.a. Note that the generating function must be expressed in terms of x', the grating coordinate instead of x.

[5]The resolution of a spectroscopic grating is inversely proportional to the number of lines in the grating.

The grating has a maximum at x' = 0; after m periods the maximum occurs at x'_m. The position of the (m + 1) th peak is calculated as follows.

After m repeats, the grating period is Λ_m, the next period is Λ_{m+1}, given by

$$\Lambda_{m+1} = \Lambda_m \left(1 + \left[\frac{d\Lambda}{dx'} \right]_{x'_m} \right) \qquad (2.3.22.)$$

and the next peak (m + 1) occurs at

$$x'_{m+1} = x'_m + \Lambda_{m+1} \qquad (2.3.23.)$$

A computer program was written to calculate $\Sigma_n \Lambda_n$ using equations (2.3.22.) and (2.3.23.) over a defined number of grating periods N.

(dΛ / dx') is obtained from (2.3.21) as [$1/\sqrt{2}$. (dΛ / dx)]

$$\frac{d\Lambda}{dx'} = -\frac{1}{2}\Lambda(0)\, 1/\sqrt{2}\, \frac{\partial^2 \phi}{\partial x^2}$$

$$= -\Lambda(0)\, \frac{a^2 x' / 2 \quad (x'^2 / 2 \quad + 3a^2)}{(x'^2 / 2 \ \theta \ - a^2)^3} \qquad (2.3.24.)$$

dΛ / dx' is a slowly varying function of x' and for small x' is approximately linear, figure 2.9.b. The grating extends as far as ~ 5.2 mm on either side of x' = 0. To a first approximation dΛ / dx' is taken to be linear in x'.

$$d\Lambda / dx' = 3\,(\Lambda(0)\, x' / 2 \quad) / a^2 \qquad (2.3.25.)$$

$\Sigma_n \Lambda_n$ is evaluated by working out the total number of repeats of the unperturbed grating, N, in the device and then working out the sum up to N terms using equations (2.3.22.) and (2.3.24.).

δr_n is simply this sum minus $N.\Lambda_1$.

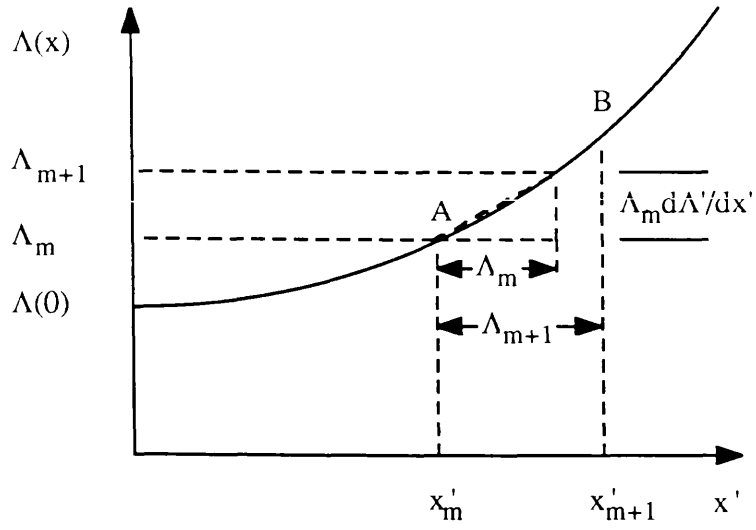

Figure 2.9.(a.) Geometry for setting up the period iterations: calculation at point A sets up a new iteration point at B.

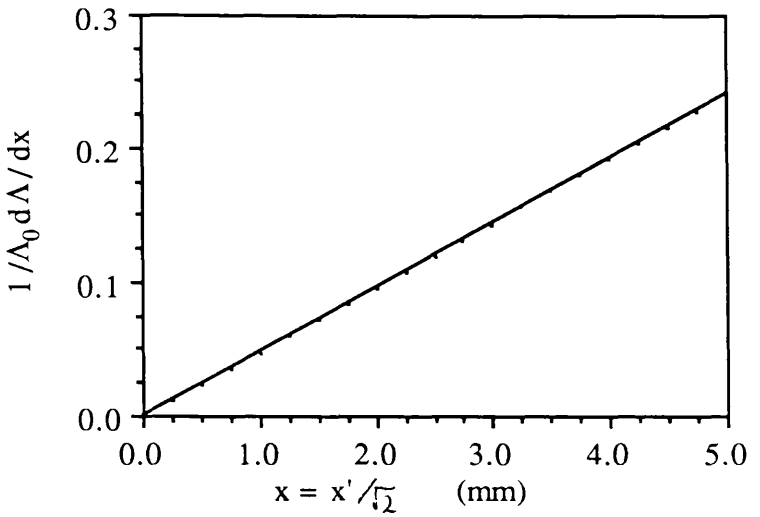

Figure 2.9.(b.) Plot of $(1/\Lambda_0)\, d\Lambda / dx$ against $x'/\sqrt{2}$ .where x' is the grating coordinate and Λ_0 is the unperturbed grating period.

Note the function is written in terms of $x = x'/\sqrt{2}$

At 457.9 nm exposure wavelength and with $\theta = 45°$, $\Lambda(0)$ is 323.8 nm. An integrated optical device 300 μm long has 926 repeats. If fabricated in the centre of the grating, the device has an overall phase shift $[(\Sigma_n \Lambda_n - N.\Lambda_1) / \Lambda_1]$ of 3.33×10^{-4}, i.e. 0.033 %.

If the device were fabricated at the grating edge, $x' = 5.23 \times 10^{-3}$m, then
$\Lambda' = 1.00035 \times 323.8$ nm ≈ 323.91 nm.

The end point is 5.53×10^{-3}m and $[(\Sigma_n \Lambda_n - N.\Lambda_1) / \Lambda_1]$ is 0.018, i.e. 1.8 %.

5.23 mm of grating contains 16152 grating repeats and $[(\Sigma_n \Lambda_n - N.\Lambda_1) / \Lambda_1]$ is 1.76, indicating that the gratings would not be suitable for spectroscopic use.

Chapter 3. Grating Recording: Experimental.

Chapter Layout.

3.1. The optical bench.

Some of the principles of grating recording by laser interference have already been discussed in Chapter 2. In this chapter the discussion is extended to include the requirements of the interferometer, presented in the first section; and the experimental work is described in the second section. This second part outlines the problems met with exposure on different substrate types.

The following chapter concludes the lithographic process with a discussion of pattern transfer by dry etching.

Interferometer Arrangement.

Various optical arrangements can be used to expose holographic gratings, such as the corner cube arrangement used by Zaidi (1988), figure 3.1.(a.), the three mirror interferometer used by Dalgoutte (1975) p 131 and Yi-Yan (1978) p 125, figure 3.1.(b.) or the symmetric two mirror interferometer used in this work and previously by Pun (1983) p 139 and Dumas (1985) p 105, figure 3.2. Each will now be briefly discussed in turn.

The three mirror arrangement.

After the beam passes through the spatial filter it is collimated to form a quasi-plane wavefront. The beam is split into two arms. Since the split beams are not filtered and are of large size, the flatness of the mirrors affects the final grating. If each beam is separately filtered and collimated just before they interfere, the problem is minimised.

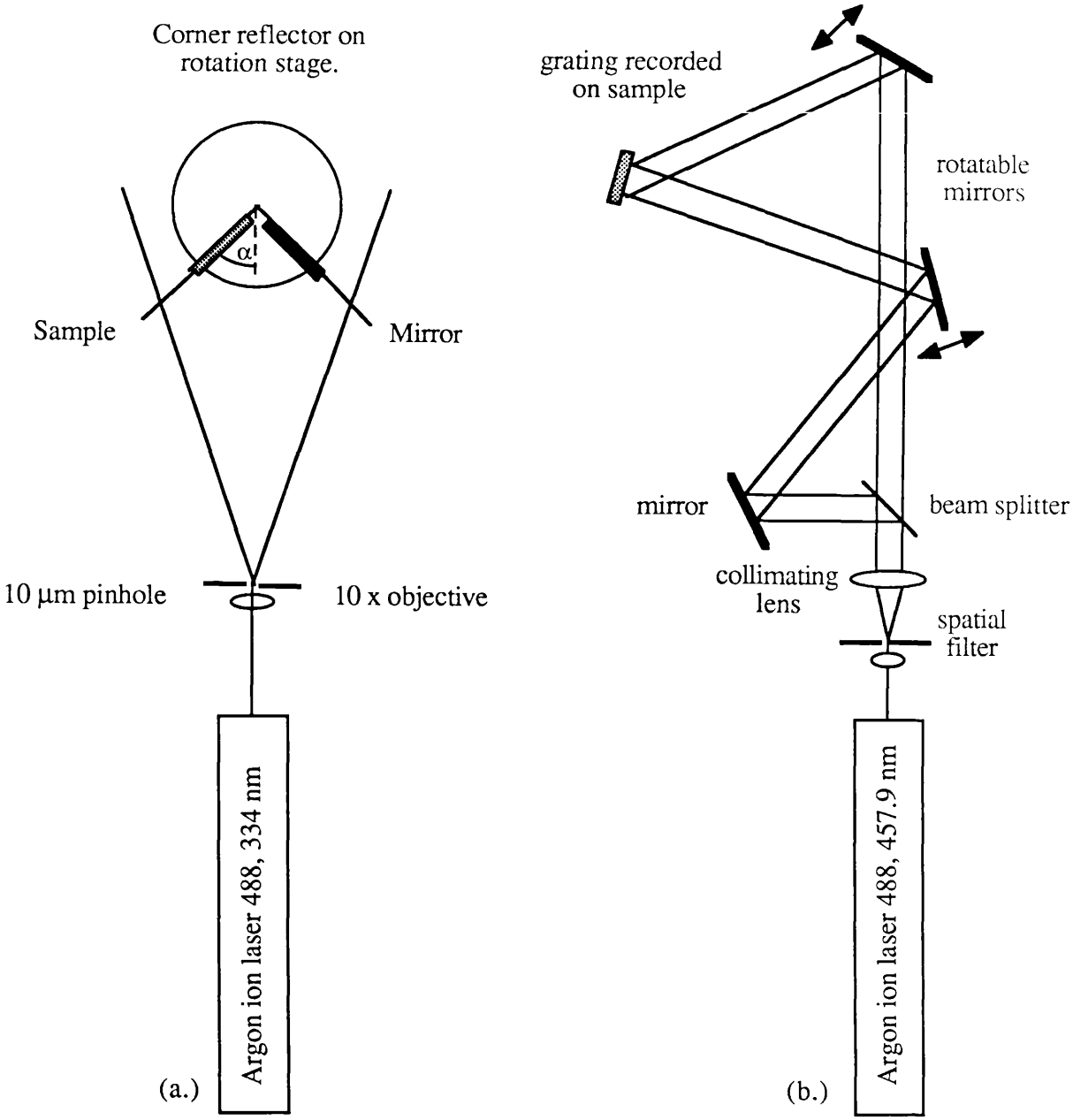

Figure 3.1. (a.) The corner cube arrangement described by Zaidi (1988), the grating period is altered by rotating the stage. The geometry has the advantage of ensuring equal angles of incidence (90° -α) and equal flux densities.

(b.) The three mirror interferometer after Dalgoutte (1975).

The arrangement has the disadvantage that it is difficult to alter the period and keep the path difference between the beams as small as possible.

An advantage is that any aberration on the wavefront is not compounded by lateral inversion.

The corner cube arrangement.

One novel system is the corner cube arrangement. It has the advantages of simplicity and stability against vibration. To produce gratings of different periods, the device is rotated. The size of sample that can be accommodated is limited by the geometry, which also limits the range of periods that can be selected. The arrangement does not use a collimating lens so that the distance between the spatial filter and the cube must be large.

The symmetric arrangement.

The 457.9 nm or 351.1 nm argon laser light is split by a beam-splitter (**BS**) into two equal intensity beams (**a, b**), then reflected by mirrors (**M1, M2**), passed through two spatial filter assemblies (**SP1, SP2**) and brought together at point **O**. The gratings are recorded in the overlap region of the two beams, figure 3.4.

Advantages and disadvantages of the symmetric arrangement.

(i.) The requirements for the temporal coherence of the source are not as stringent as for the three mirror interferometer because the optical path differences (o.p.d.) between the two (unexpanded) beams can be made arbitrarily small. In the x - z plane a path difference between the interfering beams exists across the grating surface due to the finite width of each beam. This path difference increases at larger values of θ_1, figure 3.4.

(ii.) In the overlap region any aberrations on the wavefront such as phase errors due to scattering from imperfections on the mirrors are compounded by their images laterally inverted about the y axis (figure 3.1.). High flatness mirrors (to within λ / 20) are used. These effects are reduced by setting **SP1, SP2** after **M1, M2**.

(iii.) The optical components are easily rearranged. The grating period is a function of exposure wavelength and the angle of incidence θ_1 via equation.(2.2.8). For a specific λ_0, θ_1 may in practice be varied between 20° and 70°. Workers such as Yi-Yan (1978) have reported difficulties in

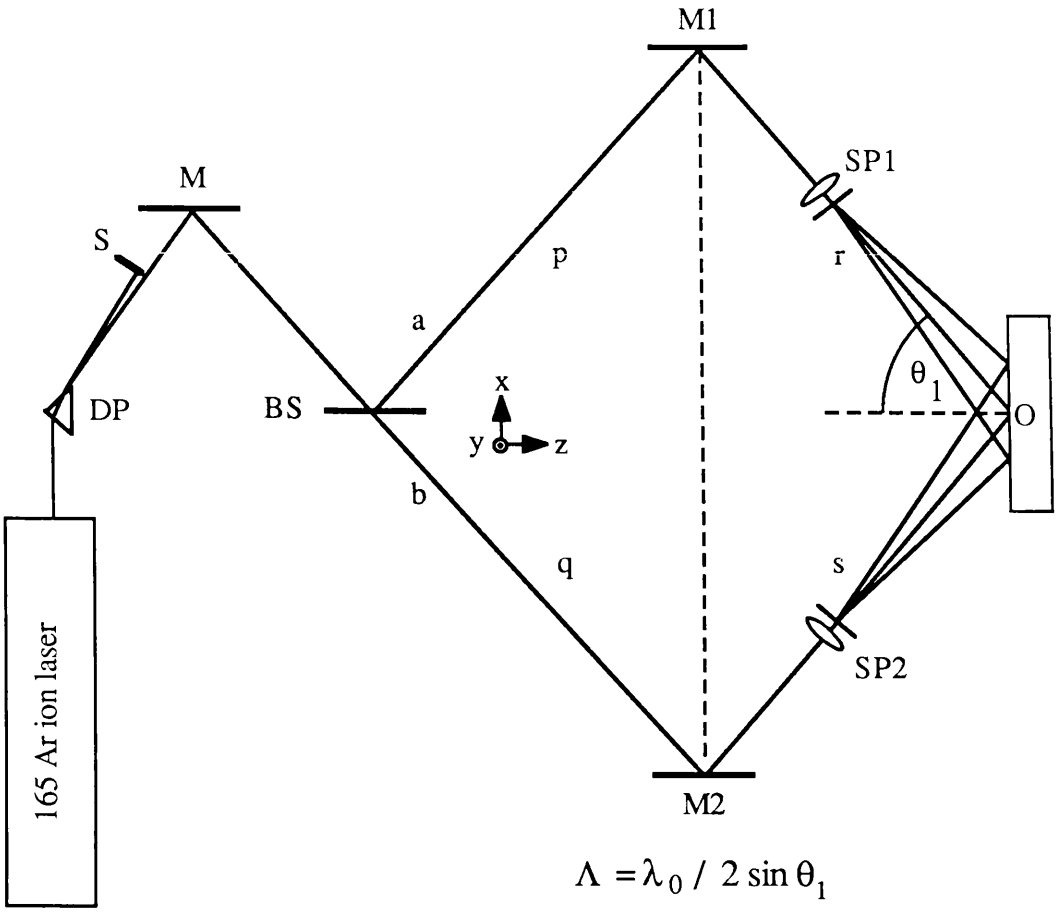

Figure 3.2. Symmetric interferometer for producing holographic gratings. (The interferometer is set for UV operation at 351.1 nm with the dispersing prism DP and beam stop S.) The back prism assembly is not shown. M is a steering mirror.

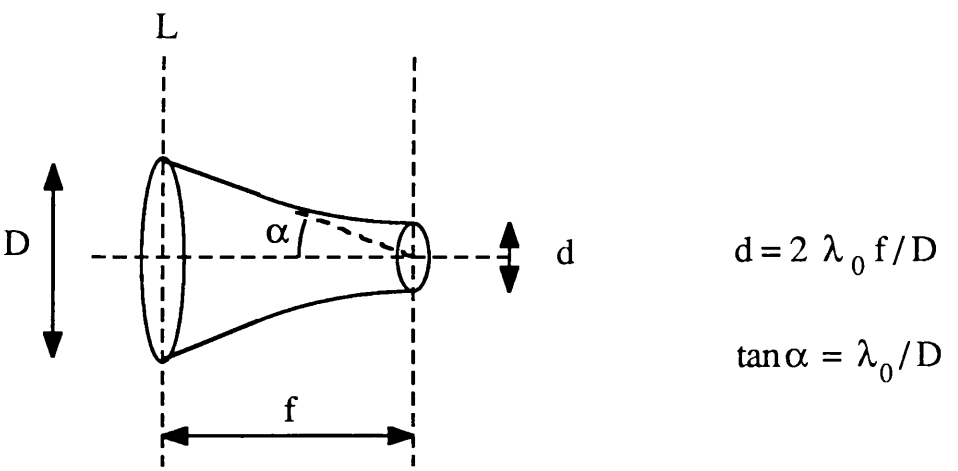

Figure 3.3. Geometry for estimating pin hole size. D is the incident beam diameter, d the diameter of the focused beam. L is the plane of the lens.

making gratings with θ_1 larger than 55°, due to phase errors on the beam and spurious modulations appearing on the grating due to the increased reflectivity at the resist-glass interface. In this work gratings were successfully made at high incidence angles up to 70°; although some occasional modulation was seen, the quality of such gratings was very good, see section 3.2.1.

The positions of **M1**, **M2** are set so that p and q are fixed irrespective of θ_1. The grating period can be easily changed from 356.2 to 285 nm for example if the beam paths corresponding to these two values of Λ are already marked out.

The production of gratings needing a large incidence angle, > 60°, or a low incidence angle, < 20°, is more difficult. A small θ_1 implies a large r, s; in fact r, s may not fit onto the table. To produce large period gratings the exterior prism technique was used, figure 3.5. (Murphy 1987). The aluminised prism shortens the apparent baseline between **M1-M2** so that r, s will fit on the table. $\Lambda = 2\ \mu m$ ($\theta_1 = 6.6°$) was achieved using $\lambda_0 = 457.9$ nm in this way. The spatial filters are positioned just before the prism.

The large values of θ_1 needed to produce short period gratings result in r and s being too short to accommodate the spatial filters. The baseline between **M1-M2** is then increased.

Accuracy in setting Λ.

The angle between the beams can be set to within 0.25°. From equation 2.2.8.a., an expression for the percentage error on the period can be obtained.

$$(\delta\Lambda / \Lambda) = 100 \cot \theta_1\, \delta\theta_1\ \% \qquad (3.1.1.)$$

The error on the period is larger at low angles of incidence, θ_1. As an example, taking $\delta\theta_1$ as 2.18×10^{-3} radians (= 0.125°), the error on the period is 0.6% and 0.2% for $\theta_1 = 20°$ and 60° respectively.

Setting up the interferometer.

In this work the interferometer is set up as follows: A black metal target marked with a white cross hair is used to set the height of the laser beam at 15 cm above the table. The beam splitter is placed in its approximate position and rotated until an equal power split is obtained. The split

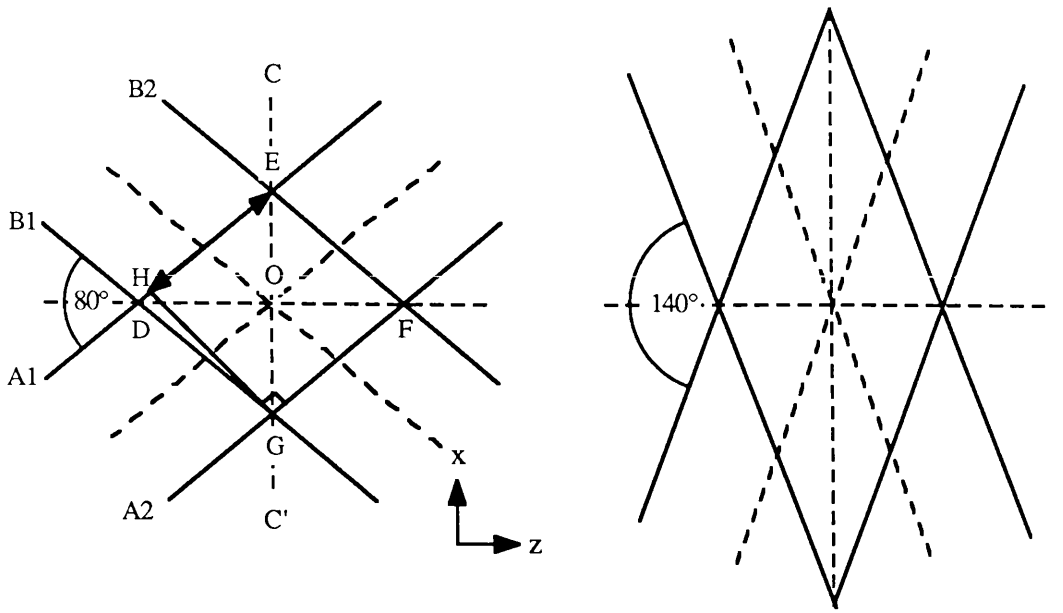

Figure 3.4. The grating pattern is formed in the overlap region of the two beams A, B which is defined by the trapezoid DEFG shown for two cases; 40° and 70° incidence. The sample is placed in the plane CC' for maximum overlap.

There is a path difference HE between the wavefronts from each beam at the grating edge. Note the increase in overlap area and in HE at high angles of incidence and the corresponding contraction in the z direction.

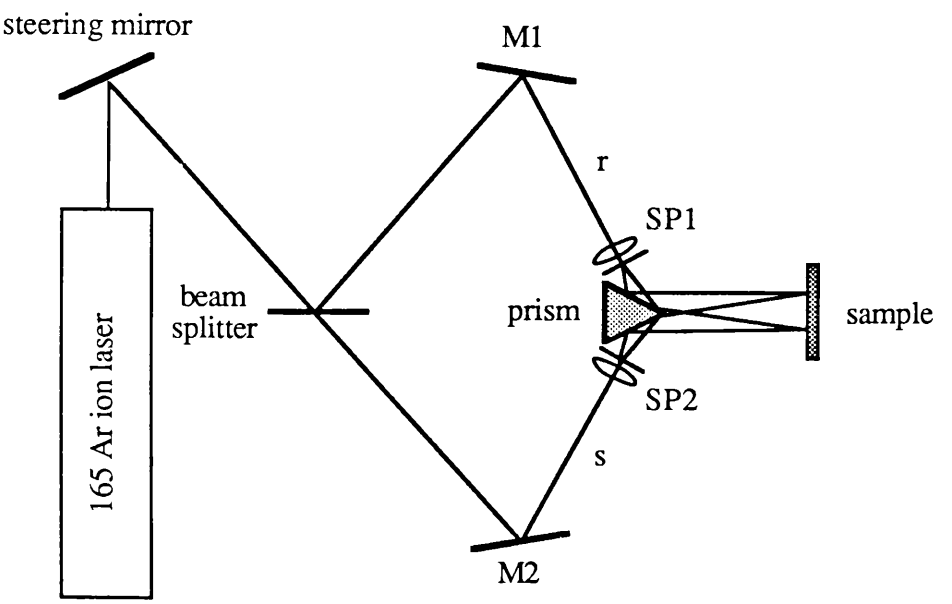

Figure 3.5. 'Exterior prism' optical configuration for producing very large period (> 600 nm) holographic gratings. Two of the prism's square faces were evaporated with a thin layer of aluminium to enhance the reflectivity. The third square face was painted matt black.

could be measured to within 0.5% for 457.9 nm and 10% for 351.1 nm.

The orientation of the splitter defines *p* and *q* which are now drawn on the bench. Two large plastic set squares held vertically between magnetic clamps are placed in the path of the beam and the position on the table is marked where the square just blocks the spot. The marks map out the beam path and a line is drawn on the table corresponding to it. If the line is correctly drawn, replacing the squares anywhere along it should just block the spot. The spot appears larger than it is because the plastic scatters the light. Viewing it through laser safety goggles, the scattering is removed and a small yellow spot is seen.

Once *p*, *q* are drawn on the bench, the separation between **BS** and **M1**, **M2** can be measured out. It is typically 40 cm. The splitter is not removed from the table after the beam power measurements are done. Originally it was removed and the two lines were measured off from their intersection point. The splitter was replaced and its alignment checked by comparing the reflected path *p*, with the line drawn on the bench. Replacing the beam splitter accurately is very difficult to do, so instead the paths are measured out by drawing lines parallel to *p*, *q* and measuring the distances from the intersection points of these lines. This may introduce a path differences of 1 mm or so between *p*, *q* which is acceptable.

The line **M1** - **M2** is now constructed. The angles between this line and *r*, *s* are calculated to produce the required intersection angle $2\theta_1$ and drawn on the bench using a 6 inch diameter circular plastic protractor marked off to 0.5°. Two marks are made on either side of the protractor for each angle. Lines *r*, *s* are now drawn and their intersection angle can be measured to within 0.25°.

The positions for the spatial filter mounts are marked on the bench, equidistant from O, the intersection point. **M1** and **M2** are positioned and the set squares are used to align the beam along the paths. The beam heights are checked again.

The sample holder is placed at O. This holder was designed by Yi-Yan (1978) p 131; the stage holding the sample and prism is held horizontally on a goniometer which can be rotated about the z direction, figure 3.6.(a.).

The spatial filter mounts are positioned so that the beam axis passes through the centre of the apertures in which the lens and pinhole are mounted. The mounts are Pi optical type with

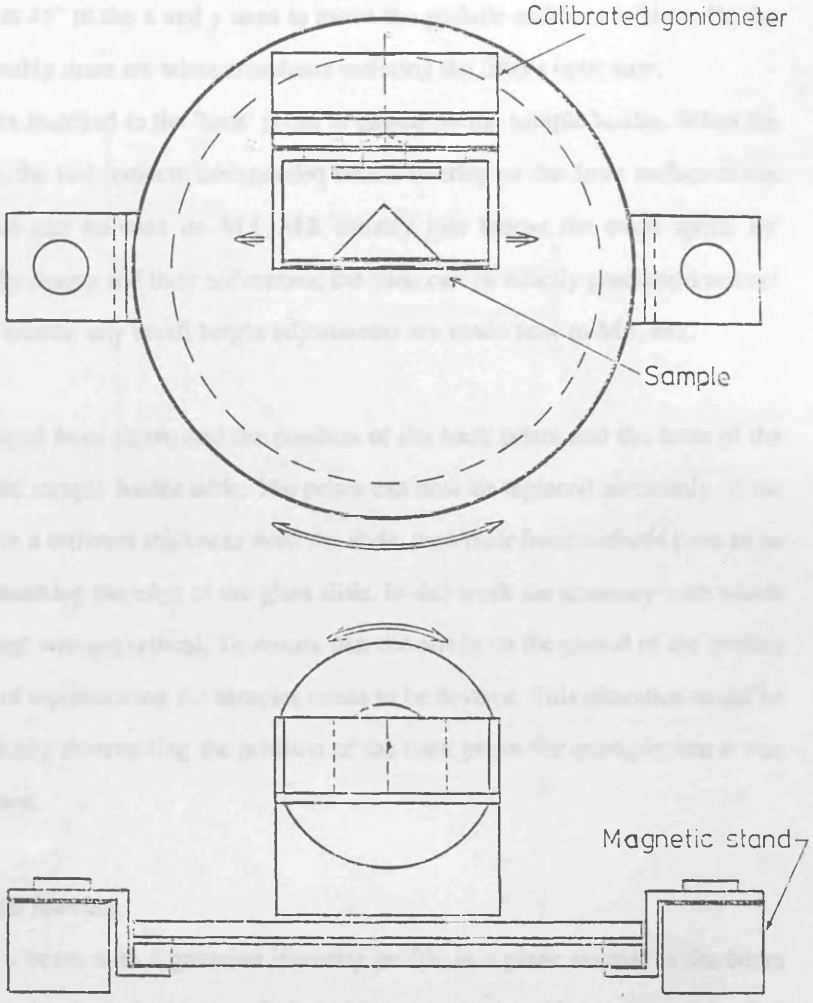

Figure 3.6.(a.) Diagram of the sample holder for exposure of holographic gratings. The unit weighs about 1 kg and is attached to the bench by magnetic clamps.

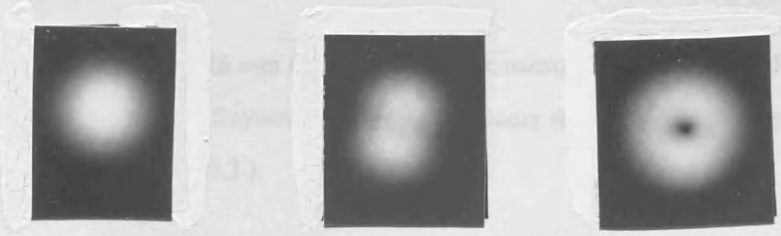

Figure 3.6.(b.). Photographs of UV spatial mode patterns (351.1 nm). The differences between the TEM_{00} gaussian mode and the TEM^*_{01}'doughnut' mode can be clearly seen. The intermediate TEM_{01} mode is also shown. Normally these mode patterns are much less distinct, but the pressure in the tube was low enough to give a high power output so that the modes could be selected by scanning the HORIZONTAL control on the laser.

micrometer screw drives at 45° to the x and y axes to move the pinhole and lens holders. On the end faces of the filter assembly there are white crosshairs indicting the filter's optic axis.

A plane glass slide index matched to the 'back' prism is placed on the sample holder. When the glass slide is set correctly, the two incident unexpanded beams overlap on the front surface of the slide and their reflections can be seen on **M1, M2** usually just below the main spots. By observing the overlap of the beams and their reflections, the slide can be exactly positioned normal to the bisector of the two beams; any small height adjustments are made now to **M1, M2.**

The back prism is clamped from above and the position of the back prism and the front of the glass slide are drawn on the sample holder table. The prism can now be replaced accurately. If the samples to be exposed have a different thickness from the slide, then their front surfaces have to be positioned along the line marking the edge of the glass slide. In this work the accuracy with which the samples were positioned was not critical. To ensure that the errors on the period of the grating are minimal a better way of repositioning the samples needs to be devised. This alteration could be done simply, by mechanically determining the position of the back prism for example; but it was not necessary to do this here.

Beam expansion and spatial filtering.

Ideally the laser emits a beam with a gaussian intensity profile in a plane normal to the beam axis. In practice there is noise from the laser and phase errors on the wavefronts caused by dust particles on the optics. The imperfections have higher spatial frequencies than the gaussian mode and can be blocked out in the Fourier transform plane of a lens (The diffraction pattern i.e. the spatial fourier transform of an object coherently illuminated in the front focal plane of a lens is located in the back focal plane, Steward (1983) pp 24-5, Klein (1986) pp 480 -482.).

The incident beam is focused down by a 16 mm focal length quartz microscope objective and passes through 30 μm diameter pinholes[1]. Beyond SP1, SP2, the beams steadily expand. The pinhole diameter d, is estimated from (figure 3.3.),

---

[1]Dumas (1985) reports using much smaller diameter (10 μm) pinholes and observing diffraction rings. At 457.9 nm several differnent sizes of pinhole were tried: 50, 30, 20 μm. There was significant noise on the wavefront transmitted through the 50 μm holes, while diffraction rings were prominent with the 20 μm holes, indicating that the focused gaussian beam was clipping the edges of the hole. The 30 μm pinholes gave the best results although some slight diffraction was still visible.

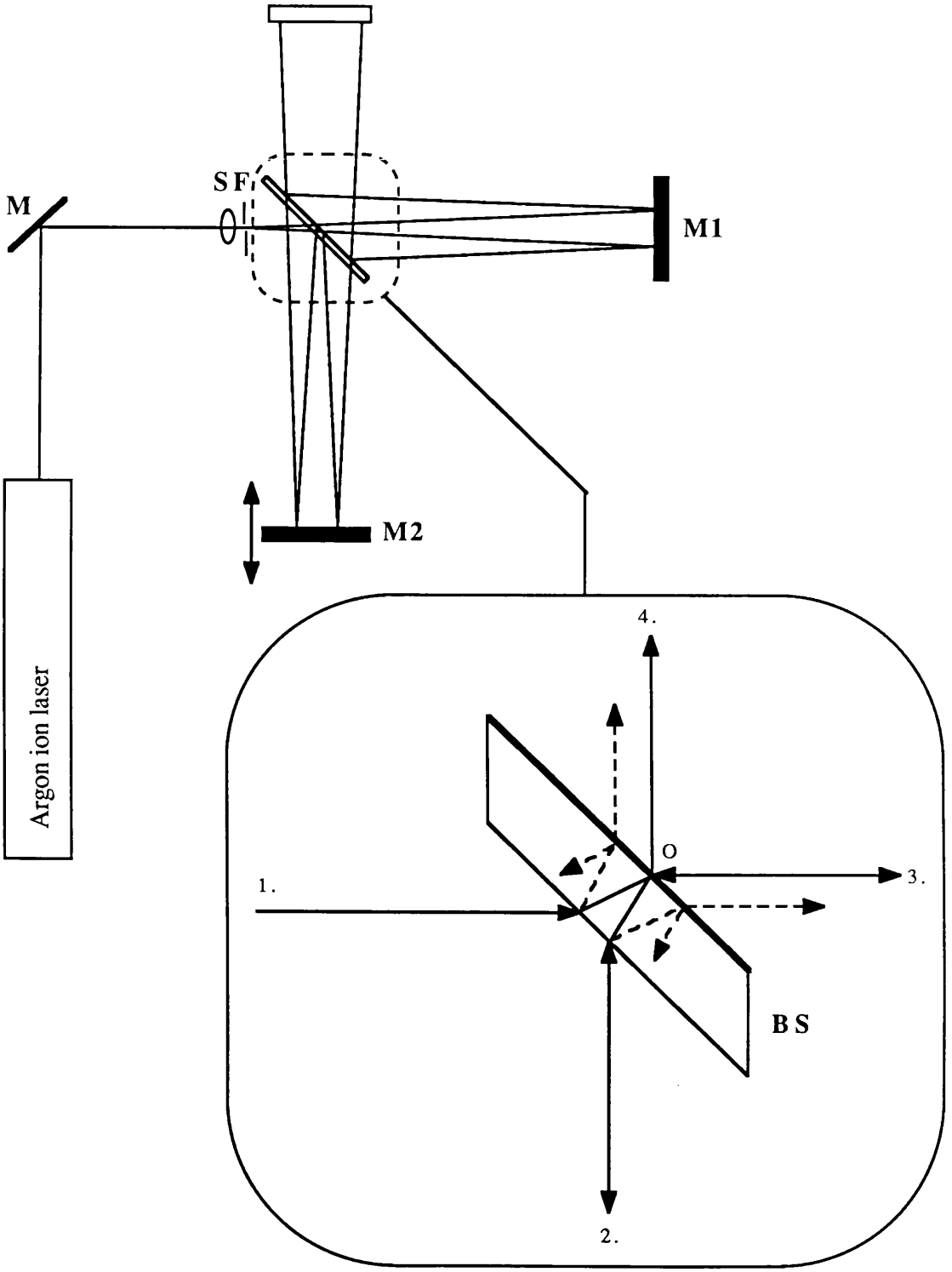

Figure 3.7. Michelson arrangement for measuring the coherence length of the Argon ion laser. M is a steering mirror, M2 is mounted on a micrometer screw drive. The beam is expanded and filtered at SF and circular fringes are visible on the screen, S. The panel shows detail of the beams produced by the beam splitter. BS is coated on the back side. There is no compensator plate.

$$d = 2 \lambda_0 f / D \qquad (3.1.2.)$$

where D is the input beam diameter. This approximate formula gives d = 16 μm for D = 1 mm and λ_0 = 457.9 nm. In practice the required pinhole diameter is usually a little larger than this.

Lens and pinhole alignment to the optic axis.

The unexpanded beam position is centred on the target. The lens is replaced in the filter assembly and the expanded beam is centred. The lens is scanned along the z axis so that the spot size at the filter plane is much larger than the pinhole diameter. When the pinhole is replaced, diffraction rings can be seen on the transmitted beam (it may be necessary to scan the pinhole in the x and y directions to see the rings). The pinhole is adjusted so that the rings are centred. The x-y controls on the lens holder are no longer touched. The lens is scanned back in along the z axis and the pinhole position changed to keep the diffraction pattern central. As the focal plane of the lens and the filter plane coincide, the diameter of the diffraction rings becomes ever larger until the rings disappear, leaving a bright centred patch. The filter is now set.

Choice of exposure wavelength , λ_0.

Photoresists in the AZ 1300 / 1400 series have sensitivities that increase in the UV. The absorption peaks occur at 350 nm and 398 nm. The laser source is a Spectraphysics 165 Ar^+ laser which can be made to oscillate on eight lines between 457.9 and 514 nm in the visible. With special optics, the laser can produce a low power UV output on two lines simultaneously: 351.1 nm and 363.8 nm. Most of the work was done with the 457.9 nm line. Exposures can be made using the powerful 488 nm line but the resist sensitivity is lower and the lower wavelength line can produce a smaller Λ for the same geometry.

The laser tube is not designed for UV operation. The laser has low gain and exhibits spatial mode instability unless the gas pressure is right. Fortunately, the UV laser radiation causes slight fluorescence when incident on most materials so the interferometer is set up as before.

Coherence requirements for the laser source.

The spatial coherence of the wavefronts used to record the gratings is ensured by the operation of the laser in single transverse mode TEM_{00}. The laser produces other spatial mode patterns simultaneously when it is run at higher power. The $TEM_{01}{}^*$ which has a circular 'doughnut'

intensity profile oscillates as well as the fundamental TEM_{00} mode. Figure 3.6.(b.). This mode is characteristic of a resonator with cylindrical symmetry about its optic axis (Maitland & Dunn. 1969).

An intercavity aperture is provided to reduce the gain (mode) volume , starving the TEM_{01}* mode and forcing the system into fundamental mode operation. At full power, when both laser modes are present, the laser produces about 50 % more power than on the TEM_{00} mode alone (measured at the 457.9 nm line).

The frequency spectrum of a source determines its temporal coherence. This can be seen as follows; Consider a beam split into the two arms of an interferometer and brought together again after introducing a path difference, or equivalently a time delay Δt, into one arm. The total intensity in the interference pattern is considered to be the sum of the different frequency components in the range n to $\nu + \Delta\nu$. The light is temporally coherent over a certain time interval Δt such that the number of maxima of frequency $\nu + \Delta\nu$ does not exceed by more than unity the number of maxima of frequency ν; i.e. Δt is the time over which the various intensity maxima stay in step. This condition implies:

$$(\nu + \Delta\nu).\Delta t - \nu.\Delta t \leq 1 \quad \text{or} \quad \Delta\nu.\,\Delta t \leq 1 \qquad (3.1.3.)$$

The equality determines the coherence time τ_c. The maximum tolerable path difference between the arms that can be tolerated before stable fringes can no longer be recorded is $D = c.\tau_c$.
(Maitland and Dunn 1969 Chapter 10.)

The frequency width of an atomic transition between energy levels E_i, E_j, $E_i > E_j$, in the argon plasma of the laser is broadened from a δ function at $\nu = \nu_{ij}$ the centre frequency defined by

$$\nu_{ij} = (E_i - E_j) / h \qquad (3.1.4.)$$

to a Lorenzian frequency spectrum whose width is determined by the finite lifetimes, i.e. the decay rates, of the states. This atomic linewidth is further broadened by collisions and thermal effects (Doppler Broadening). In the argon ion laser the laser transition linewidths are approximately 6 GHz wide.

The laser cavity produces axial modes, separated by c / 2 n L in frequency which are the allowed

standing wave solutions of the cavity. n and L are the refractive index ≈ 1.0 and the cavity length (= 1.05 m) respectively. Thus the axial mode separation is 143 MHz. These modes may oscillate inside the atomic linewidth if there is sufficient gain. In the Argon ion laser there are approximately 40 of these modes that can oscillate at a given laser transition. The maximum path difference D, is then 50 mm.

The coherence length at 457.9 nm was measured using the Michelson interferometer arrangement of figure 3.7. Circular fringes of poor visibility were still visible after **M2** has been scanned through 10 mm. The spatial filter is important. It increases the beam size and hence the extent of the ring pattern while preventing feeedback into the laser source.

The coherence length of a laser can be increased by the incorporation of an etalon in the cavity. This is an optical filter which selects one axial mode and suppresses all the others. The mode still has a finite frequency bandwidth, due largely to the losses in the laser resonator but this is now of the order of a few MHz giving a c Δt ~20 m.

Etalon operation of the laser is advisable for the three mirror interferometer arrangements because of their large path differences, but can be avoided with the symmetrical interferometer. Our laser was provided with an etalon for use at 488 nm, but the optical coating reduced the output power at 457.9 nm down from its usual 200 mW by an order of magnitude. It was not used in this work.

Argon laser: UV operation

The two UV lines lase simultaneously and cannot be dispersed inside the cavity, unlike the visible wavelengths, because of their low gain. The lines are dispersed outside the cavity by a quartz prism.

The maximum powers available on the two lines are 32 mW for the 363.8 nm line and 13 mW for the 351.1 nm lines.

The laser is used at maximum current and magnetic field. The magnetic field squeezes the discharge into a volume closer to the optic axis. Higher output power can be obtained as the gas pressure in the tube drops (less quenching due to collisions), but if the pressure becomes too low, higher order spatial modes appear which are very unstable, figure 3.6.(b.), difficult to get rid of and are unsuitable for recording gratings. A large shift in a spatial mode means a shift in the laser's

optic axis, so shifting the position of the grating pattern, washing out the photoresist exposure.

3.2. The fabrication of holographic gratings.

3.2.1. Thick resist gratings.

(a.) Transparent substrates (glasses).

Gratings are most easily fabricated on transparent substrates such as glasses or quartz. The light is transmitted though the resist layer and through the substrate. Unwanted reflections from the back surface of the substrate are suppressed by contacting it to a back prism with index matching oil, n = 1.53. The prism, figure 3.8., has the two rear square faces painted matt black which scatter and absorb the transmitted light. There will be some residual scattering from the resist (2) -glass (3) interface (r_{23}) since the refractive indices n_2, n_3 are not matched.

The amplitude reflection coefficient for 457.9 nm laser light incident at 40° on the glass though the resist is $r_{23} = 0.063$.

Inside the resist θ_2 is 22.7°, $n_2 = 1.665$, and inside the glass θ_3 is 25.4° , $n_3 \approx n_5 \approx 1.51$. (The suffices refer to figure 3.8.)

Such a small value of r_{23} has been assumed not to have an effect on the grating profile especially for thick resist gratings. The steeper sidewalls of gratings exposed in resist on an anti-reflection coated layer show that this scattering is significant, section 3.2.1.(c.). Some residual scattering will also be due to the inefficiency of the back prism.

Without the back prism the amplitude reflection coefficient for radiation incident from the glass into air, r_{34}, would be 0.28; the reflections causing interference. Figure 3.9. is a SEM[2] micrograph of a grating made on a glass slide without the back prism. The surface is mottled; there are areas 30 μm square where the grating has been completely washed out next to similarly sized areas of well developed grating. The modulations in the interference pattern over the surface of the resist are wedge fringes caused by slide faces not being parallel. Values for the reflection coefficients in the resist glass system are given in Table 3.1.

Values for the resist refractive index were obtained from Yi Yan (1978) and Dill (1975a) for

[2]All the SEM micrographs in this thesis were photographed using an S 800 Hitachi Scanning Electron Microscope.

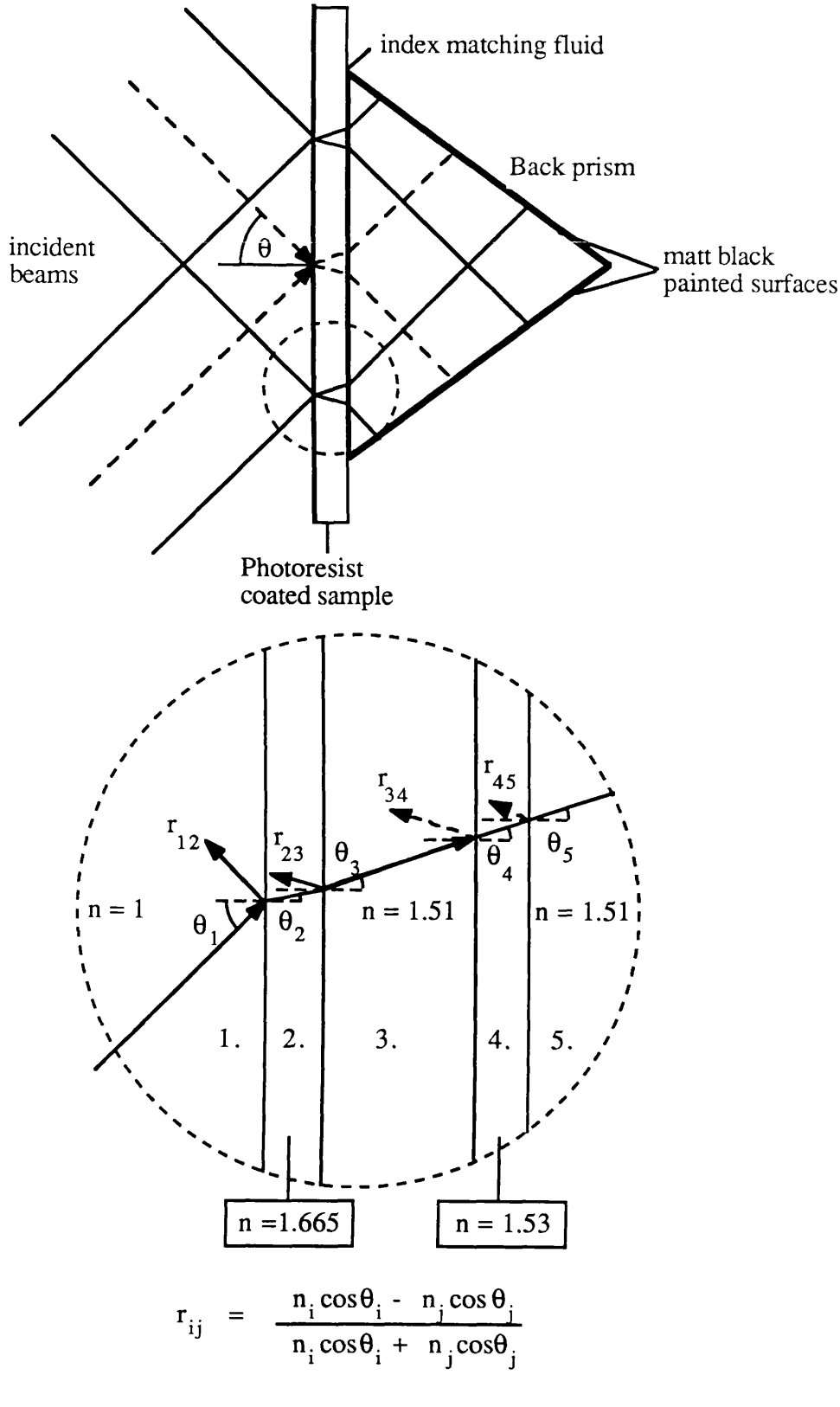

$$r_{ij} = \frac{n_i \cos\theta_i - n_j \cos\theta_j}{n_i \cos\theta_i + n_j \cos\theta_j}$$

Figure 3.8. A 'back' prism with two matt black painted faces is contacted with index matching oil to the back of a transparent substrate to suppress reflections from the glass (3)-air (4) interface.

The inset is a detail of the optical layers discussed in section 3.2.; 1 = air, 2 = resist, 3 = substrate, 4 = air (no prism), oil (prism) and 5 = prism glass. Reflections from the i th to the j th layer are denoted by r_{ij}, 's' polarisation (E vector normal to plane of incidence). The refractive indices refer to 457.9 nm.

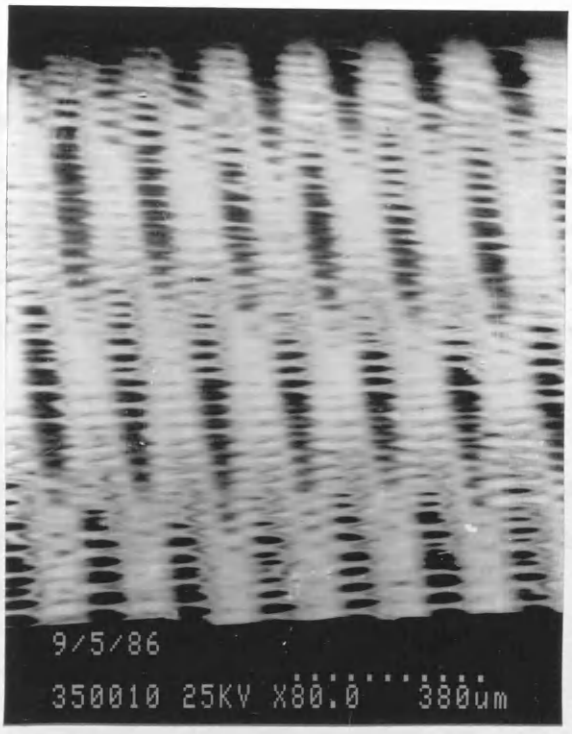

Figure 3.9. Spurious modulations appear on photoresist gratings made on glass without the back prism. These are caused by interference between reflections from the front and rear surfaces of the glass slide.

Figure 3.10. 298.9 nm period photoresist grating on glass exposed with a back prism. The micrograph was taken at 45° to the cleaved edge of the grating. The roughly sinusoidal profile is typical of such gratings.

AZ 1350 J, figure 2.1.(c.). The newer resist AZ 1450 J is based on the same resin as AZ 1350 J but has an additional component to reduce striations while spinning. Hoechst, who manufacture the AZ resist series quote the same film thicknesses versus spin speed and refractive indices for both materials. The unthinned resist is 1.76 μm thick spun at 4000 rpm for 30 seconds. Spin curves for 66% and 25% solutions (AZ 1450 J / Thinner by volume) were determined by talystep, figure 3.11.

Figure 3.10. is an SEM micrograph of the cleaved edge of a 299 nm period resist grating. There is no evidence of mottling and the grating has a 1:1 depth to linewidth ratio. The almost sinusoidal profile is typical of such gratings.

Table 3.1.

Reflection coefficients for 457.9 nm exposure on transparent substrates.layers

Angle of incidence θ_1	θ_2	θ_3	r_{12}	r_{23}	r_{34}*
40°	22.7°	25.4°	- 0.33	0.06	0.28
70°	34.4°	38.5°	- 0.60	0.08	0.55

* r_{34} is the reflection from the glass air boundary without a back prism.

Exposure and development parameters: 457.9 nm.

The gratings are exposed with laser output power 90 mW and exposure times varying between 30 seconds and 1 minute. The maximum output power is just over 200 mW. The exposure power was reduced to ensure single spatial mode operation.

Routine power measurements were made using an integrating sphere power meter manufactured by United Detector Technology Inc., model 122A, calibrated against a Coherent model 210 black body power meter. 90 mW of power was used; after the mirrors and the spatial filters, the incident power has been reduced to 60 mW.

The gratings are formed over an area approximately 2 cm in diameter, depending on the spatial

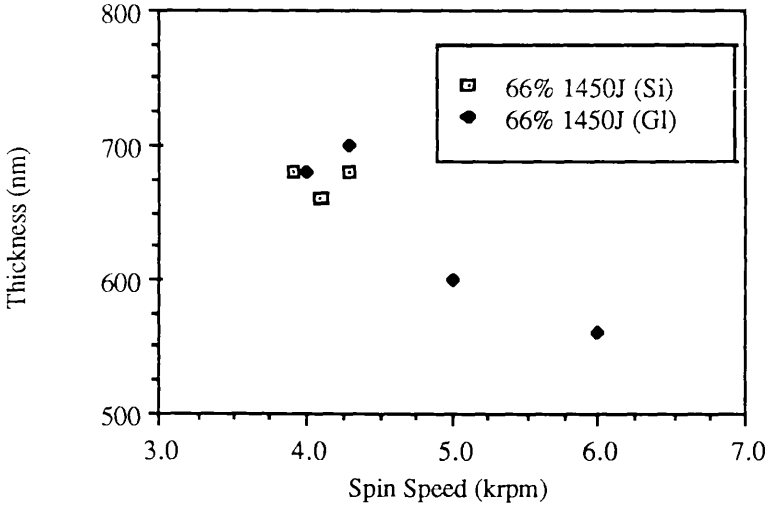

Figure 3.11.(a.) Spin curve for 66% AZ 1450J measured by talystep. The resist was spun on glass and silicon samples.

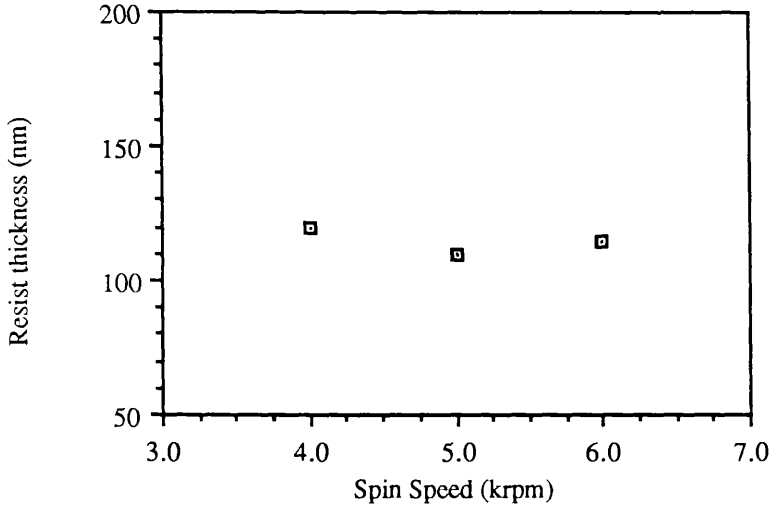

Figure 3.11.(b.) Spin curve for 25% 1450 J measured by talystep. The resist was spun on silicon samples.

filter position (25 cm), so that the power density is ~ 20 mW cm^{-2}.

Exposure times vary between 30 s and 1 m. Exposure times for AZ 1450 J are 50% greater on average than for AZ 1350 J. The power density on the sample surface decreases with increasing angle of incidence due to the larger overlap area formed by the two beams. Exposure times have to be increased slightly to take this into account and the larger reflection losses r_{12} at high angles of incidence, $\theta_1 > 55°$.

Various resist thicknesses were tried. Initially unthinned resist was used (1.76 μm) but it is difficult to dry etch through such a thick layer without the resist columns thinning out and collapsing (Chapter 4). A 66% by volume solution spun between 4000 rpm and 5000 rpm gave film thicknesses between 0.68 and 0.64 μm. A 1:2 solution AZ developer diluted with water was used throughout this work. This is a weaker concentration than that used for the exposure of optical masks (1:1). The stronger developer solution removed the resist too quickly leaving a annular area of grating surrounding a bare patch.

The exposure of holographic gratings is different from that used in optical lithography. In optical lithography, the exposure is essentially digital in character; the resist is completely developed where it has been exposed. Thick holographic gratings are exposed in an analogue process; the intensity variation is a sinusoid and the resist is not developed for longer than the grating image takes to form. Prolonged development does not tend to improve the aspect ratio of the grating and may wash it out.

All traces of the index matching oil must be removed after the exposure. The oil, a hydrogenated terphenyl, is very difficult to remove and will slowly dissolve the resist. After exposure the contaminated side of the sample is wiped against a lens tissue. The uncoated side of the sample is carefully wiped with a lens tissue impregnated with a little iso-propyl alcohol (IPA). Great care must be taken since IPA will dissolve the resist. If oil has reached the front surface, it can be removed by immersing the sample in xylene, which is one of the few solvents not to attack resist.

Limitations on resolution and aspect ratio of developed gratings.

Long exposure times make the elimination of vibration very important. This can be done by incorporating a feedback system to compensate for any vibration. In this work such a system was

unnecessary as the exposure times were short. Anderson's (1988) group at MIT have devised a feedback system which drives a piezoelectric mount on one of the mirrors in response to changes in a fringe pattern generated by combining the two incident beams at a beamsplitter.

In this work the optical table is supported on inflated tyres to reduce vibration. Back reflections from the lenses in the spatial filters produce Michelson interference fringes at the output coupler of the laser. Any movement of the bench shifts the fringes. Gratings are recorded when the fringe patterns are stationary.

Figure 3.12. is an SEM micrograph of a 210 nm period grating recorded at 60° incidence with 363.8 nm laser light. The most noticible feature is the enormous aspect ratio ~ 3:1. There appears to have been less vibration when this grating was made. Figure 3.13. is a micrograph of a grating made with nominally the same parameters on another day. The aspect ratio is 1:1.

Exposure and development times vary considerably due to a number of factors such as slight differences in resist preparation, the bake temperature and duration, and the humidity during the spin process. The developed grating patterns are weaker if the developer is old or has been exposed to the air for more than a few minutes. It is possible to use models to predict an approximate resist response, but it is more practical to do test exposures, optimising the exposure time for each sample. On different occasions, nominally the same conditions result in exposure times differing from 45 to 60 seconds.

Changes in the development time can make up for changes in the exposure process but in general long development times should be avoided. Typically a 45 second exposure, requires a development time between 12 and 20 seconds. Development is stopped when a red mist is seen to form over the grating. The sample is then rinsed in deionised water and blown dry.

UV exposure of thick resist gratings.

The resist exposures at 351.1 nm and 363.8 nm are faster than for the 457.9 nm line due to increased resist absorption.

The gratings in figure 3.12., figure 3.13. were exposed at 363.8 nm (32 mW) for 30 seconds and developed in 1:2 developer for 3 seconds. The development times tended to be short. Diluting the

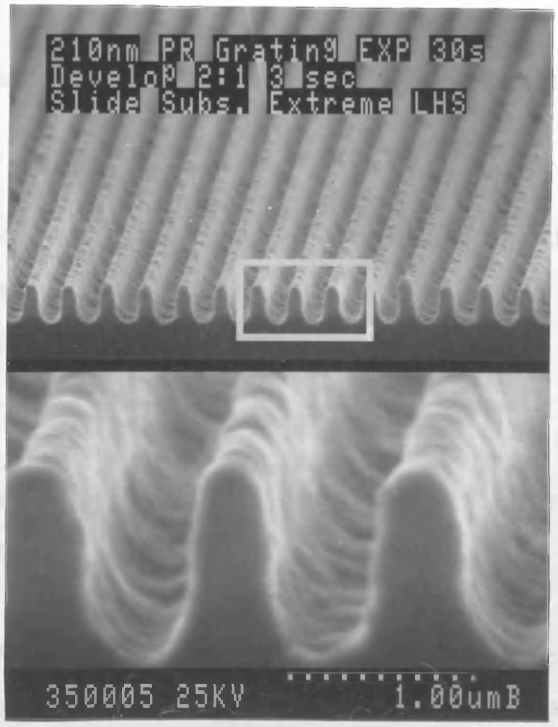

Figure 3.12. 210 nm period photoresist grating exposed by 363.8 nm laser light at 60° incidence. Thick resist on glass. 30 s exposure (32 mW), 3 s development (1:2). The grating has a high aspect ratio, 3:1, probably due to a reduction in vibration while it was recorded.

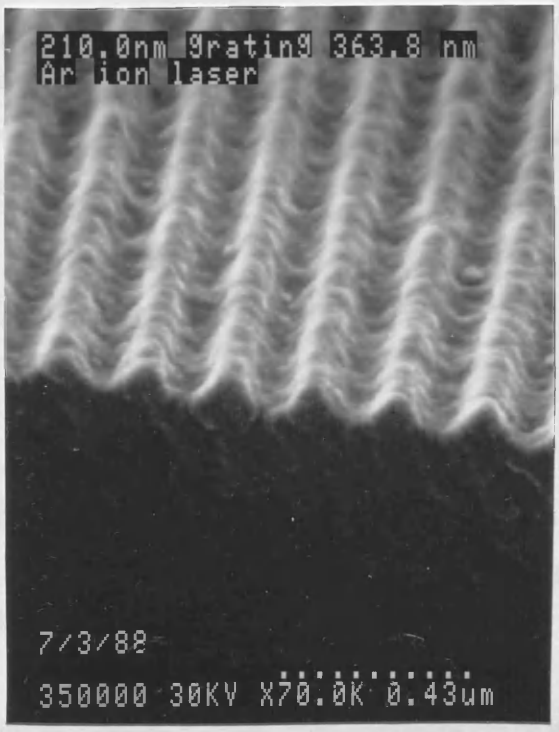

Figure 3.13. 210 nm photoresist grating. The parameters are nominally as above, but the aspect ratio is much smaller (1:1). The gratings were made on different days.

developer to 1:3 resulted in reduced contrast, figure 3.14., so the more concentrated solution was used.

Figure 3.15. is a micrograph of a 186.8 nm period grating exposed for 30 seconds by 351.1 nm laser light (13.2 mW) at 70° incidence on a glass substrate and developed for 8 seconds in 1:2 developer. This is the shortest period grating that was made by direct exposure.

Grating Quality.

A strong grating can be seen as a bright uniformly coloured patch when observed at grazing incidence with the light source behind the observer, figure 3.16.(a.).

The grating vector $G = 2\pi / \Lambda$ lies perpendicular to the grating lines in the plane of the grating. $|\mathbf{G}| > k_0 = 2\pi / \lambda_0$ for grating periods < ~ 400 nm and for visible light. The positions of the diffracted orders are given by:

$$|\mathbf{k}_{2,3}| \sin\theta_2 = |\mathbf{k}_1| \sin\theta_1 \pm n|\mathbf{G}| \qquad (3.2.1.)$$

Since $|\mathbf{k}_1| < |\mathbf{G}|$ and $|\mathbf{k}_1| = |\mathbf{k}_{2,3}| = k_0$ the only allowed solution of (3.2.1.) for θ_2 corresponds to n = - 1. Other values for n would give a larger scattered wavevector than the incident one which is not allowed. Two symmetric solutions appear above and below the grating plane oriented towards the source given by:

$$\theta_1 = \sin^{-1}\left(\lambda_0 / \Lambda - \sin\theta_1\right) \qquad (3.2.2.)$$

Inspection of equation (3.2.2.) shows that solutions exist for shorter wavelengths and large θ_1.

Only the blue light is strongly scattered towards the observer for gratings with periods below 300 nm. At 186.8 nm period, a bright patch can no longer be seen. SEM analysis is used to examine gratings with periods below 250 nm.

The grating couples some of the light into the glass and coloured fringes can be seen if the glass is cleaved, figure 3.16.(b.). In this case, the scattered wavevector is too large to emerge from the grating. This coupled light is refracted by the cleaved edges of the slide. The condition for reverse

coupling is

$$\sin \theta_1 = \lambda_0 / \Lambda - n_g \qquad (3.2.3.)$$

As θ_1 is increased the condition is met for larger wavelengths with a cut-off at $\lambda_0 = \Lambda.n_g$.

If the grating is coated with a metal it appears darker than the surrounding area due to increased absorption of the incident light.

Resist film preparation.

The substrates are given the standard three stage solvent rinses; trichlorethylene, methanol, acetone each with ultrasonic agitation for five minutes, then a deionised water rinse before blowing dry with dry nitrogen. If the samples are clean, after their removal from the water, a thin continuous film of liquid coats the substrate. If the substrates are dirty, then water drops form separated by dry areas.

In general the three stage wash is sufficient for most substrates such as slides or cover slips and semiconductors. If a sample has been ion exchanged, the surface is coated with a residue that is not removed using the solvents alone. First it is boiled in water, then cleaned in the solvents and finally soaked in a solution of 8 parts concentrated sulphuric acid to 1 part hydrogen peroxide (about 30%) for ten minutes.

The samples are allowed to dry on a hotplate for at least an hour before spinning.

The spun film quality is quite uniform over an area about 2 cm in diameter in the middle of the slide. This is shown by the colour of the film, thickness variations being detected by colour variations from mauve to green or vice versa as observed under yellow light. The thickness uniformity of resist on slides was investigated by Pun (1983) and Washo (1977).

After spinning the resist samples are baked at 90°C for 30 minutes to drive off solvents.

(b.) Highly reflecting substrates.

Some experiments were done on 1 cm side silicon chips and on 1 cm diameter germanium discs.

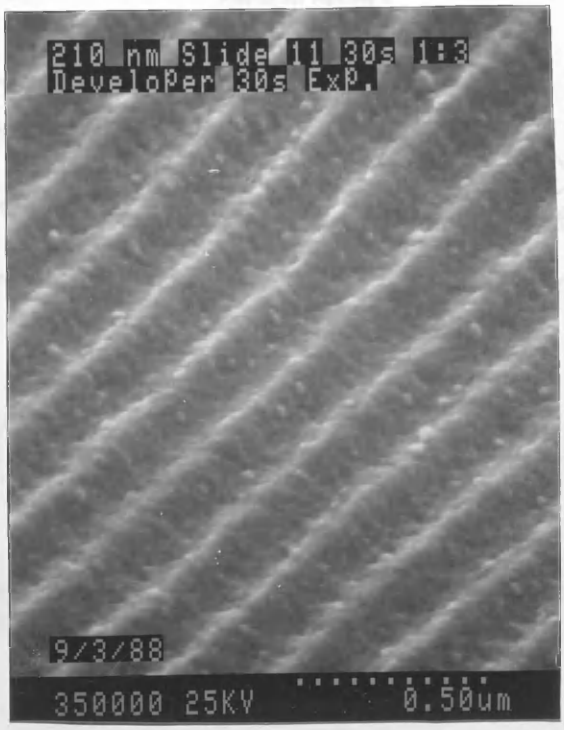

Figure 3.14. 210 nm photoresist grating. The sample was exposed for 30 seconds and developed in 1:3 developer for 30 seconds. The smaller aspect ratio is due to the lower contrast of the developer.

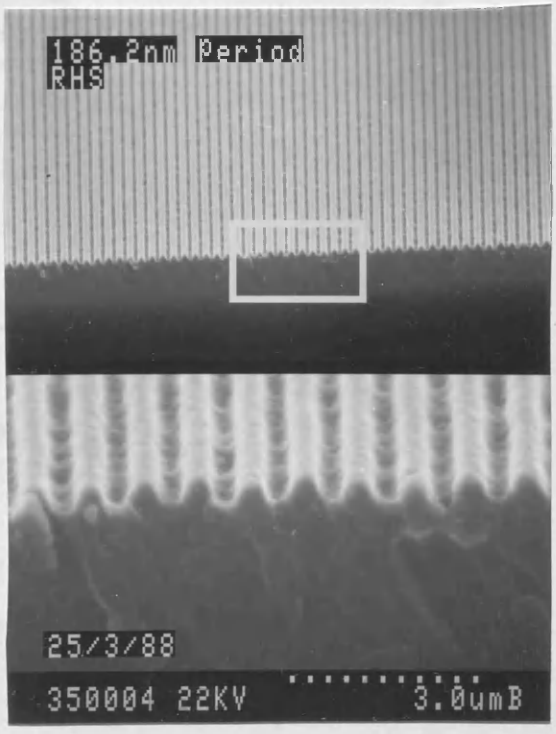

Figure 3.15. 186.8 nm period photoresist grating. The sample was exposed for 30 seconds at 351.1 nm (13.2 mW) at 70° incidence and developed in 1:2 developer for 8 seconds. This is the shortest period grating that was made by direct exposure.

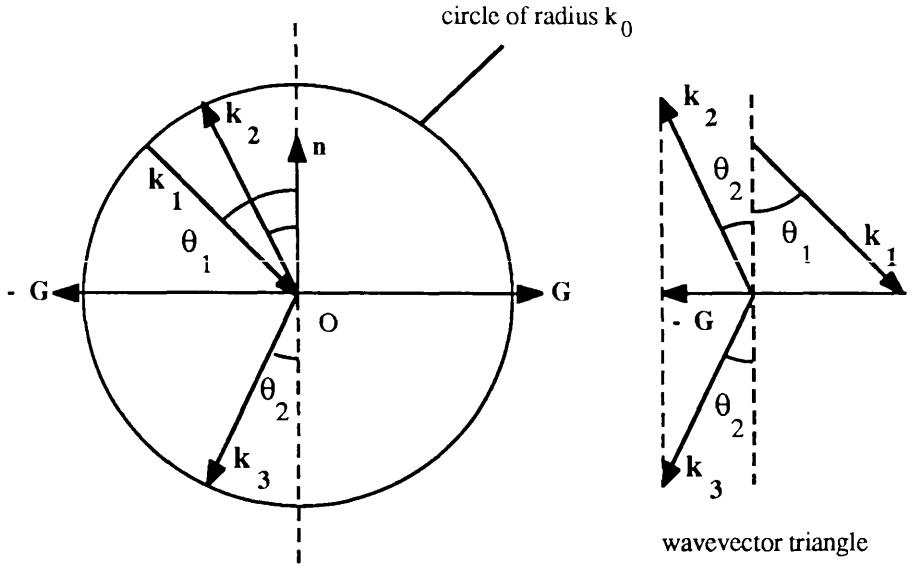

Figure 3.16.(a.) Wavevector diagram for predicting the orientation of diffracted beams outside the grating.

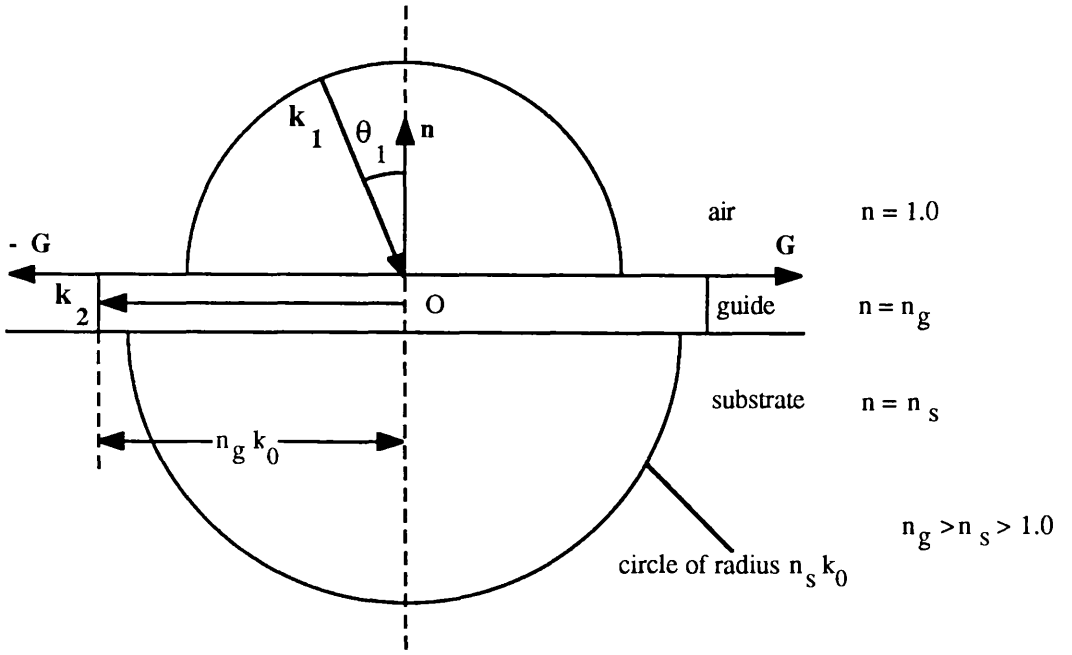

Figure 3.16.(b.) Wavevector diagram for reverse grating coupler.

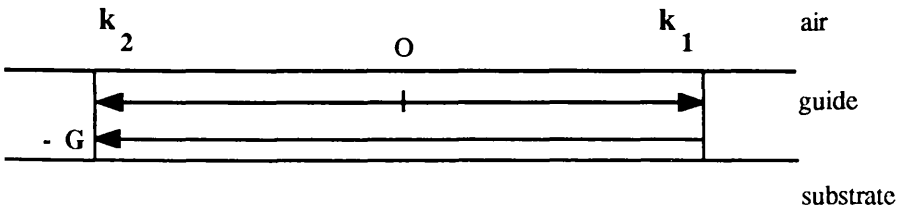

Figure 3.16.(c.) Wavevector diagram for first order Bragg reflection.

There will be a standing wave in the resist exposed on germanium and silicon according to equation (2.2.13.). Exposures on the two materials are be much the same, i.e. that there is an intensity minimum at the surface of the substrate.

The thickness of the resist layer should be (n + 1 / 2).P, for an intensity maximum at the surface.

Chip size and topography have an effect on the thickness of the resist. The resist is thicker at the edges where it accumulates during the spinning process. This is not a problem for large samples such as slides but creates difficulties with smaller samples or irregular shapes; the resist is more uniformly coated on the discs.

To produce a 356.2 nm period grating on Si (40° incidence at 457.9 nm) the resist is spun between 4.0 and 5.0 krpm to match the 4.5 P (= 671 nm) condition.

The grating aspect ratio and profile are changed by the standing wave effect. Figure 3.17 shows a grating formed on silicon in resist spun at 4.3 krpm. The aspect ratio is much lower than for the gratings produced on glass and the profile is quite different.

The exposure time would be reduced to a quarter of its value for the transparent substrates if the resist was spun on a perfect reflector. Silicon is not a perfect reflector, but the exposure times are approximately halved.
Various exposure and development times were tried but the best results were obtained with long exposure times ~ 20 seconds and short development times ~7 seconds. Shorter exposures (3 s) and longer development (20 s) produced weaker gratings. Increasing the resist thickness slightly (spinning at 4.2 krpm) reduced the aspect ratio further until it disappeared (spinning at 4.1 kpm). Talystep thickness measurements of the resist were made at the different thicknesses but are all within the error of the measurement, figure 3.11.(a.).

Figure 3.18. is a micrograph of a 356.2 nm grating in a layer spun on germanium at 4.2 krpm. The grating was exposed for 5 seconds and developed for 10 seconds.

A major difficulty is that development does not proceed uniformly. The exposed layers in the

resist develop rapidly and the unexposed layers slowly. Over-development tends to wash out the grating, since the developer etches laterally as well as vertically through the unexposed resist. Development was stopped immediately when a colour change in the resist was seen.

Altering the grating period means re-optimising the thickness of the resist.

(c.) The use of spin - on anti reflection coatings (ARC's).

The recent development of spin on anti reflection layers (ARC's) have made the exposure of resist on reflective substrates much easier, improving linewidths and the sharpness of the printed images, (Lin 1983). The material can also be used to make holographic gratings (Anderson 1988). The ARC used here is a dyed polyimide manufactured by Brewer Science. This material absorbs radiation over a wide range of wavelengths. Table 3.2. lists the percentage transmission against wavelength for a 200 nm thin film of ARC. One of the advantages of this material for conventional optical lithography is that it dissolves in standard AZ developer.

The manufactures claim that the bake temperature for the ARC is very important and should be kept between 135°C and 152°C. The temperature determines the rate at which the material develops in photoresist developer.

In these experiments a layer of ARC was spun at 5000 rpm for 120 seconds on silicon and baked at 140°C for 30 minutes. Brewer quote a thickness of 205.3 nm for this spin speed. After the bake, the substrates have a green yellow appearance. Immediately after the bake a layer of photoresist was applied (66% AZ 1450 J spun at 5000 rpm for 30 seconds and baked at 90°C for 30 seconds).

A 285 nm period grating exposed for 60 seconds with 457.9 nm light on top of the ARC layer is shown in figure 3.19. The development time was 12 seconds. The ARC layer is the coarsely grained material.

The results are remarkable, the gratings have an aspect ratio ~2.0. The effects of the standing wave are completely absent; in fact the profiles are sharper than those obtained on transparent substrates using a back prism, indicating that there is some residual scattering present even when using the prism. The ARC was used successfully to expose very strong gratings in resist on top of germanium discs.

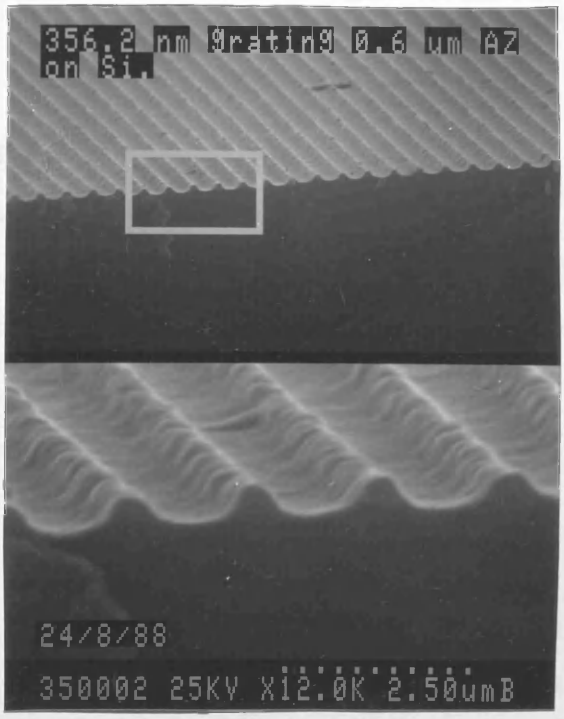

Figure 3.17. 356.2 nm period grating recorded in AZ 1450 J spun at 4.3 krpm on silicon.

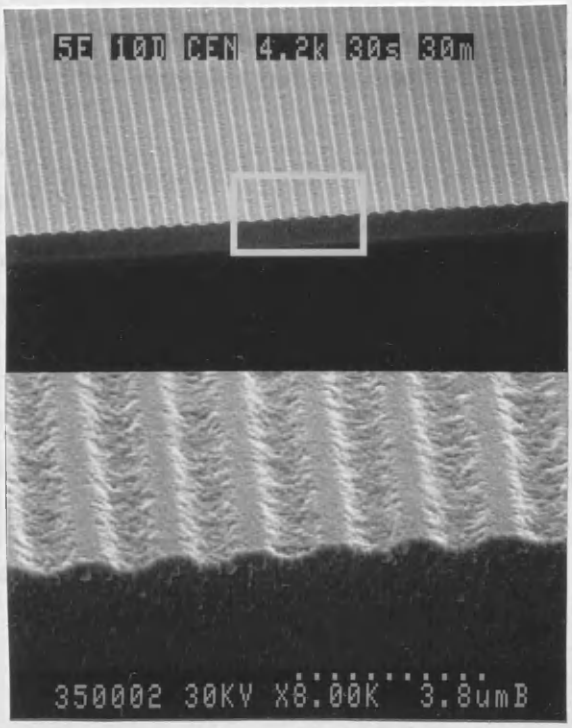

Figure 3.18. 356.2 nm period grating recorded in AZ 1450 J spun at 4.2 krpm on germanium.

Table 3.2.

Spectral data for 2000 Å film of ARC

λ (Hg line nm)	Transmittance %	Absorbence
220	3.8	1.4
254	5.0	1.3
300	20.2	0.7
313	25.0	0.6
365	13.0	0.9
405	3.2	1.5
436	1.6	1.8
546	72.0	0.1
578	83.0	0.1

Data from Brewer Inc. product details.

Although the ARC is suitable for use on highly reflective substrates, there could be problems for exposure on polyimide coated glass. After dry etching and metal deposition, the ARC is not easily removed. Acetone removes the resist and the metal which it supported, but does not completely remove the ARC. The samples are boiled in acetophenone (miscible with acetone) in a reflux condenser to remove the remaining ARC. The samples may also need to be ashed in an oxygen plasma. Acetophenone may also damage the underlying polyimide layer.

The use of an ARC layer would eliminate the spurious reflections inside small transparent samples exposed at high incidence angles due to the laser light being refracted through the sides of the samples. These reflections cause the gratings to have a mottled appearance. To avoid this the edges of the samples are painted matt black.

(d.) Blazed photoresist gratings.

If a non reflecting sample is exposed with the normal to its surface making an angle Δ' with the

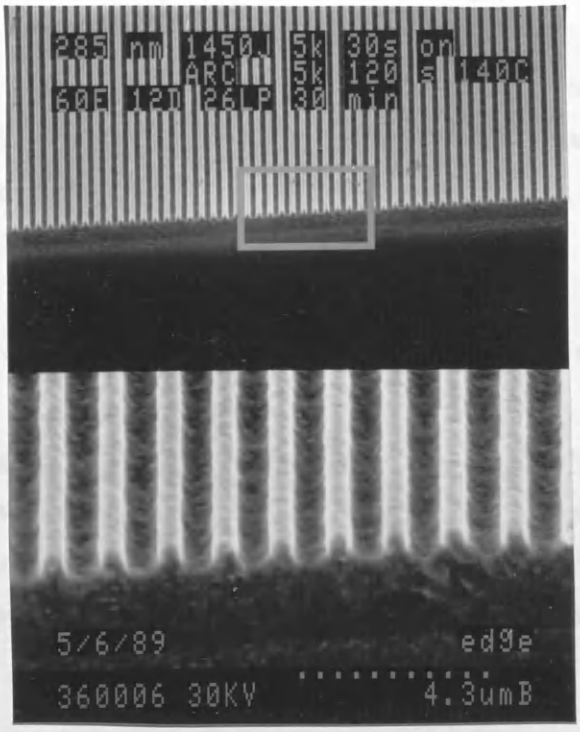

Figure 3.19. 285 nm period grating recorded in AZ 1450 J spun at 5 krpm on ARC (the grained layer) on silicon.

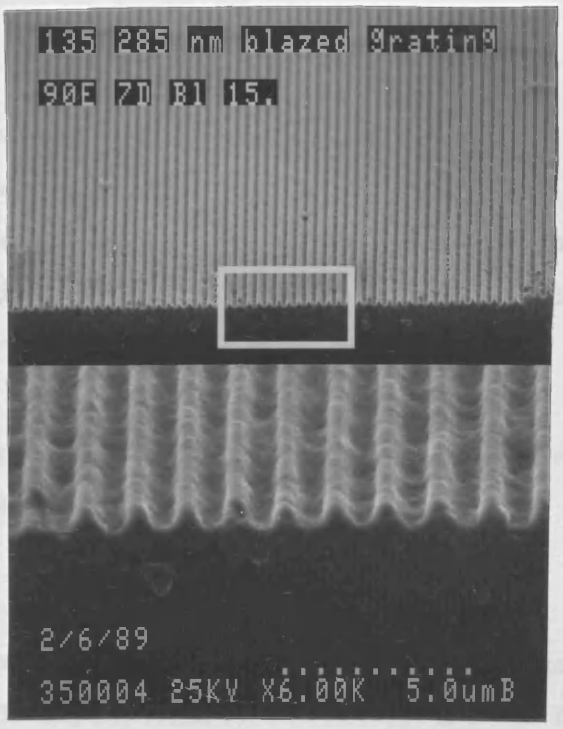

Figure 3.20. 295 nm period grating blazed at 16° recorded in AZ 1450 J spun at 4.3 krpm. The period of the spatial interference pattern is 285 nm.

bisector of the incident beams, a blazed grating will be formed; the fringes will be slanted within the resist at an angle (90° - Δ) where Δ is the slant angle in the resist. Referring to figure 2.8., the period of the slanted grating, Λ_b along the resist surface is related to the period of the spatial interference pattern, Λ, by

$$\Lambda_b = \Lambda / \cos \Delta \qquad (3.2.4.)$$

Figure 3.20 is an SEM micrograph of a blazed grating recorded at an angle Δ = 16°. There is not much evidence of the blazing on the profile except that the resist walls on the leading edge of a beak are slightly steeper than on the trailing edge. The period, however is shifted to 299 nm from 285 nm consistent with equation (3.2.4.) and the accuracy of measuring the period from the micrograph.

The grating exposure time was increased to 90 seconds to take the reduced incident intensities into account. The development time was 7 seconds.

3.2.2. Thin resist gratings.

(a.) Transparent substrates (glasses).

Thin film gratings are the traditional way to produce masks for ion beam milling (see chapter 4) or dry etching into substrates. The resist must be thin (< 0.2 μm) to prevent flowing and preferably cut down to the substrate. Pun (1983) pp 146-156 describes the milling of 300 nm period photoresist gratings 150 nm thick into sputtered glass waveguides.

Experiments were done on glasses, silicon and gallium arsenide wafers with thin resist layers, spun with (1:2) and (1:3) dilutions of AZ 1350 J with thinner.

Glass.

Figure 3.21., 3.22. are micrographs of 457.9 nm gratings exposed in 0.15 μm of resist on glass. (457.9 nm exposure at 30° angle of incidence, 1:2 resist spun at 6 krpm for 30 s). Both samples were developed in 1:2 developer for 20 s.

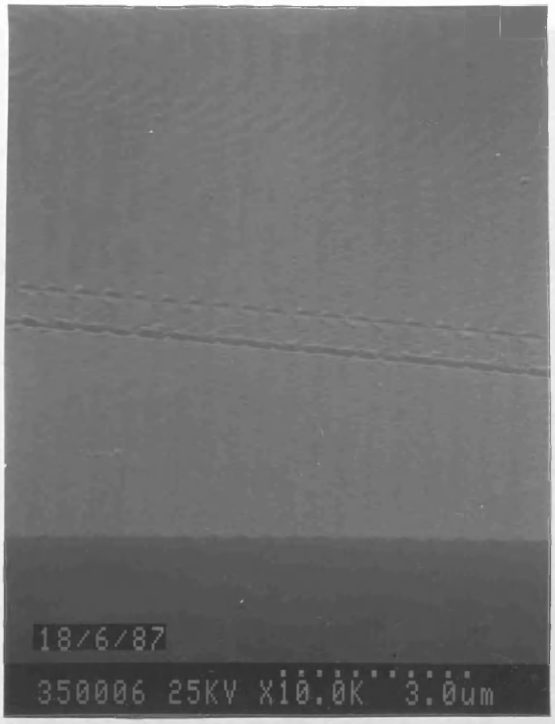

Figure 3.21. Thin resist (0.15 μm) grating; 457.9 nm period on glass. Low aspect ratio. Exposure time: 30 s, development time (1:2): 20 s.

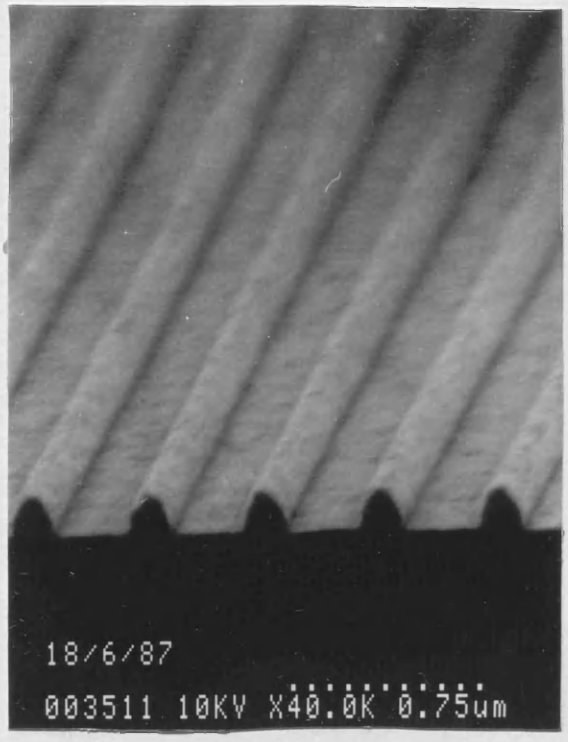

Figure 3.22. Thin resist grating (0.15 μm); 457.9 nm period on glass. Cut down to substrate. Exposure time: 60 s, development time (1:2): 20 s.

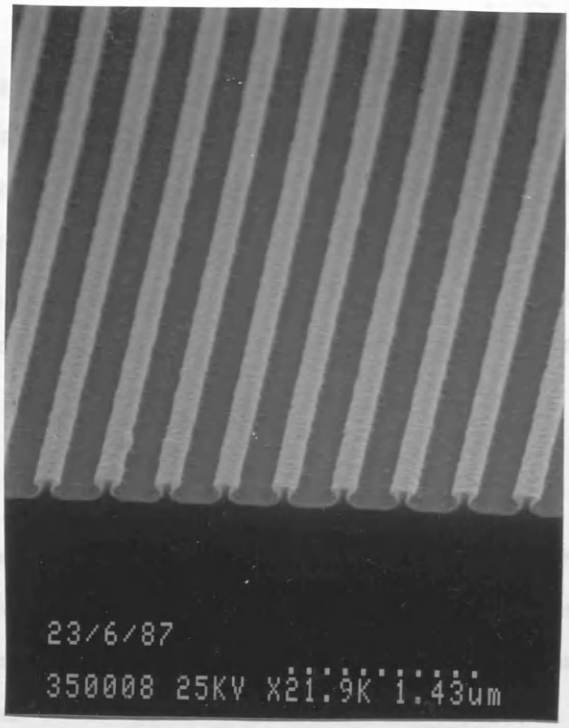

Figure 3.23. Thin resist grating (0.15 μm); 457.9 nm period on silicon. Resist profile shows a strong standing wave effect. Exposure time: 60 s, development time: 20 s.

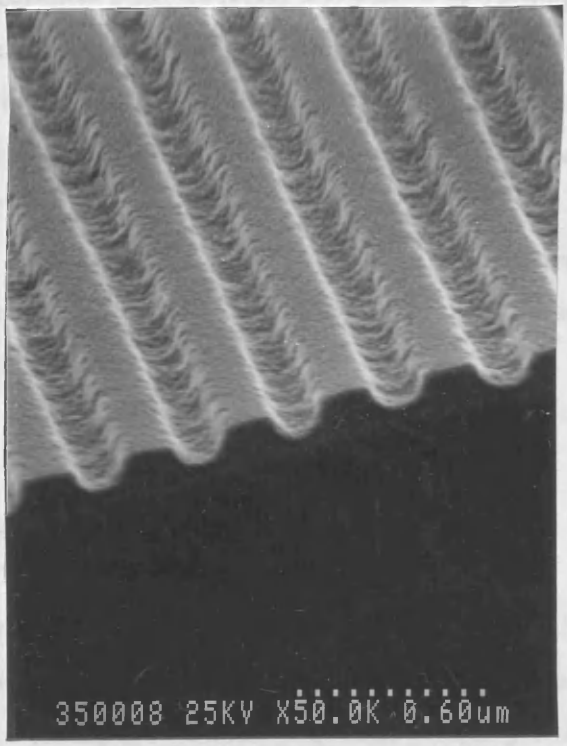

Figure 3.24. 360 nm period thin photoresist grating (0.10 μm) on GaAs. Exposure time:15 s, development time: 10 s.

The aspect ratio of the grating in figure 3.21. is very low; the exposure time was 30 s (the same for thick resist gratings), while in figure 3.22., with twice the exposure, the resist layer is cut down to the substrate. Exposure and development need to be much more carefully controlled than in the thick resist case. The variation in exposure time could be an effect of resist processing, the baking procedure for example; it does not seem to be explicable in terms of scattering from the resist surface or reflectivity (about 5% at normal incidence). This was not pursued further.

Semiconductor.

Figure 3.23. is an SEM micrograph of a grating formed in the same thickness of resist but on silicon. It clearly shows the effect of the standing wave. The grating profile is undercut and the resist is not completely removed from the troughs. Here the developed resist thickness is just less than the standing wave thickness.
The sample was exposed for 60 s and developed as above for 20 s. The exposure time was 60 s, the same as for the glass substrates.

Figure 3.24. is an SEM micrograph of a 360 nm period (457.9 nm at 39°) grating exposed in a 0.1 μm layer of 1:3 thinned resist spun at 6 krpm onto 5 x 5 mm GaAs chips. The exposure time was 15 s and the development time (1:2) was 10 s. These parameters are more in line with those discussed earlier. The resist thickness is ~ 0.7 P. The resist is not cleared down to the substrate.

One problem occasionally experienced in the making of very thin resist gratings is their tendency to peel off: 'the spaghetti effect' as reported by Dumas (1985) p 133. The lack of adhesion is probably due to dampness prior to resist application.

3.2.3. Two dimensional gratings.

Two dimensional gratings or dot patterns can be formed in positive resists simply by exposing one grating, rotating the sample and exposing another grating. The sample is then developed as normal. Yi-Yan (1978) reported making two dimensional gratings of 1 μm period on a chrome plate substrate this way.

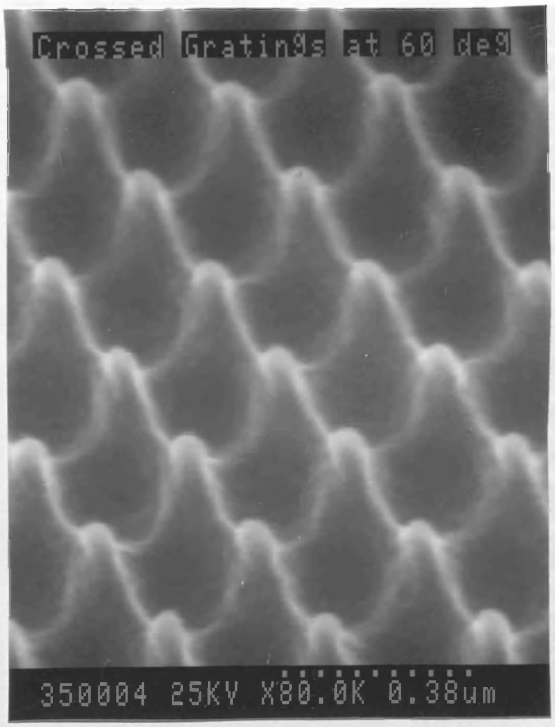

Figure 3.25. Crossed 300 nm period photoresist gratings (60°) in thick AZ 1350 J: 0.68 μm.

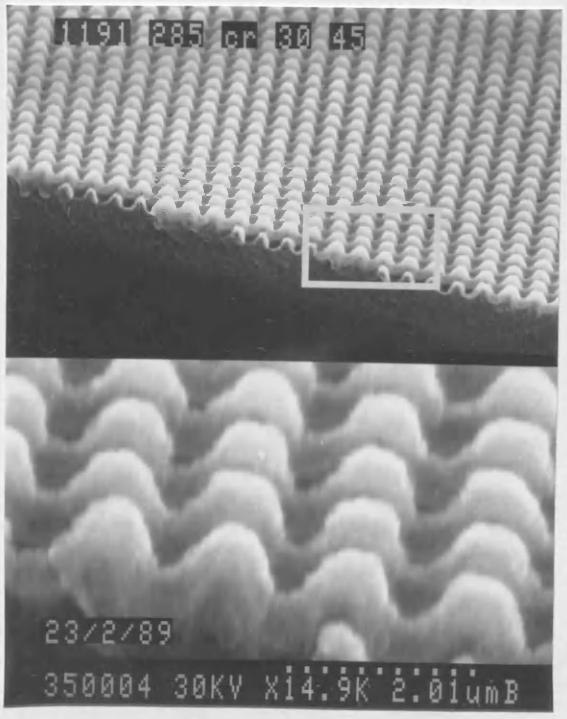

Figure 3.26. Crossed 285 nm period gratings (90°) in thick resist: 0.68 μm 1450J.

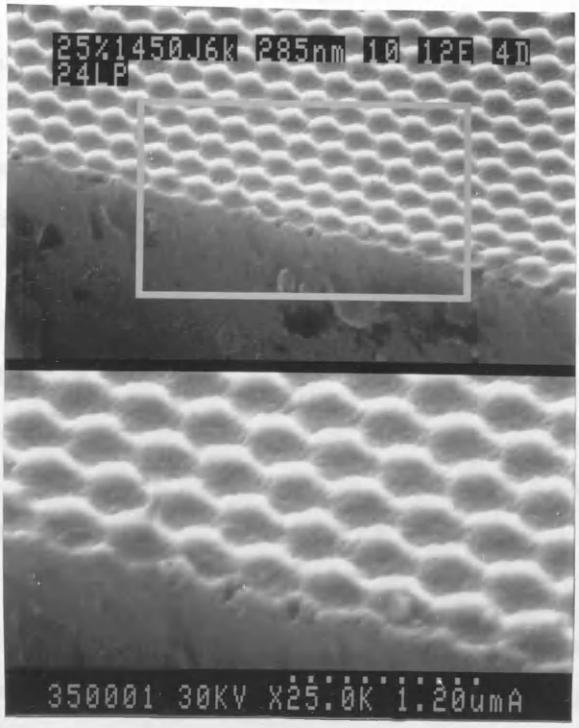

Figure 3.27. Crossed 285 nm period gratings (90°) in thin AZ 1450 J: 0.1 μm on silicon.

Test slides are used to determine the current exposure and development parameters. The second grating is usually weaker than the first but the reasons for this are not clear as the samples are replaced in exactly the same position on the holder. The crossed gratings are equally strong if the second exposure is roughly 1.5 times as long as the first exposure.

Some examples of crossed gratings are shown in figures 3.25. and 3.26. On the first sample, the two gratings were recorded at 60° to one another (each grating was exposed for 15 seconds on AZ 1350 J). The second sample was exposed for 35, 45 seconds in 0.68 μm AZ 1450 J and developed for 12 seconds in 1:2 developer. The crossed gratings have approximately twice the aspect ratio of the single gratings, resulting in the spectacular peaks of figure 3.25.

The structure of figure 3.27. was exposed in a 0.1 μm layer of 1:3 AZ 1450 J spun at 6 krpm. The structure was quite bright but the aspect ratio is reduced; the exposure and development times were 12 s, 15 s, 4 s for the crossed grating compared to 15 s, 15 s for a single grating recorded on silicon at the same time.

Crossed gratings have been made both on glasses to process X-ray masks and on semiconductors to make dot structures to study quantum effects in semiconductor devices.

Chapter 4. Pattern Transfer by Dry Etching.

Chapter Layout.

4.1. Introduction: Pattern transfer methods.

To complete the lithographic process, resist patterns must be transferred onto a substrate. This can be done by either an additive process such as lift-off or a subtractive process such as dry etching (Mogab 1983). Additive processing may be done immediately if the resist patterns are developed down to the substrate. A thin film of material is evaporated onto the structure. Solvents are used to remove the resist, loosening and lifting off any material supported on it. This process requires the resist walls to be vertical or undercut, figure 4.1. The maximum thickness of the evaporated film must be much less than the resist depth and ideally the width of the resist aperture should be less than the evaporated film thickness to prevent faceting; when this occurs, some of the evaporant attaches itself to the walls reducing the resist aperture. This effect is reduced by mounting the sample directly above the evaporation source.

Thick resist holographic gratings are not developed down to the substrate, so some form of etching is necessary to transfer the pattern. Wet etches are not suitable for this purpose since they attack amorphous materials (like resist) isotropically. However crystalline materials such as semiconductor substrates for laser applications etch anisotropically, the etch rate depending on the different packing densities in the different atomic planes [Sze 1985 p 456.]

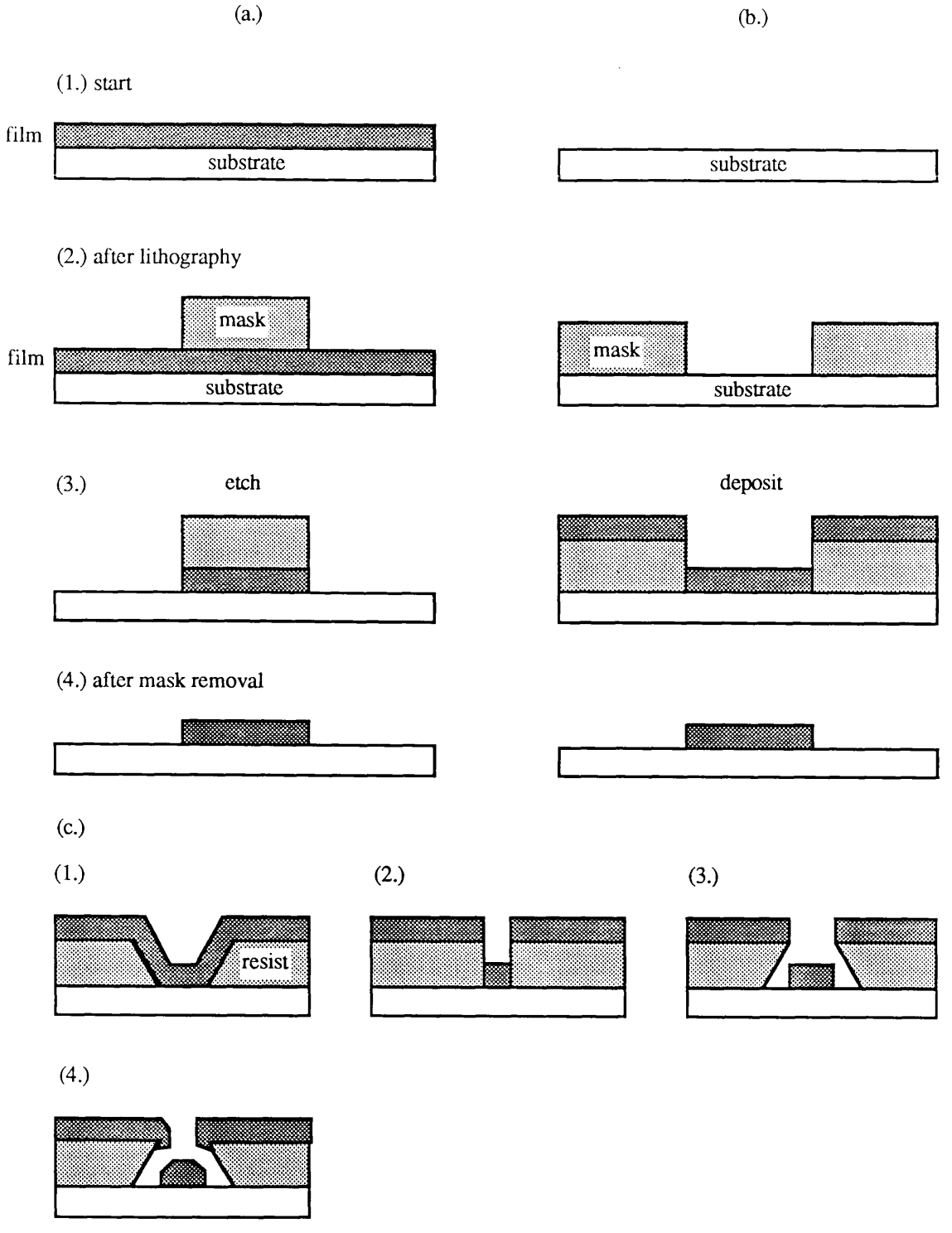

Figure 4.1. Schematic diagrams of the pattern transfer process (after Mogab 1983) for (a.) subtractive and (b.) additive methods.
(c.) The resist profile in (1.) is convex allowing a continuous film to form and unsuitable for lift-off. The vertical profile of (2.) and the concave profile of (3.) are preferred for lift-off. (3.) may be obtained using an etch process without perfect anisotropy, or by using a bilayer resist process where the lower resist layer is more soluable in the developer than the upper layer. (4.) illustrates the problem of faceting; material evaporated on the sidewalls reduces the feature width as the evaporation takes place.

Once a resist layer is baked, it will stand up to attack from most acids such as HCl or HF. Heating a fine resist structure above 140°C causes it to flow, reducing or destroying the grating pattern. Resist is rapidly stripped by most solvents, exceptions being xylene, chlorobenzine and carbon tetrachloride.

Reactive ion etching (RIE) of resist in an oxygen plasma through a deposited metal mask can produce extremely high aspect ratio[1] vertical walled structures (> 7:1 in these experiments) cut down to the substrate [Anderson 1983, Plotnik 1985]. The mask material must have a much lower etch rate than the underlying resist, figure 4.2.

RIE belongs to the dry etching family of techniques [Degraff 1980]. These etch techniques vary between highly anisotropic or isotropic depending on the electrode configurations that power the plasma. Argon ion beam milling, photoresist ashing in oxygen and sputtering are other examples of dry etch techniques.

A discussion of the RIE process for thick resist holographic gratings is presented in section 4.2. and that for producing dot structures is given in section 4.3 which deals with general applications. This section also includes a description of the transfer of 360 nm period thin resist gratings onto GaAs by a methane-hydrogen RIE process and of argon ion beam milling experiments to transfer a gold grating mask onto glass substrates.

[1]In this work the aspect ratio is defined as the ratio of height to linewidth for a rectangular profile.

4.2. Thick photoresist gratings.

The reactive ion etch process.

A schematic of the RIE process is presented in figure 4.3. Two electrodes of different areas are mounted in a vacuum chamber whose base pressure is held at <1 mtorr. One electrode is powered and the other is grounded. The samples rest on the powered electrode. The etch gas is admitted into the chamber and an RF field is applied across the plates.

The gas becomes ionised by the RF field and forms a plasma. The stripped-off electrons become confined in the space between the plates because of the rapid changes in polarity of the applied RF; the heavier ions are not affected by the RF due to their much smaller mobility. The confinement of the electrons results in the formation of ion sheaths next to the plates which are effectively insulating. The powered electrode connected to the RF supply via the blocking capacitor, C, rests at a large negative d.c. potential with respect to the plasma potential.

The ratio of $\left(V_{ps} / V_{gs}\right)$, the potential differences across the powered electrode and grounded electrode ion sheaths, is determined by $\left(A_g / A_p\right)^4$, where A_p, A_g are the areas of the powered and grounded electrodes respectively [Chapman 1980 pp 156 - 162]. When $A_p < A_g$, V_{ps} is large and $V_{gs} \approx 0$. If the powered electrode is much smaller in area than the grounded electrode, there is very little sputtering of the grounded electrode and the chamber walls.

The ions are accelerated through V_{ps}; their trajectories are determined by the field lines which in turn are fixed by the geometry of the plates.

On colliding with the sample the oxygen ions react with the organic photoresist forming volatile products which are removed by the vacuum system. RIE is thus both a chemical and a physical process (ion bombardment). Chemical activity produces smooth surfaces and is more selective but reduces the anisotropy and can produce deposited residues. Ion bombardment produces an anisotropic etch, but causes surface damage in crystalline materials.

A high degree of anisotropy is required to etch a submicron grating with a 100 nm linewidth and 200 nm period through 0.7 μm of resist without significant undercutting. A lateral etch depth of 30 nm produces significant under-cutting; this corresponds to an etch ratio $\left(R_l / R_v\right)$ of 0.043

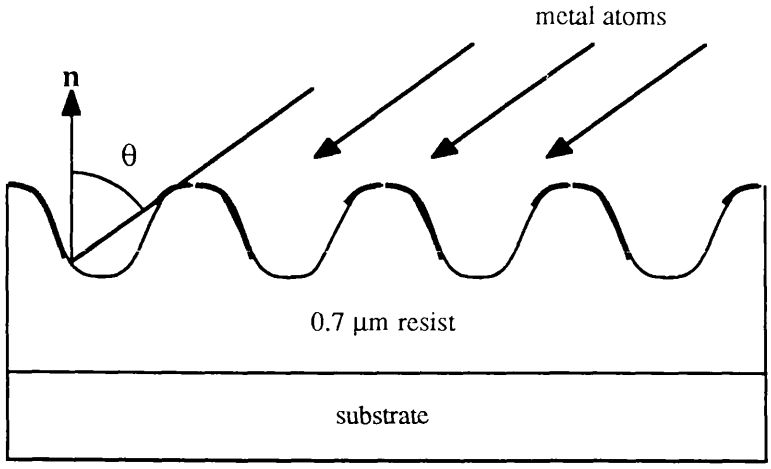

Figure 4.2.(a.). The structure is shadowed with NiCh alloy to produce a mask for RIE.

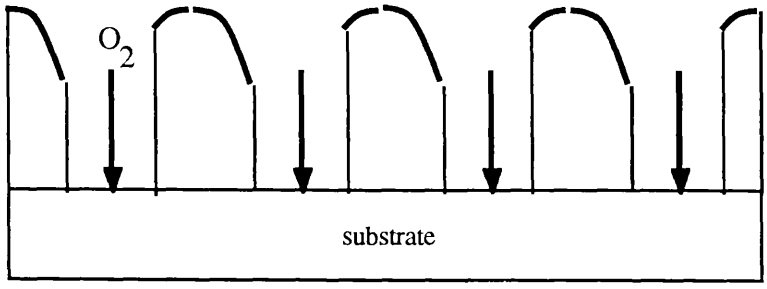

Figure 4.2.(b.). Oxygen RIE: The resist columns are etched down to the substrate to form a mask for lift-off or for a further etch process.

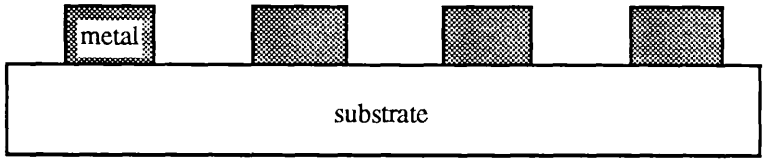

Figure 4.2.(c.). Metal deposition by lift-off (Typically 0.2 μm thick from a 0.7 μm tall structure.).

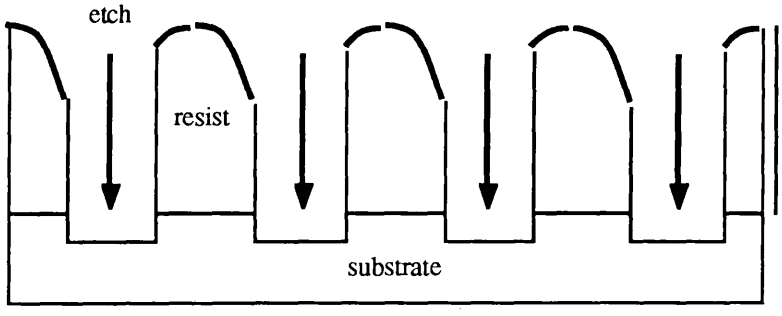

Figure 4.2.(d.). Pattern transfer by a subsequent etching process (wet or dry).

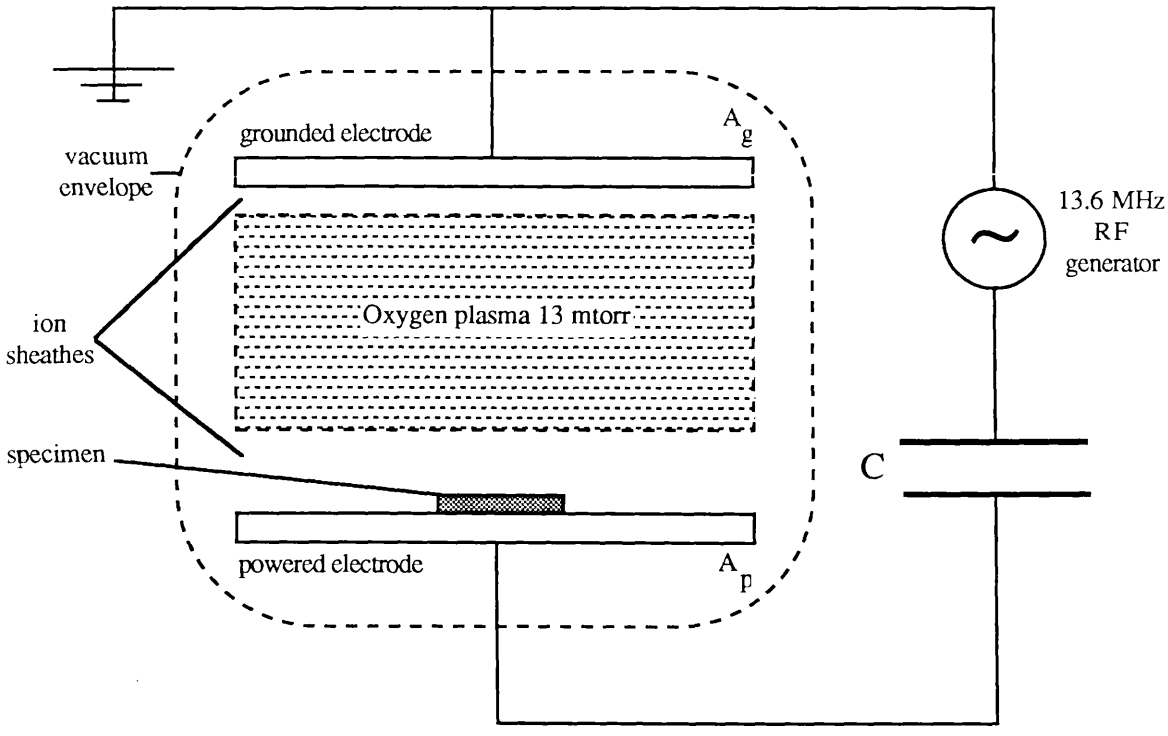

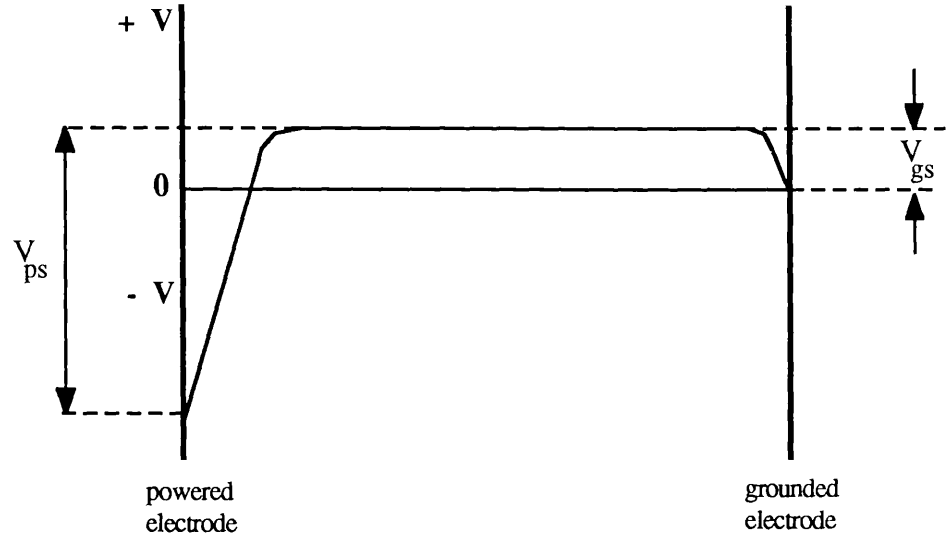

Figure 4.3. Schematic of RIE system. The potential is shown as a function of position in the discharge for the case where the area of the powered electrode is much less than the area of all grounded surfaces in contact with the discharge. (Mogab 1983).

where R_l and R_v are the lateral and vertical etch rates respectively and t is the etch time.

The etching was done in an Electrotech Plasmafab 340 RIE machine[2]. Etch times, gas flow rates (which determines the etch gas partial pressure) and forward RF power have to be optimised for each type of sample. The substrate temperature was assumed constant and the reverse RF was minimised for each run. (A tuning circuit ensures maximum RF power dissipation in the plasma.)

Typical etch parameters for a 0.7 μm photoresist layer are:

O_2 gas flow:	15 - 20 cc min^{-1}
etch pressure:	14 mtorr
forward RF:	45 - 55 W
reverse RF:	1 W
base pressure:	<1 mtorr
O_2 relative partial pressure:	13 mtorr
substrate temperature:	29°C
DC bias:	620 V
Etch time:	4.5 - 6.0 min

Contrast enhancement by angled metal evaporation (shadowing).

The metal mask is produced by shadowing the peaks of the photoresist grating with a thin metal layer evaporated at a steep angle of incidence, figure 4.2.(a.). The sample is mounted in a special holder, figure 4.4., so that the grating vector lies in the plane of incidence of the metal atoms. Such a mask was reported by Anderson (1983) 's group who evaporated 20 nm of chromium metal onto their samples.

In this work gratings were shadowed at 65° with a 15 - 20 nm (± 10%) thick layer of nichrome alloy. The nichrome forms a thin capping layer on the right hand side of the peaks of the grating

[2]Plasmafab 340 details: The aluminium walls and ceiling of the vacuum chamber of this machine form the grounded electrode. The powered electrode is stainless steel and is insulated from the walls of the chamber. This electrode is 17.4 cm in diameter and is cooled by a silicone oil heat sink at 30°C. The plate separation is 8 cm. The powered electrode to earthed electrode area ratio is 2.84:1. The RF frequency is 13.56 MHz.

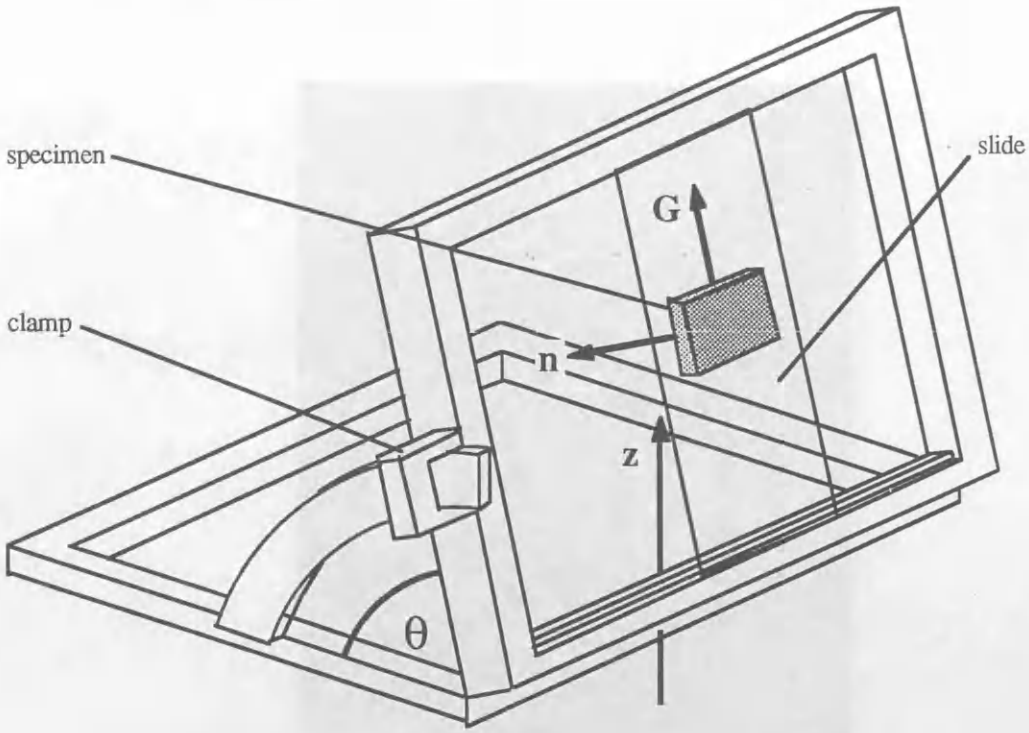

Figure 4.4. Aluminium jig for holding 3 microscope slides at an angle in the evaporator. Small samples are stuck onto slides before shadowing. The maximum shadowing angle is 65°. The sample holder interior dimensions are 80mm x 76 mm. The slides rest on a 2 mm recessed shelf.
n is the normal to the front surface of the slide.
G is the grating vector. **z** indicates the direction of the metal atoms.
θ is the angle of incidence.

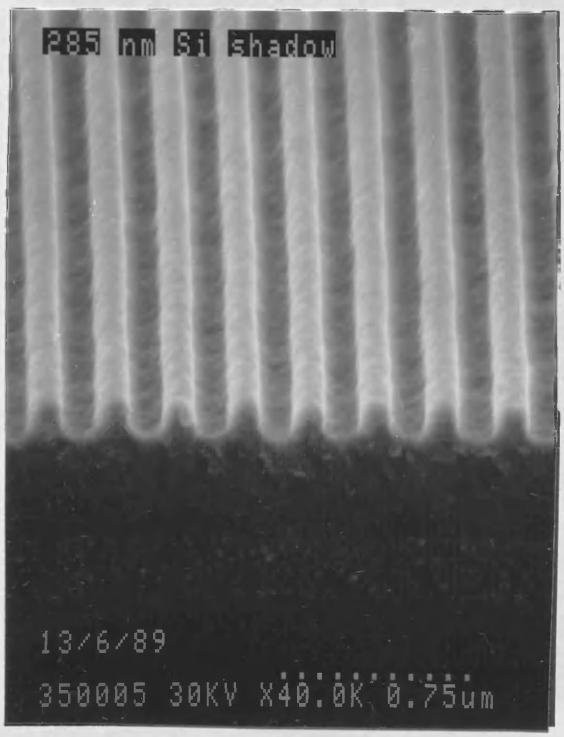

Figure 4.5. 285 nm grating on ARC on silicon after shadowing with 30 nm of nichrome alloy. The un-shadowed grating is shown in figure 3.19. for comparison.

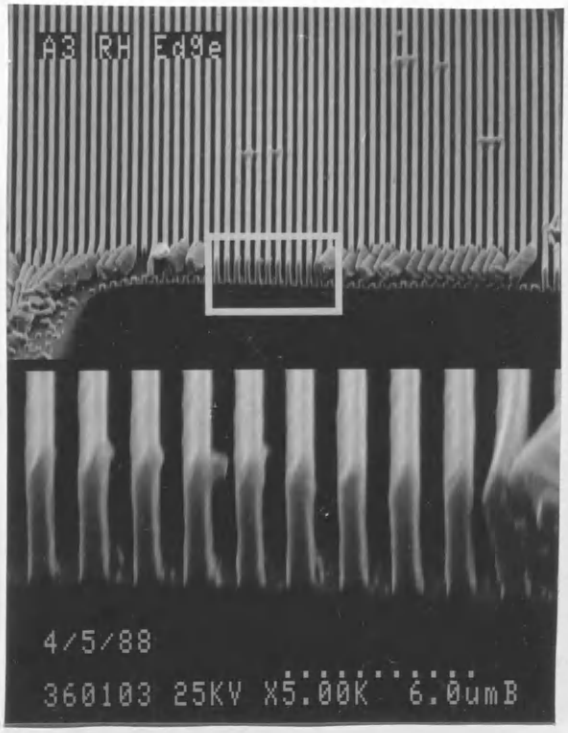

Figure 4.6. Oxygen RIE of 356.2 nm grating shadowed at 55° incidence. The mark space ratio is about 1:1. BP 80 machine: 50W 16 cc / min 5 m 12.7 mtorr partial pressure.

Figure 4.7. Oxygen RIE of 356.2 nm grating shadowed at 65° incidence. The mark space ratio is about 1:2. BP 80 machine: 50W 16 cc / min 5 m 12.7 mtorr partial pressure.

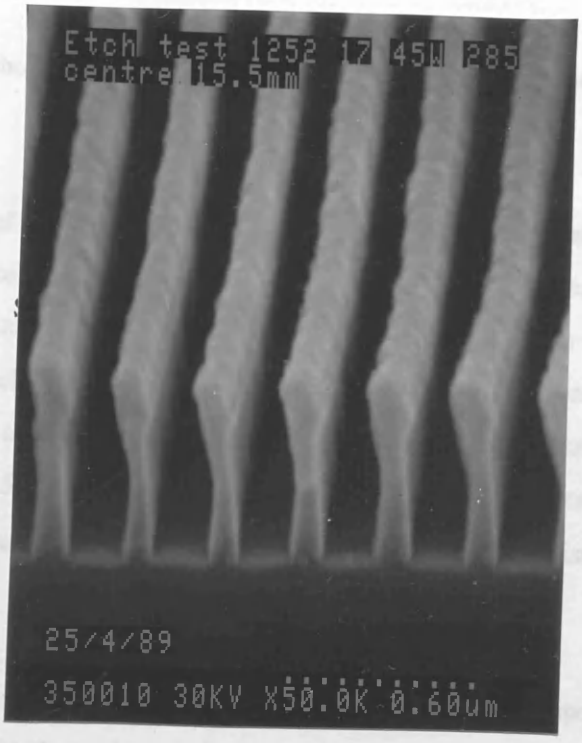

Figure 4.8. Oxygen RIE of 285 nm grating shadowed at 65° incidence. Grating centre (17.0 mm) 340: 45W 17 cc / min 4 m.

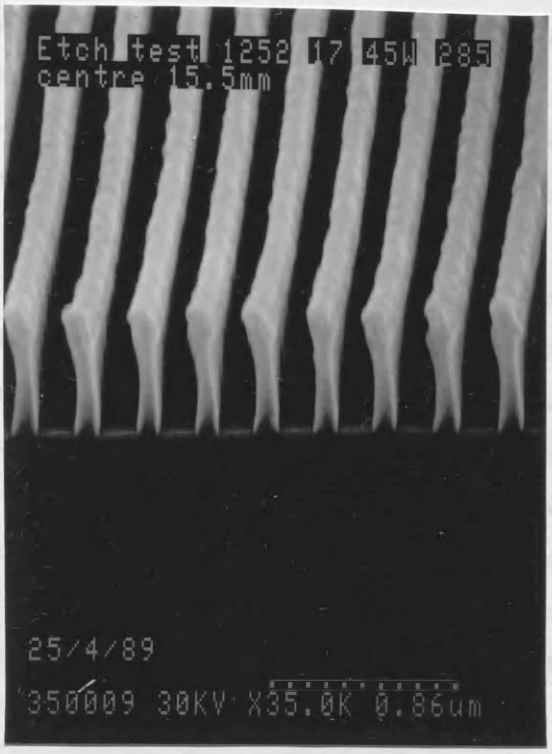

Figure 4.9. Oxygen RIE of 285 nm grating shadowed at 65° incidence. Mid-way to grating edge. Parameters as above.

in figure 4.5. and figure 3.19. show the unshadowed profile for comparison (the nichrome layer is just discernable).

Nichrome alloy is a mixture of 10% chromium and 90% nickel. The choice of metal depends on its grain size and its resistance to the etch. Although the oxygen ions do not react with the nichrome alloy, the metal is slowly sputtered away. After 4 minutes most of the nichrome is sputtered away, and the resist columns start to be etched. If the etch time is longer than 5 minutes, a thicker nichrome layer (30 nm) is required. For a typical etch: 20 nm nichrome, 0.7 μm photoresist etched at 50 W for 5 minutes, the mask sputter rate and the resist etch rate are about 0.07 nm s^{-1} and 2.33 nm s^{-1} respectively, so that the selectivity of the etch (resist etch rate / metal mask sputter rate) ≈ 30.

The fraction, F, of the grating period which is unmasked by the metal depends upon the resist topography and θ, the angle of incidence. Large values of θ produce narrow photoresist columns. The difference in mark space ratio of the etched gratings is shown by SEM micrographs of two gratings one shadowed at 55° and the other at 65° (figures 4.6., 4.7.)

The mark space ratio of the etched resist grating changes slowly from the centre of the grating to its edges. The aspect ratio[3] of the resist modulation decreases towards the edges of the grating. This decrease in contrast in turn decreases F (figure 4.13.(c.)) and increases the mark space ratio of the etched resist grating at the edges; i.e. the resist columns are thinner in the middle.

The etch at the outer region of the grating is also not as deep as the etch in the centre for a given etch time. The narrower gaps in the nichrome mask at the grating edge tend to trap the etch products slowing the vertical etch rate. The vertical etch speeds up when the gaps widen. As an example consider the etched resist profiles of figures 4.8., 4.9., and 4.10. The micrographs were taken at the centre, half way to the edge, and at the edge of 10 mm diameter grating of 285 nm period. At the centre, figure 4.8., the grating is overetched, there is some thinning of the resist pillars and some distortion. Half way to the edge, figure 4.9., the resist profile exhibits less thinning and distortion. At the grating edge, figure 4.10., the resist structure is under-etched and the resist columns are much thicker.

[3]For a quasi-sinusoidal grating the aspect ratio is defined as the peak to trough depth of the modulation divided by half the grating period.

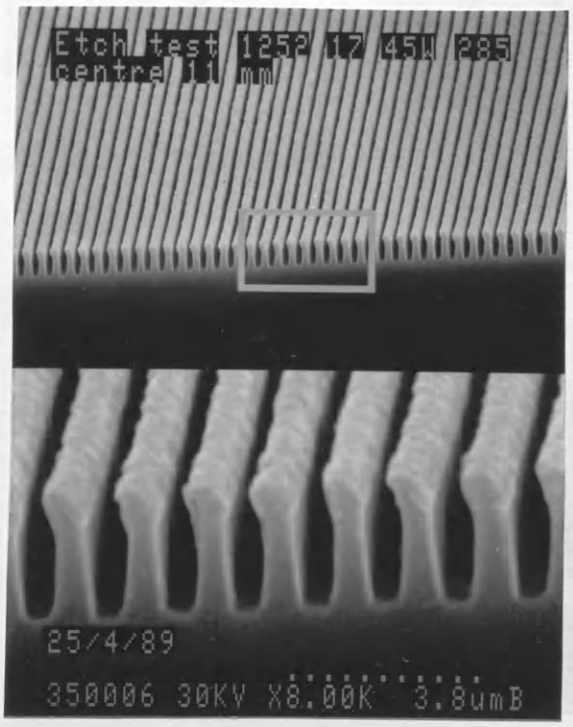

Figure 4.10. Oxygen RIE of 285 nm period grating shadowed at 65° incidence. Grating edge (11.0 mm) 340: 45W 17 cc / min, 4 m.

Figure 4.11. Oxygen RIE of 356.2 nm period grating on germanium shadowed at 65° incidence. Grating centre (12.5 mm). 340: 18 cc / min, 45 W, 7.25 m.

Figure 4.12. Oxygen RIE of 356.2 nm period grating on germanium shadowed at 65° incidence. Grating edge 7.0 mm. 340: 45W 18 cc / min, 7.25 m.

Figure 4.15. Resist collapse due to over-etching. The structure is a 356.2 nm period grating etched for 6 min, 20 cc / min, 50 W.

Thick resist gratings on a highly reflecting substrate such as germanium, see figure 3.17., have a much smaller F after shadowing (except at very high incidence angles) compared with the quasi-sinusoid gratings already discussed (see figures 4.13., 4.14.).

Figures 4.11., 4.12. are SEM micrographs of a 356.2 nm photoresist grating etched on germanium. The etch time is much longer, 7.25 min, and the mark space ratio is much greater than for the gratings of figures 4.8. - 4.10.

The effects of gas flow rate.

In these experiments, test samples are etched to optimise the etch conditions before each etching session is begun. The RF power is constant, but the etch times may change slightly: perhaps by ± 10%. This variability is reasonable considering the machine is constantly used with different etch gases (such as the methane hydrogen mix mentioned in section 4.3.). To remove any residue, the chamber is given a half-hour clean in a hydrogen plasma before oxygen is introduced into the system.

Too large a partial pressure of the etch gas in the chamber reduces the isotropy of the etch and can cause significant undercutting or even resist collapse. The amount of etch gas is regulated by the gas flow control. Figure 4.15. shows resist collapse using a gas flow ratio of 20 cc min^{-1}. Reducing the gas flow to makes the etch more anisotropic also slows the etch rate slightly, so that the RF power is increased to compensate.

Figures 4.16., 4.17. show the effect of increasing anisotropy with decreased gas flow for two 356.2 nm period gratings.

285 nm period gratings are etched at a lower gas flow rate, 17 cc min^{-1}, than the coarser 356.2 nm period gratings, 18 cc min^{-1}.

A further example of these effects can be seen in figures 4.18., 4.19. Here a 0.7 μm thick photoresist layer is to be etched over an ARC polyimide layer (see section 3.21.(c.)). The etch rate of the ARC is slower than the photoresist causing the resist columns are to collapse, figure 4.18., whereas the ARC is almost unetched. Decreasing the gas flow from 17 cc min^{-1} to 15 cc min^{-1},

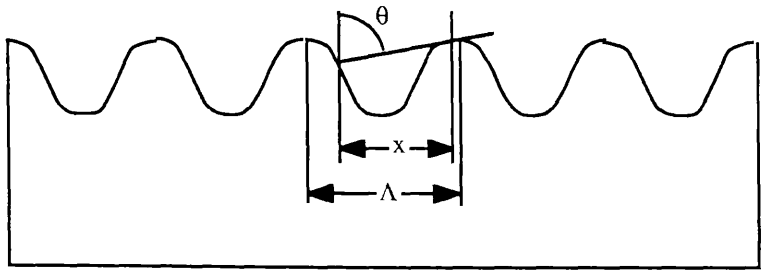

$$F = x / \Lambda$$

Figure 4.13.(a.). Typical photoresist profile for a grating formed on a transparent substrate with a back prism. F is calculated by drawing the tangent to the grating at the angle of incidence θ and measuring the distance between the two intercepts.

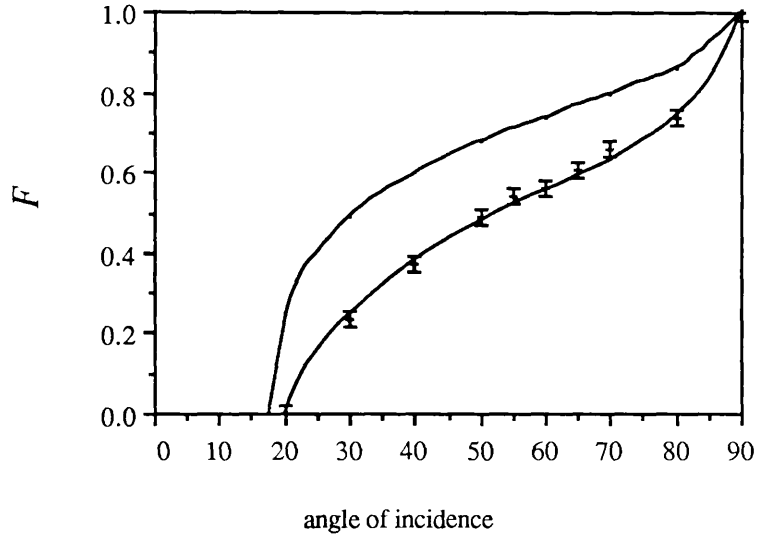

Ξ. figure 14.13.(a.)

Figure 4.13.(b.). Plots of F against angle of incidence for the profile of (a.) measured as above (error bars) and calculated for a perfect sinusoid (Appendix 4).

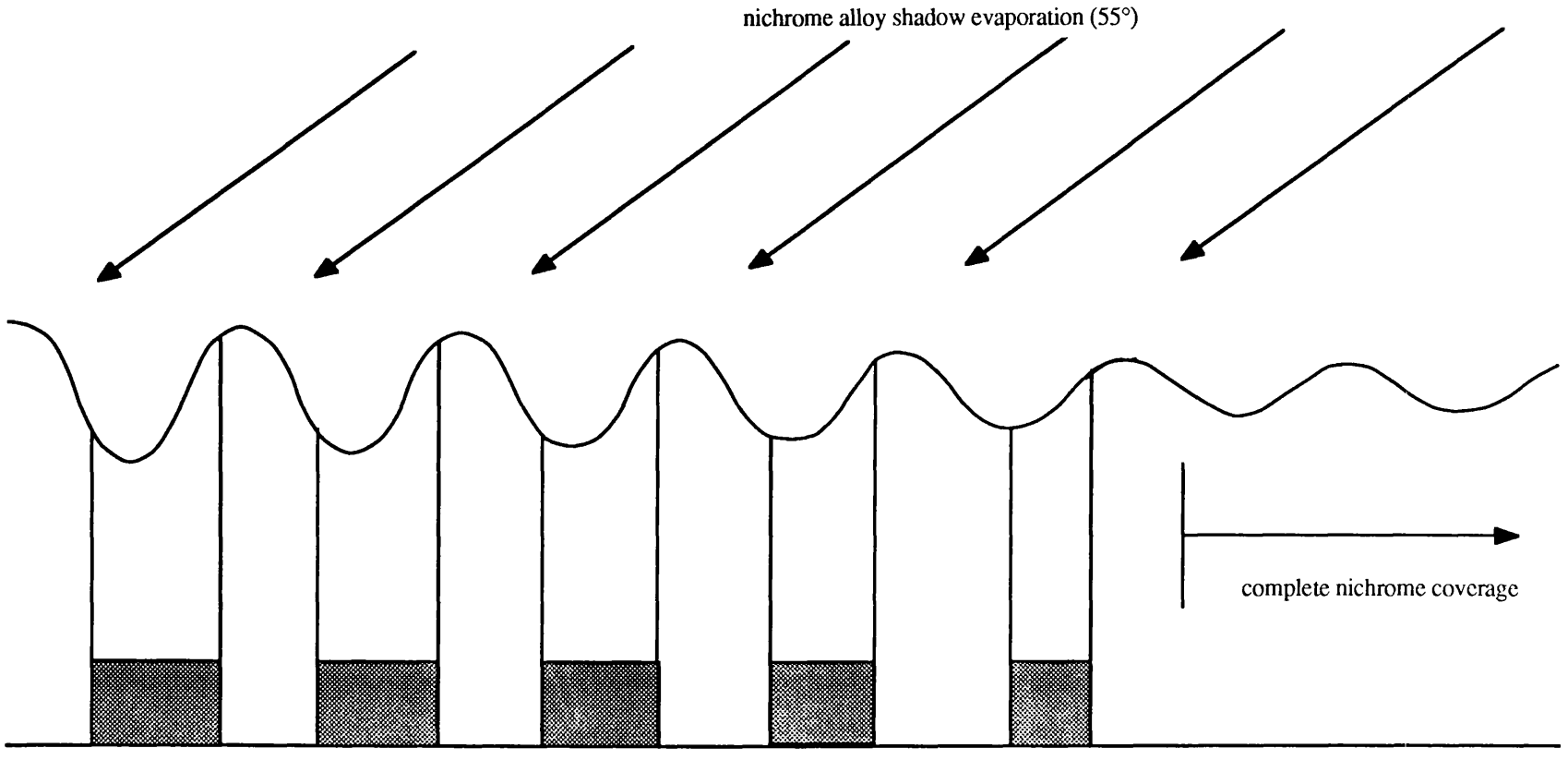

Figure 4.13.(c). Sketch of the variation of F, and hence the mark space ratio of the etched resist structure, due to the progressive reduction of the aspect ratio of the photoresist grating towards the grating edge. The scales are greatly exaggerated. The filled rectanges represent deposited metal structures after lift-off.

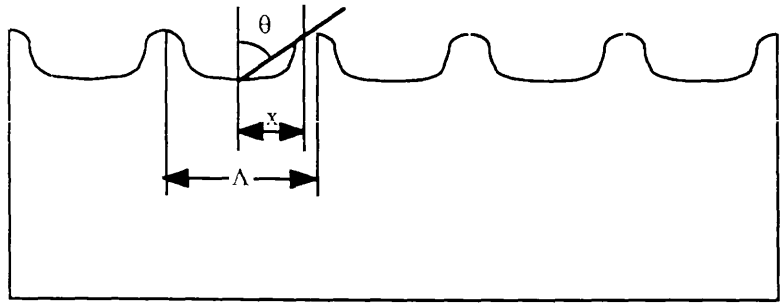

$$F = x \ / \ \Lambda$$

Figure 4.14.(a.). Typical photoresist profile for a grating formed on a highly reflecting substrate. F is calculated by drawing the tangent to the grating at the angle of incidence θ and measuring the the distance between the two intercepts.

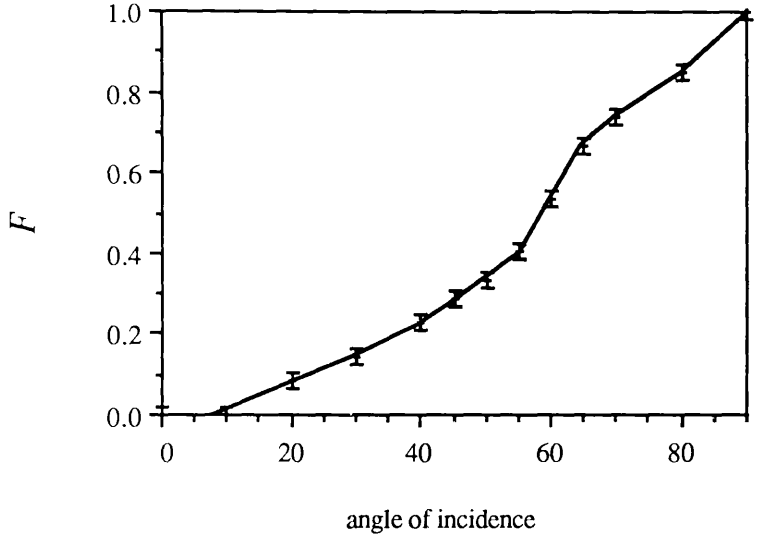

Figure 4.14.(b.) Plot of F against angle of incidence for the profile of (a.) measured as above. The error bars indicate the accuracy with which the lengths could be measured.

Figure 4.16. Oxygen RIE of 356.2 nm period grating shadowed at 65° incidence. 340: 50W 20 cc / min, 4 min. Severe thinning of resist columns.

Figure 4.17. Oxygen RIE of 356.2 nm period grating shadowed at 65° incidence. 340: 18 cc / min, 50 W, 4 min. Resist columns well etched.

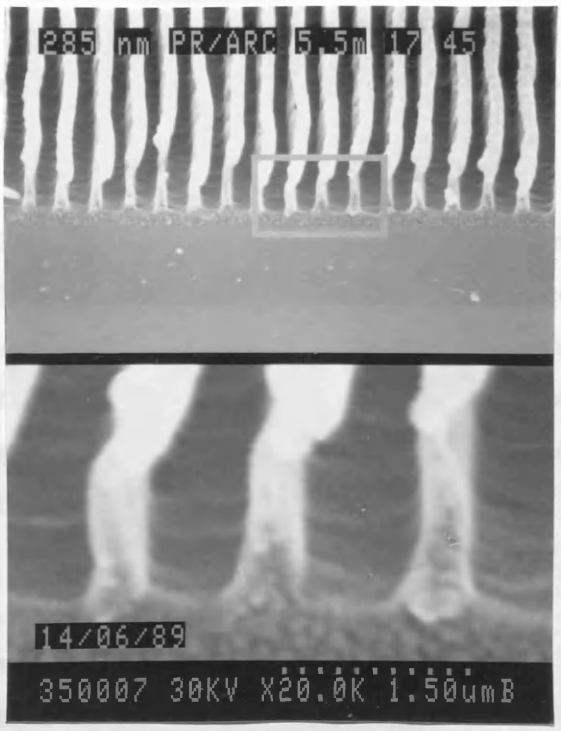

Figure 4.18. Oxygen RIE of 285 nm period grating on ARC on silicon.
340: 45W 17 cc / min, 5.5 min. Severe thinning of resist columns.

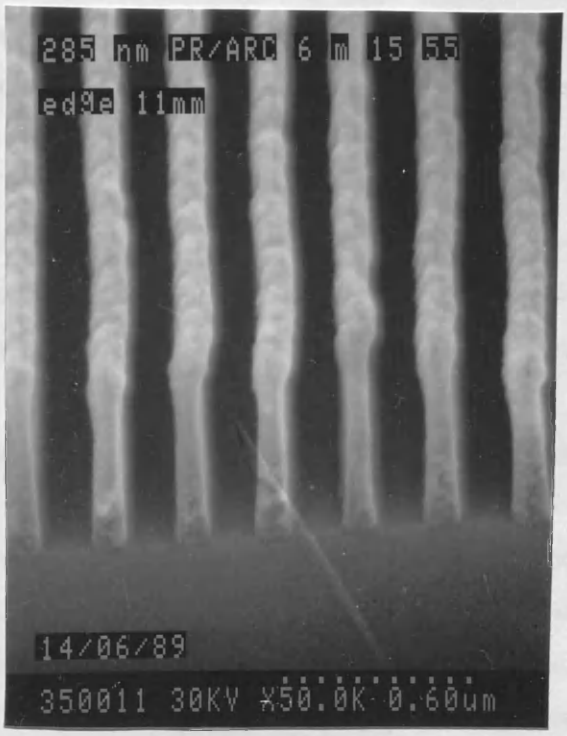

Figure 4.19. Oxygen RIE of 285 nm period grating on ARC on silicon.
340: 15 cc / min, 55 W, 6 min. Resist columns and ARC well etched.

and compensating for the lower etch rate by increasing the RF power from 45 W to 55W produced the uniform fully etched resist structures of figure 4.19.

To summarise, the effects of resist topography on the mark space ratio of etched resist gratings have been described and the effects of the etch parameters discussed. This work has concentrated on establishing the possible techniques; for example it was not necessary to worry too much about the exact mark space ratio of the gratings produced for the x-ray masks, since we were only trying to illustrate the contact printing process. Such considerations are important in real devices, and the information discussed in this section indicates how these requirements can be met.

Pattern transfer from etched photoresist gratings: metallisation and further etching.

In this work, the resist patterns were metallised in a thermal evaporator machine. This system can accommodate up to six thermal evaporation boats, arranged in a line. The chamber base pressure is 8.0×10^{-6} mtorr, rising to 2.0×10^{-5} mtorr during an evaporation. The samples are supported 20 cm over the sources. The change in the resonant frequency as metal is deposited on the monitor crystal is monitored by an Intellemetrics thickness monitor, Model IL002. The thickness of the deposited metal is obtained from calibration curves specific to this evaporator system. The thickness calibration curve for nichrome metal, as measured by talystep, is shown in figure 4.20.

An attractive feature of this evaporator system is its ability to accommodate the shadowing jig during the evaporation of the metal RIE masks. Since the evaporation sources are arranged along, differences in the angles of incidence of evaporants from different sources can be minimised.

0.3 μm of pure gold is thermally evaporated to form the x-ray absorber on the membrane masks. The grating must be arranged directly over the gold source to avoid any shadowing or faceting effects due to the high aspect ratio (7:1) resist structures. A 15 - 20 nm thick layer of nichrome metal is evaporated before the gold metal to provide an adhesive layer, otherwise the gold pattern falls off at the lift-off stage. The grating sample is oriented so that the grating lines run parallel to the line of sources. The gold and nichrome sources are brought as close as possible together underneath the sample.

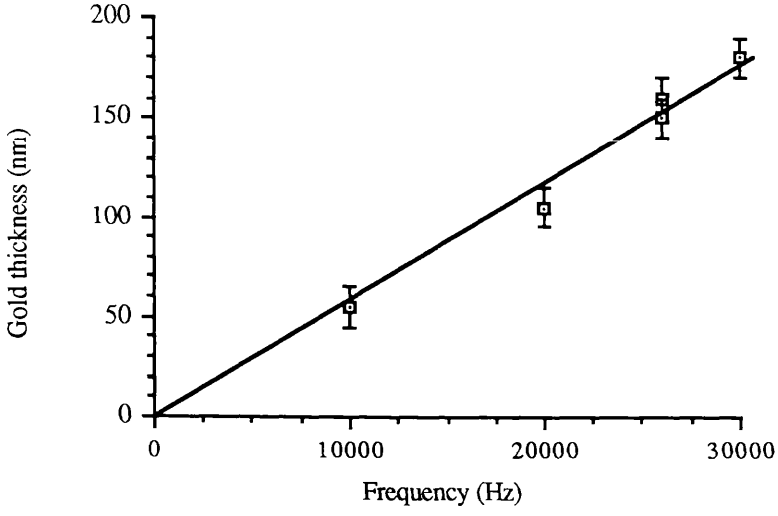

Figure 4.20.(a.) Gold metal thickness against monitor crystal frequency for the old evaporator. Measurements by talystep. Error ~ 10 nm.

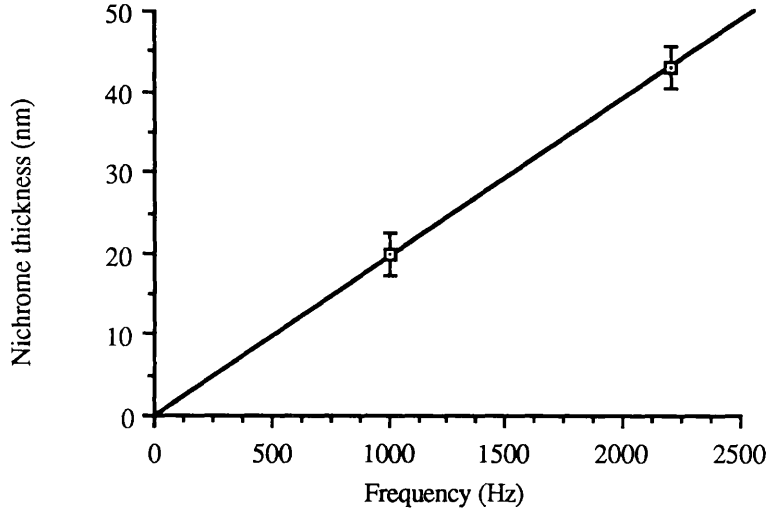

Figure 4.20.(b.) Nichrome thickness against monitor crystal frequency for the old evaporator. Measured by talystep. Error ~ 3 nm.

The metal thickness was determined to within an error of 5% depending on the evaporation rate. The samples were shielded from the sources by a mechanical shutter until an appropriate evaporation rate was reached; this was around 15 Hz s^{-1} for nichrome and 100 Hz s^{-1} for gold. Lower gold evaporation rates, < 60 Hz s^{-1}, produced very rough surfaces and lift-off was difficult, figure 4.21. Much smoother walls were obtained at the higher rate, figure 4.22.

The metallised resist structure is soaked in acetone and agitated ultrasonically for a minimum of 5 minutes to dissolve the resist and lift-off the excess metal. The adhesion grating pattern does not seem to be adversely effected by the agitation. In this work, 1 cm diameter areas of metal grating are produced. This area is reduced if the sample is underetched.

Metallised gratings made on ARC may need an additional stage to remove the polyimide-based coating. This is done by boiling the samples in acetophenone in a reflux column for 20 minutes. The samples are directly transferred from the acetone into the acetophenone. On removal from the acetophenone, the samples are rinsed in iso propyl alcohol (IPA) and blow dry with oxygen free nitrogen. Occasionally there is still a residue; this can be removed by subjecting the samples to an oxygen plasma ashing step.

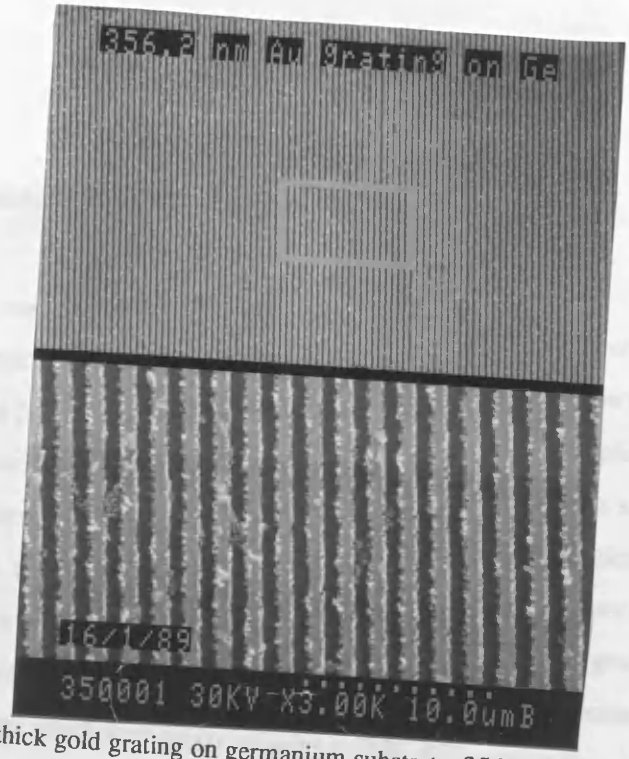

Figure 4.21. 68 nm thick gold grating on germanium substrate. 356.2 nm period.

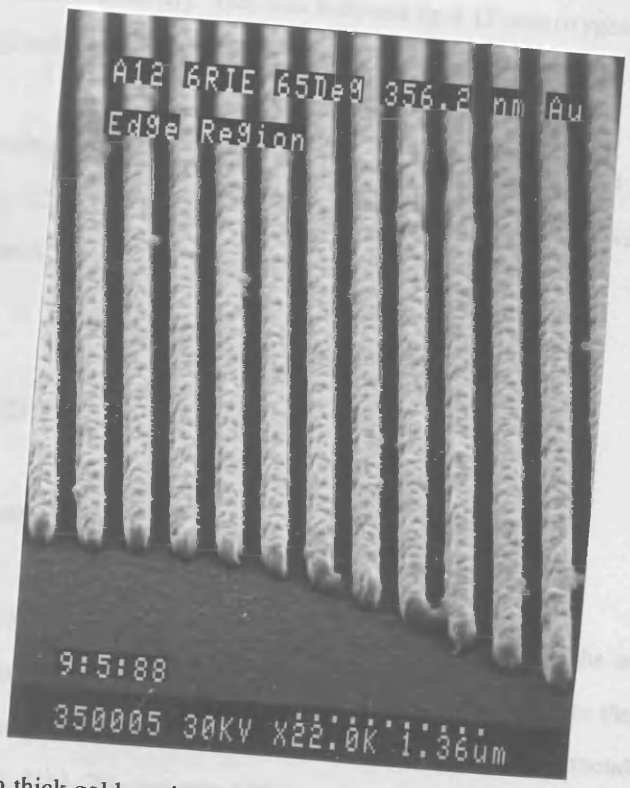

Figure 4.22. 160 nm thick gold grating on glass. 356.2 nm period.

4.3. Applications.

Thick resist gratings - etching of quartz for bioelectronics.

The etched resist grating may itself be used as an etch mask for a subsequent process, figure 4.2.(d.). Currently the response of biological cells to the topography of the surfaces on which they are deposited is being studied [Clark 1987, Dow 1987]. These studies could have implications for the stimulation of cell growth and the regeneration of nerve cells. [Clark 1989] has studied the response of different cell types: fibroblastic, epithelial and neuronal, to microtopological features such as sub-micron gratings. Differences in growth response between the cell types has been observed. On such surfaces a significant number of cell were guided along the groove lines compared to a control. To study such systems a neutral chemical environment is needed. In his work, Clark used quartz gratings which were produced using a CHF_3 RIE process through a thick resist grating mask fabricated as already described. Two of the quartz gratings are shown in figures 4.23., 4.24. The samples were etched in the CHF_3 plasma at 100 W RF power, 30(15) cc min^{-1} gas flow for 10 and 20 minutes respectively. This was followed by a 15 min oxygen RIE at 30W, 30 cc min^{-1} to clean up any residual polymer.

After 10 minutes the grating was etched to a depth of 0.26 ± 0.01 μm, figure 4.23. After 20 minutes, the etch depth was 0.53 μm ± 0.01 μm, figure 4.24.). The grating period was 356.2 nm. The quartz grooves are remarkably smooth.

Two dimensional gratings - dot structures.

There are two ways of transferring dot patterns from photoresist:

(i.) A negative process in which the pattern is transferred through the troughs and not the peaks: a crossed grating is exposed in a thick layer of photoresist (0.7 μm) similar to the structure of figure 3.26. This structure is shadowed along the grating planes with nichrome metal as in the one dimensional case (section 4.2.). The oxygen RIE step is much the same; the etch time is about 20% longer, and it may be necessary to reduce the gas flow slightly to increase the anisotropy

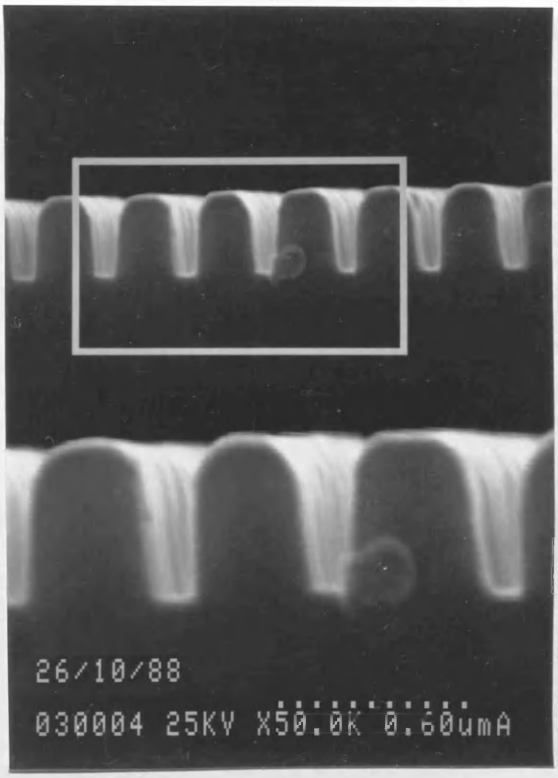

Figure 4.23. 356.2 nm period grating etched into quartz 0.26 μm deep. CHF_3 RIE 100W 10min..

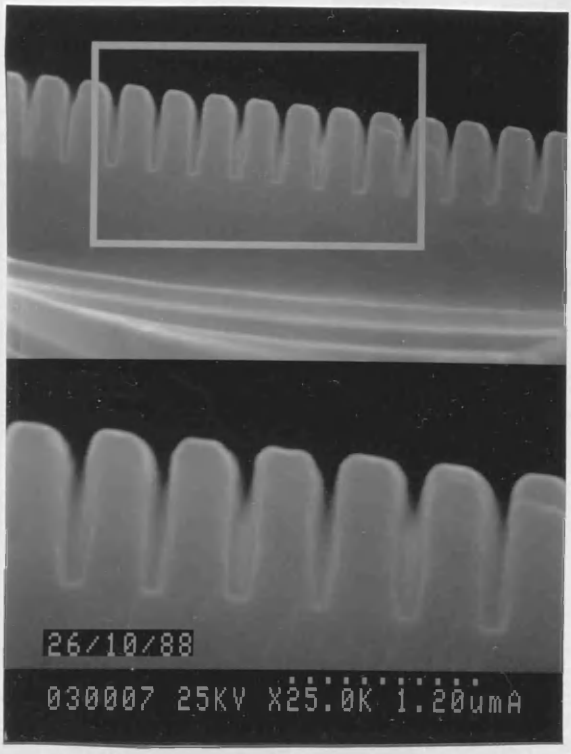

Figure 4.24. 356.2 nm period grating etched into quartz 0.53 μm deep. CHF_3 RIE 100W 20 min.

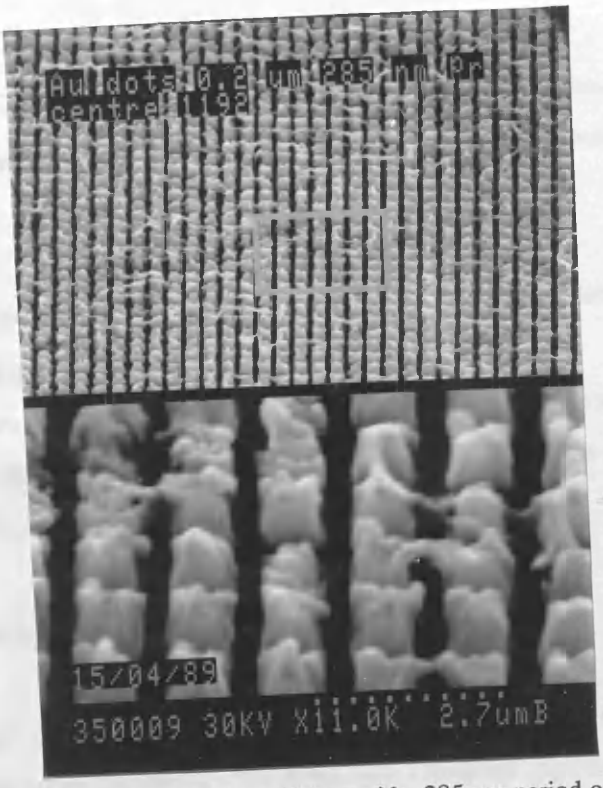

Figure 4.25. 0.2 μm high gold metal dots, 180 nm side, 285 nm period on glass.

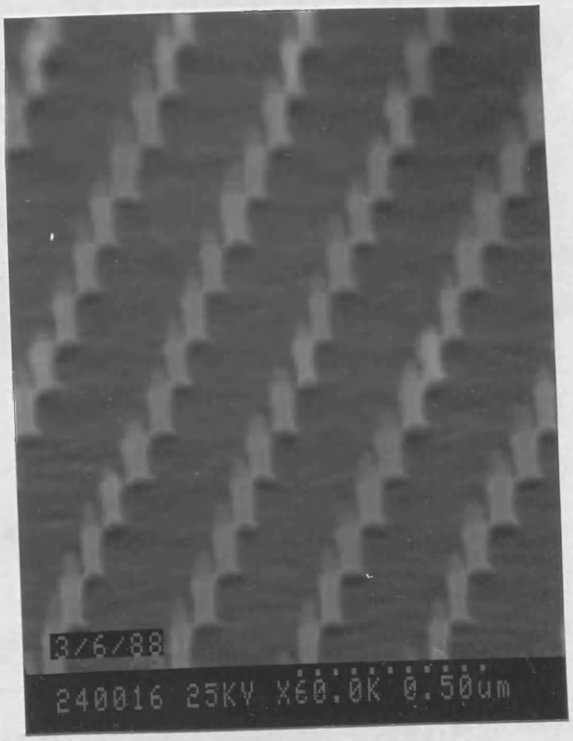

Figure 4.26. 50 nm diameter dots etched into GaAs by SiC_4 RIE photograph courtesy of H.E.G. Arnot.

of the etch. As in the case of gratings etched onto germanium the holes are about 100 nm in diameter. The reaction products tend to remain inside the interstices causing more undercutting than in the one dimensional case.

Metal is evaporated onto the structure and lifted off in acetone to produce the dots, figure 4.25. The figure shows the central area of a 1 cm diameter gold metal dot field.
To make this pattern, 0.2 μm of gold was evaporated on top of a 20 nm nichrome adhesion layer. The dots are square of side 180 nm and are remarkably uniform. They form a square array of period 285 nm. Lift-off was done in acetone and under ultrasonic agitation for 30 seconds.

The metal dot pattern can be used as a mask for subsequent processing.

(ii.) Positive process[4]. The whole structure is etched uniformly without a mask until only the dot peaks are left isolated from one another. The peaks form a mask for subsequent etching into the underlying substrate. This was done on GaAs (figure 4.26.). The dots formed in this way are uniform over very large areas (1 cm^2) and form a periodic two dimensional array. The number of dots formed in this way is very large indeed; it would take an e-beam machine several days to pattern a similar area which is patterned holographically in a few minutes. One major disadvantage of this process is the lack of control over the original etch, there is no etch mask to enhance the pattern contrast: the end point has to be guessed unlike case (i.).

The dots on the original photoresist mask have a diameter in the range of 50 - 100 nm, this is really too large to see quantum confinement in GaAs, but could be used to fabricate quantum dots on InP where the excitonic radius is larger. Further discussion of this application is beyond the scope of this thesis.

Thin resist gratings; etching of GaAs by CH_4 - H_2 RIE[5]

The thin resist gratings of figure 3.24. were etched into the GaAs substrates using a methane

[4]This process was used by J.J Thompson (née Bates) and H.E.G. Arnot to make quantum dot patterns on GaAs but is now superceeded by the double x-ray exposure of a grating mask described in Chapter 5.
[5]The etching was performed by Steven Thoms.

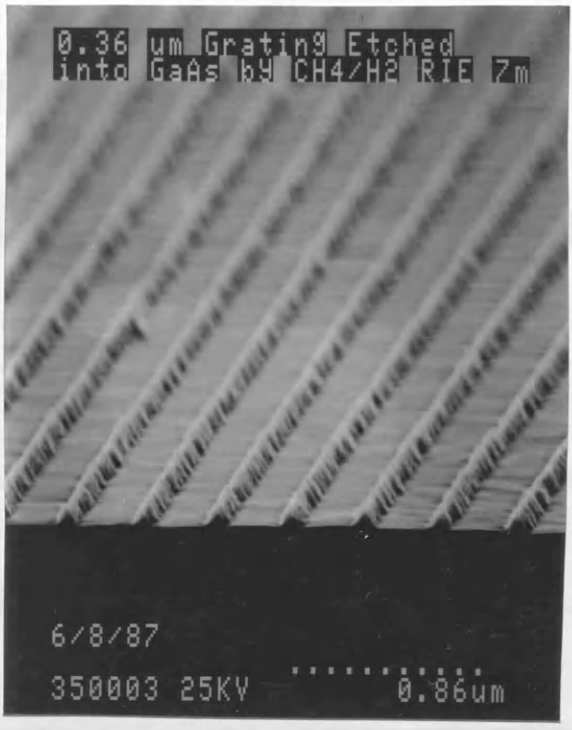

Figure 4.27. 360 nm period grating etched into GaAs ~0.15 μm deep. CH_4 / H_2 RIE 7 min 150 W.

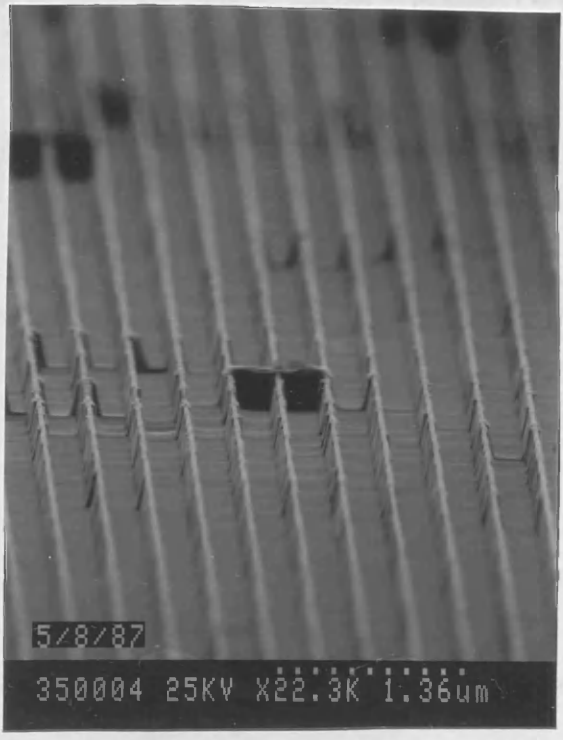

Figure 4.28. 360 nm period grating etched into GaAS ~ 0.25 μm deep. CH_4 / H_2 RIE 10 min 150W.

(a.) initial resist mask on crystalline substrate

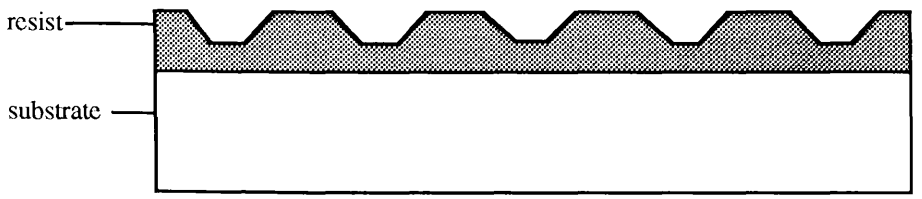

(b.) the substrate is just exposed, the substrate etch rate > mask etch rate

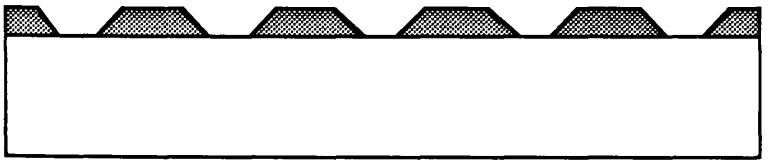

(c.) all the mask has been removed. The model assumes a perfectly anisotropic etch rate. The original resist pattern has preserved its lateral dimensions but has been stretched in the vertical direction in proportion to the ratio of the crystal and mask etch rates.

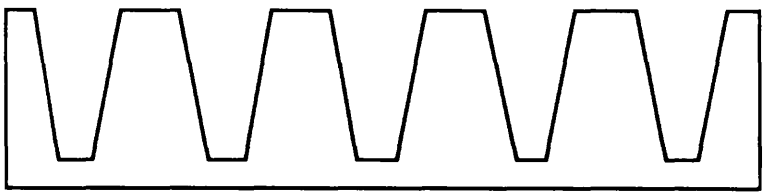

Figure 4.29. Schematic illustration of the stretching process caused by non vertical walled resist mask.

hydrogen reactive ion etch process developed at Glasgow [Cheung 1987]. This dry etch technique has the advantages of high resolution, low damage and an etch rate in the 0.02 μm range.
The gratings were made as part of work to fabricate third order DFB lasers on GaAs / AlGaAs laser substrates.

The maximum depth of the photoresist is 0.1 μm. These structures were etched in the Plasmafab 340 with a 1:5 CH_4 / H_2 (6.9 / 25 cc min^{-1}) mixture for 5, 7 and 10 minutes respectively at 150 W forward RF power. The DC self bias varied between 950V and 1000 V. The residual resist was stripped in acetone. The resist was not completely etched after 5 minutes but figures 4.27., 4.28. are SEM micrographs of the GaAs structures after etching for 7 minutes and 10 minutes respectively.

The triangular grating profile of figure 4.27. is suitable for a third order DFB laser diode. The triangular shape has a large third harmonic component which determines the reflection efficiency of the DFB structure (see Appendix 5.). Non anisotropic etching of the resist mask can cause faceting in in the semiconductor. Anisotropic etching causes the mask profile to be 'stretched' in the semiconductor in the vertical direction, figure 4.29.

Ion beam milling of glass substrates.

As described Appendix 5., work is currently in progress to make a first order Bragg reflection filter for 860 nm light in slab waveguides produced in glass microscope slides (Blue Star type) by a potassium ion exchange process. The grating is formed either by a second ion exchange or by argon ion beam milling through a gold metal mask.

A schematic of the Oxford OAR 2255D ion beam milling machine is presented in figure 4.32. The ion source is a dc discharge, physically separated from the substrate by a set of grid electrodes. The grids are biased to extract an argon ion beam. Ion voltages exceeding 500 V are required for practical beam densities. The beam is well collimated so that the angle of incidence on the samples can be controlled by tilting the sample holder. A hot filament emitter is placed in the beam path to provide low energy electrons for beam neutralisation.

Figure 4.30. 356.2 nm period grating milled into Blue Star microscope slide glass through a 0.16 µm thick gold mask. 500 V, 10 mA ,10 min.

Figure 4.31. 356.2 nm period grating milled into Blue Star microscope slide glass through a 0.16 µm thick gold mask. 500 V, 10 mA ,15 min.

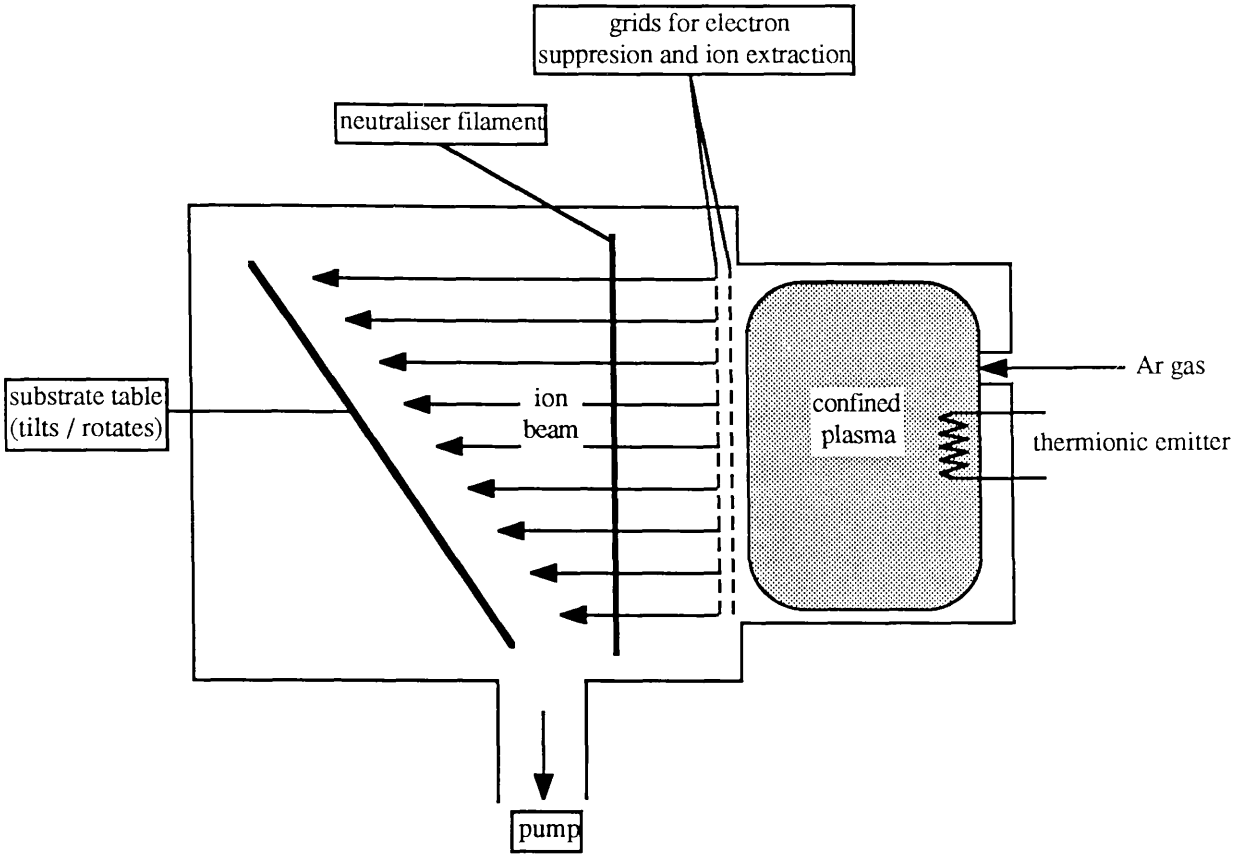

Figure 4.32. Schematic of ion beam milling apparatus.

The sample surface is eroded by the physical bombardment (sputtering) of the incident ions.

The sputter yield, i.e. the number of displaced atoms per incident particle, depends on the ion energy and the angle of incidence. For most VLSI materials argon ions have sputtering yields between 0.5 and 1.5 so that etch selectivity between materials is poor. Ions arriving with oblique angles of incidence have a higher probability of displacing a substrate atom with a momentum oriented away from the surface (Mogab 1983).

In this work the glass samples were supported at 15° incidence to the ion beam on a water cooled stage. The stage is rotated during the milling process to prevent shadowing. The ions are accelerated through 500 V (10 mA ion current). Typical values for the argon partial pressure and the chamber pressure were 9.0×10^{-5} mbar and 4.0×10^{-4} mbar.

The gratings of figures 4.30., 4.31. were milled for 10 min and 15 min respectively. The etch depth is estimated to be ~ 0.1 μm. The longer etch produced wider grooves with smoother walls. The gold mask is 0.16 μm thick and of 356.2 nm period. Traces of the mask remained after 10 minutes, and were removed by soaking in concentrated HCl. After 15 minutes all traces of the mask were absent.

An extra photolithographic step before milling is required to limit the length of the grating (see Chapter 6); a 500 μm x 5 mm region of resist is isolated over the region of metal grating to be etched. A 0.2 μm gold layer is evaporated and lifted off. After etching, any residual metal is dissolved away in HCl or Gold etch (a saturated solution of iodine in potassium iodide).

Chapter 5. X-ray Contact Printing.

Chapter Layout.

5.1. X-ray contact printing: introduction and overview.

The x-ray printing technique was first demonstrated seventeen years ago by Spears and Smith [Spears 1972], who printed 0.6 μm linewidth electrode structures through a boron doped n-type silicon membrane mask, 3 μm thick, into the e-beam resist polymethylmethacrylate (PMMA). The resist was exposed by 0.834 nm Al K_α radiation, produced from a converted electron beam evaporator source [Smith 1973].

X-ray shadow or contact printing[1] at wavelengths between 0.5 nm and 5.0 nm is a high resolution (< 100 nm linewidth) pattern replication process which is similar in principle to optical contact printing: a source of radiation is used to induce chemical changes in a polymeric resist film through a thin mask substrate (> 1 μm) on which the patterns to be reproduced are defined in some absorbing material usually a few hundred nanometers of gold. The source may radiate isotropically as in an electron beam bombardment system or a laser induced plasma source [Nagel 1983, Pircher 1986], or it may be highly collimated as in a synchrotron [Grobman 1980b, Spiller 1976, Heuberger 1985, 1986].

[1]X-ray contact printing is often referred to in the literature as x-ray lithography or synchrotron lithography (for those systems that use a synchrotron source). The term lithography implies both pattern generation and pattern transfer. Since replication of fine structures using x-rays does not involve pattern generation, the terms x-ray contact or shadow printing have been used here.

Once the patterns on the original mask have been fabricated either by optical, e-beam or holographic lithographies, daughter masks can be produced from it by x-ray printing.

Reported applications of x-ray lithography using e-beam or holographic lithographically written x-ray masks include Fresnel zone plates [Shaver 1988], lateral surface superlattice devices [Warren 1986, Ismail 1988], sub 100 nm gate length Si MOSFETS [Chou 1986], submicron gratings [Flanders 1978 a, b]. and DFB lasers [Nakao 1989].

Resolution.

Because of the lower x-ray wavelengths much fine features can be reproduced by x-ray contact printing than by optical methods since diffraction effects are much smaller. The ultimate resolution[2] of the printing process (at wavelengths below 4.4 nm, the carbon K line) is determined by the range of the secondary electrons (photoelectrons and Auger electrons) that are produced by atoms in the resist after the absorption of an x-ray photon. The photoelectron range increases rapidly with increasing photon energy, reducing the resolution of the printing process. At the carbon wavelength, the photoelectron range in PMMA is between 5 nm and 10 nm. Using the 4.4 nm line Flanders [1979a, 1980], in a demonstration experiment, replicated 175 Å wide lines and spaces in PMMA resist. These structures probably indicate the minimum linewidth that can be produced in PMMA. The 175 Å wide mask patterns were made by shadow evaporating a thin layer of metal onto a vertical walled step on the polyimide mask surface. The step on the membrane was produced by etching a vertical walled groove on a silicon wafer and then encapsulating the wafer with polyimide. The underlying silicon is etched away to leave the profiled membrane.

The insensitivity of the printing process to diffraction means that mask features can be reproduced over a large depth of field. Since x-ray lithography is a parallel process, complex submicron patterns that would require several days for an e-beam system to define can be printed over large areas in much shorter times.

Exposure time.

The exposure times associated with electron bombardment sources (such as the one used in this work) are long (several hours) due to two factors: first: the quantum efficiencies for such targets are small $<10^{-4}$ photons / steradian / electron, [Spears 1972, Green 1968], second: the source sample

[2]The ultimate resolution is also determined by the intrinsic resolution of the resist material. For PMMA this resolution is probably of the order of 10 nm [Smith 1989].

distance D is made large (>5 cm) to minimise geometrical errors in the resist pattern caused by the lack of collimation in such systems. Since the radiation is emitted over 2π sterad, the intensity falls off as $1 / D^2$. A trade-off exists between the geometrical effects in the printed image which increase the minimum linewidth of the printing process and the exposure time. The long exposure times limit the use of these systems to pure research.

Using brighter and more collimated sources (synchrotrons) mask patterns up to 10 cm in diameter can be reproduced in times ranging from a few seconds to several minutes [Pircher 1986, Broers 1986][3].

Unfortunately the collimation of e-beam bombardment sources cannot be improved due to the lack of focussing optics in the soft x-ray region. The real part of the refractive index for most materials is approximately unity at x-ray wavelengths [Eisberg 1961, p 476]. Low atomic number (Z) materials have attenuation lengths of the order of microns to soft x-rays. This attenuation increases with wavelength above 1.0 nm. It is not possible to produce refractive x-ray lenses; the thickness of material required to produce an acceptably short focal length would introduce too much attenuation. Fresnel zone plates are currently under development for use in x-ray microscopy but their efficiencies are very low ~ 5% [Michette 1988].

The low sensitivity of PMMA resist is another factor which increases the exposure time. X-rays in the 1 - 50 nm range are not very strongly absorbed by polymer resists ($\alpha \approx 0.4$ dB μm^{-1}), compared with visible or UV light, but they are strongly attenuated by high atomic number (Z) materials such as gold (α ranges form 10 dB μm^{-1} at 0.5 nm to 120 dB μm^{-1} at 4.4 nm). The search for a high contrast, high sensitivity x-ray resist is an active area of research (see for example [Dössel 1986]).

The relative transparency of low Z materials to x-rays does mean that contact printing is relatively insensitive to organic contamination on the mask or substrate. Any errors that are caused by dust particles during resist exposure can be removed by simply increasing the exposure time [DellaGuardia 1989].

X-ray exposure of resist is unaffected by the underlying substrate: there are no coherent effects in the resist due to substrate reflectivity as in optical lithography, or a proximity effect due to

[3]Laser induced plasma sources are brighter than conventional e-beam bombardment sources but they are uncollimated.

backscattering from the substrate as in e-beam lithography.

X-ray masks.

The mask substrates must be thin, low Z material , dimensionally stable and strong [Wilkinson 1985]. Ideally the membrane should be optically transparent to allow registration. These requirements are not easy to meet; much of the current effort is in the development of new mask technologies. Recent work has concentrated on dielectric membranes, especially for synchrotron lithography. Several material systems have been investigated: SiN [Dana 1986, Suzuki 1982, Sekimoto 1981], polycrystalline Si [Heuberger1986], and SiC [Yamada 1989]. These masks h ave to last for several thousand exposures. Consequently the measurement of distortions due to thermal effects and material stresses are an important area of research [Karnezos 1986]. Polyimide membranes are more suitable for low power exposure systems.

The geometrical errors produced in the resist pattern due to lack of source collimation are reduced by making the gap between the mask and sample as small as possible. For small linewidths patterns ≤100 nm wide, the mask and sample must be in intimate contact. This usually results in mechanical damage induced in the mask, reducing its working life.

Synchrotron sources can be operated with much larger mask sample gaps up to 40 μm. In this case thicker (stronger) mask substrates can be used because of the increased source brightness. However, diffraction in the gap limits the technique to 0.5 μm- 0.3 μm linewidths. Ku et al [1988] and Hasegawa et al [Hasegawa 1989] have shown that it is possible to reduce the effects of diffraction at least in the near field by tailoring the absorber thickness to give a π phase shift to the weak transmitted radiation which partially cancels out the weak diffracted component of the intensity through the mask apertures.

Synchrotron lithography systems are very sophisticated and hence very expensive and so must be used to run several exposure stations simultaneously so as to make the process more economical. At present, despite the development of step and repeat facilities and sample registration schemes for use with these systems, synchrotron lithography belongs more to the area of 'big science' than to a reliable industrial technology [Mackens U., 1989, Deguchi K., 1989].

A discussion of the merits of these high power sources is beyond the scope of this thesis; relevant information can be obtained from the reviews quoted above.

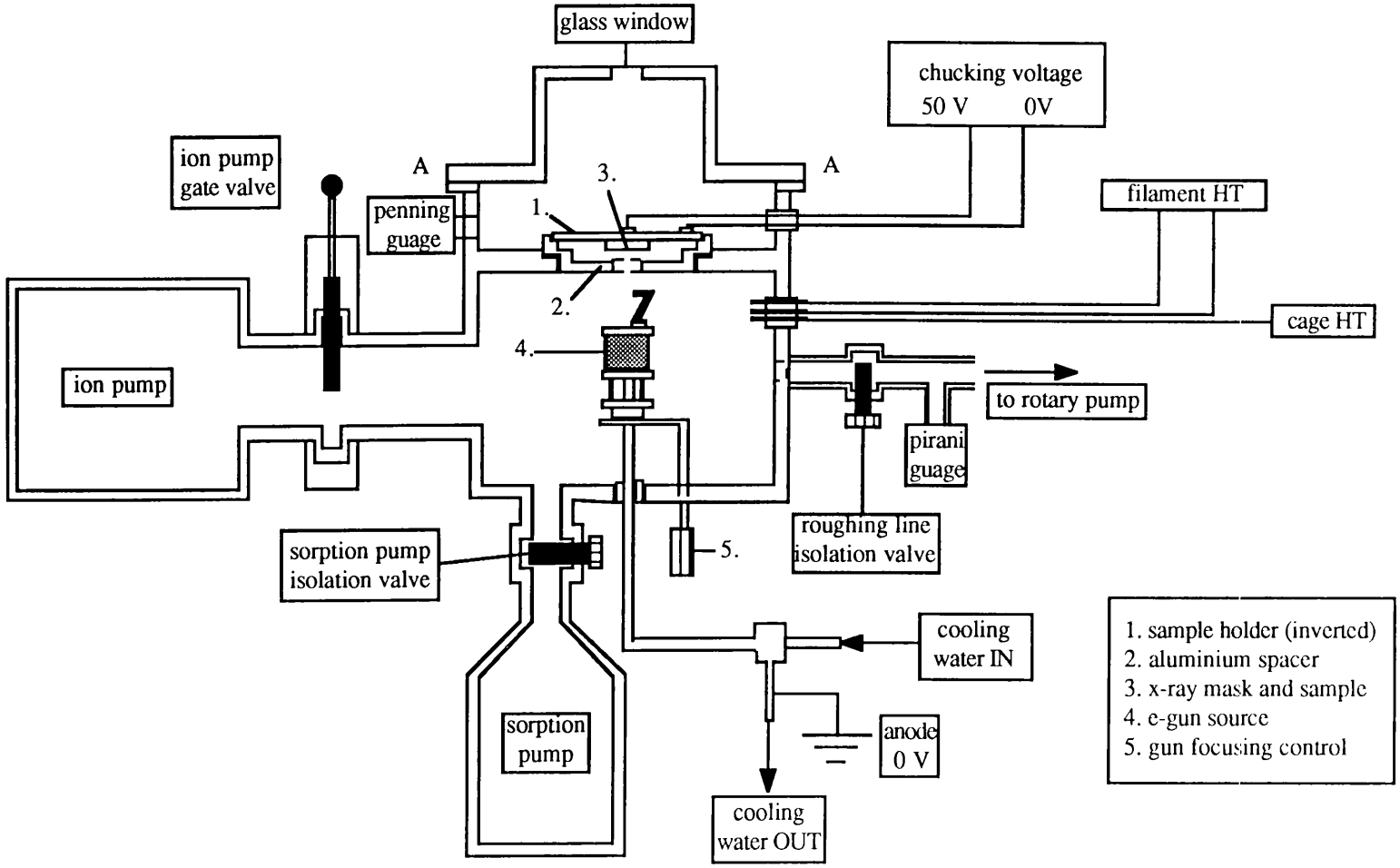

Figure 5.1. X-ray contact printer: schematic of vacuum system and electrical connections.

The rest of this chapter.

The development of a contact printing system, figures 5.1., 5.2., 5.3., based on an electron bombardment source producing copper L_α radiation will be described. This system uses a polyimide membrane mask technology similar to that developed by Smith's group at MIT [Plotnik 1983, Flanders 1977].

Section 5.2. will summarise the mask fabrication process and a description of the contact printer is given in Section 5.3.

The contact printing results are discussed in Section 5.4.; 285 nm period grating patterns have been printed onto 0.2 μm thick BDH Poly methyl methacrylate (PMMA) resist on 5 x 5 mm silicon and titanium-coated glass wafers, after exposure for 6 hours at the copper L_α wavelength, 1.33 nm. Sub 100 nm side PMMA dots, 0.2 μm high, with vertical walls have also been produced by a double x-ray exposure of the same grating mask.

A detailed account of the system operating procedure is provided in Appendix 4.

Electron bombardment sources: choice of x-ray wavelength.

With an electron bombardment source such as the one used in these experiments, figure 5.2., the choice of wavelength depends on the available materials, the minimum linewidth to be printed and the absorption in the membrane mask and the resist.

Factors affecting the minimum linewidth:

1.Secondary electron range.

The minimum linewidth is determined by the range of the secondary electrons produced in the resist. When soft x-rays pass through matter, their energy is much higher than the binding energies of the electrons in the outer shells of the atoms in the material so that there is little interaction. Most of the photons simply pass through the material.

At these energies, the most probable interaction is the excitation and ionisation of inner K shell

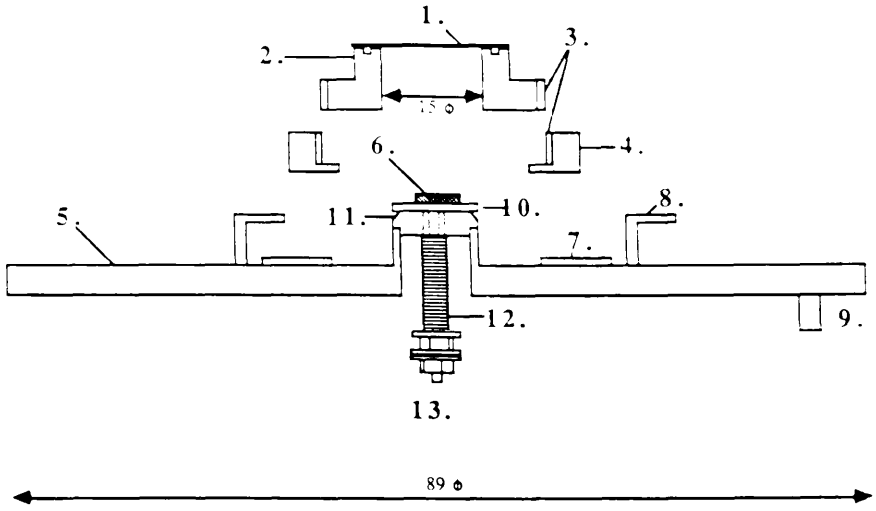

1. polyimide membrane mask.
2. phosphor bronze mask insert, with circular groove, forming two rings.
3. 40 turns per inch locating thread.
4. stainless steel support ring.
5. sample holder plate.
6. semiconductor sample.
7. PTFE blank plate.
8. screw clamps.
9. electrical connection (electrostatic chucking earth).
10. electrode plate.
11. PTFE insulator.
12. spring plate to keep electrode plate taut.
13. electrical connection (50 V)

(all diameters are in mm.)

Figure 5.2. X-ray contact printer: sample holder.

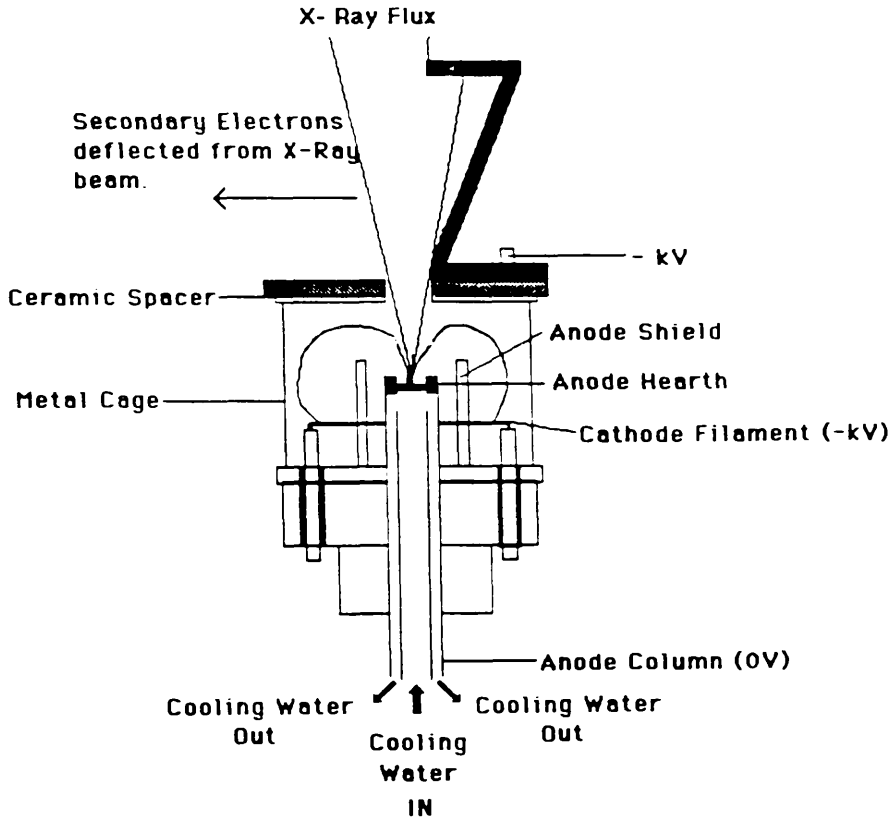

Figure 5.3. X-ray contact printer: e-gun source.

electrons via the photoelectric effect [Eisberg 1961].

Absorption via the photoelectric effect is a strong function of the atomic number Z of the material ~ Z^5 so that materials like gold have attenuation coefficients several orders of magnitude higher than low Z materials like PMMA or polyimide (figure 5.5., 5.8.). When a sufficiently energetic photon comes close enough to the inner shell electrons of a polymer atom to be absorbed the atom becomes ionised ejecting a photoelectron, and forming a hole in one of its inner shells. The emitted photoelectron can have an energy up to the incident photon energy minus the shell binding energy and tends to be emitted [Compton 1927 p.240]. along the polarisation direction of the photon with a cosine squared distribution ie in the plane of the resist for normally incident photons.

The excited atom relaxes either by the transition of an electron from a higher shell to fill the hole in the low shell (K) with the emission of a secondary x-ray of lower energy (fluorescence) or by an Auger process (the electron gives up its energy to another electron, ionising the atom further). The fluorescent x-ray may be reabsorbed to produce further electrons. The net effect is the production of secondary electrons. These electrons collide with the polymer chains causing chain scission (in PMMA), and hence expose the resist. The developer selectively dissolves lower molecular weight fragments of the polymer.

Resolution is thus determined by the range of these low energy secondary electrons. The resist exposure mechanism is the same as in e-beam lithography, except that the electron energies are much smaller (1 KeV compared to 50 KeV for the incident e-beam). The secondary electron range increases approximately as $1 / \lambda^2$, so that very soft copper L_α 1.33 nm or carbon K_α 4.4 nm radiation must be used for high resolution work. Diffraction becomes important again at these wavelengths necessitating intimate contact between the mask and sample to minimise edge blurring.

Experimental data for secondary electron ranges vary by a factor of two. Smith [Smith 1977, 1974] quotes values of 20 nm and 5 nm for the Cu L_α and the C K_α lines. In this work, values obtained by Rishton [1984, Chapter 3] have been used, figure 5.4. Rishton built a low energy electron exposure system (20 eV to 2500 eV) to examine the electron range in PMMA. Samples were exposed through a copper mesh at a constant dose (5×10^{-5} C / cm^2) at a given acceleration potential and then developed. The electron range was estimated from the depth of the developed pattern. His results indicate secondary electron ranges of 50 nm and 10 nm for the Cu L_α and C

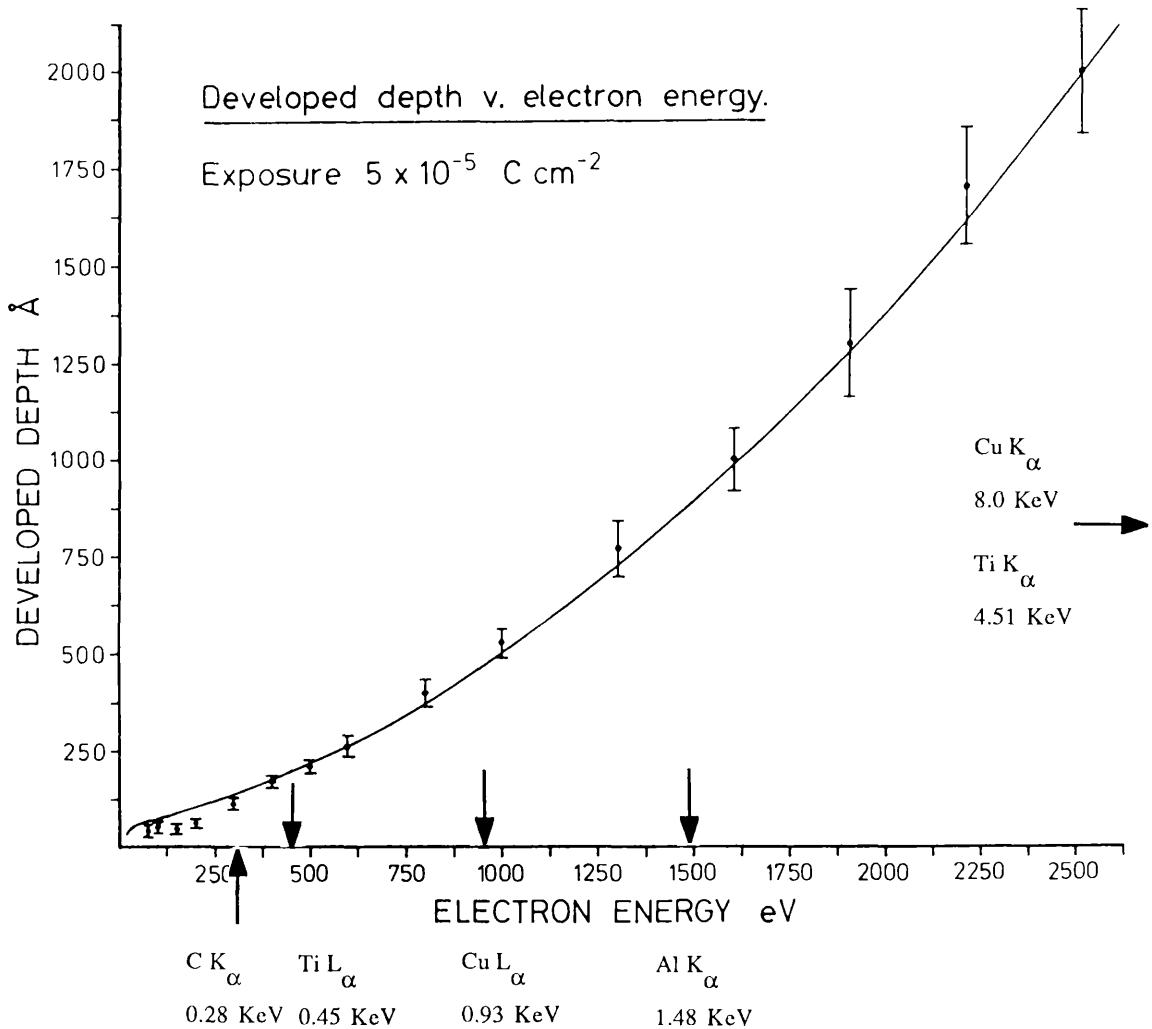

Figure 5.4. Data from [Rishton 1984]. Developed depth of Elvacite PMMA film against incident electron energy. The PMMA films were 0.24 μm thick. Development was in 1:3 MIBK:IPA at 23° for 3 minutes. Maximum electron energies associated with absorbed x-ray photon energies are indicated on the diagram.

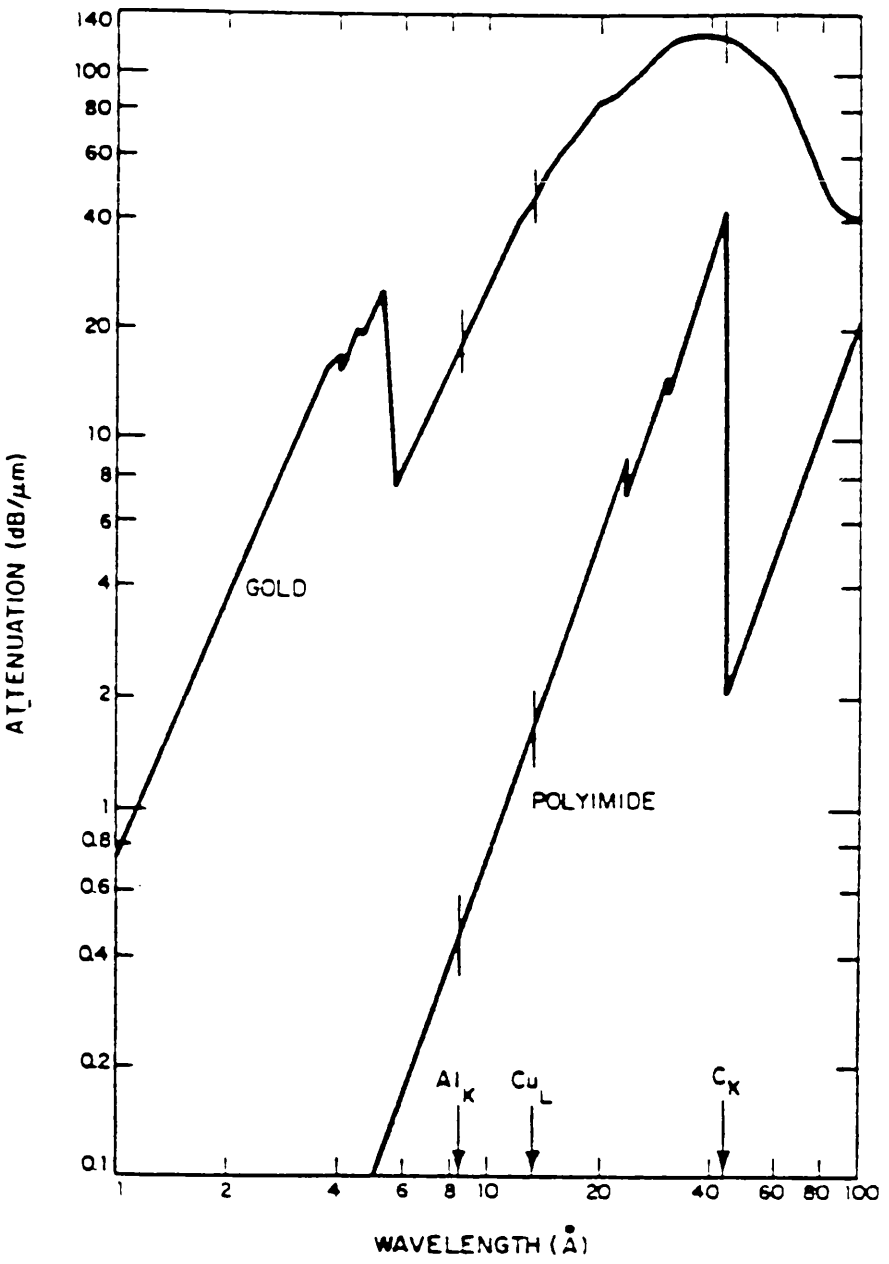

Figure 5.5. Absorption coefficients of polyimide and gold as a function of x-ray wavelength. Data from [Plotnik 198?].

K_α lines respectively.

The secondary electron range due to Al K_α radiation (0.834 nm) is ~ 100 nm - double that of copper. An aluminium source is not suitable for high resolution replication.

2.Diffraction.

The impact on resolution due to diffraction may be estimated from Fresnel diffraction theory. In intimate contact, the resist thickness is many wavelengths allowing the Kirchoff approximation to be used. The minimum linewidth due to diffraction, l_{min}, printed through a gap of width g, is estimated from:

$$l_{min} = \sqrt{\lambda_0 g} \qquad (5.1.1.)$$

where λ_0 is the exposure wavelength.

In intimate contact g is the same as the resist thickness ~ 0.2 μm. Substituting λ_0 = 0.834 nm, 1.3 nm or 4.4 nm (Al K_α, Cu L_α or C K_α lines) into (5.1.1.) yields values of l_{min} = 13 nm, 16 nm or 30 nm. Thus diffraction effects are not the limiting factor in this case.

Out of intimate contact the maximum tolerable gap between mask and sample can also be estimated; assuming a minimum linewidth of 100 nm, equation (5.1.1.) predicts that the maximum tolerable gap is 12 μm, 7.7 μm or 2.7 μm (Al K_α, Cu L_α or C K_α lines).

When Al K_α (1.48 KeV) radiation is passed through a 40 μm gap, the minimum linewidth due to diffraction is 183 nm. Printing through a large mask substrate gap increases the lifetime of the mask since it is no longer being pressed against the substrate. The gap also allows the development of an accurate mask alignment scheme. For contact printing, mask alignment must be done out of contact before the mask is brought into contact. The mask may shift relative to the substrate during this process, introducing an unacceptable overlay error if more than one pattern is to be printed.

3. Geometric effects.

The minimum linewidth and the accuracy of the printed image are affected by penumbral blurring

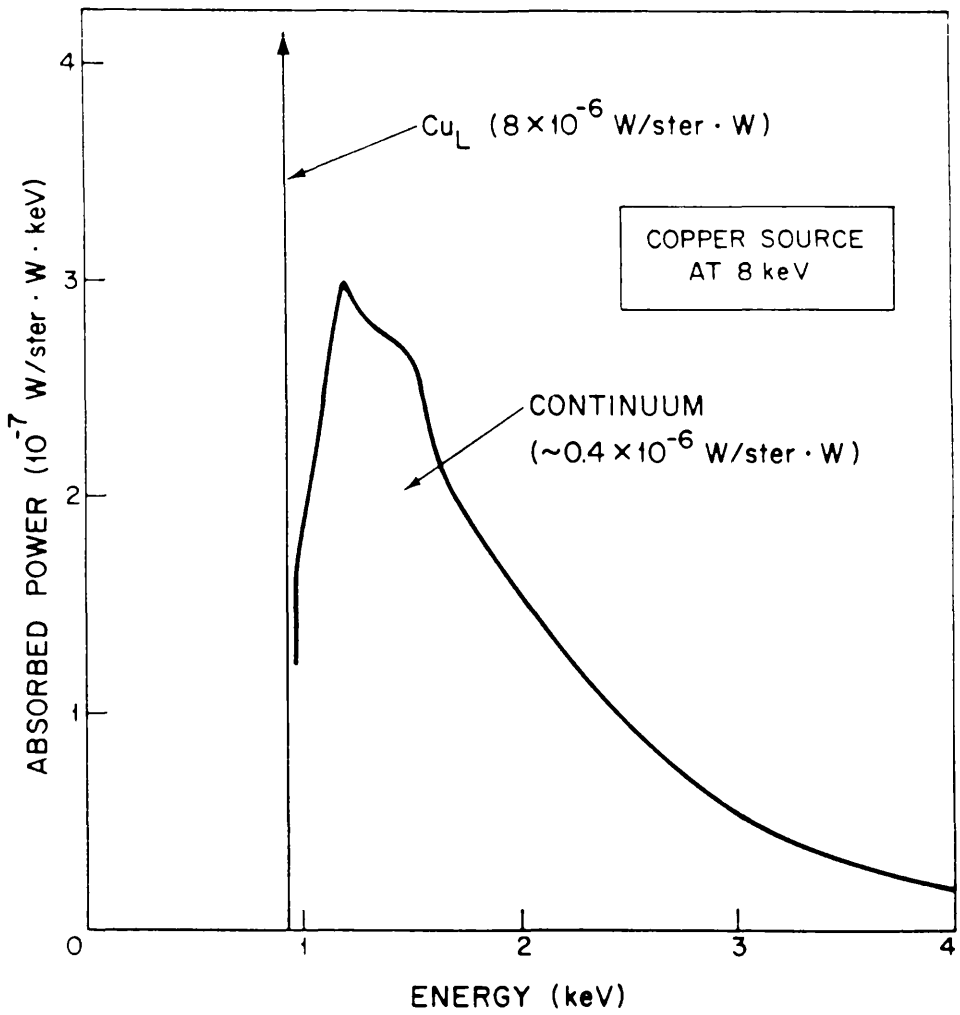

Figure 5.6. Calculation of power absorbed in a polymer resist film in Watts / Watt / sterad / KeV interval plotted as a function of photon energy for a copper target at a voltage of 8 KV, taking into account target reabsorption, and then multiplying by the fractional absorption of the polymer resist. Data from [Smith 1977].

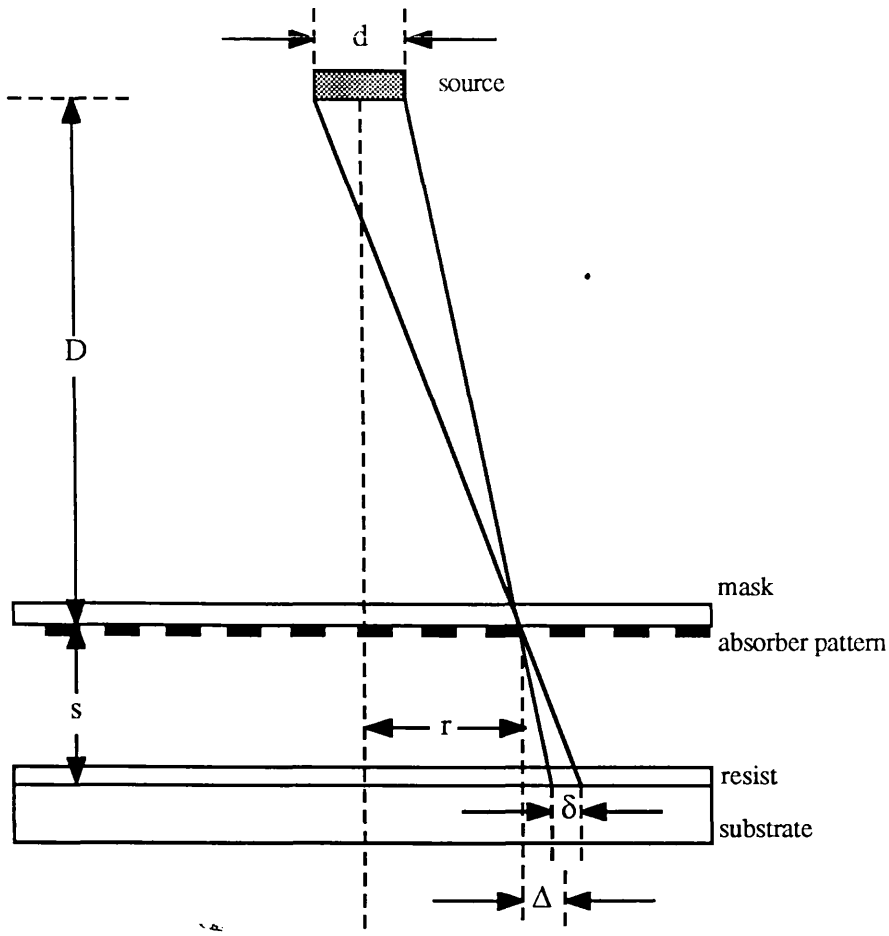

Figure 5.7. Geometrical distortions arrising in the resist image of the mask pattern because of the finite size of the source (penumbral distortion δ) and its lack of collimation (lateral magnification error Δ) where δ and Δ are given by:

$$\delta = s \, . \, d / D$$

$$\Delta = s \, . \, r / D$$

and a lateral magnification error due to the finite size of the x-ray source. Penumbral blurring δ arises because of the slight change in incidence angle seen at the mask for radiation from different parts of the source and the lateral magnification error Δ is due to its lack of collimation. These effects are minimised by printing the mask in intimate contact, figure 5.7. From the figure we have:

$$\delta = s\frac{d}{D} \qquad (5.1.2.)$$

$$\Delta = s\frac{r}{D} \qquad (5.1.3.)$$

where s is the mask-sample separation (which equals the resist thickness in intimate contact), D is the target-mask separation, d is the diameter of the source and r is the displacement along the sample surface from a position directly over the centre of the source. In these experiments, d was 2 mm, D = 88 mm, r = 2.5 mm and s = 0.2 μm, giving $\delta < 5$ nm, $\Delta < 7$ nm. If the gap had been 10 μm, then d and r would have been > 200 nm which is obviously unacceptable. Note that lateral magnification error is not cumulative c.f. the error on the grating period discussed in chapter 2. These small errors < 7 nm are tolerable.

Suitable anode materials.

Practically, the choice of exposure wavelength to produce sub-100 nm structures is restricted to the copper L_α and carbon K_α lines where the secondary electron range is lower. In this work the copper line was used. A copper target can be water cooled directly whereas heat dissipated from a carbon target must first pass through the thermal joint between it and the water cooled hearth in which it rests. Amorphous carbon has a much lower thermal conductivity than copper. Although carbon has a much higher melting point than copper, the anode cannot be run at such a high power without melting the indium solder which forms the thermal joint with the hearth. Since the yield of the source depends on the electron beam energy (and hence on the power dissipated in the target for a given electron current) copper sources are brighter than carbon ones leading to a shorter resist exposure time.

For a copper anode the maximum electron current that can be dissipated at an accelerating voltage V can be estimated from:

$$i_e = \pi\ r^2\, k \frac{T_m - T_w}{V\, d} \qquad (5.1.4.)$$

where r is the radius of the focused spot on the anode (= 1 mm), k is its thermal conductivity (Cu: ~ 400 $Wm^{-1}K^{-1}$, d its thickness (=1 mm); T_m and T_w are the anode material melting point (Cu: 1356 K) and the cooling water (~ 313 K) temperatures respectively. V is the electron accelerating voltage (6 kV). The thermal data was obtained from the Handbook of Chemistry and Physics published by the Chemical Rubber Company. Equation (5.1.4.) predicts $i_e \approx 200$ mA for copper. Running the anode at high powers near its melting point produces pitting [Plotnik 1983 p.14. and Yoshimatsu 1977].

High power running of the anode is desirable since this increases the ratio between characteristic and continuous x-ray radiation. A high ratio is desirable for x-ray contact printing since the cut-off for continuous radiation has a much higher energy than the characteristic radiation. Higher energy continuous photons produce higher energy secondary electrons which would reduce the resolution.

Characteristic and continuous x-ray radiation.

When electrons bombard a target two types of x-ray radiation are produced: discrete wavelengths that are characteristic of the target material and a continuous spectrum whose shape does not depend on the material. The maximum (cut-off) frequency ν_0 for continuous radiation is determined by E_0, the maximum kinetic energy of the incident electrons:

$$h\nu_0 = E_0 \qquad (5.1.5.)$$

Continuous x-ray radiation is emitted by electrons accelerated as they interact electrostatically with the nuclei of the atoms in the anode. Characteristic radiation is produced following the close collision of an incident electron with inner shell atomic electrons creating a hole in the shell. The atom is excited and an electron from a higher shell falls into the vacancy emitting a characteristic x-ray line in the process. The efficiency of the two emission processes depends on the incident electron energy E_0 and hence the power dissipation in the anode. The number of photons emitted per incident electron in the continuous spectrum is given by:

$$N(E)\,dE = kZ\frac{E_0 - E}{E}dE \qquad (E \text{ expressed in KeV}) \tag{5.1.6.}$$

where N (E) is the number of photons of energy E in a range dE around E. k is a constant independent of Z ~ 2 x 10^{-6}(KeV)$^{-1}$ Examination of equation (5.1.6.) shows that the continuous radiative intensity is smaller for low Z materials such as Carbon (Z = 6) than for higher Z materials such as copper (Z = 29). Continuous spectrum x-rays are emitted anisotropically with minimum intensity in a direction back along the electron beam [Bernacki 1975].

Characteristic x-rays are emitted isotropically. The number of characteristic photons emitted per incident electron per steradian, the internal quantum efficiency, is given by N / 4π where

$$N = N_0(E_0 - E_X)^{1.63} \tag{5.1.7.}$$

and N_0 is a constant for a specific material[4]. E_X is the ionisation energy of the atomic shell. All energies are in KeV. The ionisation energy can be estimated from:

$$E_X = (-)13.6\frac{(Z-a)^2}{n^2}\,(eV) \tag{5.1.8.}$$

where *a* represents a screening factor and n is the principal quantum number for the shell. (N.B. only positive values for E_X are substituted into (5.1.7.)). For the L_α shell n = 2 and a = 7.4 so that $E_{L\alpha}$ is - 1.6 KeV for copper (Z = 29).

Substituting N_0 = 0.5 x 10^{-4} [Green 1968] E_X = 1.6 KeV, values of 0.45 x 10^{-4} and 0.82 x 10^{-4} quanta per electron per steradian are obtained for the internal quantum efficiency at accelerating potentials of 6 KV and 8 KV respectively. The observed, external, quantum efficiency is denoted by ε which can be written as ε = N.f / 4π. f (≤ 1) is a parameter which takes into account x-ray absorption inside the target material itself since x-rays are generated at some finite depth in the material. Here the effects of target reabsorption have been neglected as we are only interested in an order of magnitude calculation of the source brightness.

---

[4] N_0 has been measured by Green and Coslett [1968]. For the carbon K_α and copper L_α lines N_0 ~ 2 x 10^{-4}, 0.5 x 10^{-4} (extrapolated value) respectively.

The incident characteristic x-ray flux density at the resist surface is estimated from:

$$I_0 = p\left(\frac{i_e}{e}\right)\varepsilon\left(\frac{h\nu}{D^2}\right) \qquad (5.1.9.)$$

where i_e is the electron current supplied to the gun, e the electronic charge, ε the external quantum efficiency, $h\nu$ is the photon energy, $1 / D^2$ is the solid angle subtended by unit area on the sample separated from the source by D and p is the fractional transmittance of the (polyimide) membrane mask.

The attenuation of x-rays through a material is described by expressions of the form:

$$I = I_0 \exp(-\mu.x) \qquad (5.1.10.)$$

where μ is the wavelength dependent attenuation coefficient; I, I_0 are the transmitted and incident intensities respectively and x is the thickness of the material. Attenuation coefficients are usually given in cm^{-1} or dB μm^{-1}. The attenuation of polyimide is 2.0 dB μm^{-1} at the 1.33 nm copper wavelength (figure 5.5.) so that $p \approx 0.63$ for a 1 μm thick membrane.

In these experiments, i_e = 50 mA, D = 8.8 cm, $h\nu = 1.495 \times 10^{-16}$ J. Substituting these values into equation (5.1.9.) and the appropriate quantum efficiency, values for I_0 = 17 μWcm^{-2} (6 kV) and 31 μWcm^{-2} (8 KV) at the resist surface are obtained.

The instantaneous power density absorbed by the resist may also be calculated. Data from [McGillis 1983] for PMMA, figure 5.8., predicts an attenuation coefficient μ of ~0.4 μm^{-1} or 1.7 dB μm^{-1} at 1.33 nm.

The resist absorbs a fraction $(I - I_0) / I_0$ of the incident flux density, I_0, where I is given by equation (5.1.10.). Substituting μ = 0.39 μm^{-1}, a value of 0.08 is obtained for the fractional flux density absorbed in a 0.2 μm thick layer of PMMA.
The resist layer absorbs approximately 1.4 μWcm^{-2} (6 KV, 50 mA) or 2.5 μWcm^{-2} (8 KV, 50 mA) of the incident x-ray flux.

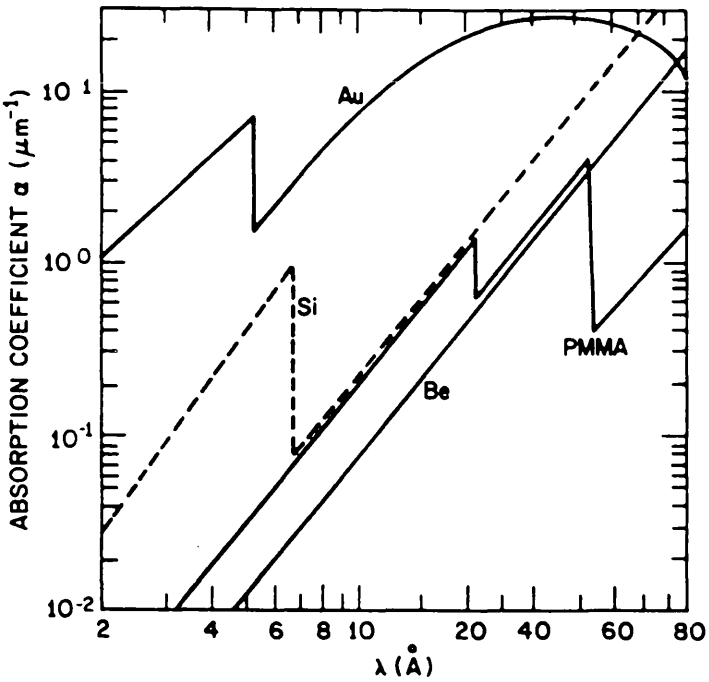

Figure 5.8. Absorption coefficients of several materials against x-ray wavelength. (Taken from [McGillis 1983] p 290.)

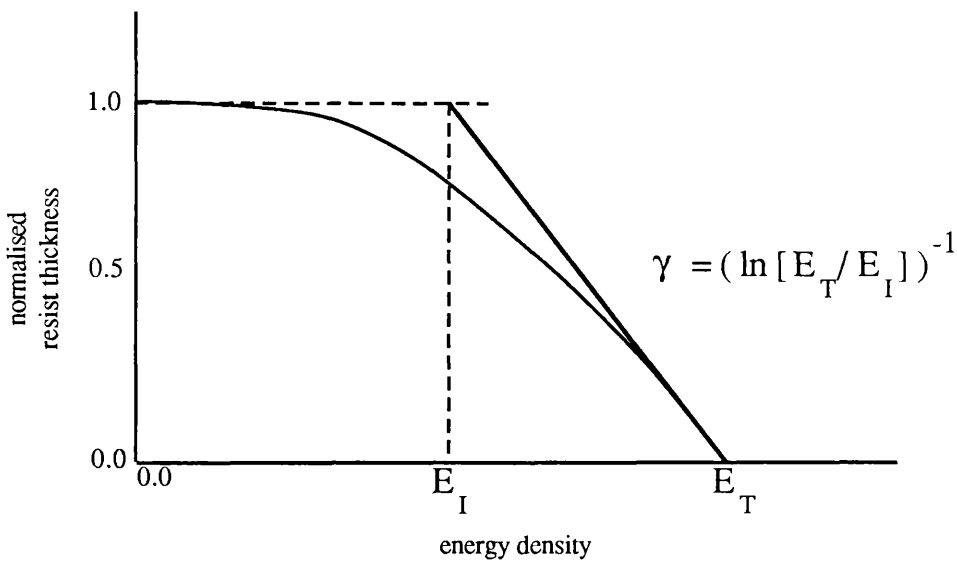

Figure 5.9. Definition of the sensitivity E_T and contrast γ of a positive polymer resist.

Figure 5.6. gives an estimate [Smith 1977] of the power absorbed in a 1 μm thick polymer resist film in Watts per Watt (power dissipation in the target) per sterad per KeV interval as a function of photon energy for a copper target operating at 8 KeV, taking into account target reabsorption and then multiplying by the fractional absorption of the polymer resist. The absorption of the mask is neglected. A 1 μm thickness of PMMA absorbs 4.3 times as much power as a 0.2 μm thickness. Substituting 400 W for the input power (50 mA, 8 KV), a solid angle of 8.8^{-2}, and multiplying by the mask transmittance, p = 0.63, Smith would obtain a value of 6.0 μWcm^{-2} for a 0.2 μm thick PMMA layer. This compares with 2.5 μWcm^{-2} obtained as above. The discrepancies indicate the difficulty with which these estimates have to be made. Smith also includes a calculation for the continuum and finds that at 8 KV this only represents 5% of the radiation emitted in the characteristic line. Thus the effects of the continuum can be neglected.

Other target materials

The possibility of using a titanium anode instead of a copper one was also considered for this work. A titanium source emits softer L radiation than copper ($L_{\alpha, \beta 1}$ 2.74 nm, 2.71 nm). The idea was abandoned because of increased absorption in the polymeric mask material (15 dB μm^{-1}) between the copper and carbon wavelengths. Polyimide has an acceptable attenuation (~2 dB μm^{-1}) at the Cu and C wavelengths. Between these two wavelengths, polyimide has an absorption edge rising to 40 dB μm^{-1} (at 4.0 nm).

Another potential difficulty is caused by the emission of K series radiation from the Titanium at relatively low electron energies. This also happens in Copper, but at a much higher energy. The very light elements, with Z < 20 have K series characteristic lines only. The K series wavelengths (absorption edges) decrease rapidly with increasing atomic number. Copper and Titanium both have K and L series characteristic radiation[5]; for Cu: L_α = 1.33 nm (0.93 KeV), K_α = 0.154 nm (8 KeV), for Ti: L_α = 2.74 nm (0.45 KeV), K_α = 0.275 nm (4.51 KeV). For Carbon the energy may be increased until the target starts to evaporate; there is no L series. At low electron accelerating potentials, above threshold, L series radiation is emitted from both copper and titanium targets. However if the incident electron energy exceeds the K shell ionisation energy[6]: 10.3 KV for copper or 6 KV for titanium, higher energy K radiation would be emitted inducing higher energy secondary electrons in the resist. This is to be avoided. In these experiments the copper target was

[5]Data taken from tables of principal emission lines of x-ray spectra of the elements (K, L, M series) in [Jenkins 1974]

[6]Calculated from equation (5.1.8.) with a =1.

run at 6 KV, well below the threshold for the K radiation.

An examination of tables of the x-ray wavelengths of the elements indicates that amongst the lighter elements for K series radiation, after C, the next softest wavelength target material is Al, followed by Si. The intervening elements are either gaseous or reactive metals like Na or Mg. Looking at L series spectra in the range of Z = 20 to Z =29 (Cu), only Ti, Fe and Ni are possibilities. Their L series radiation is all softer than that of copper and they all have lower energy thresholds for their K series spectra. A Ni target would have broadly similar wavelengths to a copper one. Copper is thus the next preferred soft x-ray source after carbon.

Early x-ray printing experiments were done with aluminium targets (Al K_a: 0.84 nm); many workers discussed mask combinations and working distances to minimise the long exposure times [Sullivan 1975]. In the first systems the x-rays were generated in vacuo and then passed through a 30 μm thick Beryllium window into a chamber filled with helium at atmospheric pressure. The window also acts as a radiation shield to filter out unwanted higher energy continuum radiation.

The attenuation coefficients for polyimide are 2.0 dB μm^{-1} at the 4.4 nm and 1.33 nm wavelengths compared with 0.56 dB μm^{-1} at the 8.34 nm wavelength. At very soft x-ray wavelengths there is also a reduction in the ratio of the power absorbed from the characteristic radiation to the power absorbed from the continuum, so that no radiation filters or windows should be used [Smith 1977]. Exposure must take place in a vacuum environment.

Choice of mask material.

In this work 1 μm thick polyimide membrane layers were used as the mask substrates after Flanders [1978c]. The membranes are easy to produce, dimensionally stable, even during long exposures (see Section 5.4.). When coated with a metal layer, they can be conformed into intimate contact by applying an electric field between the mask and sample surface and they are reusable (at least 5 x in these experiments).

In some previous work done in this department, Beaumont et al [Beaumont 1981] used carbon film x-ray masks deposited in intimate contact with resist coated Si wafers. The patterns were printed with C K radiation. The integrated masks demonstrated the feasibility of the contact

printing process, but are obviously not an acceptable lithography system. Dumas [1985] was developing a mask system based on Si_3N_4 membranes.

A practical lithography system requires the development of a reliable and reusable mask system. The silicon nitride system was abandoned because this material has a very high tensile stress (1 x 10^{10} dyn / cm^2), which limits the area of a self supporting membrane to less than 1 mm^2. Non stoichiometric SiN material which has a much smaller tensile stress can be grown by a low temperature LPCVD[7] process. The stress in the film can be adjusted from tensile to compressive by altering the gas flow parameters during the LPCVD process. Several groups have succeeded in making large diameter transparent membranes from SiN [Suzuki 1982, Seikimoto 1981, Dana 1986] More recently, these membranes have been replaced by SiC membranes which are less susceptible to radiation degradation (several hundred exposures). Because of the unavailability of the SiN material and the restrictions of the Si_3N_4 membranes: fragility and limited area, it was decided to try to make masks with polyimide.

Resist material.

A Positive PMMA electron beam resist was used in these experiments. This resist has a low molecular weight distribution (140 000) and was spun coated to a depth of 0.2 μm.

At the end of a six hour exposure, the incident dose at the surface of the resist is approximately 370 mJ cm^{-2} and the resist absorbs 1.5 KJ cm^{-3}. These calculated values are probably optimistic since no contamination effects have been included in the estimate, but they do compare well with values quoted in the literature giving the exposure doses to produce chain scission in PMMA: incident dose ~ 300 - 1000 mJ cm^{-2}, absorbed dose 300 - 1000 J cm^{-3} [Spiller 1977].

To minimise noise effects during exposure, high resolution resists, like PMMA, must have a low sensitivity (i.e. a high incident exposure dose per unit area to produce complete development). The contrast of the mask (defined as the ratio of the transmitted and attenuated x-ray fluxes) also affects the number of exposure defects - hence low contrast masks require higher exposures.

A highly sensitive resist has in general a low contrast γ. The contrast of a resist is defined from the slope of the exposure energy versus developed depth curve (for a given resist thickness and

[7]Low Pressure Chemical Vapour Deposition.

developer concentration), figure 5.9:

$$\gamma = \frac{1}{\ln\left(\frac{E_T}{E_I}\right)} \qquad (5.1.11.)$$

where E_T is the sensitivity and E_I is the energy density obtained by drawing the tangent at E_T to reach 100 % resist thickness.

Lower contrast resists require higher contrast masks. Spears [1972] states that the mask contrast should be better than 3:1 for PMMA. In these experiments the x-ray masks had very high contrast (10:1), so that with a high contrast resist like PMMA (γ = 2 - 3), the defect density should be negligible.

In this work development rates for unexposed and exposed PMMA in 1:3 MIBK / IPA developer were adopted from Beaumont [1981], who also used lower contrast masks (2:1) (Section 5.4.).

Although PMMA was used here, there are other x-ray resists. PMMA has the lowest sensitivity and one of the highest resolutions of the x-ray resists. This makes it ideal for research work but not for industrial production. Much research has been done to develop faster x-ray resists but nearly always at the expense of resolution. Faster x-ray resists often incorporate heavier elements to increase the absorption in the vicinity of the exposure wavelength. For example negative resists with sensitivities below 10 mJ cm^{-2} have been made by incorporating Chlorine into the resist polymer. Chlorine has an absorption edge at 0.44 nm which strongly absorbs the 0.437 Pd_α wavelength [Taylor 1981], [McGillis 1983].

Recently three component positive resist systems have been developed [Dössel 1986]. The resist is a novolak based resin in which the dissolution inhibitor is destroyed via a catalytic agent generated by the radiation, and not by the radiation directly. Sensitivities of < 50 mJ cm^{-2} and resolution at least as good as 0.3 µm were reported. The technique takes advantage of the higher resolution of positive resists as opposed to negative ones which tend to swell on wet development. Unfortunately, these resists are not available commercially unfortunately so their performance at resolutions below 0.3 µm cannot be assessed.

5.2. X-ray mask manufacturing process.

Polyimide membranes are much cheaper and more easily made into x-ray masks than are semiconductor membranes.

In the microelectronics industry polyimide is used to planarise the surfaces of semiconductor devices. The precursor polymer becomes fully cross-linked above ~350 °C. After curing it is more or less chemically inert and resists most acids and solvents. Below 450°C above which thermal decomposition sets in, the polymer has a very high thermal resistance. The coefficient of thermal expansion is ~ 5×10^{-5} K^{-1} [Hitachi Data Sheet].

The fabrication steps to make an x-ray mask are simple; the precursor material is spin coated onto a suitable substrate and then cured in a high temperature oven. Before applying the polyimide, the substrate has to be carefully cleaned; dust particles on the surface create tide marks during the spin coating process and may cause pin holes in the final film. The final membranes are extremely fragile and must be handled very carefully to avoid tearing them, especially during the etching process to remove the supporting substrate.

Substrate material.

In this work both thin glass coverslips and silicon wafers were used as substrates. Some work had been done previously by Stark [1985] in this department to make polyimide membranes, but it was never carried beyond the membrane fabrication stage.

Glass substrates were chosen as the most convenient substrates on which to make x-ray masks. Work on silicon was abandoned because of the difficulties of holographic exposure on a reflective substrate and problems experienced with wet etching the silicon. On glass the polyimide forms a transparent layer and reflections can be eliminated using a back prism as was seen in Chapter 3. Silicon requires either an accurately controlled resist thickness or an anti reflective layer such as ARC.

Glass substrates can be etched in 50% hydrofluoric acid in a few minutes provided that they are thinner than 1 mm or so. Complications arise for thicker samples: an insoluble white residue tends to form at the glass surface reducing the etch rate [Stark 1985].

To etch silicon, a 5: 1 mixture (by volume) of concentrated nitric acid [69-71% HNO_3] to concentrated hydrofluoric acid [40% HF] was used. This is a standard recipe [Sze 1985]. In this reaction the acid becomes quite hot ~ 80°C and brown oxides of nitrogen are evolved. The increase in temperature was sufficient to melt the wax that protects the glue between the polyimide and the mask holder. The membrane was often ruptured by the evolution of gas. This etch scheme is more complex and generally more unpleasant to use than the etch for glass.

Polyimide application and curing.

X-ray masks were processed on 22 mm side glass coverslips ≈ 200 μm thick (Chance Propper Ltd. no. 2). The finished membrane internal diameter was 15 mm, which is about the maximum that can be exposed with the printer geometry.

Since the glass is thin, great care had to be taken in handling it. The coverslips were cleaned in the standard way (see Chapter 3) by ultrasonically agitating them in trichlorethylene, methanol, acetone and de-ionised water. Then they were polished in a sulphuric peroxide bath (8 parts conc. sulphuric acid to 1 part hydrogen peroxide (~ 33 %)) to remove any residual contamination on their surfaces. After polishing, the coverslips were rinsed once more in de-ionised water and blown dry using a filtered compressed air gun. They were left to dry on a hot plate at 50°C over night.

Two different types of polyimide solution were used: a commercial polyimide marketed by Hitachi: PIQ - 13 and solutions made up from a precursor material (Ciba Geigy XU 218). Precursor material was dissolved in a 35 % - 65 % mixture (by volume) of o-xylene and acetophenone to reach the desired concentration (by weight).

Except for very weak concentrations (< 4% by weight), polyimide solutions are too viscous to filter out contaminants smaller than about 50 μm. The solvents also tend to dissolve the synthetic filters increasing contamination in the spun film.

Several membrane thicknesses were tried out in this work. Initially, following [Stark 1985] an 8 % solution of precursor was used. The resulting 0.3 μm thick layers were too fragile. Some work was also done on bi-layers to try and avoid pin holes in the finished films, but again without success. Curing the first layer before applying the second one induced stresses into the bi-layer caused by the shrinkage of the second film on curing. If the second layer was spun onto the first

one after it had been baked at 150°C to drive off solvents, the two layers tended to dissolve one another causing thickness variations.

Particle contamination in the precursor solutions was a severe problem and poor quality films were produced often leading to mask failure especially during the wet etching of the glass.

Much better film quality has been obtained using the Hitachi PIQ - 13 solution. A 1 μm thick layer was produced by spinning PIQ - 13 at 6000 rpm for 60 seconds. The polyimide was much cleaner and produced strong membranes which could even stand being blown dry with filtered compressed air. The thicker layer does not introduce an unacceptably large attenuation to x-rays.

Polyimide curing.

The curing process is in three stages; a bake at 100°C for 30 minutes to drive off solvents, a bake at 200°C for 60 minutes to partially cross-link the polymer, and a bake at 350°C for 60 minutes to fully cross-link the polymer. The covered samples are placed in a temperature-programmable fan oven for the curing process. The exact details of the curing process are not sacrosanct; some manufacturers advise a four stage baking process, and the first two stages can be equally well carried out at 150°C and 250°C.

Pattern definition.

The processes of Chapters 3, 4 produce a metal grating pattern of arbitrary shape and area but with the groove lines running parallel to one edge of the coverslip. A reduced grating area, required for some applications, may be defined on the mask using photolithography followed by either etching or lift-off. Unmasked regions of the grating can be removed using gold etch followed by HCl to remove the nichrome. Once the pattern has been defined, and the photoresist removed, the metallised surface is encapsulated in a thin layer of polyimide (8 %: 0.4 μm), figure 5.11. This protects the pattern from the acid etch.

Glass etching.

The x-ray mask is cemented to the membrane mask holder. The mask holders are machined from phosphorous bronze metal and have a 15 mm internal diameter (Figure 5.10., 5.11.). The top surface of the support ring consists of two 1 mm thick concentric circular ridges mechanically polished, and separated by a 1 mm wide groove 1 mm deep. A rubber based adhesive (Evostik) is applied to the outer ridge as a cement and the polyimide-coated face of the x-ray mask is contacted

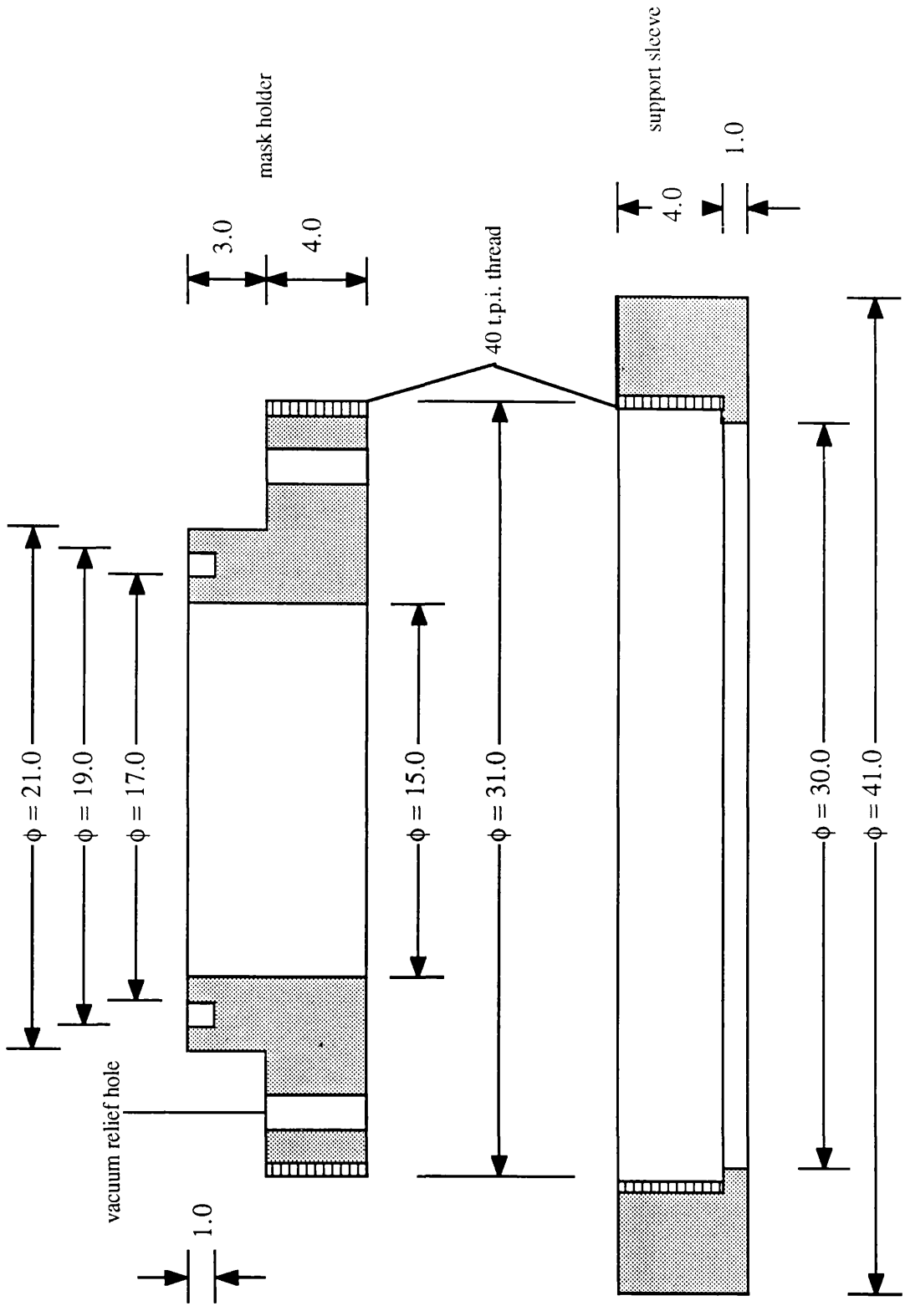

Figure 5.10. Details of the mask holder and support sleeve. All dimensions are in mm.

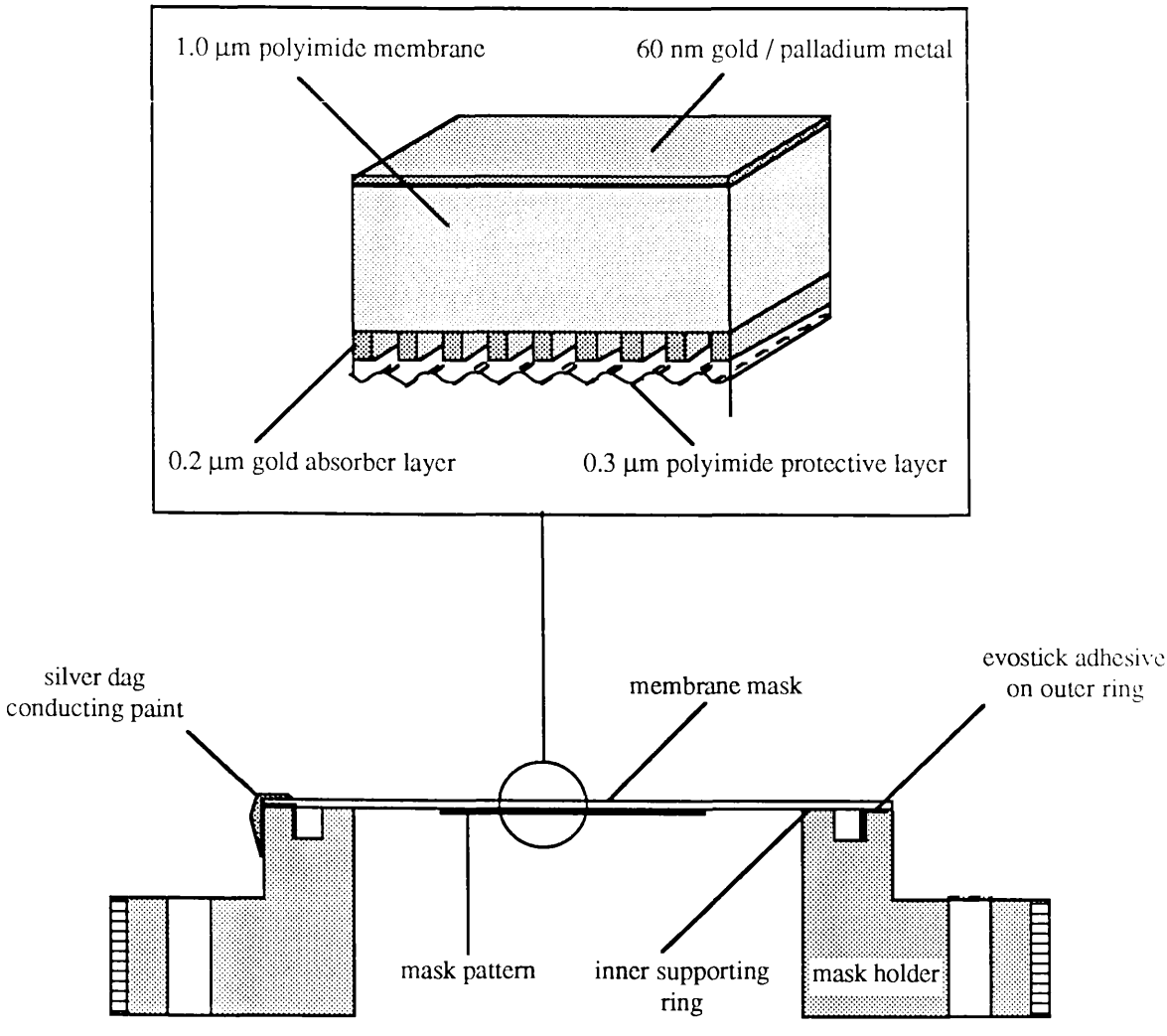

Figure 5.11. Diagram of mask holder with finished polyimide membrane mask cemented to it. The insert shows details of the mask layers.

to it. The adhesive is left to dry overnight.

The glass substrate is dissolved away in conc. hydrofluoric acid (40 - 50 %). HF will attack the adhesive that bonds the polyimide to the mask holder. Before etching, the exposed edges of the coverslip and the joint between the coverslip and the mask holder are sealed with low melting point medical wax. The wax is applied sparingly, using one leg of a pair of metal tweezers. If too much wax is applied, it tends to pull away from the metal exposing the glue. Once the mask holder is sealed it is screwed into the stainless steel support sleeve, figure 5.10. Mask holder and support sleeve are then inverted and loaded into a PVC holder. This supports the support sleeve so that the exposed glass touches the surface of the acid.

A large PVC beaker is filled to a depth of 1 cm with the acid and the holder positioned in it. At this stage a few drops of water may be added in the well formed by the mask holder and the polyimide layer. The water helps to quench any acid that might penetrate through a pin hole in the film. After 10 to 15 minutes, the glass dissolves away and the polyimide layer appears to be wrinkled. Moving the PVC holder carefully, the polyimide can be seen to move with the surface of the liquid. The mask holder is carefully removed from the acid and the whole assembly immersed in de-ionised water. The polyimide film is held vertically in the water to avoid rupture. After rinsing, the mask holder and support sleeve are covered to protect the membrane and left to dry. As the film dries, the wrinkles disappear and the film appears clear and smooth.

The mask set is left to dry overnight. The wax may now be carefully removed from the sides of the mask holder. A scalpel blade is used to remove the wax and to trim the polyimide film. The mask is now examined using an optical microscope to check the condition of the adhesive and to see if there is any water trapped below the film in the circular groove.

The membrane must be made conducting if it is to be electrostatically chucked into intimate contact with a sample. This is done by evaporating a thin metal layer. The mask set is loaded into an evaporator with the unpatterned face above the evaporation sources. A 60 nm thick film of Au / Pd alloy is evaporated onto the membrane to form the chucking layer. This layer is thick enough to produce an even coverage of metal and thin enough to have good optical transparency. If there are any weaknesses in the polyimide ,the mask set will fail when it is subjected to the vacuum.

The electrical contact between the Au / Pd coated polyimide surface and the mask holder is made by painting the sides of the mask holder and the edge top surface of the polyimide with conductive silver dag paint. The x-ray mask is left to dry overnight after which it can then be used.

5.3. Contact printer design.

Figure 5.1. is a schematic of the contact printer, showing the vacuum system and the electrical connections. The chamber consists of two main sections; a lower section housing the e-gun and an upper section in which the sample holder is inverted and supported directly over the gun. The chamber walls are made from stainless steel, except for the aluminium bell jar. This has an observation window in the top to assist with focussing the e-gun. The steel sections are bolted together and sealed with viton 'o' ring gaskets; the smaller pipe pieces are sealed with copper gaskets.

The ion pump and sorption pumps can be isolated from the gun chamber by gate valves to allow the chamber to be opened and roughed out. As far as possible the sorption and ion pumps should not be let up to atmospheric pressure.

The main vacuum pump is the titanium diode ion pump Varian model 911 (60 litres s^{-1}). The main advantage of this pump is its cleanliness.; there is little organic contamination in the system as a result.

The power supply is a standard VG electron beam evaporator power unit supplying up to 10 kV across the gun at electron currents up to 200 mA.

The e-gun itself is mounted in the lower chamber. During operation of the gun, the chamber is pumped by both the ion pump and a sorption pump mounted underneath the chamber. After switching on the gun, the chamber pressure rises to ~ 5 x 10^{-5} mbar due to out-gassing from the filament and the gun. The pressure falls to 10^{-6} mbar again after half an hour and remains stable thereafter.

The e-gun is based on a VG EG-2 design (figure 5.3.) The anode is a 1 cm diameter stainless steel tube with a copper cap 1 mm thick brazed onto the tube with silver solder. The anode is water cooled; a 7 mm diameter tube is inserted inside the anode tube so that there is a 2 mm gap just below the copper cap. Cooling water is admitted via the inner tube and drained down the inside of the anode. The flow rate should exceed 2.3 litres /min [VG operating instructions].

The gun assembly is in two parts: a lower stainless steel piece that rests against the anode shaft on a metal plate that can be raised or lowered to provide the gun focusing, and an upper piece, separated from the anode, and supported from the lower piece by three ceramic rods 2 cm long. The gun focusing control is a micrometer drive mounted underneath the gun chamber. The whole gun assembly can be moved relative to the anode by 2 cm.

The power supply provides three HT connections (and an earth to the contact printer case). Two leads are the filament supply. The third lead goes to the gun shield.

The electrons are emitted from a circular filament concentric with the anode and separated from it in the direct line of sight by the cylindrical anode shield. The two HT leads are biased at a large negative voltage - V, (up to - 10 KV) but one lead is 6 V higher than the other. The resulting current heats the filament, producing the electrons. The filament is insulated from the rest of the gun assembly by ceramic spacers. The electron trajectories are fixed by the geometry of the metal cage and the anode shield. From figure 5.3., the electrons have an approximately circular trajectory in the vertical plane through the gun centre. The cage is also held at -V, connected to the power supply via the third HT lead. Raising or lowering the gun assembly with respect to the anode alters the size of the circular region on the target where the electrons collide. This circular spot can be seen through the observation window as a bright spot on the anode surface. The focus cannot be exactly determined within more than a millimeter in diameter by this method. A measurement of the melted spot on the anode indicates a spot diameter of just under 2 mm. The gun is focused when the anode surface is 6 mm below the top surface of the cage.When an adequate focus has been obtained, the lower part of the gun assembly may be clamped to the anode tube.

Secondary electrons and x-rays emitted from the anode pass through a 5 mm diameter hole in the cage above the anode. These secondary electrons will happily expose PMMA resist in about 5 minutes and must be removed from the x-ray beam. A 'Z' shaped copper electrode 4.2 cm high is mounted on top of the gun cage to act as an electron deflector. The top piece, 2 cm long lies, exactly over the gun cage up to the edge of the 5 mm hole in the cage top. The electrons are deflected by the electrode potential, also - V, towards the chamber walls.

Care must be taken in assembling the gun to avoid contamination which can cause short circuits and to keep the HT leads separate inside the chamber. The copper braids which form these leads are

mounted from the side of the chamber instead of the bottom and kept as short as possible.

The sample holder.

The sample holder consists of a circular stainless steel base plate, 89 mm in diameter, with a hollow raised cylindrical section at the centre 4 mm above the surface of the base on which is mounted the electrode plate insulated from it by a 2 mm PTFE spacer, figure 5.2. The electrode plate is spring loaded to the back of the PTFE spacer. This arrangement is designed to accommodate any differential thermal expansion in the electrode.

The electrode is 1 cm in diameter and completely covers the PTFE insulator. This design allows the sample and the mask to be brought into intimate contact by electrostatic chucking. In operation, the electrode plate is held at 50 V and the base plate is earthed.

Sample mounting.

The sample is attached to the electrode plate using conductive 'silver dag' paint. The x-ray mask holder is carefully screwed into the support sleeve so that the thread is only just started. The assembly is then placed on the base plate over the electrode plate and sample, resting on an annular PTFE shim. The shim acts as a lubricant and prevents any bonding between the base plate and support sleeve. The support sleeve overlaps the shim, so that there is a 1 mm gap between the metal surfaces. The support sleeve is marked along the edge in fortieths of a revolution. The membrane height can be adjusted by 16 μm increments simply by rotating the mask holder through one division inside the support sleeve. If the sample and membrane are nearly in contact, the mask assembly should be removed from the base plate to prevent tearing. The mask and sample are registered by observing the sample through the gold - palladium chucking layer on the membrane.

Once registration and the height of the membrane is adequate, the mask assembly is attached to the base plate using the screw clamps. The electric field is applied and the mask conforms to the sample. The membrane is not significantly stretched in this process, as the edges of the sample were already making contact before the field was applied. Any residual air bubbles trapped between the sample and the membrane can be smoothed away using a cotton bud. Great care must be taken not to come near the edges of the sample with the bud or the membrane tears.

The electrostatic chucking is very efficient. The sample and membrane remain in intimate

contact throughout the exposure. To remove the mask after exposure, the electrode plate is earthed, and then the membrane is removed. Great care is needed at this stage to lift off the mask holder vertically and avoid rupture. Two pairs of broad bladed tweezers on either side of the holder are used to support it. The sample is removed using a scalpel blade.

5.4. Contact printing.

As described in section 5.1., a positive-tone e-beam resist, PMMA,was used in these x-ray experiments. The resist development parameters were estimated from data obtained from high resolution e-beam patterning experiments done in this department.

Since the patterns were going to be high resolution (≈ 100 nm linewidth), work was begun with the two layer resist system used in e-beam lithography[8]. The substrate was spun with 4 % BDH PMMA solution (low molecular weight ≈ 140 000) to form a layer 0.07 μm thick and baked at 180°C for one hour. Next a 4 % Elvacite PMMA solution (high molecular weight ≈ 450 000) was spun on top of the BDH layer and baked at the same temperature over night. The total resist thickness is ≈ 0.2 μm.

These resist solutions were made up by dissolving PMMA powder in 'o' xylene. Percentages are calculated by weight. The thicknesses were determined by talystep to within 5 %.

The advantage of this bilayer resist system is that an undercut profile results after exposure and development by e-beam. This profile allows the lift-off of very fine lines.

All development work was done using a mixture of Methyl isobutyl ketone (MIBK) and Iso propyl alcohol (IPA). For high resolution e-beam patterning, a 1:3 MIBK : IPA solution is used. Consistent results are obtained by fixing the developer temperature; for example at 23 °C. Some data on development rates for different exposures and developer strengths is given in figure 5.12.

PMMA is a positive e-beam resist. Electron exposure breaks the polymer chains into lower molecular weight fragments.. The developer preferentially dissolves the shorter polymer chains; hence the lower molecular weight material is more rapidly dissolved. Increasing the developer strength i.e. increasing the ratio of MIBK : IPA, decreases its selectivity; longer polymer chains are removed, so that a weaker developer has a higher resolution [Thoms 1989].

Figure 5.12. (b.) is taken from [Beaumont 1982] plotting the developed depth of a 0.3 μm Elvacite PMMA layer against development time. The mask had a contrast ratio of 2:1 and the resist was exposed with C K_α x-rays (225 W e-gun power, 4 hours exposure time, D = 4.5 cm).

[8]See for example [Beaumont 1981]

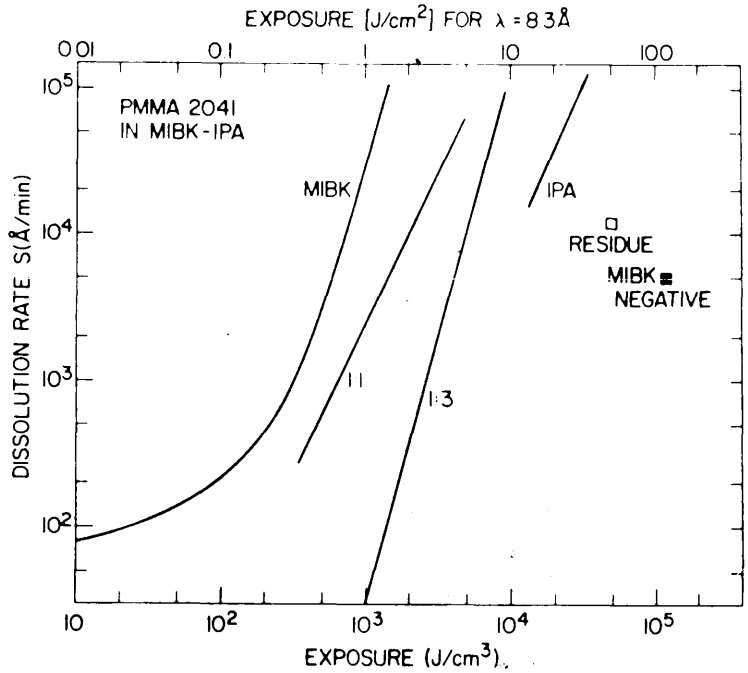

Figure 5.12. (a). Characterisation of PMMA: Dissolution rate versus exposure for PMMA developed in MIBK and IPA mixtures. At exposures above 0.1 MJ / cc cross-linking begins to dominate and the resist is less soluble than the unexposed. Graph taken from [Spiller 1977]

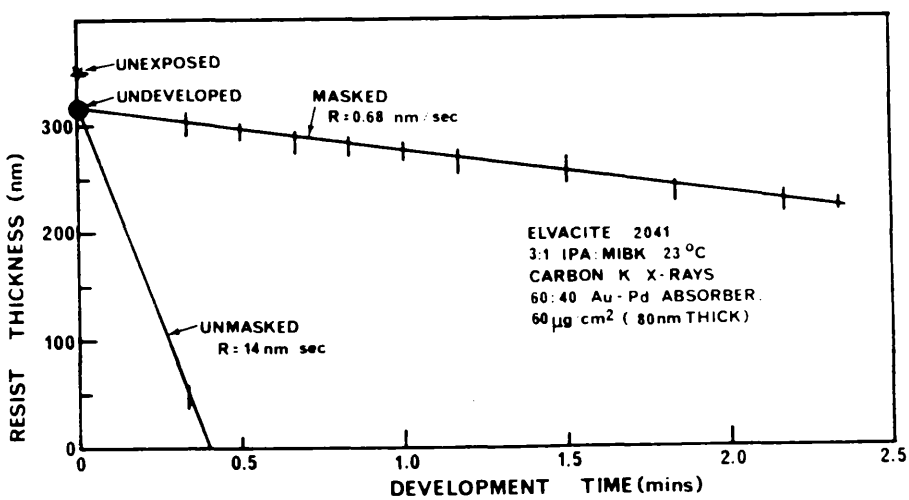

Figure 5.12. (b). Characterisation of PMMA: Data from [Beaumont 1981] plotting developed depth against development time in 3:1 IPA : MIBK developer. The mask had a contrast ratio of 2:1.

The unmasked PMMA is completely developed in under 30 seconds, giving a development rate of 14 nm s^{-1}. The masked resist has a much slower development rate (0.68 nm s^{-1}). In these experiments the mask contrast was 10:1. The masked portions of the resist are effectively unexposed.

Initial experiments with this bilayer resist system were unsuccessful, mainly because the exposure times were too short and the electrostatic chucking system was not working efficiently. The masks tended to fail after or during exposure due to inexperienced handling.

The resist system was changed to a single BDH PMMA layer in the hope that evidence of exposure would be more obvious. An 8 % solution in 'o' xylene was spun at 5000 rpm to form a layer 0.2 μm thick on silicon substrates.

Figure 5.13. is an SEM micrograph of the first PMMA grating that was successfully reproduced from a 356.2 nm period gold grating mask on to.a 5 mm x 5 mm Si chip. It was exposed to Cu L_{α} radiation through a second 1 μm thick polyimide membrane acting as a heat shield for two hours. This membrane rested on the aluminium holder in between the mask and the gun.

The e-gun was run at 6 kV and 50 mA electron current. The mask perished after removal from the sample. The sample itself was developed in 1:3 developer for 75 s at 23°C. The grating pattern could be seen as a very faint modulation on the surface.

This result was improved on by increasing the exposure time to to 6 hours. No heat shield membrane was used. Figures 5.14., 5.15., are SEM micrographs showing the developed PMMA gratings that resulted. Development was in 1:3 developer for 30 s at 23°C. These samples were exposed on silicon; the grating (285 nm period) covering the whole area (5 mm x 5 mm). This structure was also successfully reproduced on pieces of glass microscope slide. The slight distortions are due to scratches on the original mask. The glass microscope slides had to be coated with a conductive metal layer (evaporated Ti), before spinning on the resist, so that electrostatic chucking would work. The sides of the sample were carefully painted using silver dag to make the electrical connection between the metal coated layer and the sample electrode.

The same polyimide membrane mask was used to replicate patterns on 3 chips; two plain

Figure 5.13. PMMA relief grating on silicon. The sample was exposed for 2 hours to Cu (1.33 nm) radiation. The e-gun power was 300 W. The PMMA was developed in 3:1 IPA / MIBK developer at 23°C for 75 seconds. The 8 % BDH resist was spun to form a 0.2 μm thick film. The mask was a 356 nm period gold grating, supported on a 1 μm thick polyimide membrane.

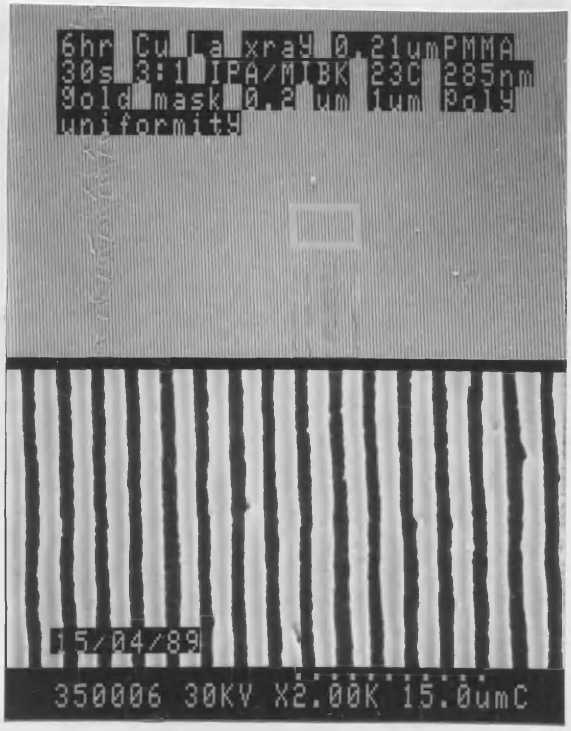

Figure 5.14. PMMA grating on Ti coated-glass. The sample was exposed for 6 hours to Cu (1.33 nm) radiation. The e-gun power was 300 W. The PMMA was developed in 3:1 IPA / MIBK developer at 23°C for 30 seconds. The 8 % BDH resist was spun to form a 0.2 μm thick film. The mask was a 285 nm period gold grating, supported on a 1 μm thick polyimide membrane and encapsulated with a 0.3 μm polyimide layer.

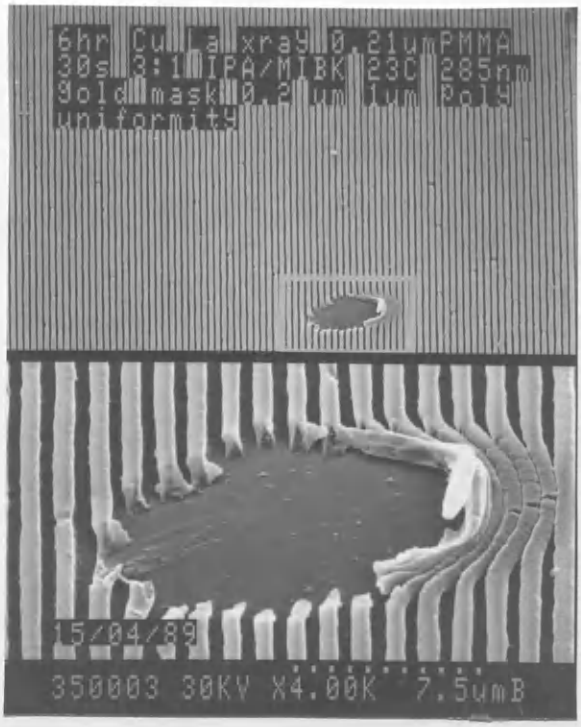

Figure 5.15. PMMA grating as in figure 5.14. The damage is shown to indicate the profile of the developed resist lines.

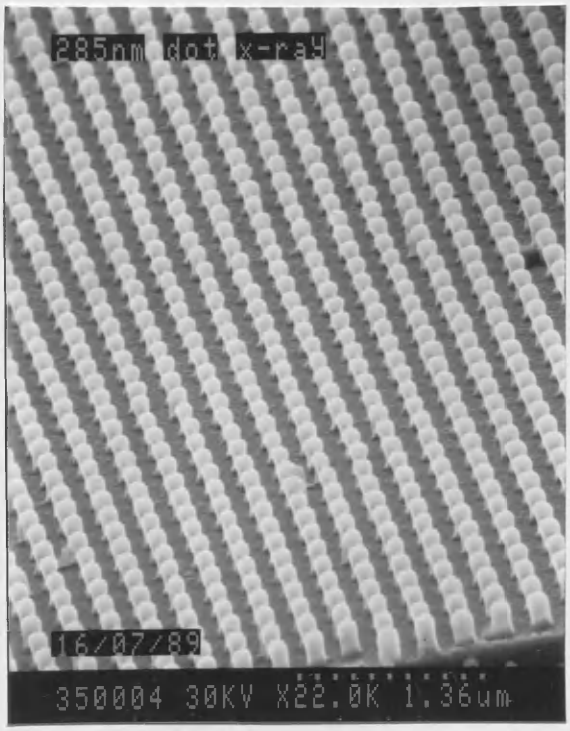

Figure 5.16. PMMA dot structures on Ti-coated glass. Two grating patterns (such as figure 5.14.) were exposed orthogonally to one another. Each exposure was 6 hours long. The development time was 15 seconds. All other parameters were the same as those in figures 5.14., 5.15. The dot array is uniform over a 5 x 5 mm area. The grating period was 285 nm and the dot width is ≈ 100 nm.

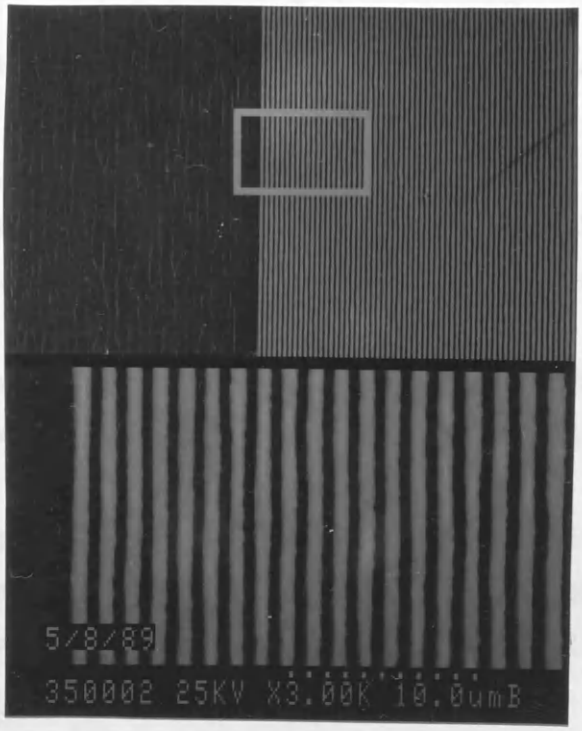

Figure 5.17. Gold grating x-ray mask. The picture shows the edge of a 500 μm wide region, 5 mm The grating period is 285 nm and the lines are 130 nm wide (± 10 nm).

grating samples and one double exposure with the gratings crossed at 90° to one another, figure 5.16.

This mask set had been damaged before use due to careless handling. An undamaged mask could certainly have been used further, however the repeatability of the system has been demonstrated.

Further experiments now need to be performed to determine any distortions induced by the printing process itself and in the mask making process (see the conclusion, Chapter 6).

The mask structure certainly appears to be stable, any differential thermal drift would have resulted in distortions in the dot structures of figure 5.16. Polyimide is a thermally resistant material, but any heating effects, due to radiation from the source, are minimised because the membrane is locked in intimate contact with a substrate that acts as a heat sink.

This technique produces very uniform structures, with vertical sidewalls over very large areas. The edge quality of the dots is very good over the 5 mm x 5 mm sample area. The walls are vertical and smooth. These structures are 0.2 nm high and of 90 nm side. These structures will shortly be utilised to make lateral surface superlattice devices.

Comparing the mark space ratio of the developed grating with that of the original mask, figure 5.17., it is evident that there is little significant shrinkage of the resist lines (< 5 %).

Chapter 6. Conclusions and Further Work.

Chapter Layout.

6.1. Summary

The work presented in this thesis covers a wide spectrum of topics concerned with the development of a lithographic system to print sub-micron gratings. Such structures are incorporated in integrated optical devices such as 1 st order Distributed Feedback (DFB) InGaAsP / InP semiconductor lasers and waveguide filters. The gratings were defined by holographic lithography and reproduced by x-ray contact printing.

Holographic lithography can be used to produce large area submicron gratings but its success depends upon the reflectivity of the substrate and the processing of the resist. X-ray lithography is conceptually a much simpler technology and has the advantage resist exposure is relatively insensitive to the substrate. The technique may provide a simple reliable route to high resolution (<100 nm linewidth) pattern replication with a potentially high throughput.

A two mirror symmetric interferometer arrangement was used to define the gratings. Collimating lenses were not used. A theoretical analysis of gaussian beam interference was used to predict the size of variations in period from the plane wave case.

Holographic gratings with periods down to 187 nm were exposed in AZ 1350 J photoresist with the UV lines of an argon ion laser.

Conventional thin resist holography was used to define thin resist (0.15 μm AZ 1350 J) patterns which were reactive ion etched (RIE) into GaAs wafers (360 nm period) using a CH_4: H_2 plasma.

Thick resist holographic and O_2 RIE techniques were developed to produce thick metal absorber patterns (0.3 μm high), lines and metal dot arrays, suitable for a high contrast (10:1) mask for x-ray contact printing. The metal dot arrays were produced by double holographic exposure of resist followed by angled metal evaporation (shadowing) along the lattice planes, O_2 RIE and lift-off processes.

The use of the metal patterns as masks for subsequent etching or diffusion (ion exchange in glass) into the underlying material was demonstrated.

The use of a spin - on anti reflection coating (ARC) under the resist was shown to eliminate coherent reflection effects inside the resist during holographic exposure.

Polyimide in solution was spun on to microscope coverslips and cured to form an x-ray mask substrate. Polyimide membrane masks are cheap to produce and can be conformed into intimate contact with the sample to be printed. After definition of the gold absorber pattern, a 0.3 μm polyimide layer is spun over the metal to protect it during the subsequent etching step and to provide extra strength. After attachment to metal rings the glass was dissolved away in hydrofluoric acid to produce free standing polyimide membranes 1.3 μm thick, 15 mm in diameter. The membranes are coated with a 60 nm layer of gold-palladium alloy, which is optically transparent, to form a conductive layer and to allow registration.

A soft x-ray contact printing system was designed and built to transfer the mask patterns into 0.2 μm thick PMMA (BDH) resist layers with copper L_α radiation [1.33 nm]. The x-ray source is an electron bombardment type; based on a VG - EG 2 electron evaporator gun. The anode is a copper hearth. A sample stage was designed to allow simple registration between sample and mask. Intimate contact between mask and sample which is necessary for high contrast pattern replication at 100 nm linewidths was achieved by an electrostatic hold-down mechanism.

285 nm period gold grating patterns were transferred into vertical walled resist patterns after 6 hour exposures at 300 W e-gun power with negligible resist shrinkage after development. The resist was developed in 1:3 mixture MIBK : IPA at 23°C for 30 seconds. Gratings were replicated on Si and Ti-coated glass substrates. The contact printing process is insensitive to the substrate material.

A two dimensional array of square PMMA dots of sub-100 nm side and 285 nm period, was produced on a chip (5 mm x 5 mm area) by a double x-ray exposure of a gold grating on a polyimide membrane.

The polyimide masks can be reused (at least five times in these experiments). Further studies of distortions in the mask and PMMA resist response to x-ray exposure remain to be done.

6.2. General conclusions and outlines for further work.

6.2.1. Holographic Lithography.

Holographic lithography is the only technique currently available for accurately defining sub-micron gratings over large areas (several cm^2). The necessary equipment is much cheaper than the investment required for an e-beam system which is the other method of writing submicron features. Although the length of grating that can be written by e-beam lithography is approaching the millimeter range, large area gratings require an unacceptably long writing time.

The standard holographic system is quite simple in terms of the number of components and cost; most items are available commercially and only the sample holder needs to be carefully designed. The configuration used in these experiments employed a beam splitter, two mirrors, two spatial filter units and a sample holder. Although a clean environment during sample exposure is not necessary, clean room facilities are essential for resist film preparation.

The success of the technique is dependent on several factors including the skill of the operator in setting the optics, the resist processing, the presence of vibration which increase the cost of the method for industrial production.

An advantage of holographic resist exposure is that its results can be rapidly assessed. In the system used in this work, development and grating inspection were done in the same area as exposure, enabling a rapid readjustment of parameters.

The holographic technique is very good at defining uniform gratings but cannot easily be adjusted to produce complex periodic structures such as a $\lambda / 4$ phase jump, which is required for some DFB laser applications, or gratings with chirps or curved lines. These structures have been made holographically; for example the phase jump was made by simultaneously exposing positive and negative resists [Utaka 1984], but the accuracy with which the phase jump was located was only to within 1 μm and the resist preparation was very complex. Such devices are better produced individually by e-beam lithography, see for example [Sekartedjo 1984]. Since complex grating structures were not the aim of this project the conventional holographic scheme was adopted.

Substrate reflectivity and its limitations for lift-off.

The effect of substrate reflectivity on the exposure and development of gratings is the greatest disadvantage of holographic lithography. In this work, following earlier work in this department, a prism, whose rear faces have been painted black to absorb reflections, was optically contacted to the back surface of a sample with matching oil. This method eliminates reflection problems in transparent substrates at low angles of incidence when the beams do not overlap the edges of the sample. At higher angles of incidence irregularities in the developed grating can be removed by masking the edges of a transparent sample; light can otherwise couple through the sides of a small sample.

The elimination of reflections on semiconductor substrates is a more difficult problem. gratings for DFB lasers or waveguide filters are defined on reflective III-V semiconductor substrates. Previously the gratings have been exposed in thin photoresist layers, whose depth was half the standing wave period (150 nm). These structures on their own are not suitable for the lift-off of thick metal layers, because they are usually not cut down to the substrate and they are extremely thin, but they can be ion beam milled or reactive ion etched into the surface (Chapter 4.).

Thick resist holography and O_2 RIE.

These problems were solved using the thick resist holography technique (Chapter 3.) Instead of trying to open a resist grating down to the substrate directly, the grating is defined at the surface of a thick resist layer (0.7 μm deep). The grating lines are opened down to the substrate by an oxygen plasma reactive ion etching process through a mask defining the grating which is produced by an angled evaporation of nichrome metal (shadowing).

Thick resist holography may be used in any thickness of resist on transparent substrates and in layers corresponding to (n + 0.5) P on semiconductor substrates (where n is an integer and P is the standing wave period). The etched grating has very high aspect ratio (7:1) lines 100 nm wide with vertical side walls enabling the lift-off of very thick metal layers (up to 0.3 μm in this work).

Apart from the increased metal thicknesses that can be lifted off, the thick resist technique has one other very important advantage: it allows an increase in processing latitude; it does not matter whether the resist under the developed grating is 0.68 μm or 0.62 μm thick if a 0.2 μm metal layer is to be lifted off from it.

The mark space ratio of the final grating can be determined by varying the shadowing angle to define the nichrome mask. A quantity F, the unmasked fraction of a grating period, and its effect on the etched grating have been studied as a function of shadowing angle for various grating profiles (Chapter 4 and Appendix 1.).

The addition of the shadowing and dry etching steps help to reduce demands on the development process. These demands are quite severe if thin resist layers are to be patterned; slight differences in exposure may make the difference between well developed resist lines cut to the substrate and lines that lift-off. Dumas [1985] made a study of thin resist exposure and development on grating profile, both on semiconductors and dielectric layers on semiconductors. The thick resist technique is much more forgiving.

The use of a commercially available spin on anti-reflection coating (ARC) in the form of a dyed polyimide has been used to improve the results of the thick resist holography technique further. The use of the ARC effectively eliminates the standing wave effect, dramatically increasing the process latitude for exposure on semiconductor substrates. The ARC is spun on and cured prior to resist application; for thin resist layers, it is developed away along with the exposed resist, for thick layers, it may be reactive ion etched at the same time as the resist in the oxygen plasma. The ARC has a similar grain size (~ 30 nm) to the resist and is hence compatible with resist processing to that resolution.

The removal of the unetched ARC is a potential problem which needs more investigation. In this work lift-off of the resist structures has been a two stage process; agitation in acetone to remove the resist and immersion in boiling acetophenone to dissolve the ARC. Even after this treatment there are sometimes traces of residue. Methods of ARC removal need to be studied further.

Apart from their application to x-ray masks, the high aspect ratio resist structures can be used themselves as a mask for further etching processes. The metal patterns can be used as masks for ion exchange techniques and ion beam milling to fabricate gratings on glass waveguides. In Chapter 4 the use of the resist structure to etch a quartz substrate has been described. The quartz substrates have been successfully used in studies of cell guidance along corrugated surfaces carried out in this department by Clark [1989].

The symmetric two mirror configuration.

The interferometric configuration used in this work followed that already used by Dumas [1985] in previous work done in this department. The beams in the interferometer undergo a lateral inversion, thus compounding phase errors on the original unsplit beam. Placing the spatial filters after the final mirrors minimises the problem at least for small area (~1 - 2 cm^2) gratings.

An important fact that has emerged form the theoretical analysis of grating fringe position in Chapter 2 is that the current arrangement produces an unacceptable period variation and phase shift over the whole grating area. This period variation is due to the difference in the radii of curvature of the two beams at the exposure plane. Previous work [Dumas 1985] had suggested that collimating lenses after the spatial filters would be unnecessary as long as the spatial filter - sample distances were large compared with the filter's objective lens's focal length (25 cm compared with 1.6 cm in this work). This assumption was invalidated only after the present work was completed. However, the effect is small for short length grating devices (Chapter 2) and irrelevant for the demonstration of the x-ray mask fabrication and contact printing. In further work collimating lenses will need to be incorporated to make higher quality gratings and larger area patterns (several cms in diameter).

Grating period.

The production of uniform gratings at much higher incidence angles has been successfully achieved. Previously, periods of sub-200 nm have been fabricated optically using front prism techniques or achromatic holographic lithography [Anderson 1988a.]. A grating of period 187 nm was achieved by directly exposing resist at 70° incidence with 351.1 nm radiation: a much higher angle of incidence than was thought possible (50°). The use of an ARC coating under the resist should simplify this type of exposure further by reducing reflection problems at these incidence angles.

To fabricate first order DFB devices in GaAs / AlGaAs, smaller grating periods are required (110 nm - 120 nm). The production of such fine structures is very difficult since complex optical systems are required and their dimensions are approaching the resolution limits of the resist (30 nm for photoresists). The simplest method to reach such dimensions is the front prism technique. Its success depends on the optical uniformity of the prism glass, and the control of the gap between the prism and resist surface which determines the degree of evanescent coupling into the resist. A lanthanum crown glass prism (LAC A691547 (Pilkington), figures 6.1., 6.2.) has been made for front prism experiments (30° half angle). This material has a high transmission in the UV (> 80°

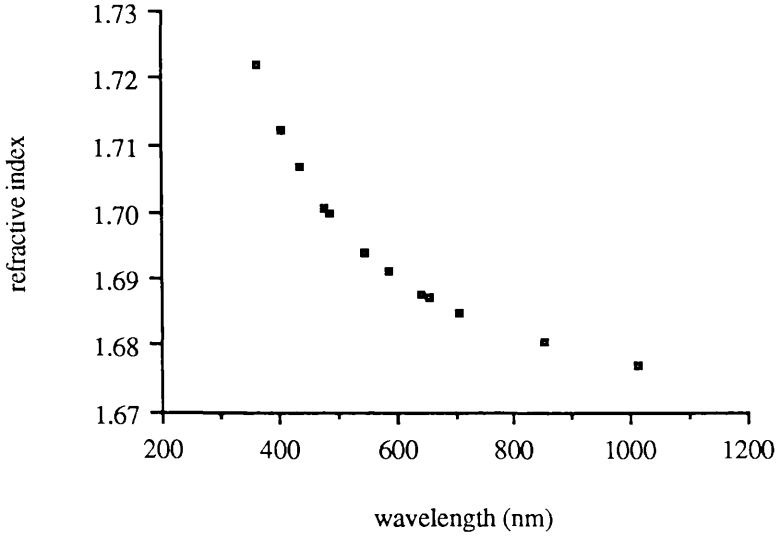

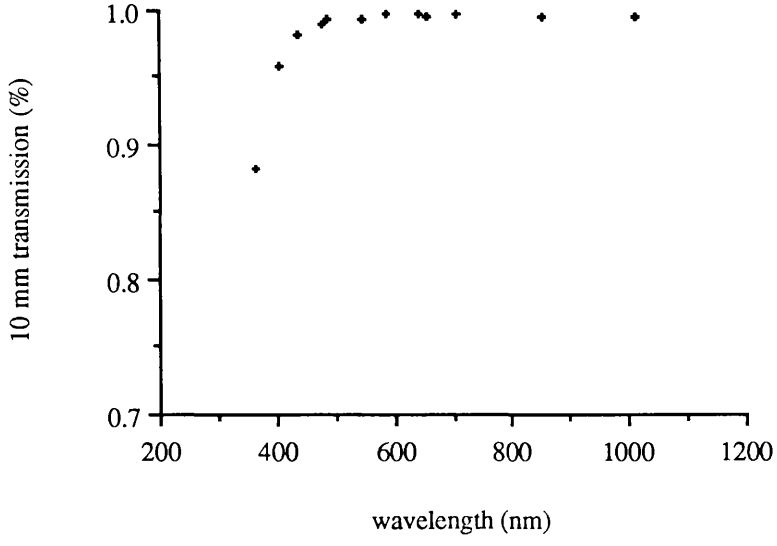

Figure 6.1. Refractive index and transmission for a 10 mm thickness of LAC A691547 Lanthanum Crown glass.

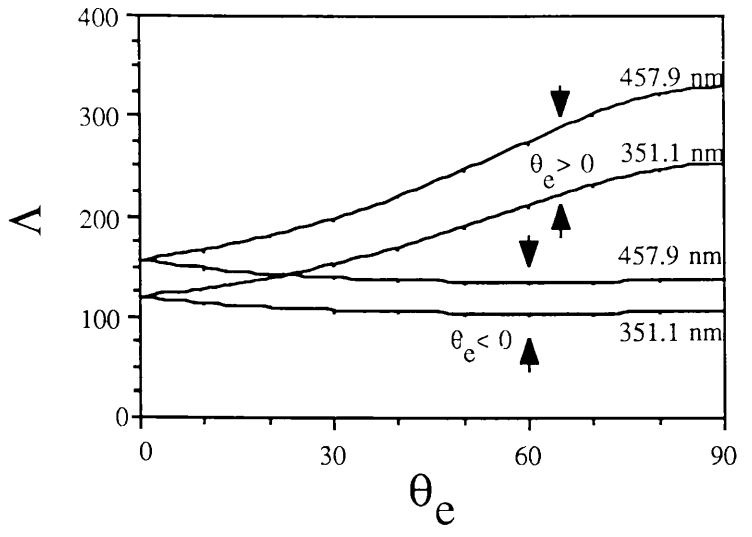

Figure 6.2. Front prism technique. Lanthanum crown glass prism (LAC A691547), 30° half angle. The figure shows the grating period against external angle of incidence (both positive and negative values) for the two argon laser exposure wavelengths.

The prism index is 1.705, 1.726 at 457.9 nm, 351.1 nm respectively.

for 10 mm) and a high refractive index: n = 1.705 (457.9 nm), n = 1.725 (351.1 nm). A high refractive index matching oil (n = 1.7) and ARC coated samples will be used try and make 110 nm period gratings (figure 6.2.) The effort involved is justified if the gratings can be used to make x-ray masks.

The achromatic holographic scheme incorporates two gratings arranged parallel and closely spaced as the beam splitting and reflective elements. The splitter and recombining gratings have the same period. First order diffracted radiation from the splitter grating is further diffracted by the recombiner grating. Zero order radiation is blocked. The second order beams overlap and have twice the spatial frequency of the parent gratings, independent of the exposure wavelength (as long as it is smaller than the period so that diffraction is possible). 125 nm period gratings have been produced in this way from two 250 nm gratings etched into fused silica. The source was a short coherence length ArF excimer laser operating at 193 nm. The grating was recorded in PMMA resist which has a higher resolution than photoresist but is only sensitive to radiation below 200 nm wavelength. The determining factors of this system is the optical quality of the silica flats used to make the parent gratings, their registration to one another and the optical quality of the original holographic gratings used to define them. These original gratings obviously have to be large (several cm) to produce a reasonable area of the fine period grating.(several mm), since the diffraction angles are large.

If the front prism technique does not prove successful achromatic holography may provide an answer, if technologically difficult. Larger more uniform gratings would be required than are used at the moment to generate the parent masks. This means the redesign of the sample stage and probably the incorporation of a feedback mechanism to reduce vibration problems emphasised by longer exposure times (up to 30 minutes).

A more sophisticated measure of grating uniformity is needed; such a system could also be used to monitor distortions in the x-ray masks. A possible interferometric technique could be the following [Flanders 1978c]: the finished grating or x-ray mask pattern is reinstalled at the exposure site of the interferometer and interference between the transmitted and diffracted beams is analysed. Wavefront uniformity could be examined using a shearing interferometer arrangement [Yi-Yan 1978].

6.2.2. X-ray contact printing.

A low cost x-ray contact printing system has been constructed around a commercially available electron bombardment x-ray source. An x-ray mask technology based on polyimide membranes has also been developed. A sample holder has been designed to accommodate 5 mm x 5 mm chips and the membrane mask in intimate contact using an electrostatic chucking mechanism.

This system has been used successfully to replicate 285 nm period structures (gratings and dots) in 0.2 μm layers of BDH PMMA resist. Although exposure times are long (6 hrs) because the power transferred from the water cooled copper target (~10^{-5} W cm^{-2} at the resist surface) is small compared with the power dissipated in the target by the electron beam (300 W), the system appears stable over the long exposure times with negligible pattern distortion. Since x-ray contact printing is a parallel process these exposure times are acceptable compared with the time needed to pattern the 0.3 billion resist dots produced over a 5 mm side chip by e-beam techniques.

Much work remains to be done to characterise the present system: for example a study of resist response needs to be done. The exposure time of 6 hrs was a good estimate at the power level used in these experiments and shorter exposures (2 hrs) were unsuccessful. The well discussed insensitivity to resist exposure and development parameters of x-ray lithography (above a critical dose) has yet to be examined here. Current resist response is estimated from data derived from e-beam work carried out in the department.

Other resist schemes could also be tried; at the time of writing the availability of some experimental novolak based resist material [Dössel 1986] which has a sensitivity of 50 mJ cm^{-2} (compared with 1000 mJ cm^{-2} for PMMA) is being investigated.

Polyimide membrane masks are quite rugged and can be reused several times. The induced distortion present in the mask due to internal stresses and the presence of the absorber are yet to be determined in detail. This is the most important task for the future: at present devices can be made to a sufficient accuracy but more information is needed - this is not a trivial task since there are whole groups of people in the US (IBM) and in West Germany and Japan working on mask technology, its associated reliability and distortion characterisation.

Many improvements could be made to the present system; for example the current design of the sample holder only allows samples smaller that the mask diameter to be replicated. Simple

modifications will be made to allow daughter masks to be replicated from the holographically defined master mask.

Smith [1989] is suggesting the use of amorphous SiN membrane masks 1 μm thick as x-ray masks. The material can be made strong enough to hold a 1 atmosphere pressure differential across a 4 cm diameter, 1 μm thick. There should be little problem with degradation of the material under irradiation since the power densities used in electron bombardment systems is much lower by several orders of magnitude than those used to expose resist rapidly (seconds) in synchrotrons, where this problem occurs. This material can be made in this department and the possibilities are worth investigating.

A very recent discussion[1] [Smith 1989] concerning the mechanism of resist exposure has very important implications for x-ray contact printing as described in this work. Smith's group at MIT have succeeded in replicating 30 nm lines in PMMA from a 30 nm wide Au structure formed by etching a silicon wafer to produce a vertical edge, spinning polyimide solution, curing it and etching away the Si, and defining the Au absorber on the polyimide membrane by an angled metal evaporation. The resist structures were printed using C K_{α}, Cu L_{α}, and Al K_{α} radiation. These new results indicate that estimates on the limitation of resolution due to secondary electron range are very wide of the mark. The implications are obvious and exciting: the shorter wavelengths allow the use of a gap of several microns between mask and sample so that damage to the mask due to intimate contact should be eliminated and more sophisticated registration systems can be designed.

The copper x-ray thus represents the optimum wavelength for high resolution replication down to 30 nm linewidths (at least) compared with <100 nm as was previously thought since good mask contrast can still be maintained at this wavelength.

The suggested mechanism [Smith 1989] is that in low Z materials, such as C based resists the excited atoms decay predominantly via the Auger effect which results in showers of low energy electrons which have an estimated range of only 5 nm compared to the photoelectron range in Cu of 50 nm!

[1]The discussion was held after the this thesis was complete.

Appendices.

1. Reflection coefficient from a conductor.

2. Changing the optics on the Argon Ion laser.

3. Calculation of F for a sinusoidal profile grating.

4. The X-ray contact printer: Operation procedure.

5. Application to a double ion exchanged Bragg waveguide filter.

1. Reflection Coefficient from a Conductor.

At a dielectric conductor boundary, Snell's law becomes complex because the conductor has a complex refractive index, $\boldsymbol{n}_2 = n_2 - j\,k_2$

The reflection coefficient (s polarisation), is:

$$\boldsymbol{r} = \frac{n_1 \cos\theta_1 - \boldsymbol{n}_2 \cos\theta_2}{n_1 \cos\theta_1 + \boldsymbol{n}_2 \cos\theta_2} \qquad \text{(A1.1.)}$$

and

$$\boldsymbol{n}_2 \cos\theta_2 = \sqrt{\boldsymbol{n}_2^2 - n_1^2 \sin^2\theta_1} = \alpha - j\beta \qquad \text{(A1.2.)}$$

where $$\alpha^2 - \beta^2 = n_2^2 - k_2^2 - n_1^2 \sin^2\theta_1 \qquad \text{(A1.3.a)}$$

$$\alpha.\beta = n_2 k_2 \qquad \text{(A1.3b)}$$

solving for α^2 (there is only one positive solution):

$$\alpha^2 = \frac{1}{2}\left[n_2^2 - k_2^2 - n_1^2 \sin^2\theta_1 + \sqrt{(n_2^2 - k_2^2 - n_1^2 \sin^2\theta_1)^2 + 4 n_2^2 k_2^2} \right]$$

and

$$\beta^2 = n_2^2 k_2^2 / \alpha^2 \qquad \text{(A1.4.)}$$

finally we obtain:

$$\boldsymbol{r} = \frac{n_1 \cos\theta_1 - \alpha + j\beta}{n_1 \cos\theta_1 + \alpha - j\beta}$$

$$\boldsymbol{r} = \sqrt{\frac{\beta^2 + (n_1 \cos\theta_1 - \alpha)^2}{\beta^2 + (n_1 \cos\theta_1 + \alpha)^2}} \exp\left\{ j \tan^{-1}\left[\frac{2\beta\, n_1 \cos\theta_1}{n_1^2 \cos^2\theta_1 - \alpha^2 - \beta^2} \right] \right\} \qquad \text{(A1.5.)}$$

which is of the form

$$\boldsymbol{r} = |r| \exp\{j\phi\} \qquad \text{(A1.6.)}$$

The complex refractive index introduces a phase shift ϕ between 0 and π radians into the reflectivity.

In the case of a pure dielectric which has $n_2 > n_1$, $\boldsymbol{r}$ is real and negative implying a phase change of π. The phase shift is zero when $n_2 < n_1$. Values of ϕ were calculated for 356.2 nm period gratings on different materials (Table A1.). The phase shifts determine the position of the nodes of the standing wave pattern (Section 2.2.).

Example: Reflection Coefficient of Silicon.

At 457.9 nm Si has a refractive index of 4.575 - j 0.1305. To produce a 356.2 nm period grating at 457.9 nm exposure wavelength, θ_1 (in the resist) is 22.9° and n_1 is 1.665. If Si were a pure dielectric, i.e. if $k_2 = 0$, $\boldsymbol{r}$ would be - 0.494, i.e. r = 0.49, $\phi = \pi$. Including the complex part of $\boldsymbol{n}_2$, $\boldsymbol{r} = 0.494\ e^{j\,0.98\,\pi}$. The complex index gives the same result for $\boldsymbol{r}$ as in the dielectric case with a slight reduction in phase from π because $k_2 < n_2$.

Table A1.

Reflection coefficients of some materials ($n_1 = 1.665$, $\theta_1 = 22.9°$)

Material	λ	n_2	k_2	α	β	r	$\phi\ (.\pi^c)$
Silicon[1]	457.9 nm	4.575	0.131	4.530	0.132	0.494	0.98
Nickel	457.9 nm	1.638	2.702	1.624	2.725	0.428	0.74
Germanium	457.9 nm	4.077	2.235	4.037	2.257	0.315	0.89
Gallium Arsenide	457.9 nm	4.711	0.712	4.667	0.718	0.266	0.96

[1] n and k values are interpolated from data presented in E. Palik (Ed.) 'Handbook of Optical Constants of Solids.' Academic Press, 1985.

2. Changing the optics on the Argon Ion laser.

This section relates to the Spectraphysics model 165 argon ion laser used in these experiments.

There are three sets of optics for the argon ion laser:

(i.) for broadband operation in the visible, (all eight lines),

(ii.) for discrete wavelength operation in the visible,

(iii.) for broadband operation in the ultra violet[2].

Discrete operation in the visible, (457.9 nm), is the most usual configuration used to make holographic gratings.

(1.) Wavelength selection in the visible.

Front mirror: broadband output coupler (o/c)

Rear mirror: prism assembly.

To adjust the wavelength, remove the top covers. On the top of the rear mirror assembly there are two thumb-wheel controls marked **HORIZONTAL** and **VERTICAL**, which change the orientation of the rear mirror. In routine operation these controls are gently tuned to produce the maximum output power on a given line.

The vertical control is turned anticlockwise, looking towards the front of the laser, to select the lower wavelength lines. This control selects any of the nine lines which oscillate between 454.5 nm and 514.5 nm. At low tube pressures the blue lines, and the ultraviolet lines have more gain; for instance the 454.5 nm line, which is not quoted as available in the manual, may have as much as half the power of the 457.9 nm line.

The brightest line is 488.0 nm (1.3 W cw). The ghost of this line can be seen at an adjacent position to the main line on the thumb-wheel control. Great care must be taken if scanning

[2] The UV lines are dispersed outside the cavity in the horizontal plane by a Schlieren grade fused silica prism. [Spectraphysics Catalogue Number G0044-000 'Brewster Angle Prism' angles: 55 30', 55 30', 69; faces: flat to l / 20] The line to be used is selected by an aperture (extra-cavity).

through this line or observing the all lines, i.e. broadband output. The laser produces 4 W on all lines and even observing the diffuse scattering of this beam on a low reflectivity object can cause irreparable damage to the eyes. Laser safety goggles should be worn at all times. If the bellows assemblies that shield the optical paths between the mirrors and the plasma tube are removed, care must be taken to block a strong reflection from the top of the plasma tube at the rear Brewster angle window. If adjustments are to be made to the rear mirror, the top of the plasma tube should be covered by a card to block this reflection.

(2.) Broadband operation in the visible.

Mirrors: broadband o/c, rear reflector.

The o/c has a radius of curvature of 1.05 m and the rear reflector is planar .

The laser must be tuned to maximum power on all lines in the visible before changing to all lines operation in the UV where the gain is weak.

The prism assembly is removed and replaced by the broadband rear reflector. Lasing will not be seen. Remove the connecting bellows assemblies and detune the coarse vertical thumb-wheel control at the side of the rear mirror assembly; this is normally covered. The mirror is scanned vertically by rocking the rear mirror assembly back and forth while scanning the horizontal thumb-wheel control clockwise (from the position used with the prism) until lasing is obtained. Retune the coarse vertical control until lasing is obtained in that direction also. The output can now be tuned using the top thumb-wheels.

(3.) Broadband operation in the UV.

UV o/c, UV reflector.

The laser cavity is 'walked' to optimise the power output on all lines (visible) operation.

The optical axis, which is defined by the orientation of both cavity reflectors, is altered by adjusting the mirrors sequentially until it corresponds to the line of maximum gain. This is done as follows:

The horizontal and vertical controls on the o/c assembly are reached by screwdrivers through holes in the front panel of the laser. The horizontal controls are altered to walk the beam horizontally and then after optimisation, the vertical controls are optimised. To walk the beam in the horizontal direction, the front horizontal control is detuned slightly and then the rear control is retuned. If the new output power is larger than before, the process is continued until a maximum power is reached. If the power is less than it was before, the front horizontal control is detuned in the opposite sense until a maximum is reached. The same procedure is then applied to the vertical controls.

If the cavity has been correctly optimised, the replacement of the visible broadband optics with the UV broadband optics should result in lasing in the UV. The output can be tuned as before using the thumb-wheel controls. The output beam can be observed by placing a white flourescent card in the way of the beam; the laser output is seen as a bright blue white spot 2 mm or so in diameter.

If lasing is not seen, the mirrors may still be slightly detuned so a similar procedure is used to scan the vertical and horizontal rear mirror controls as above.

3. Calculation of *F* for a sinusoidal profile grating.

The grating profile can be described as

$$y = y_0 + y_1 \cos\frac{2\pi x}{\Lambda} \qquad \text{(A3.1.)}$$

where y_1 is the perturbation amplitude on the flat resist layer of thickness y_0. The other symbols have their usual meanings. The region between A and B of figure A1. will be in the shadow of metal atoms incident on the grating at angle θ. At A the paths of the incident atoms are tangential to the grating surface.

Comparing the gradient of (A3.1.) with cot θ we obtain an expression for x_A:

$$x_A = \frac{\Lambda}{2\pi}\left(2\pi - \sin^{-1}\left[\frac{\Lambda}{2\pi\, y_1 \tan\theta}\right]\right) \qquad \text{(A3.2.)}$$

y_A is obtained from (A3.1.) Hence the line AB can be written as

$$y = x\cot\theta + \left(y_A - x_A\cot\theta\right) \qquad \text{(A3.3.)}$$

where the bracketed term is the y axis intercept.

The coordinates of point B are determined from the solution of:

$$x_B\cot\theta + (y_A - x_A\cot\theta) = y_1\cos\frac{2\pi x_B}{\Lambda} \qquad \text{(A3.4.)}$$

and equation (A3.1.). Equation (A3.4.) is a transcendental equation for x_B. Solutions were found using a Newton - Raphson iteration.

F is obtained from:

$$F = \frac{x_A - x_B}{\Lambda} \qquad \text{(A3.5.)}$$

Values of *F* for various angles of incidence are given in table A2. and figure 4.13.(b).

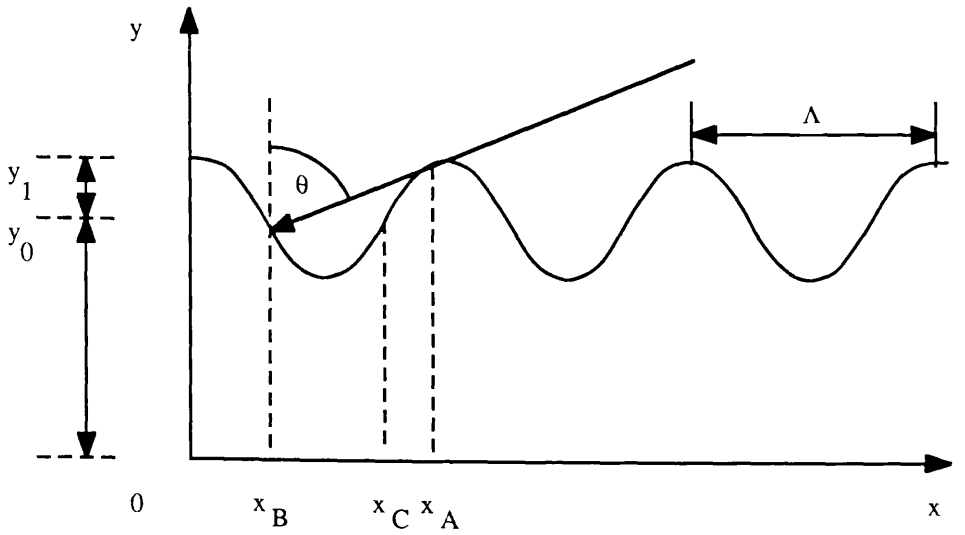

Figure A1. Calculation of F for a sinusoidal grating: $y = y_0 + y_1 \cos \frac{2\pi x}{\Lambda}$

$$F = \frac{x_A - x_B}{\Lambda}$$

The method assumes that the evaporated layer is infinitely thin. In practice, metal grows out over the shadowed part of the grating to a depth approximately equal to the thickness of the metal layer (~ 20 nm), thus decreasing F slightly.

$F = 0$ when the gradient of AB equals the gradient of the sinusoid at point C; $x_C = 3\,\Lambda / 4$. At C the rate of change of the gradient goes to zero. The minimum angle at which shadowing starts to occur is given by:

$$\cot\theta_{min} = \frac{2\pi\, y_1}{\Lambda} \qquad \text{(A3.6.)}$$

Defining the aspect ratio as $4\, y_1 / \Lambda$; the ratio of the peak to peak height over a half period, equation (A3.6.) predicts $\theta_{min} = 17.7°$ for a 2:1 aspect ratio grating ($y_1 = \Lambda / 2$).

Table A2.

Example: calculation of F for a 2:1 aspect ratio grating (put $\Lambda = 1$).

θ°	x_A	y_A	equation of AB	x_B	F
20.0	0.83	0.24	y = 2.75 x - 2.04	0.58	0.25
30.0	0.91	0.42	y = 1.73 x - 1.16	0.42	0.49
40.0	0.94	0.46	y = 1.19 x - 0.66	0.34	0.60
50.0	0.96	0.48	y = 0.84 x - 0.33	0.28	0.68
60.0	0.97	0.49	y = 0.58 x - 0.07	0.23	0.74
70.0	0.98	0.49(6)	y = 0.36 x + 0.14	0.18	0.80
80.0	0.99	0.49(9)	y = 0.18 x + 0.32	0.13	0.86

4. The X-ray contact printer: Operation procedure.

Sample Exchange.

The contact printer has an exposure chamber which is held under high vacuum (10^{-6} mbar) at all times except for specimen exchange. The chamber houses electron gun x-ray source, the support structure for the sample holder and the electrical connections to the deflector electrode and the electrostatic chucking leads, figure 5.1. The sample holder is supported upside down over the source. The chamber is pumped by an ion pump, backed by a sorption pump, and roughed out by a rotary pump. There is an observation window directly over the electron gun.

Before opening the exposure chamber the ion and sorption pumps must be isolated by closing the ion pump gate valve, (this is closed when the lever is in its lowest position) and the sorption pump isolation valve, underneath the chamber. The Penning gauge should be switched off.

Open the roughing line isolation valve. Switch off the rotary pump and open the roughing valve. Open the air admittance valve; this lets air into the roughing line. Do not open the dry nitrogen inlet valve. Filling the chamber with dry nitrogen causes an overpressure which can rupture the membrane mask. The valve seating is weak and prone to leaks.

Lift off the exposure chamber lid at **AA**, taking care not to let the o-ring drop out. The sample holder rests on the aluminium spacer.

Remove the sample holder from the chamber, taking care to avoid touching the screw contact to the sample electrode which protrudes from the bottom of the sample holder. Do not disconnect the two PTFE coated wires from the sample holder. Handle the wires carefully as they can be easily pulled away from the vacuum feed-through.

The sample holder is carefully put down onto its annular support. The chip and membrane mask can now be loaded. Once the sample and mask have been registered, the chucking voltage (50 V) is applied. The power supply for the chucking field is mounted on the e-gun supply cabinet and is joined to the contact printer via a coax cable. The membrane may not immediately deform under the field. It may be necessary to press the mask gently onto the chip using a cotton bud.

The sample holder is inverted and reloaded onto the heat shield ring, avoiding touching the protruding sample electrode; movement of this spring loaded electrode would rip the membrane mask. The exposure chamber lid is replaced, taking care not to trap its o-ring seal or the PTFE wires. The air admittance valve, and the roughing line valve, are closed and the rotary pump switched on. The roughing line isolation valve is opened and the chamber is pumped out by the rotary pump. The roughing line pressure is measured by a Pirani head situated just before the chamber admittance valve. The chamber pressure is monitored by a Penning Gauge. This gauge should not be used at pressures greater than 10^{-2} mbar.

Fill the cold trap of the sorption pump with liquid nitrogen and wait 15 minutes for the pump to cool down. When the chamber pressure has fallen below 5 x 10^{-3} mbar, close the roughing line isolation valve, and switch on the Penning gauge. The rotary pump can now be switched off. Open the sorption pump isolation valve. If the sorption pump has not been used for a long time, it should be roughed out along with the specimen chamber. Wait until the pressure in the chamber falls onto the 10^{-5} mbar range. Slowly open the ion pump gate valve. The ion pump HT will fall to about 3 kV slowly recovering to 5 kV as the pressure decreases.

Loading mask and sample.

A 5 x 5 mm chip is the maximum size that can be comfortably exposed in the system.

There must be a good electrical contact between the chip and the sample electrode for electrostatic chucking to work. Electrostatic chucking is capacitative; its efficiency increasing with decreasing plate separation. The applied pd (50 V) is not large enough to produce chucking over both the membrane and the chip. If the chip is not conductive a metal layer [e.g. gold palladium] should be evaporated onto it.

The chip is fixed to the sample electrode with conductive silver dag paint.

Screw the phosphorus (p-) bronze mask insert into the stainless steel support sleeve, until the membrane is about 20 μm above the chip surface. Very great care must be taken. The mask is easily ripped. Several points of contact with the chip will be visible, probably at one chip edge. The sample surface and polymer membrane should only just be touching; they will not be completely parallel.

A small two pronged tool has been made to key into the bronze mask inserts. The stainless steel sleeve has 40 divisions marked on it. The screw thread has a pitch of 40 tpi. Rotating the mask insert through one of these divisions raises or lowers the mask with respect to the sample by about 16 μm.

Line up the mask and sample by eye. Clamp the stainless steel ring down onto the sample holder using the three small screw clamps. Apply the chucking voltage.

E-gun operation.

The x-ray source is a modified VG EG-2 e-gun design. The gun is already focused. It is connected with the power supply cabinet via an umbilical cable.

Before operation check that:

1. There is an adequate water supply to the e-gun (it is plumbed into the cold water main).

2. The earth lead is making a good connection between the chamber and the water pipes.

The VG manual gives a more detailed description of the gun and its maintenance, but some routine information will be given here.

Make sure that the back door of the e-gun power supply cabinet is securely shut; there is an interlock switch at the bottom of the door to prevent it being opened during operation.

Switch on the mains power.

Turn the HT potentiometer to zero (fully anticlockwise-a small click can be heard).

Select [HT **on**, filament **off**] on the multi selector switch.

Turn the evaporate / outgas switch to [**outgas**].

Press the green button [**HT on**] and slowly increase the HT on the potentiometer to 2 kV. Some sparking may occur but there shouldn't be any steady emission current. If the unit trips out, return the potentiometer to zero and try again. This tests the breakdown voltage across the ceramic insulators separating the filament from the gun cage.

Press the red [**HT-off**] button and return the HT potentiometer to zero.

Turn the evaporate / outgas switch to [**evaporate**].

Press the green button [**HT on**] and slowly increase the HT on the potentiometer to 10 kV (fsd). The unit should sit at this voltage for a few seconds. If the unit trips below 5 kV, the e-gun may require cleaning. The breakdown voltage may increase with successive tests - a process called high voltage conditioning. The gun can be operated satisfactorily, if the unit can sit at 8 kV. This tests the breakdown voltage across the ceramic support rods.

Press the red [**HT-off**] button and return the HT potentiometer to zero.

Check to see that the trip circuitry is working.

Turn the multi selector switch to [**start**] and the outgas / evaporate switch to [**outgas**].

Turn the HT potentiometer to zero and press the [**HT on**] button. Increase the HT to 1 kV quite rapidly. The emission current will rise to 30 or 40 mA and then become limited to 10mA. The machine will trip out if the 1 kV value is not reached within 10 seconds of pressing [**HT on**].

Look to see that the filament is on. At this point the pressure will rise quite dramatically as the filament and gun housing outgases. If the pressure approaches 10^{-4} mbar the ion pump should be isolated and the green [**HT off**] button pressed to cut the power to the e-gun. This procedure needs to be repeated several times before the pressure becomes stable.

Press the red [**HT-off**] button and return the HT potentiometer to zero.

Turn the outgas / evaporate switch to [**evaporate**] and press [**HT on**].

Increase the HT smoothly to 6 kV. The pressure will rise again. Turn the multiselector switch to 25 and then 50 mA emission current. The ion pump HT will drop to below 2 kV. It should slowly recover over half an hour to 4.5 kV. As long as the sorption pump is kept topped up with liquid nitrogen, the vacuum pumps should be able to hold the gas load. The system should be checked every 15 minutes or so in case the pressure becomes too high or a flash-over occurs which will trip out the gun power supply. If the pressure does rise unacceptably the gun may be switched off and the ion pump isolated until it recovers. The exposure chamber should stabilise at a pressure of the order of 10^{-6} mbar.

After the exposure is complete. The [**HT off**] button is pressed and the HT potentiometer returned to zero. The contact printer is left to cool down under vacuum before the chamber is opened again. The ion pump will slowly take over the gas load from the sorption pump as that pump slowly heats up to room temperature.

Note 1. The ion pump.

The pump is a Varian model [911 5034 448 / T] and has a pumping speed of 60 litres per minute. The ion pump power supply is located on top of the VG e-gun power supply cabinet. The supply has a power switch and combined ion pump **pressure / current / kV** gauge. The pressure gauge is inaccurate except at very low pressure. The meter range is usually set to [**kV**].

The potential difference maintained across the ion pump's titanium elements depends on the amount of gas in the chamber; the pd increasing as the pressure decreases. The limit is about 5 kV corresponding to a chamber pressure of 10^{-6} mbar. The pd should never be allowed to fall below about 1.5 kV. This pd corresponds to a pressure around 10^{-4} mbar. Above this pressure a plasma forms which sputters the titanium electrodes. If the pressure increases further the elements start to burn and become corroded. There is a trip circuit in the ion pump power supply to avoid this but it should not be relied upon. If the ion pump is going to be exposed to atmospheric pressure for maintenance, the power supply should be switched off before the chamber is let up to air. If the pressure in the chamber does accidentally rise, the pump will recover, if it is then isolated and left to pump itself.

CAUTION: NEVER REMOVE THE ION PUMP POWER LEADS OR THE EARTHING STRIP WHILE THE PUMP IS OPERATING.

Note 2. The sorption pump.

Before opening the exposure chamber the sorption pump is normally inert and is pumped by the ion pump through the chamber. The pump contains zeolite granules which adsorb gas molecules when the pump is cooled to liquid nitrogen temperatures. Periodically the pump needs to be baked out to remove the accumulated gas molecules which gradually reduce the pumping efficiency. The pump can be used in the 10^{-1} to 10^{-6} mbar range, but it will pump faster at lower starting pressures around 5×10^{-2} mbar.

5. Application to a double ion exchanged Bragg waveguide filter.

Although optical devices that incorporate gratings have been frequently referred to in this thesis no such devices have been analysed here in detail. As mentioned in the introduction, the original aim of this project was to use an already operational x-ray contact printer to replicate grating patterns for first order DFB lasers[3] in the InGaAsP / InP semiconductor system. In the event, the x-ray system required extensive work to make it operational: the machine had to be rebuilt and the mask and sample technology had to be developed. Then it became obvious half way through the project that the InGaAsP material would not be available for this work.

Semiconductor material (GaAs / AlGaAs) is now available in this department grown by in - house Molecular Beam Epitaxy, so that the techniques developed in this work will soon be applied to real optical devices.

As an example of a DFB system, some work has been done towards the fabrication of a simple DFB type device in the form of a glass waveguide filter whose reflection bandwidth is centred at the 860 nm wavelength. The fabrication process will be described although the reflection measurements have not yet been done. A brief description of Bragg reflection is also given.

Both the waveguide and grating are defined using a potassium - sodium ion exchange (interdiffusion) process which takes place at the surface of a soda lime glass microscope slide immersed in a solution of KNO_3 at temperatures above 350°C.[4] The slab waveguides are

---

[3]The advantage of DFB structures is that they may (potentially) be integrated into an optical waveguiding chip. Conventional semiconductor lasers use cleaved end facets to provide optical feedback. Such structures are incompatible with optical device integration.

[4] Ion exchange processes [Findakly 1985] have been used to make inhomogeneous waveguides in glasses for several years. Sodium ions present in soda lime and borosilicate glasses are known for their high mobility and exchange well with monovalent alkali ions from an alkali salt melt. Ag^+, K^+ have a higher electronic polarisability than the Na^+ ions in the glass so that exchange results in an increased refractive index. The index change in Ag^+ - Na^+ ion exchange [Walker 1983 a, b.] is quite high (~0.09) even for interdiffussion at low temperatures (<300°C) leading to the production of strongly multimode guides in a few hours. The guides tend to be quite lossy (a few dB / cm) due to high silver concentration in the waveguides.

The K^+ - Na^+ ion exchange process [Pinak 1982, Yip 1985, Albert 1985] is slower than the above and results in a smaller refractive index change (~0.006 - 0.009). This technique is applicable to the formation of single mode optical waveguides. The waveguide losses are lower, typically ≤ 0.2 dB cm^{-1}.

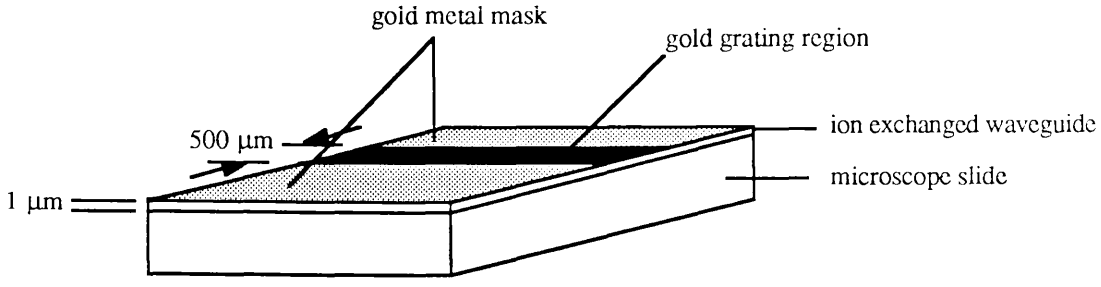

Figure A2.(a.) Glass waveguide Bragg filter. The sample has a slab waveguide defined at its surface by Potassium-Sodium ion exchange. A gold grating mask (285 nm period) is defined as in Chapters 3, 4. A 500 μm long grating region is defined with a photomask. Outside this region, the guide is completely masked with gold metal. After the second ion exchange, the gold metal is removed with Gold etch and HCl acid.

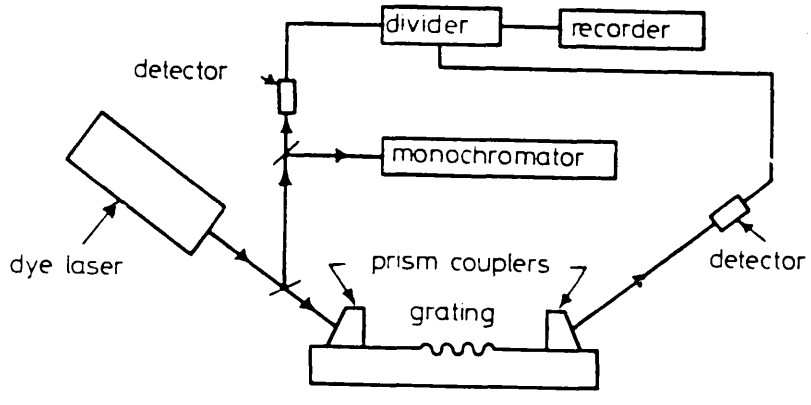

Figure A2.(b.) Schematic diagram of experimental equipment used in the evaluation of filter response (taken from [Yi-Yan 1980]).

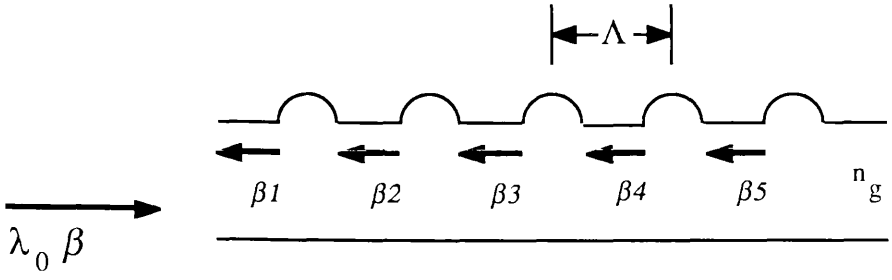

Figure A3. A wavefront of wavevector β ($= 2.\pi.n_g / \lambda_0$) in a waveguide is progressively scattered by the periodic perturbation. The local reflections $\beta 1$, $\beta 2$ etc. combine coherently to produce a large reflection in the $-\beta$ direction when the Bragg condition is met:

$\Lambda = \lambda_0 / 2.n_g$ or $2.\beta = \mathbf{G}$

where **G** is the grating vector in a direction parallel to β and $|\mathbf{G}| = 2.\pi. / \Lambda$.

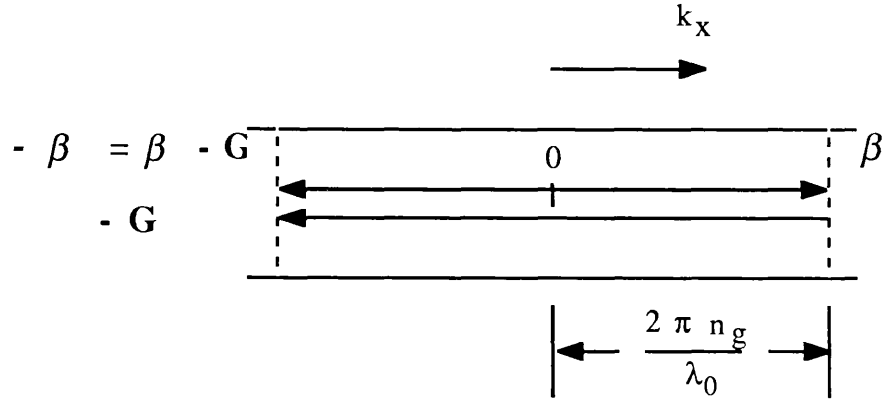

Figure A4. Wavevector diagram for Bragg reflection from a first order grating: $|\mathbf{G}| = 2\,|\beta|$. n_g is the guide effective index.

monomode of 2 - 3 μm depth and are exchanged for 1 hour at 374°C. To satisfy the Bragg condition at first order , see below, for 860 nm radiation in a medium of refractive index 1.51, the grating period must be 285 nm. This type of device has not been made before at such a fine period, using a double ion exchange process: i.e. an ion exchange to define a slab waveguide followed by the deposition of a metal grating mask for a second ion exchange step[5]. The metal grating mask is defined by the methods of Chapter 4, and the sample ion exchanged at 374°C for a further 20 minutes. The grating region is 500 μm long, figure A2. After ion exchange the gold metal mask is removed by chemical etching in Gold etch (a saturated solution of iodine in potassium iodide) followed by immersion in HCl to remove the nichrome adhesion layer. The exchanged grating is weak, measured diffraction efficiencies (outside the guide) are only 4 - 5 % of the values for a developed photoresist grating at the argon ion laser wavelengths. Such a device could eventually be used in linewidth narrowing experiments with a GaAs laser ([Park] describes a similar experiment using a grating on a fibre and a 1.55 μm multimode laser). A detailed discussion of waveguiding in periodic structures is out of place in this conclusion but some general remarks may be made to indicate what is meant by Bragg reflection in the context of distributed feedback structures.

DFB devices in integrated optics incorporate gratings to provide a distributed reflection, which is wavelength dependent. A very simple picture is given in figure A3; a guided mode with propagation constant β encounters a perturbed region of fundamental period Λ_0. This perturbation may be a physical corrugation (Type II filter [Yi-Yan 1978]) or an index modulation (type I filter [Yi-Yan 1978]), such as a pattern ion exchanged through a grating mask. The incident mode is scattered by the perturbation as a whole but individual reflections in the - β direction only combine constructively if the modulus of the grating vector **G** ($|\mathbf{G}| = 2\pi / \Lambda_0$) is exactly twice the propagation constant β figure A4.

$$\beta = \frac{|\mathbf{G}|}{2} = \frac{\pi}{\Lambda_0} \qquad (6.2.1.)$$

Equation (6.2.1.) is known as the Bragg reflection condition.

Reflection for wavevectors near to the value of $\beta = \pi / \Lambda_0$ will be less efficient. The spread in wavelengths around $\lambda_{Bragg} = \Lambda_0 / 2$ for which reflection takes place is inversely proportional to the number of grating lines (for weak coupling).

---

[5] The ion exchange work and filter measurement are being done in collaboration with J. Bell.

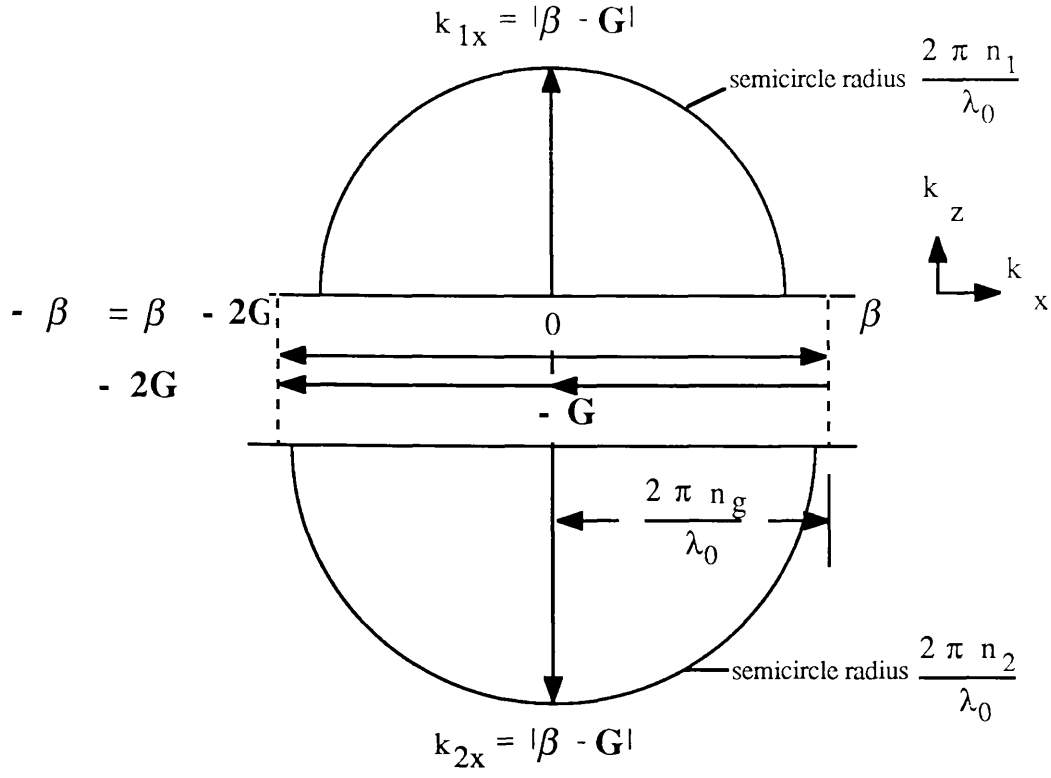

Figure A5. Wavevector diagram for Bragg reflection from a second order grating: $|G| = |\beta|$. In addition to the Bragg reflection $|\beta - 2G|$ along the waveguide, there are allowed solutions radiating normally into the substrate and superstrate, refractive indices $n_2, n_1, n_g > n_1 > n_2$.

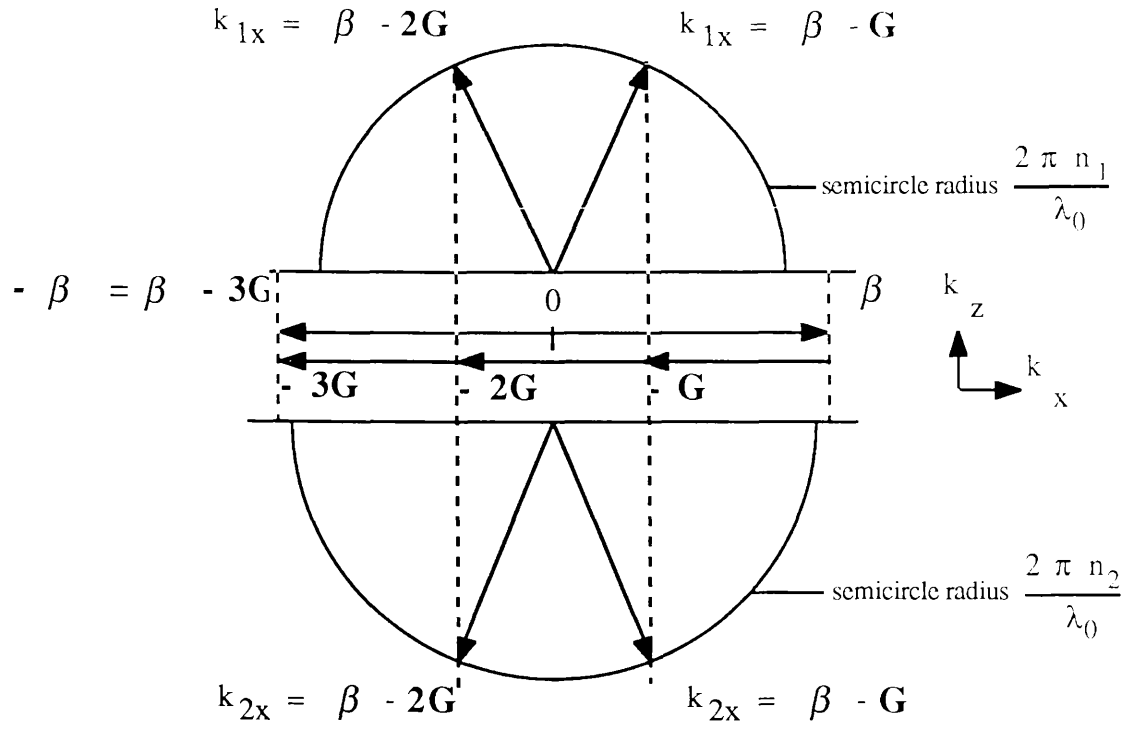

Figure A6. Wavevector diagram for Bragg reflection from a third order grating: $|G| = |2\beta/3|$. Bragg reflection occurs for $-\beta = |\beta - 3G|$. Radiation is also coupled out of the guide with wavevector x components as in the figure, reducing the waveguide reflection efficiency.

The Bragg condition can also be met for gratings with periods of $2\Lambda_0$, $3\Lambda_0$. Bragg reflection is less efficient as the smaller values of $G_{(2)} = \pi / \Lambda$ and $G_{(3)} = 2\pi / 3\Lambda_0$ allow light to be coupled out of the guiding layer (figures A5., A6.). These cases are referred to as 2nd and 3rd order Bragg reflection. In these cases the Bragg reflection can be made more efficient by engineering the grating profile to have a strong Fourier component corresponding to the fundamental Bragg condition periodicity, Λ_0. DFB lasers, especially made in the GaAs / AlGaAs system have very small first order periodicities (~120 nm) due to their high refractive indices (3.6) at their emission wavelengths (~860 nm). Most of these DFB lasers are therefore designed for operation in higher orders (usually the third) to ease fabrication problems [Hunsperger 1984].

Exact field solutions for waves propagating in Type I passive periodic waveguides exist and consist of an infinite series of space harmonics equivalent to the Bloch modes of the electron wavefunction in a lattice (Nearly Free Electron model). In such systems the propagation wavevector is a periodic function of G, the grating vector;

$$\beta = \beta_0 \pm n\frac{2\pi}{\Lambda} \qquad (6.2.2.)$$

i.e. the slab waveguide dispersion diagram (ω v. β) can be considered to repeat itself indefinitely with its origin shifted from $\beta = 0$ in steps of $\pm n|G|$, figure A7. The maximum allowed size of β is restricted by the speed of wave propagation in the guide, so that coupling between modes travelling with wavevectors β and $\beta + |G|$ is not allowed from physical considerations. The $-\beta$ arm of the dispersion diagram shifted to a new origin at $\beta = +G$, now overlaps the $+\beta$ arm of the dispersion diagram centred at $\beta = 0$.

Where the forward and backward propagating modes lines cross on the dispersion diagram, $(|-\beta| = \beta = G / 2 = \pi / \Lambda$, a band gap appears. Wavevectors corresponding to frequencies (ω) inside the gap are complex, having a real part equal to π / Λ and an imaginary part which produces attenuation. The allowed wavevectors outside the gap propagate almost as unperturbed modes of the waveguide; inside the gap a standing wave appears and there is strong reflection. The width of the band gap is determined by the strength of coupling between the forward and backwards propagating modes.

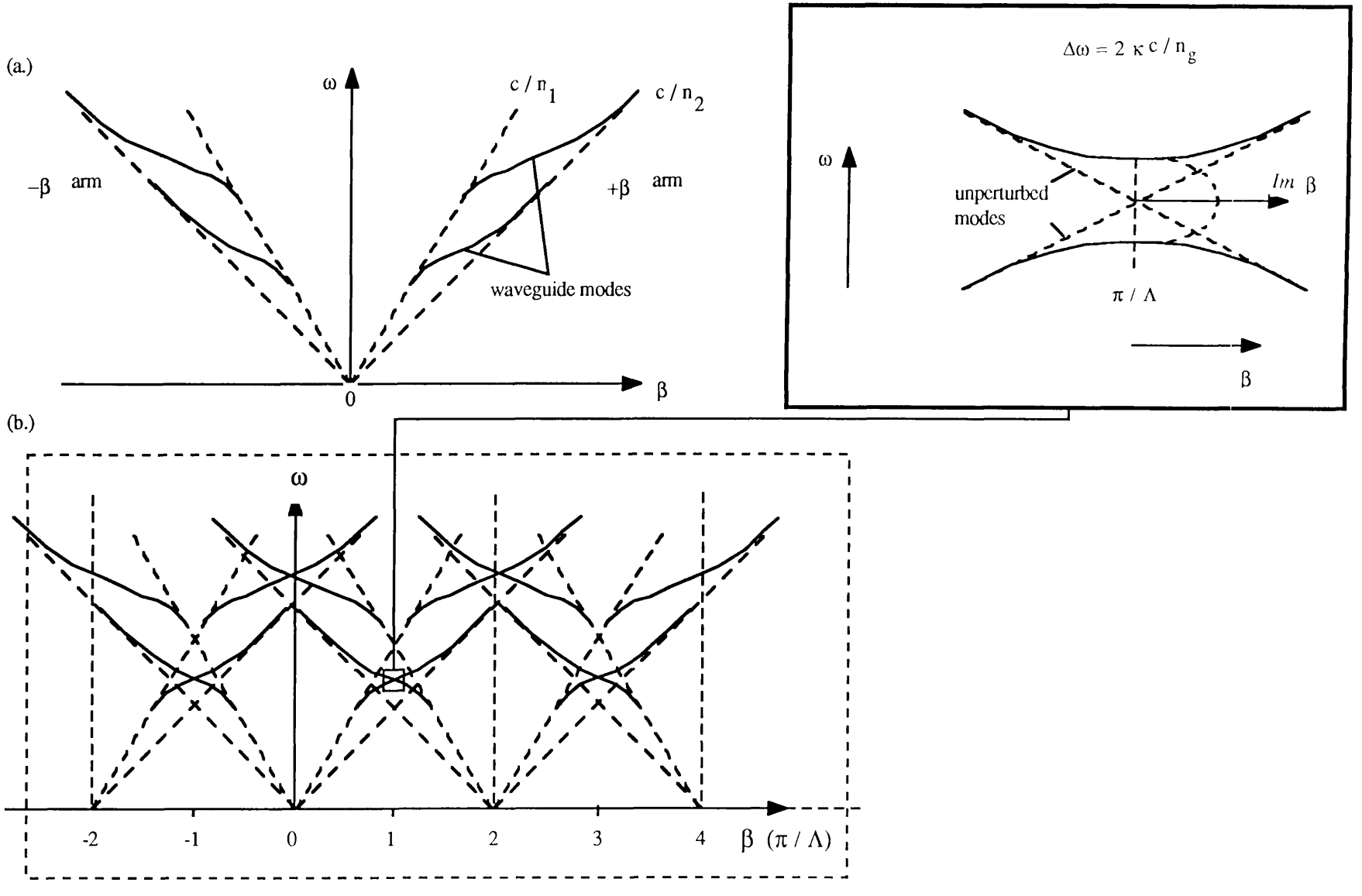

Figure A7. Wavevector dispersion diagram to illustrate Bragg reflection. (a.) is the dispersion diagram of an antisymmetric waveguide with n_2 the guide index $> n_1$ the substrate index. (b.) shows the situation when β is a periodic function of G, the grating vector. The insert shows the band gap that appears due to Bragg reflection, coupling between the $-\beta$ arm shifted to a new origin at G and the $+\beta$ arm. Wavevectors in the gap are complex.

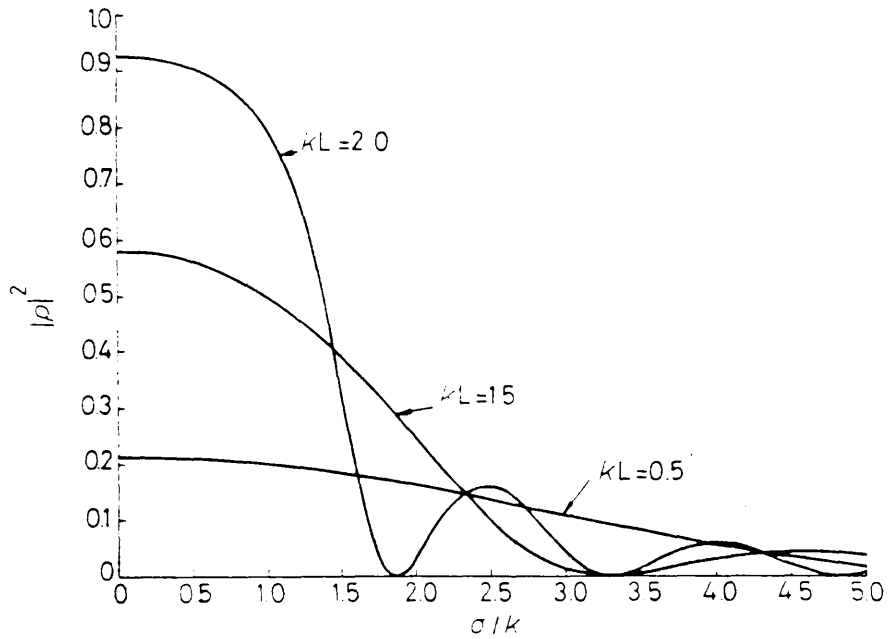

Figure A8. Theoretical plot of filter reflectivity for κ L = 0.5, 1.0, 2.0. (taken from [Yi-Yan 1980])

Mathematically this situation can be approximated by a pair of coupled differential equations, the coupled mode equations [Yi-Yan 1978, 1980], which describe the power interchange between the two interacting modes. The resulting expression for the reflectivity is strongly dependent on the quantity κL where κ is the coupling coefficient that appears in the coupled mode equations and L is the grating length. Reflectivity curves plotted as a function of the wavevector offset from the Bragg condition are shown in figure A8. A larger value of κL results in a narrow bandwidth higher reflectivity filter than a lower value of κL. The calculation of κ, which depends on the overlap of the fields in the grating region and the refractive index perturbation is generally difficult and often involves numerical integration. In the case of weak coupling the characteristics of the grating are determined more by L.

In the case of the ion exchanged filter experiments a grating length of 500 μm should result in a fractional (wavelength) bandwidth of 1 / 1750 or 0.5 nm at 860 nm. Detailed calculations of the waveguide structure will be made once the reflectivity has been measured.

General References.

Publication Index.

The following list contains all the references cited in the thesis, listed alphabetically by principal author and year. Co-authors are listed after the principal author.

Albert J.; Yip G.L., 'Refractive-index profiles of planar waveguides made by ion-exchange in glass.' Appl.Opt.**24**, 22, pp 3692-3693, **1985**.

Anderson E.H.; Horwitz C.M., Smith H.I., 'Holographic lithography with thick photoresist', Appl. Phys. Lett. **43** (9), pp 874- 875, **1983**.

Anderson E.H.; Komatsu K., Smith H.I., 'Achromatic holographic lithography in the deep UV', J.Vac.Sci.Technol. **B6**, p 216, **1988a**.

Anderson E.H.; private communication, **1988b**.

Bäcklin L.; 'Photo-electrochemical laser interference etching for fabrication of 235 nm diffraction gratings on InP', Elect.Lett.**23**, 12, pp 657-659, **1987**.

Beaumont S.P.; Bower P.G., Singh B., Tamamura T., Wilkinson C.D.W., 'Replication of very high resolution e-beam written masks by carbon Kα x-ray contact printing', Microcircuit Engineering 81, pp 34-43, **1981**.

Beesley M.J.; Castledine J.G., Cooper D.P., 'Sensitivity of resist coated silicon slices to argon laser wavelengths', Elect.Lett.**5**, 12, pp 257-258, **1969**.

Beesley M.J.; Castledine J.G., 'The use of photoresist as a holographic recording medium', Appl Opt.**9**, 12, pp 2720 - 2724, **1970**.

Bernacki S.E.; Smith H.I., 'Fabrication of silicon MOS devices using x-ray lithography', IEEE Trans. **ED-22**, 7, pp 421-428, **1975**.

Broers A.N.; 'High Resolution Lithography', Proc. Winter School, Les Houches, France, pp.2-14, **1986**.

Chapman B.N.; 'Glow discharge processes, sputtering and plasma etching', Wiley Interscience, **1980**.

Cheung R. Thoms S., Beaumont S.P., Doughty G., Law V., Wilkinson C.D.W., 'Reactive ion etching of GaAs using a mixture of methane and hydrogen', Elect. Lett. **23**, 16, pp 857 - 859 **1987**.

Chou S.Y.; Smith H.I., Antoniadis D.A., 'Sub-100 nm channel length transistors fabricated using x-ray lithography', J.Vac.Sci. Technol. **B4**(1), pp 253-255, **1986**.

Clark P.; Connolly P., Curtis A.S.G., Dow J.A.T., Wilkinson C.D.W., 'Topographical control of cell behaviour: 1. Simple step clues', Development **99**, pp 439-448, **1987**.

Clark P.; personal communication, **1989**.

Compton A.H.; 'X-rays and electrons', MacMillan and Co., **1927**.

Dalgoutte D.G.; Wilkinson C.D.W., 'Thin grating couplers for integrated optics: an experimental and theoretical study', Applied Optics **14**, 12, pp 2983 - 2997, **1975**.

Dana S.S.; 'Low pressure chemical vapour deposition boro-hydro-nitride films and their use in x-ray masks', J.Vac.Sci.Technol. **B4**(1), pp 235-239, **1986**.

DeGraff P.D.; Flanders D.C., 'Directional oxygen-ion-beam etching of carbonaceous materials', J.Vac.Sci.Technol., **16**(6), pp 1906-1908, **1979**.

Deguchi K.; Ohki S., Hriuchi T., 'A double contrast x-ray mask for high overlay accuracy', Microelectronic Engineering **9**, pp 113-116, North Holland **1989**.

DellaGuardia R.A.; Seeger D.E., Mauer J.L., 'X-ray transmission through low atomic number particles', Microcircuit Engineering **9**, pp 139-142, North Holland **1989**.

Dill F.H.; Hornberger W.P., Hauge P.S., Shaw J.M., 'Characterisation of positive photoresist', IEEE Trans **ED 22**, 7, pp. 445-452, **1975a**.

Dill F.H.; 'Optical lithography', IEEE Trans **ED 22**, 7, pp 440 - 444, **1975b**.

Dill F.H.; Neureuther A.R.,Tuttle J.A., Walker E.J., 'Modeling projection printing of positive photoresists', IEEE Trans.**ED-22**, 7, pp 456-464, **1975c**.

Dill F.H.; Shaw J.M., 'Thermal effects on the photoresist AZ 1350 J', IBM J.Res.Develop. pp 210-218, **1977**.

Dössel K.-F.; Huber H.L., Oertel H., 'Highly-sensitive novolak-based positive X-ray resist', Microcircuit Engineering **5**, pp 97-104, **1986**.

Dow J.A.T.; Clark P., Connolly P., Curtis A.S.G., Wilkinson C.D.W., 'Novel methods for the guidance and monitoring of single cells and simple networks in culture', J.Cell.Sci.Suppl.8, pp 55-79, **1987**.

Dumas R.H.M.; 'Holography application to a grating x-ray mask', PhD thesis, Glasgow University, **1985**.

Efremow N.N.; Economou N.P., 'A simple technique for modifying the profile of resist exposed by holographic lithography', J.Vac.Sci.Technol. **19**(4), pp 1234 - 1237, **1981**.

Eisberg E; 'Fundamentals of modern physics', Wiley **1961**.

Findakly T.; 'Glass waveguides by ion exchange: a review', Optical Engineering, **24**, 2, pp. 244-250, **1985**.

Flanders D.C.; Kogelnik H., Schmidt R.V., Shank C.V.,'Grating filters for thin-film optical waveguides', Appl.Phys.Lett.**24**, 4, pp 194-196, **1974**.

Flanders D.C.; Smith H.I., Lehmann H.W., Widmer R., Shaver D.C., 'Surface relief structures with linewidths below 2000 Å', Appl.Phys.Lett. **32**(2), pp 112-114,**1978a**.

Flanders D.C.; Smith H.I., 'Surface relief gratings of 3200 Å period fabrication techniques and influence on thin film growth', J.Vac.Sci.Technol. **15**(3), pp 1001-1003, **1978b**.

Flanders D.C.; Smith H.I., 'Polyimide membrane x-ray masks - fabrication and distortion measurements', J.Vac.Sci.Technol.**15**(3), pp 995-997, **1978c**.

Flanders D.C.; 'X-ray lithography at ~100 Å linewidths using x-ray masks fabricated by shadowing techniques', J.Vac.Sci.Technol.**16**, 6, pp 1615-1619, **1979**.

Flanders D.C.; 'Replication of 175 Å lines and spaces in polymethylmethacrylate using x-ray lithography', Appl.Phys.Lett. **36**(1), pp 93-96, **1980**.

Gerber J., Hoffman M., Kowarschik R., Sedlacek U., 'Fabrication and application of imaging holographic gratings (chirped gratings) for integrated optics', Optical & Quantum Electronics **19**, pp 247-251, **1987**.

Green M; Cosslett V.E., 'Measurements of K, L and M shell x-ray production efficiencies', Brit. J.Appl.Phys.(J.Phys.D), Ser 2, **1**, pp 425-436, **1968**.

Grobman W.D.; 'Status of x-ray lithography', Proc. International electron devices meeting, pp 415-419, **1980a**.

Grobman W.D.; 'Synchrotron radiation x-ray lithography', Research Report, IBM Yorktown Heights, NY, **1980b**.

Hasegawa S., Itoh J., Atoda N., 'Mask contrast enhancement using beveled edge in x-ray lithography', Microelectronic Engineering **9**, pp 127-130, North Holland **1989**.

Haus H.A. 'Waves and fields in optoelectronics', Chapter 8: Distributed feedback structures, Prentice-Hall, **1984**.

Hecht E.; Zajac A., 'Optics', Addison Wesley, **1974**.

Heuberger A.; 'X-ray lithography with synchrotron radiation', Z.Phys.B.**61**, 473-476, **1985**.

Heuberger A.; 'X-ray lithography', Microcircuit Engineering **5**, pp 3-38, **1986**.

Hunsperger R.G.; 'Integrated optics: theory and technology', 2 nd. Ed. Springer Series in Optical Sciences **33**, Springer-Verlag **1984**.

Ismail K.; Chu W., Antoniadis D.A., Smith H.I., 'Lateral-surface-superlattice and quasi-one dimensional GaAs / GaAlAs MODFETs fabricated using x-ray and deep-UV lithography', J.Vac.Sci.Technol.**B6**, 6, pp 1824-1827, **1988**.

Jaros M.; 'Physics and applications of semiconductor microstructures', Series on semiconductor science and technology **1**, O.U.P. **1989**.

Jenkins R; 'An introduction to x-ray spectrometry', Heyden, **1974**.

Johnson L.F.; Kammlott G.W., Ingersoll K.A., 'Generation of periodic surface corrugations', Applied Optics **17**, 8, pp 1165 - 1181, **1978**.

Karnezos M.; 'Effect of stress on the stability of x-ray masks', J.Vac.Sci.Technol. **B4**(1), pp 226-229, **1986**.

Katzir A.; Livanos A.C., Shellan J.B., Yariv A., 'Chirped gratings in integrated optics', IEEE J.**QE-13**, 4, pp 296-304, **1977**.

Klein M.V.; Furtak T.E., 'Optics', 2nd. ed., Wiley International Edition, **1986.**

Kogelnik H.; Shank C.V., 'Stimulated emission in a periodic structure', Appl.Phys.Lett.**18**, 4, pp 152-154 **1971.**

Kogelnik H.; Shank C.V., 'Coupled wave theory of distributed feedback lasers', J.Appl.Phys.**43**, 5, pp 2327-2335, **1972.**

Kogelnik H.; 'Theory of dielectric waveguides', in T.Tamir (Ed.) 'Integrated Optics', 2nd. Ed., Topics in Applied Physics **7**, Springer-Verlag **1979.**

Ku Y.-C.; Anderson E.H., Schattenburg M.L., Smith H.I., 'Use of a π-phase shifting x-ray mask to increase the intensity slope at feature edges', J.Vac.Sci.Technol.**B6**, p 150, **1988.**

Lin Yi Ching; Jones S., Fuller G., 'Use of anti-reflection coating in bilayer resist process', J.Vac.Sci.Technol. **B.1**(4), pp 1215 - 1218, **1983.**

Livanos A.C., Katzir A., Yariv A., 'Fabrication of grating structures with variable period', Opt.Comm.**20**, 1, pp 179-182, **1977.**

McGillis D.A.; 'Lithography', in Sze Ed. 'VLSI Technology', McGraw Hill, **1983.**

Mackens U.; Mescheder U., Mund F., Lüthje H., 'Fabrication of 0.5 µm NMOS-devices by all level x-ray lithography', Microelectronic Engineering **9**, pp 89-92, **1989.**

Maitland A.; Dunn M.H., 'Laser Physics', North Holland, **1969.**

Michette A.G.; 'X-ray microscopy', Rep.Prog.Phys.**51**, 12, pp 1525-1603, **1988.**

Mogab C.J.; 'Dry etching', in Sze Ed. 'VLSI Techology', McGraw-Hill, **1983.**

Murphy P.; Final year project, Glasgow University **1987.**

Nagel D.J.; 'Plasma sources for x-ray lithography', Chapter 6, VLSI Electronics Microstructure Science Vol. 8, **1983**.

Nakano Y.; Tada K., 'In situ monitoring technique for fabrication of high quality diffraction gratings', Opt.Lett. **13**, 1, pp 7-9, **1988**.

Nakao M.; Sato K., Nishida T., Tamamura T., Ozawa A., Saito Y., Okada I., Yoshihara H., '1.55 μm DFB laser array with λ / 4 -shifted first order gratings fabricated by x-ray lithography', Elect.Lett. **25**, 2, pp 148-149, **1989**.

Palmer E.W.; Hutley M.C., Franks A., Verrill J.F., Gale B., 'Diffraction Gratings', Rep. Prog. Phys. **38**, p 975-1048, **1975**.

Park C.A.; Rowe C.J., Buus J., Reid D.C.J., Carter A., Bennion I., 'Single-mode behaviour of a multimode 1.55 μm laser with a fibre grating external cavity', Elect.Lett.**22**, 21, pp 1132-1134, **1986**.

Pinak J.; Jerontnek H., Opilski Z., Wojtala K., 'Planar diffusion glass waveguides obtained by immersing in molten KNO_3', Optics Applications **XII**, 1, pp 11 - 17, **1982**.

Pircher G.; Perrocheau J., 'Submicron lithography tools', Proc. Winter School, Les Houches, France, pp.15-35, **1986**.

Plotnik I.; 'Reactive-ion etching of Tungsten for sub-50 nm, high contrast x-ray mask fabrication', M.Sc. thesis, Massachusetts Institute of Technology, May **1983**.

Podlesnik D.V.; Gilgen H.H., 'Laser-controlled etching of semiconductors in solutions', in Ibbs K.G. and Osgood R.M. Ed.'Laser Chemical Processing for Microelectronics', Cambridge U.P., **1989**.

Pun E.Y.B.; 'Thin film Bragg deflection gratings for integrated optics', PhD thesis, Glasgow University, **1983**.

Rishton S.A.; 'Resolution limits in electron beam lithography', Ph.D. thesis, Glasgow University, **1984**.

Rudolph G.; Schmahl G., 'Spektroskopische Beugungsgitter Hoher Teilungsgenauigkeit erzeugt mit Hilfe von Laserlicht und Photoresistschichten', Optik **30**, pp 475-487, **1970**.

Sekartedjo K.; Eda N., Furuya K., Suematsu Y., Koyama F., Tanbun-Ek T.,'1.5 μm Phase shifted DFB lasers for single mode operation.', Elect.Lett. **20**, 2, pp 80-81, **1984**.

Sekimoto M.; Yoshihara H., Ohkubo T., Saitoh Y., 'Silicon nitride single layer x-ray mask', Japan.J.Appl.Phys. **20**, 9, L669-L672, **1981**.

Shank C.V.; Schmidt R.V., 'Optical technique for producing 0.1 μm periodic surface structures', Appl.Phys.Lett.**23**, 3, pp 154-155, **1973**.

Shaver D.C.; Flanders D.C., Ceglio N.M., Smith H.I., 'X-ray zone plates fabricated using electron-beam and x-ray lithography', J.Vac.Sci.Technol. **16**, 6, pp 1626-1630, **1979**.

Shaw J.M.; Frisch M.A., Dill F.H., 'Thermal analysis of positive photoresist films by mass spectrometry', IBM J.Res.Develop. pp 219-226, May **1977**.

Shellan J.B.; Hong C.S., Yariv A., 'Theory of chirped gratings in broad band filters', Opt.Com.**23**, 3, pp 398-400, **1977**.

Smith H.I.; Spears D.L., Bernacki S.E., 'X-ray lithography: a complimentary technique to electron beam lithography', J.Vac.Sci.Technol.**10**, 6, pp 913-917, **1973**.

Smith H.I.; 'Fabrication techniques for surface-acoustic wave and thin-film optical devices', Proc. IEEE, **62**, 10, **1974**.

Smith H.I., Flanders D.C., 'X-ray lithography', Japan J.Appl.Phys.**16(S16)**, pp 61-65, **1977**.

Smith H.I.; 'A review of submicron lithography', Superlattices and Microstructures, **2**, 2, pp 129-142, **1986**.

Smith H.I.; personal communication, **1989**.

Spears D.L.; Smith H.I., 'High resolution pattern replication using soft x-rays', Elect.Lett. **8**, 4, pp 102-104, **1972**.

Spiller E.; Feder R., Topalian J., Gudat W., Eastman D., 'X-ray lithography with synchrotron radiation', Research Report:IBM Yorktown Heights, NY, **1976**.

Spiller E.; Feder R., 'X-ray lithography', in H.J. Queisser (Ed.) 'X-ray Optics, Applications to Solids', Topics in Applied Physics **22**, Springer-Verlag **1977**.

Stark A; personal communication, Glasgow University, **1985**.

Steward E.G.; 'Fourier Optics: an introduction', Ellis Horwood, **1983**.

Suhara T.; Nishihara H., 'Integrated optics components and devices using periodic structures' , IEEE J. **QE-22**, 6, pp 845-867, **1986**.

Sullivan P.A.; McCoy J.H., 'Optimised source for x-ray lithography of small area devices', J.Vac.Sci.Technol. **12**, 6, pp 1325-1328, **1975**.

Suzuki K.; Matsui J., 'SiN membrane masks for x-ray lithography', J.Vac.Sci.Technol. **20**(2), pp 191-194, **1982**.

Sze S.M.; 'Semiconductor devices; physics and technology', Wiley **1985**.

Taylor G.N.; 'Organosilicon monomers for plasma-developed x-ray resists', J.Vac.Sci. Technol. **19**(4), pp 872-880, **1981**.

Thomas K.M.; Beaumont S.P., Wilkinson C.D.W., 'Soft x-ray contact printing of periodic structures for distributed feedback (DFB) semiconductor lasers and integrated optics', SPIE Proc **993**, Integrated Optical Circuit Engineering VI, Boston, **1988**.

Thoms S.; personal communication **1989**.

Tsang W. -T.; Wang S., 'Simultaneous exposure and development technique for making gratings on positive photoresist', Appl.Phys.Lett.**24**, 4, pp 196-199, **1974**.

Tsang W. -T.; Wang S., 'Grating masks suitable for ion-beam machining and chemical etching', Appl.Phys.Lett.**25**, 7, 415-418, **1974b**.

Tsang W. -T.; Wang S., 'Experimental studies of photoresist gratings', Wave Electronics **1**, pp 85-95, **1974-75**.

Utaka K.; Akiba S., Sakai K., Matsushima Y., ' λ / 4 shifted InGaAsP / InP DFB lasers by simultaneous holographic exposure of positive and negative photoresists', Elect.Lett.**20**, 24, pp 1008-1010, **1984**.

Walker E.J.; 'Reduction of photoresist standing wave effects by post exposure bake', IEEE Trans.**ED-22**, pp 464-466, **1975**.

Walker R.G.; Wilkinson C.D.W., Wilkinson J.A.H., 'Integrated optical waveguiding structures made by silver ion exchange in glass. 1: The propagation characteristics of stripe ion exchanged waveguides; a theoretical and experimental investigation', Appl.Opt.**22**, 12, pp 1923-1928, **1983a**.

Walker R.G.; Wilkinson C.D.W., 'Integrated optical waveguiding structures made by silver ion exchange in glass. 2: Directional coupler and bends', Appl.Opt.**22**, 12, pp 1929-1936, **1983b**.

Warren A.C.; Plotnik I., Anderson E.H., Schatternburg M.L., Antoniadis D.A., Smith H.I., 'Fabrication of sub-100 nm linewidth periodic structures for study of quantum effects from interference and confinement in Si inversion layers', J.Vac.Sci.Technol. **B4**(1), pp 365-367, **1986**.

Washo B.D.; 'Rheology and Modelling of the spin coating process', IBM J. Res. Develop. March **1977**.

Widmann D.W.; Binder H., 'Linewidth variations in photoresist patterns on profiled surfaces', IEEE Trans.**ED-22**, 7, pp 467-471, **1975**.

Wilkinson C.D.W.; Beaumont S.P., 'High resolution fabrication', in SERC Low Dimensional Structures Summer School, **1985**.

Wilkinson C.D.W.; Beaumont S.P., 'Electron beam nanolithography', Proc. Winter School, Les Houches, France, pp.36-50, **1986**.

Yahimatsu M; Kozaki S., 'High brilliance X-ray sources', in H.J.Queisser (Ed.) 'X-ray Optics, Applications to Solids', Topics in Applied Physics **22**, Springer-Verlag **1977**.

Yamada M.; Nakaishi M., Kudou J., Eshita T., Furumura Y., 'An x-ray mask using Ta and heteroepitaxially grown SiC', Microelectronic Engineering **9**, pp 135-138, **1989**.

Yariv A.; 'Coupled mode theory for guided wave optics', IEEE J.**QE-9**, 9, pp 919-933, **1973**.

Yariv A.; Nakamura M., 'Periodic structures for integrated optics', IEEE J.**QE-13**, 4, pp 233-253, **1977**.

Yip G.L.; Albert J., 'Characterisation of planar optical waveguides by K^+- ion exchange in glass', Optics Lett.**10**, 3, pp 251-253, **1985**.

Yi-Yan A.; 'Frequency selective grating filters for integrated optics', PhD thesis, Glasgow University, **1978**.

Yi-Yan A.; Wilkinson J.A.H., Wilkinson C.D.W., 'Optical waveguide filters for the visible spectrum', IEE Proc.**127**, H, 6, pp 335-341, **1980**.

Zaidi S.H.; Brueck S.R.J., 'High aspect ratio holographic gratings', Appl.Opt.**27**, 14, pp 2999-3002, **1988**.

Product Index.

ARC; Brewer Scientific inc. P.O.Box GG, Rolla MO 65401 USA; UK distributor: Micro-Image Technology Ltd., Amber Business Centre, Riddings, Derbyshire DE55 4DA, 0773 609409.

AZ 1300, AZ 1400, AZ 1500 series photoresists; **AZ Developer**; technical data, Hoechst UK Ltd., Electronic Products Division, 56 Stewarts Rd., Finedon Rd Industrial Estate, Wellingborough, Northhants NN8 4RJ, 0993 226060.

Hitatchi PIQ-13 Polyimide; Hitachi Chemical C0. Ltd., 1-1, 2 - chome, Nishishinjuku, Shinjuku-ku, Tokyo, Japan 160. Tokyo (346) 3111.

Index matching oils; Cargille Laboratories Inc., Cedar Grove, N.J. 07009, USA, (0101) 201 239 6633.